ISSN: 2224-2007
E-ISSN: 2707-7365

# MIJST

# MIST International Journal of Science and Technology

*A Peer Reviewed Online Open Access Journal*

Volume 13
December 2025

Military Institute of Science and Technology (MIST)
*https://mijst.mist.ac.bd/mijst*

# MIJST

MIST International Journal of Science and Technology

Volume 13

December 2025

# EDITORIAL BOARD




**CHIEF PATRON**

***Maj Gen Md Nasim Parvez, BSP, ndc, afwc, psc***
*Commandant*
*Military Institute of Science and Technology (MIST)*
*Dhaka, Bangladesh*
*chief.patron@mijst.mist.ac.bd*





**PUBLICATION ADVISOR**

***Col Khalid Mahmud***
*Acting Director, R&D Wing*
*Military Institute of Science and Technology (MIST)*
*Dhaka, Bangladesh*
*publication.advisor@mijst.mist.ac.bd*





**EDITOR-IN-CHIEF**

***Dr. Firoz Alam***
*Professor, School of Engineering, RMIT University*
*Melbourne, Australia*
*chief.editor@mijst.mist.ac.bd*





**EXECUTIVE EDITOR**

***Dr. A.K.M. Nurul Amin***
*Professor, Industrial and Production Engineering*
*Military Institute of Science and Technology (MIST)*
*Dhaka, Bangladesh*
*executive.editor@mijst.mist.ac.bd*





**ASSOCIATE EDITOR**

***Lt Col Md Altab Hossain, PhD, CEng, EME***
*Associate Professor, Nuclear Science and Engineering*
*Military Institute of Science and Technology (MIST)*
*Dhaka, Bangladesh*
*associate.editor1@mijst.mist.ac.bd*





**ASSOCIATE EDITOR**

***Lt Col Muhammad Nazrul Islam, PhD, Sigs***
*Associate Professor, Computer Science and Engineering*
*Military Institute of Science and Technology (MIST)*
*Dhaka, Bangladesh*
*associate.editor2@mijst.mist.ac.bd*



**COPY EDITOR**

***Dr. Md Enamul Hoque***
*Professor, Biomedical Engineering*
*Military Institute of Science and Technology (MIST)*
*Dhaka, Bangladesh*
*enamul1973@gmail.com*

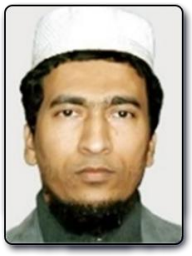
## EDITORIAL BOARD MEMBERS



***Dr. G. M. Jahid Hasan***
*Professor, MIST, Bangladesh*
*jahid@ce.mist.ac.bd*



***Dr. Md. Tauhid Ur Rahman***
*Professor, MIST, Bangladesh*
*tauhid@ce.mist.ac.bd*



***Dr. Md. Mahbubur Rahman***
*Professor, MIST, Bangladesh*
*mahbub@cse.mist.ac.bd*



***Dr. AKM Badrul Alam***
*Professor, MIST, Bangladesh*
*badrul.alam@pme.mist.ac.bd*



***Md. Sazzad Hossain***
*Professor, MIST, Bangladesh*
*sazzad@arch.mist.ac.bd*



***Dr. Abdul Hasib Chowdhury***
*Professor, BUET, Bangladesh*
*hasib@eee.buet.ac.bd*



***Dr. Shahjada Tarafder***
*Professor, BUET, Bangladesh*
*mshahjadatarafder@name.buet.ac.bd*



***Dr. Mohammad Ali***
*Professor, BUET, Bangladesh*
*mali@me.buet.ac.bd*



***Prof. Dr Mokhlesur Rahman***
*Professor, MIST, Bangladesh*
*mokhlesur@nse.mist.ac.bd*



***Dr. Ataur Rahman***
*Professor, International Islamic University Malaysia, Malaysia*
*arat@iium.edu.my*



***Dr. Azam Ali***
*Professor, University of Otago, New Zealand*
*azam.ali@otago.ac.nz*



***Dr. Bashir Ahmmad Arima***
*Professor, Yamagata University, Japan*
*arima@yz.yamagatau.ac.jp*



***Dr. Nawshad Ul Haque***
*Professor, Commonwealth Scientific and Industrial Research Organisation (CSIRO), Australia*
*nawshad.Haque@csiro.au*



***Dr. Mamdud Hossain***
*Professor, Robert Gordon University, UK*
*m.hossain@rgu.ac.uk*



***Dr. Reza N. Jazar***
*Professor, RMIT University, Australia*
*reza.nakahiejazar@rmit.edu.au*



***Dr. Mohamed H. M. Hassan***
*Professor, Alexandria University, Egypt*
*mhmheg@yahoo.com*



***Dr. Xiaolin Wang***
*Professor, University of Tasmania, Australia*
*xiaolin.wang@utas.edu.au*



***Dr. Santanu Bandyopadhyay***
*Professor, Indian Institute of Technology (IIT) Bombay, India*
*santanub@iitb.ac.in*



***Dr. Nakorn Tippayawong***
*Professor, Chiangmai University, Thailand*
*n.tippayawong@yahoo.com*



***Dr. Yingai Jin***
*Professor, Jilin University, China*
*jinya@jlu.edu.cn*



***Dr. Simon Watkins***
*Professor, RMIT University, Australia*
*simon.watkins@rmit.edu.au*



***Dr. Somnath Chattopadhyaya***
*Professor, Indian Institute of Technology (IIT) Dhanbad, India*
*somnathchattopadhyaya@iitism.ac.in*



***Dr. Anupam Basu***
*Professor, Jadavpur University, India*
*anupambas@gmail.com*



***Dr. Arnab Roy***
*Professor, Indian Institute of Technology (IIT) Kharagpur, India*
*arnab@aero.iitkgp.ac.in*



***Dr. Drazan Kozak***
*Professor, University of Zagreb, Croatia*
*dkozak@unisb.hr*



***Dr. Akshoy Ranjan Paul***
*Professor, Motilal Nehru National Institute of Technology Allahabad, India*
arpaul@mnnit.ac.in



***Lt Col Muhammad Rabiul Islam, PhD, EME***
*Associate Professor, MIST, Bangladesh*
*mrabi77@yahoo.com*



***Lt Col Khondaker Sakil Ahmed, PhD, PEng, CEng, Engrs***
*Associate Professor, MIST, Bangladesh*
*drksa@ce.mist.ac.bd*



***Lt Col Mahabubar Rahman Shah, MPhil, PhD, AEC***
*Associate Professor, MIST, Bangladesh*



***Lt Col Kazi Shamima Akter, PhD, Engrs***
*Associate Professor, MIST, Bangladesh*
*shamima@ewce.mist.ac.bd*



***Lt Col Hussain Md Abu Nyeem, PhD, EME***
*Associate Professor, MIST, Bangladesh*
*h.nyeem@eece.mist.ac.bd*



***Lt Col Md Aminul Islam, PhD, EME***
*Associate Professor, MIST, Bangladesh*
*aminul@eece.mist.ac.bd*



***Dr. T. M. Shahriar Sazzad***
*Associate Professor, MIST, Bangladesh*
*tss7standrews@gmail.com*



***Dr. Tanser ali***
*Associate Professor, AIUB, Bangladesh*
*tanseer@aiub.edu*



***Tariq Mahbub***
*Assistant Professor, MIST, Bangladesh*
*mahbubtariq@me.mist.ac.bd*



***Maj Md. Manwarul Haq, PhD, AEC***
*Assistant Professor, MIST, Bangladesh*
*manwar.haque@sh.mist.ac.bd*



***Mahbuba Ferdous***
*Assistant Professor, Department of Aeronautical Engineering (AE)*
*mahbuba@ae.mist.ac.bd*



***Major Md. Manwarul Haq, PhD, AEC***
*Assistant Professor, Department of Science & Humanities (SH)*
*manwar.haque@sh.mist.ac.bd*



***Lt Col Sanjeev Delwar, psc, Engrs***
*GSO-1 (Research), MIST, Bangladesh*
*gso1@rnd.mist.ac.bd*



***Maj Kazi Imtiaz Kabir, SGP, Engrs***
*GSO-2 (ARSTC), MIST, Bangladesh*
*kazi.kabir@rnd.mist.ac.bd*



***Md Moslem Uddin***
*Librarian, MIST, Bangladesh*
*librarian@mist.ac.bd*



**WEB CONSULTANT**

***Dr. Kazy Noor e Alam Siddiquee***
*Associate Professor, CSE, MIST, Bangladesh*
*web.consultant@mijst.mist.ac.bd*



**ASST. WEB CONSULTANT**

***Mehedi Hasan Hemel***
*Assistant System Engineer, R&D Wing, MIST, Bangladesh*
*assistant.web.consultant@mijst.mist.ac.bd*

## DISCLAIMER

The analysis, opinions, and conclusions expressed or implied in this Journal are those of the authors and do not necessarily represent the views of the MIST, Bangladesh Armed Forces, or any other agencies of Bangladesh Government. Statements of fact or opinion appearing in MIJST Journal are solely those of the authors and do not imply endorsement by the editors or publisher.

**ISSN: 2224-2007**
**E-ISSN: 2707-7365**

## QUERIES ON SUBMISSION

For any query on submission the author(s) should contact: MIST, Mirpur Cantonment, Dhaka-1216, Bangladesh; Tel: 88 02 8034194, FAX: 88 02 9011311, email: *mijst@mist.ac.bd*. For detailed information on submission of articles, the author(s) should refer to the Call for Papers and About MIJST at the back cover of the MIJST Journal. Authors must browse MIJST website through the journal link (*https://mijst.mist.ac.bd/mijst*) for electronic submission of their manuscripts.

## PUBLISHER

**Military Institute of Science and Technology (MIST), Dhaka, Bangladesh**
All rights reserved. No part of this publication may be reproduced, stored in retrieval system, or transmitted in any form, or by any means, electrical, photocopying, recording, or otherwise, without the prior permission of the publisher.

## DESIGN AND PRINTING

**Research and Development Wing**
Military Institute of Science and Technology (MIST)
Dhaka, Bangladesh

# FOREWORD

**Bismillahir Rahmanir Rahim**

It gives me an immense pleasure to present the December 2025 (volume 13) of the MIST International Journal of science and Technology (MIJST). MIJST is an international interdisciplinary, open-access, peer-reviewed journal that publishes articles in science, engineering and technology. MIJST is a bi-annual journal dedicated to fostering intellectual curiosity, academic excellence and creative expression.

Military Institute of Science and Technology (MIST) started its journey from 1998 with a vision of becoming a "Center of Excellence". Since its inception, MIST plays a vital role in nation - building by providing quality and exceptional engineering education. MIST also has got remarkable contribution on the research field on science and technology. MIJST is not only a collection of articles but also a testament to the vibrant scholarly community that thrives within our institution. MIJST has already been indexed by a number of databases and efforts are underway to have indexed in Scopus and Web of Science for global recognition.

We take great pleasure in unveiling the December issue, volume 13 of our journal-MIJST. All the articles are related to the pioneer research and beacons of knowledge, innovation and ethical responsibility. Through this research, researchers demonstrate their commitment to advancing ideas, technological excellence and contribute meaningful to the society.

I extend my heartfelt appreciation to the editorial team, contributors and reviewers whose dedication has ensured the quality and relevance of this publication. My gratitude to all the authors whose contributions have enriched the content of journal. I also extend my deepest thanks to all national and international board members of MIJST for their constant advice and recommendations for the development of MIJST.

As the Chief Patron, I am proud to endorse the endeavor and encourage all readers to engage with the insights presented herein. May MIJST uphold its role as a pillar of technological excellence in the years to follow.



**Major General Md Nasim Parvez, BSP, ndc, afwc, psc**
*Commandant, MIST, Bangladesh*
*Chief Patron, MIJST, Bangladesh*

# EDITORIAL

I am delighted to inform you that we published the December issue well ahead of the deadline set. My deepest gratitude goes to authors, reviewers, editorial and production teams for this success.

The editorial board and MIST have decided to apply for the indexing of the MIST International Journal of Science and Technology (MIJST) by SCOPUS and WoS in 2026. It is worthwhile to mention that MIJST is already indexed by BanglaJOL, Publons, Creative Commons, Open Journal System, Google Scholar, DOI Crossref, and Microsoft Academic Search.

Our journal invites original, creative, and unpublished scholarly works in the domains of science, engineering, technology, or related topics. All contributions undergo a double-blind peer review process with detailed comments and suggestions to authors for enhancing the quality and uniqueness of articles.

The December 2025 issue consists of ten scholarly articles encompassing potential health impacts from radioactive releases of a nuclear power plant accident, evaluation of properties of limestone power blended concrete, agar from red algae, flexural response of stainless-steel reinforced concrete beams, biometric authentication and digital certificate verification through block technology, visual and genetic distance analysis of Gamma-irradiated lemon leaf mutants developed using leaf-cut method, impact of inverter control and solar photovoltaic integration on small signal stability augmented with battery, power consumption analysis of UAVs with varying payloads, the Dera heterotopia: meaning of home for transgender community, and a neural network based software defect prediction approach using SMOTE and noise filtering-CLNI. Each of the ten articles deals with an important topic.

My humble request is to disseminate the word about the MIST International Journal of Science and Technology among your fellow academics, researchers, research students, and library liaisons.

Your comments and suggestions are wholeheartedly welcomed. Please feel free to call at +61 3 99256103 or contact via email: mijst@mist.ac.bd or firoz.alam@rmit.edu.au.

Yours sincerely,



**Prof. Dr. Firoz Alam**
*Editor in Chief*

# INDEX


| Serial | Articles | Pages |
|---|---|---|
| 1. | **Evaluation of Physical, Mechanical, and Durability Properties of Limestone Powder Blended Concrete**<br>*Md. Jahidul Islam, Tasnia Ahmed[*] , Nishat Naila Meghna, Ismat Abida, and Nayeem Mohammad Mashfiq* | 01-13 |
| 2. | **Potential Health Impacts from Radioactive Releases at Rooppur Nuclear Power Plant Under Hypothetical Accident Scenario**<br>*Md Rosaidul Mawla1,[*] , Radmim Ryean[1] , Anisur Rahman[2] , Abdus Sattar Mollah[3] , Md. Shafiqul Islam[4] , Kazi Imtiaz Kabir[5]* | 15-25 |
| 3. | **Agar from Red Algae (Gracilaria tenuistipitata) as a Valuable Biopolymer: Extraction and Characterization**<br>*Fawzia Afrin Rimpy[1] , Md Enamul Hoque1[*], Quazi Farsheed Mahmud[1] , Itmam Nowroj[1] , Sazedur Rahman[2] , Tarek El-Bialy[3] , M. Azam Ali[4]* | 27-38 |
| 4. | **Numerical Investigation for Flexural Response of Stainless-Steel Reinforced Concrete Beams**<br>*Nusrat Tabassum[1], Abdullah Al-Moneim[1,*,] Said Razu[1], Aziz Ahmed[2], Khondaker Sakil Ahmed[1]* | 39-46 |
| 5. | **Decentralized LRM System Architecture with Biometric Authentication and Digital Certificate Verification through Blockchain Technology**<br>*Shakil Mosharrof[1] , Farhan Nasif Nizami[1] , Mahdi Mohtasim[1] , Mahdi Adib[1] , M. Akhtaruzzaman[*2] , Md Shofiqul Islam[3] , Muhammad Towfiqur Rahman[4] , and Hosney Jahan[5]* | 47-63 |
| 6. | **Visual Assessment and Genetic Distance Analysis of Gamma-Irradiated Lemon Leaf Mutants Developed Using the Leaf-Cut Method**<br>*Jawata Afnan[*1], Moriom Azad[1], Mokhlesur Rahman[1] and Md Shaheen Sarkar[2]* | 65-71 |
| 7. | **Impact of Inverter Control and Solar Photovoltaic Integration on Small Signal Stability Augmented with Battery: Modal Analysis Approach**<br>*Md. Mahadi Hasan[*] , Md. Imranul Hasan Emon, Hasan Monir, and Md Ahsan Kabir* | 73-84 |
| 8. | **Power Consumption Analysis of UAVs with Varying Payloads for Next Generation Wireless Networks**<br>*Saif Ahmed[*], and Nimul Islam Emon* | 85-95 |
| 9. | **The Dera Heterotopia: Meaning of Home for the Hijra Community**<br>*S. Sameen[1*] , A. R. Hossain[2] , F. Jerin[1] , S. Shreya[1] , S. A. Anjum[1] , A. Mumtarin[1] and T. Tabassum* | 97-110 |
| 10. | **A Neural Network Based Software Defect Prediction Approach Using SMOTE and Noise Filtering-CLNI**<br>*Ahmmed Bin Ashfaque[1] , Abdus Sattar[2] , Hosney Jahan[*3] , M. Akhtaruzzaman[4] , and Fernaz Narin Nur[5]* | 111-121 |

MIJST
MIST International Journal of Science and Technology

# Evaluation of Physical, Mechanical, and Durability Properties of Limestone Powder Blended Concrete

**Md. Jahidul Islam, Tasnia Ahmed*, Nishat Naila Meghna, Ismat Abida, and Nayeem Mohammad Mashfiq**

Department of Civil Engineering, Military Institute of Science and Technology, Dhaka, Bangladesh

***Corresponding Email:** *tasnia@ce.mist.ac.bd*

**ARTICLE INFO**

**Article History:**

*Received: 13th July 2025*
*Revised: 29th September 2025*
*Accepted: 06th October 2025*
*Published: 30th December 2025*

**Keywords**:

*Blended cement concrete*
*Limestone powder*
*Tensile strength prediction*
*Flexural strength*
*Durability*

**ABSTRACT**

Reducing the amount of cement in construction has become a challenge in the 21st century. In this study, limestone powder (LSP) is adopted to partially replace cement at different weight percentages (5%, 10%, 15% and 20%). The influence of LSP on engineering properties such as workability, compressive strength, splitting tensile strength, flexural strength and toughness, water permeability, and surface resistivity is investigated to assess the acceptability of LSP blended concrete and to find the optimum replacement level considering these properties. At low replacement levels (5% and 10%), the mechanical and durability properties are improved due to the nucleation effect of LSP. Beyond 10% replacement, the dilution effect dominates which disadvantages the concrete. The workability linearly rises with the increase in the LSP content. The compressive and tensile strength does not vary much from the control specimen up to a 10% replacement level. The highest compressive and flexural strength is recorded for 10% LSP replacement. Toughness calculated from the beam load-deflection curve showed an increased value with increased LSP replacement. In comparison to the control specimens, 6.4% higher flexural strength and 90% higher toughness index are achieved for 10% LSP. An equation has been proposed using a machine learning approach to predict the tensile strength of LSP blended concrete with 87% accuracy. Water permeability and chloride ion penetrability are reduced for higher LSP content as LSP works as a filler and enhances pore structure. This study summarizes that 10% cement substitution with the LSP can be adopted for overall better mechanical and durability properties of concrete.

This work is licensed under a *Creative Commons Attribution-Non-commercial 4.0 International License.*

## 1. INTRODUCTION

Concrete is a multi-component and versatile composite material. It is used at a much higher rate today on account of the expanding population and urbanization. Concrete manufacturing has put a lot of pressure on the atmosphere. The global cement production, a key component of concrete, has been increasing steadily, reaching over 4.3 billion tons in 2022 (Barbhuiya *et al.*, 2024). The annual cement supply accounts for around 7-8% of global $CO_2$ emissions, hence contributing significantly to climate change and the greenhouse effect (Amran *et al.*, 2022).

Over the last few decades, using various byproducts in concrete production has become a common practice. Natural pozzolans, silica fume, slag, fly ash, and limestone powder can be used as cementing materials (Meghna *et al.*, 2025; T. Ahmed *et al.*, 2024; Islam *et al.*, 2023a; Islam *et al.*, 2023b; P. P. Li *et al.*, 2020; EN, 2000; T. Ahmed *et al.*, 2025; Araf *et al.*, 2023). The use of such materials reduces the environmental impact of Portland cement manufacturing, conserves natural resources, and increases concrete's mechanical and durability properties (Meddah *et al.*, 2014). Limestone powder (LSP), a byproduct of limestone quarry, has long been utilized in cement-based products. It is natural and readily available at a low cost. Various standards allow LSP applications in cement manufacturing (ASTM C150, 2022; ACI 211.7R-15, 2015). Additionally, structures made with LSP as cement substitution are proven to produce 30% less $CO_2$ than traditional concrete (Barbhuiya *et al.*, 2023).

LSP exhibits limited pozzolanic activity due to its primary composition of calcium carbonate ($CaCO_3$), which does not readily react with calcium hydroxide (CH) to form additional calcium silicate hydrate (C-S-H) gel. (Liu & Yan, 2010). Although the pozzolanic activity of LSP is minimal, its role in refining concrete microstructure can positively influence the mechanical properties through its micro-filler effect, particle packing, and reducing porosity over time (Zhao *et al.*, 2024; Mahi *et al.*, 2025).

P. P. Li *et al.* (2020) substituted LSP with binder by 0 to 80% volume. Their results indicate that even though a high volume of LSP produces cost-effective and eco-friendly concrete, a 50% LSP replacement level appeared to be the optimum, considering the compressive strength, porosity, and binder efficiency. Gesoğlu *et al.* (2012) found that for 5%, 10% and 20% LSP, the compressive strength increased respectively by 8%, 5% and 7% compared to control cylinders. Their study suggests a 10% LSP replacement level to be the optimum percentage. Vance *et al.* (2013) illustrated the workability of concrete replacing cement with LSP up to 40% and using different particle sizes of LSP. With the increase in the percentage of LSP, the workability of concrete decreased. LSP has a filler effect here, and as particle size grows, plastic viscosity and yield stress drop, reducing the workability of concrete.

Lothenbach *et al.* (2008) found that the early compressive strength decreases with a large volume of LSP; however, it increases with concrete age. On the other hand, Celik *et al.* (2019) found that the control sample, which contains no replacement of cement, showed higher strength than the sample containing 15% replacement of cement at 1 day and 3 days, respectively. However, the strength of concrete having 15% LSP was just 2% lower after 7 days. Although this is an excellent early age strength growth, the concrete containing a 15% LSP mixture provided 15% less strength than the concrete containing no LSP content after 91 days of hydration. According to Dhir *et al.* (2007), regardless of curing age, there was a consistent decrease in compressive strength test results with increasing LSP content.

Moreover, Demirhan *et al.* (2019) observed that the reduction in mortar compressive strength was 14%, 22%, and 28% for LSP replacement of 15%, 25%, and 35%, respectively, compared to the no replacement mortar at 28 days. The study indicated that LSP content greater than 15% did not continue hydration processes, leading to intensified matrices with reduced compressive strength. Tensile strength also decreases in the presence of LSP. Q. Wang *et al.* (2017) demonstrated that the splitting tensile strength of concretes containing LSP stayed virtually constant (within a limited fluctuation range) from 1 to 5 years. In contrast, plain cement concrete showed increased strength over the same period. Mohammed and Al-Numan (2024) found that replacing cement with 15% or 20% LSP reduced the 28-day splitting tensile strength by 39%, compressive strength by 71%, and flexural strength by 43% compared to the samples without LSP.

The addition of LSP can reduce porosity and pore size of concrete up to a certain replacement level. Several studies have demonstrated that using up to 8-10% LSP as a cement replacement can lower the water permeability of concrete (Lin *et al.*, 2020; L. G. Li & Kwan, 2015; Jiajian Chen *et al.*, 2014). JJ Chen *et al.* (2014) observed that, at the same w/c ratio, the water penetration depth decreased as the volume of LSP increased. This effect of LSP was generally more significant at higher w/c ratios. They observed that with 8% limestone filler added as cement paste replacement, the water penetration depth was reduced by 40 %, 59 %, and 61% at w/c ratios of 0.4, 0.5, and 0.6, respectively. When a small proportion of fine LSP was used to replace cement, it essentially functioned as a filler material and reduced the concrete's chloride permeability. The chloride permeability of the concrete was lowered when LSP substitution was less than 20% (Gesoğlu *et al.*, 2012). However, according to Meddah *et al.* (2014), up to 15% LSP did not affect the chloride diffusion coefficients. LSP also minimizes shrinkage by reducing the w/c ratio and improving internal curing, which lessens the overall volume change during drying and hardening (Ratsarahasina *et al.*, 2022).

The inclusion of LSP has several advantages, including reduced hydration heat, improved workability, lower $CO_2$ emissions, and improved concrete sustainability (X.-Y. Wang, 2020). Based on the literature review, different researchers used various percentages of LSP to find several mechanical properties. However, none of the reported studies performed an extensive study to find the various physical, mechanical, and durability characteristics and suggested an optimum LSP percentage. Thus, the objective of this study is to investigate the optimum content of LSP to get the best possible result while considering numerous physical, mechanical, and durability properties of concrete. Four different volumetric replacement percentages, such as 5%, 10%, 15%, and 20% have been considered in this regard to assess the application of LSP as a cement substitute in concrete.

## 2. EXPERIMENTAL INVESTIGATION

### 2.1 Materials

Ordinary Portland cement (OPC) is used as the binding material in this study. Limestone powder (LSP) is used to replace OPC partially. For this purpose, LSP was collected from a quarry in the United Arab Emirates through a local company. Figure 1 shows the pictures of OPC and LSP. The pictures show that OPC has a greyish colour, whereas LSP has a white colour. The compressive strength of the cement mortar was determined following the ASTM C109 [25]. Mortar compressive strength was 22 MPa, 27 MPa, and 37 MPa at 3, 7, and 28 days, respectively. Other physical tests of OPC and LSP were performed following the standard methods and are presented in Table 1. Chemical analysis of OPC and LSP was also performed and shown in Table 2. The test results indicate that OPC has a good amount of calcium oxide (CaO) and LSP has a high calcium carbonate ($CaCO_3$) content with a pH of 6-9.



(a) (b)

**Figure 1:** Concrete Ingredients: (a) Cement and (b) Limestone powder.

**Table 1:** Physical Properties of OPC and LSP

| Property | Normal consistency | Specific gravity | Fineness | Initial setting time | Final setting time |
|---|---|---|---|---|---|
| Standard | ASTM C187 (2023) | ASTM C188 (2023) | ASTM C204 (2024) | ASTM C191 (2021) | |
| OPC | 28% | 3.15 | 397 $m^2$/kg | 195 min | 240 min |
| LSP | - | 2.90 | 480 $m^2$/kg | - | - |

**Table 2:** Chemical composition of OPC and LSP

| Compound | % mass | |
|---|---|---|
| | OPC | LSP |
| $CaCO_3$ | - | 98.4 |
| CaO | 61.24 | - |
| $SiO_2$ | 23.14 | 0.03 |
| $Al_2O_3$ | 6.58 | 0.02 |
| $Fe_2O_3$ | 2.69 | 0.02 |
| $SO_3$ | 2.56 | - |
| MgO | 1.52 | 0.02 |
| $K_2O$ | 0.70 | - |
| $Na_2O$ | 0.21 | - |
| LOI | 1.36 | - |
| Moisture | - | 0.10 |

Locally available Sylhet sand with a nominal maximum size of 4.75 mm was used. It is a moderately coarse fine aggregate with a fineness modulus (FM) of 2.73. The adopted coarse aggregate had a maximum grain size of 19 mm with FM 6.85. The gradation curve of fine aggregate is depicted in Figure 2, which falls within the ASTM C33 (2023) defined range for fine aggregate used for concrete.

### 2.2 Mixture Proportions and Specimens

Five distinct concrete mixes are prepared for this investigation to assist in the comparative analysis. Concrete mix proportion was performed following the ACI 211.1 (1991) with a constant w/c ratio of 0.45. The water content was kept constant at 205 kg/$m^3$. Based on the literature review, it was revealed that the mechanical and durability properties of LSP blended cement concrete would decrease with the increase in LSP content. Studies suggest that different LSP content is optimum for different properties based on the curing age (Celik *et al.*, 2019; Pliya & Cree, 2015; Gesoğlu *et al.*, 2012). On the other hand, LSP content greater than 15% averts the hydration processes (Demirhan *et al.*, 2019). Therefore, a maximum of 20% of OPC is replaced with LSP. To find the optimum LSP percentage to achieve the best result while considering physical, mechanical, and durability properties of concrete, four different volumetric replacement percentages, such as 5%, 10%, 15%, and 20% have been considered for the present study. Since the specific gravity of LSP is lower than OPC, LSP content would have been higher on a weight basis mix design. Aggregate contents are designed considering Saturated Surface Dry (SSD) conditions. Table 3 presents the quantities of different materials in concrete mixes for five distinct combinations. C100L0 denotes no cement replacement, whereas C85L15 means 85% cement and 15% LSP.

A total of 90 cylinders is cast for conducting different mechanical and durability tests. The mold size for the cylinders is 100 mm in diameter x 200 mm in height. 15 beams with mold sizes of 100 mm x 100 mm x 500 mm are prepared for five different concrete mixes to evaluate the flexural strength at 28 days.

### 2.3 Test Procedure

A concrete mixer machine was used to mix the concrete ingredients. The LSP and cement are carefully blended by hand before being poured into the mixing device. Coarse aggregate was first put into the machine. Then sand, cement, and LSP mix, and water are added in that order. The mixer machine rotated appropriately to ensure proper mixing of the ingredients. For the slump test, freshly produced concrete is utilized. The slump value of concrete mixtures was measured using the ASTM C143 [40] standard. Specimens were stored in a moist room for the first 24 hours. After that, the samples were carefully demolded and placed in a temperature-controlled (23±2°C) curing tank.

The compressive strength test was performed using a 1500 kN capacity compression testing machine per ASTM C39 (2021). The load was applied at a rate of 0.25 MPa/s. Before testing, both surfaces of each cylinder were levelled using a grinder machine. The splitting tensile strength test was performed in the compression machine, following ASTM C496 (2017) at a loading rate of 0.2 MPa/s. The flexural strength of the concrete beams was evaluated in a 1000 kN capacity universal testing machine (UTM) following ASTM C78 (2022) at a displacement-controlled loading rate of 0.15 mm/min. Support-to-support distance was 300 mm, and the load was applied at 100 mm from the supports (Figure 3(a)).

The chloride ion penetrability of the concrete was determined by the surface resistivity test using a surface resistivity meter following the guidelines of AASHTO TP 95 (2011). After curing, the cylinders were kept outside to dry out before performing the surface resistivity test. The tip of the machine was then dipped in water before being placed against the cylinder to get the reading, and the data was obtained from all four sides of the cylinder by repeating the same procedure.

One cylinder from each combination was kept under 5 bar hydrostatic pressure for the water permeability test for 72 hours. BS EN 12390–8:2009 (2009) regulates the test procedure that involves injecting water under pressure into one surface of the specimen for a certain period, dividing the specimen perpendicular to the injected face, and measuring the depth of penetration visually. The hydrostatic pressure was applied at the centre from the bottom side of the cylinder by using a water permeability test apparatus (Figure 3(b)). The reading of permeability was manually measured from the divided cylinder.

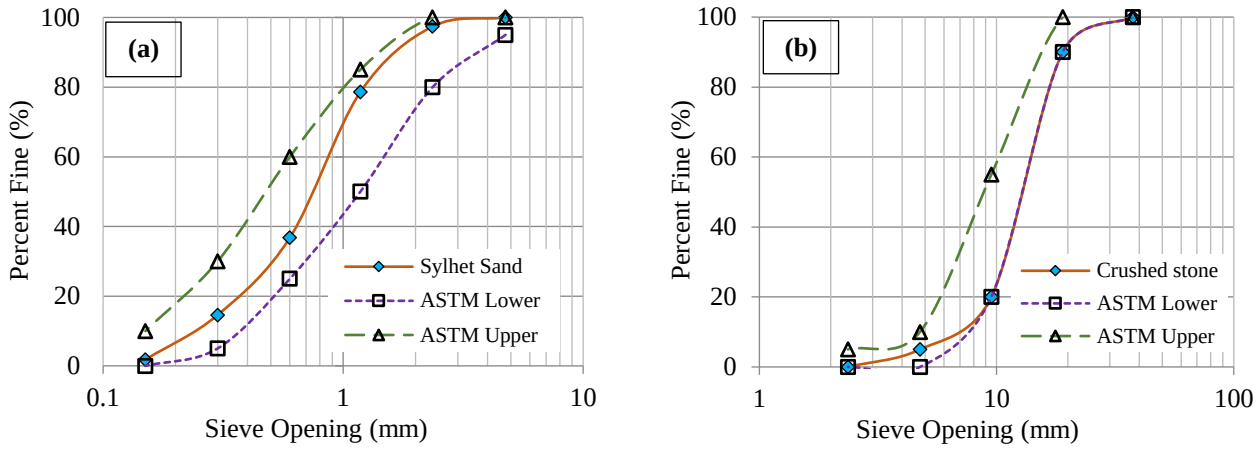



**Figure 2:** Gradation curves for (a) Fine aggregate and (b) Coarse aggregate

**Table 3:** The proportion of materials for one cubic meter of concrete mix

| Batch Code | LSP replacement (%) | Water (kg) | Cement (kg) | LSP (kg) | FA (kg) | CA (kg) |
|---|---|---|---|---|---|---|
| C100L0 | 0 | 205 | 456.00 | 0.00 | 731.4 | 979.6 |
| C95L5 | 5 | 205 | 433.20 | 22.80 | 729.6 | 979.6 |
| C90L10 | 10 | 205 | 410.40 | 45.60 | 727.7 | 979.6 |
| C85L15 | 15 | 205 | 387.60 | 68.40 | 725.9 | 979.6 |
| C80L20 | 20 | 205 | 364.80 | 91.20 | 724.1 | 979.6 |

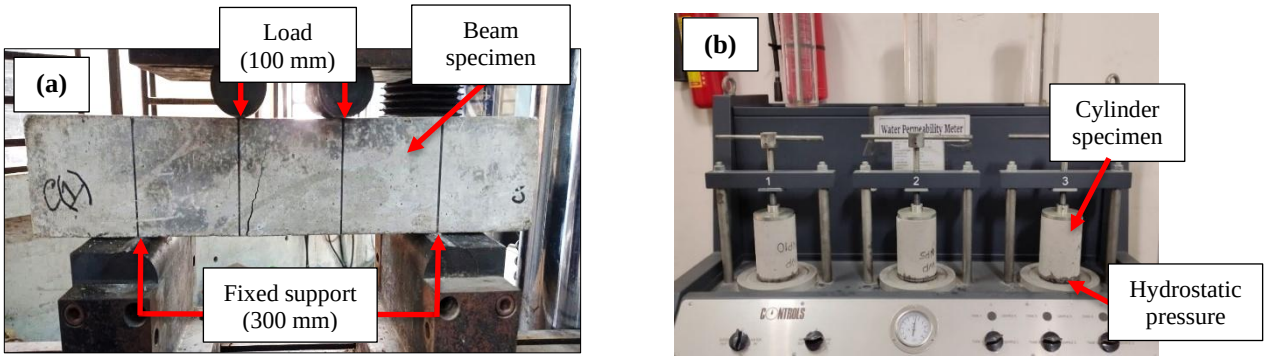



**Figure 3:** Test setup (a) Quasi-static flexural test (b) Water permeability test

## 3. RESULTS AND DISCUSSIONS

### 3.1 Workability

The slump value was measured immediately after the concrete was poured from the mixer machine to evaluate the workability. Figure 4 shows the slump value of all five concrete mixtures. Results show that the control combination had the lowest workability of the specimens under consideration in this investigation. Slump value increased with increasing LSP content, and the highest slump value was found for concrete with 20% LSP (C80L20). Slump value increases by 27%, 44%, 104% and 119% compared to the control sample for 5%, 10%, 15% and 20% LSP replacement, respectively.

The impacts of LSP on concrete workability are primarily due to the morphological influence, filler effect, and dilution effect. Since LSP is finer than the cement particles, the filler effect predominates in this case. LSP enhances workability by filling voids between larger particles, reducing water requirement, and improving the consistency of the concrete mix and ease of handling (Ratsarahasina *et al.*, 2022). When the particle size of LSP is equal to or larger than the particle size of cement particles, LSP demonstrates a diluting impact (D. Wang *et al.*, 2018a). Direct grinding of LSP enhances concrete flow values, mostly connected to the particles' surface morphology and fineness, increasing concrete flow values.

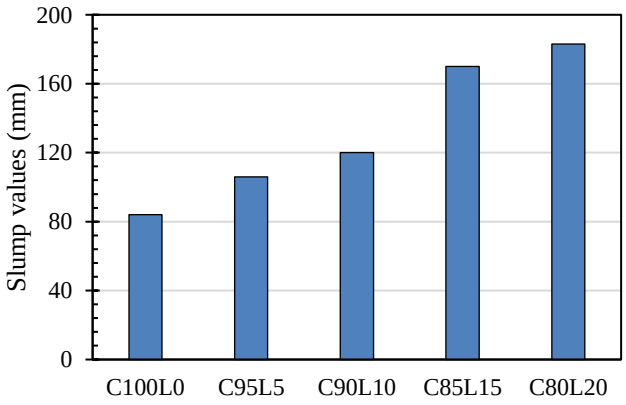



**Figure 4:** Slump value of different concrete mixtures

### 3.2 Compressive Strength

Figure 5 illustrates a summary of the compressive strength of concrete at 7, 28, and 56 days. Progressive growth in concrete strength with age for all combinations of concrete specimens has been observed. For example, the compressive strength of the control specimen differs by 12% from 28 days to 56 days. With the increasing percentage of LSP replacement, the compressive strength decreases initially and reaches a maximum of 10% LSP replaced concrete. A similar result was observed by Zhao *et al.* (2024) when sand was replaced by 10% LSP. However, beyond 10% LSP replacement, a decrease has been observed. The highest compressive strengths are 39.45 MPa and 44.28 MPa at 28 and 56 days, respectively, for 10% LSP replaced concrete (C90L10). As LSP enhances the pore structure of hardened concrete, the strength boosts up in later days (Yu *et al.*, 2014). At 28 days, strength increased by 1% for concrete with 10% LSP compared to the control specimen, but strength decreased by 5%, 16% and 18%, respectively, for concrete with 5%, 15% and 20% LSP. Compared to the control concrete specimen, strength increased by 1% at 56 days for concrete containing 10% LSP, but decreased by 4%, 11% and 17%, respectively for concrete with 5%, 15% and 20% LSP.

The result indicates that the inclusion of LSP decreases the compressive strength of concrete. The reason is the reduction of the hydraulically active clinker fraction of cement upon the LSP replacement (Sezer, 2012). At 10% LSP level, the compressive strength increases due to the nucleation effect of LSP. Beyond 15% replacement level, the dilution effect triggers, where the cement content is reduced, causing a slower hydration rate and potentially lowering the mechanical performance (A. H. Ahmed *et al.*, 2023). The less reactive calcite dilutes the more reactive cement when LSP replaces ordinary Portland Cement by more than 15%, resulting in reduced compressive strengths and physical changes (Benachour *et al.*, 2008; Dhir *et al.*, 2007). Also, the decrease in strength might be attributed to the reduced cementing qualities and an increase in non-cementing elements of the limestone fillers (Pliya & Cree, 2015). Liu and Yan (2010) reported from XRD analysis that LSP remains unhydrated at 28 days, even without having pozzolanic properties. The LSP used in this research was finer than the cement particle, and when a high amount of fine LSP was utilized to substitute cement, the LSP showed a dilution effect and decreased compressive strength. This pattern demonstrates that the beneficial filler and nucleation effects of LSP are effective up to an optimum replacement level, beyond which the dilution effect dominates and adversely affects concrete strength. At higher replacement levels, LSP mostly acts as an inert filler, which reduces the amount of reactive clinker and thereby lowers strength (Bonavetti *et al.*, 2003). Figure 6 depicts failure patterns, and in most cases, a diagonal fracture with no cracking through the ends is observed in cylinders. Samples with 5% LSP have columnar failure. Higher content than that results in a cone and shear crack.

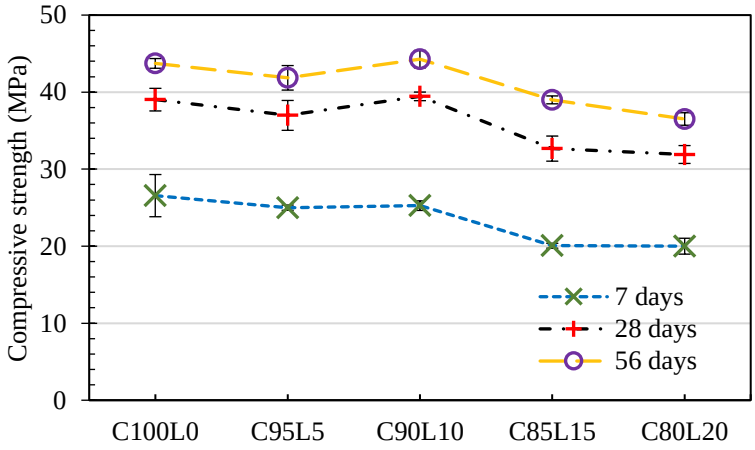



**Figure 5:** Compressive strength at 7, 28 and 56 days



(a) (b) (c) (d) (e)

**Figure 6:** Failure patterns of cylinders subjected to a compressive force at 56 days (a) C100L0, (b) C95L5, (c) C90L10, (d) C85L15, (e) C80L20.

### 3.3 Splitting Tensile Strength

Figure 7 represents the summary of the splitting tensile strengths of concrete at 7 and 28 days. The tensile strength of concrete has been observed to grow with age. As illustrated in Figure 7, the inclusion of LSP decreases concrete's tensile strength. For example, the tensile strength increases for 5% LSP at 7 days. However, for 10% LSP, it is almost the same as the control specimen and again drops by 21% and 14% for 15% LSP at 7 and 28 days, respectively, compared to the control mix. Tensile strength is the highest for 5% LSP for both 7 days and 28 days of curing. For 28 days, the highest strength is 3.49 MPa for 5% LSP. However, the increment of strength is not much compared to the control specimen, only 1.2%. Thus, adding LSP does not increase the strength by a noticeable amount. The addition of 10% LSP has a similar tensile strength as the specimen without any LSP. Although a slight increment is observed for 20% LSP at 7 days (19%) and 28 days (1%) compared to 15% LSP containing samples.

LSP serves as an inert filler element. Too much of that results in a poor fiber-matrix interface (Zhou *et al.*, 2010) and cementitious material's strain-hardening activity is harmed by an excessively weak interface (V. C. Li, 2003). A smaller dosage of LSP (up to 10%) optimizes the pore structures of aggregates and facilitates the early hydration of cement due to the filler and nucleation effects (Zhao *et al.*, 2024). At 15% LSP dosage, the dilution of cement dominates, which limits available clinkers for hydration in the matrix, causing a decrease in tensile strength. For these reasons, tensile strength decreases with the increment of the percentage of LSP. However, at a 20% dosage, LSP provides additional nucleation sites for calcium silicate hydrate (C-S-H) formation, which compensates for the dilution effect of cement to some extent. Thus, an increment in tensile strength is observed at more than 15% LSP level (Shi *et al.*, 2023).

From the failure patterns (Figure 8), it can be seen that vertical cracking occurred through both ends for up to 10% LSP content. The 15% and 20% LSP containing cylinders have horizontal cracks, which made them fail at lower tensile stress levels. Samples with 10% LSP also shows a few thin horizontal cracks. These horizontal cracks indicate that adding a higher amount of LSP increases the brittle behaviour of concrete.

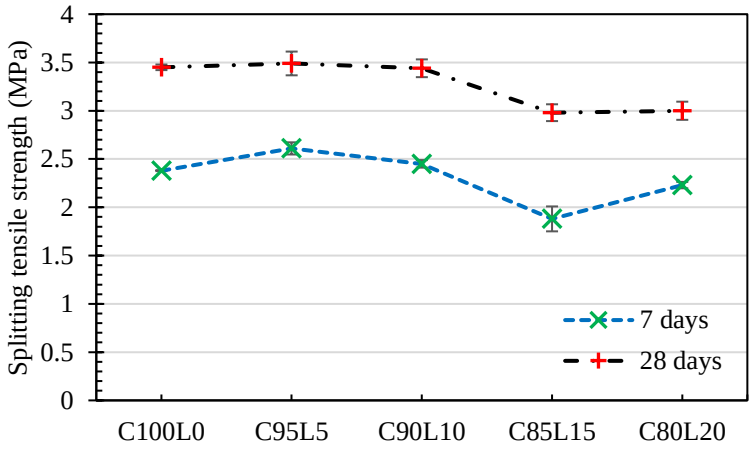



**Figure 7:** Influence of LSP on splitting tensile strength of concrete



(a) (b) (c) (d) (e)

**Figure 8:** Failure patterns of cylinders subjected to a tensile force at 28 days (a) C100L0, (b) C95L5, (c) C90L10, (d) C85L15, (e) C80L20.

### 3.4 Relationship between Compressive Strength and Splitting Tensile Strength

Several design codes refer to equations to calculate the tensile strength of concrete from the compressive strength values. However, these design codes do not take LSP into account. The experimental splitting tensile strength from this study is compared with the ACI 318-14 (2014), fib 2010 (2010), and Eurocode 2 (2005) equations, which are shown in Figure 9. The code equations overestimate the 7 days results and underestimate the 28 days results. LSP hydrates at a later days, thus its strength gain is slow. This

is why the inconsistency with the code occurs. ACI318-14, fib 2010, and Eurocode 2, respectively overestimate tensile strength up to 32%, 18% and 19% for 7 days and underestimates by up to 3%, 5% and 13% for 28 days. Thus, a new equation has been proposed by a machine learning approach using python programming language by adopting a linear regression model on the experimental data from this study along with other data from previous studies (Mohammed & Al-Numan, 2024; Ahmad *et al.*, 2022; Demirhan *et al.*, 2019; Hyun *et al.*, 2018; Kim *et al.*, 2018; Diab *et al.*, 2016; Nikbin *et al.*, 2014; Adel Mohammed *et al.*, 2010). The input features the percentage of LSP and compressive strength, and the outcome gives the prediction of tensile strength. Using a total of 50 datasets, 100000 iterations have been performed with a learning rate of 0.00000005 to reduce error (Figure 10(a)). $R^2$, RMSE, and MAE of the model have been found to be 0.547, 0.587 and 0.515, respectively. Considering the presence of LSP as supplementary cementitious material, Equation 1 has been proposed to predict the tensile strength from compressive strength.

$$\text{Splitting tensile strength} = 0.073f_c' - 0.013\text{LSP} \quad (1)$$

Where, $f_c'$ = compressive strength and LSP = percentage of limestone powder. This equation has 12.67% accuracy, which means that the proposed equation is accurate and can be used for practical applications. The performance of the regression model has been evaluated using 10-fold cross-validation. The model achieved an average $R^2$ of 0.614±0.124, with RMSE and MAE values of 0.602±0.178 and 0.545±0.188, respectively, across the folds. Figure 10(b) shows the linear relation between compressive strength and splitting tensile strength obtained from the machine learning procedure.

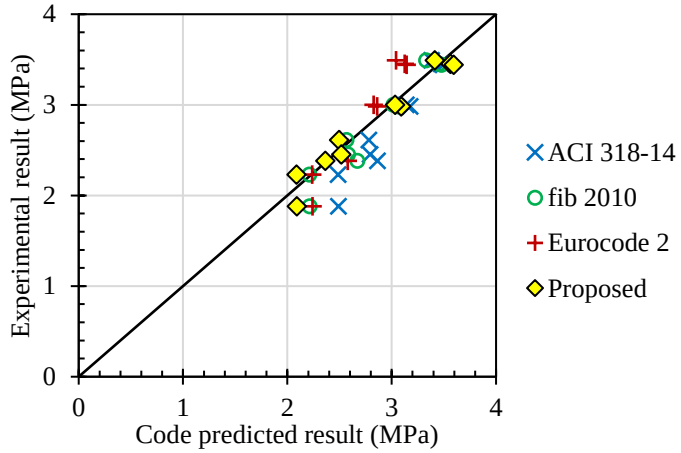



**Figure 9:** Comparison of experimental tensile strength data with various code-predicted data

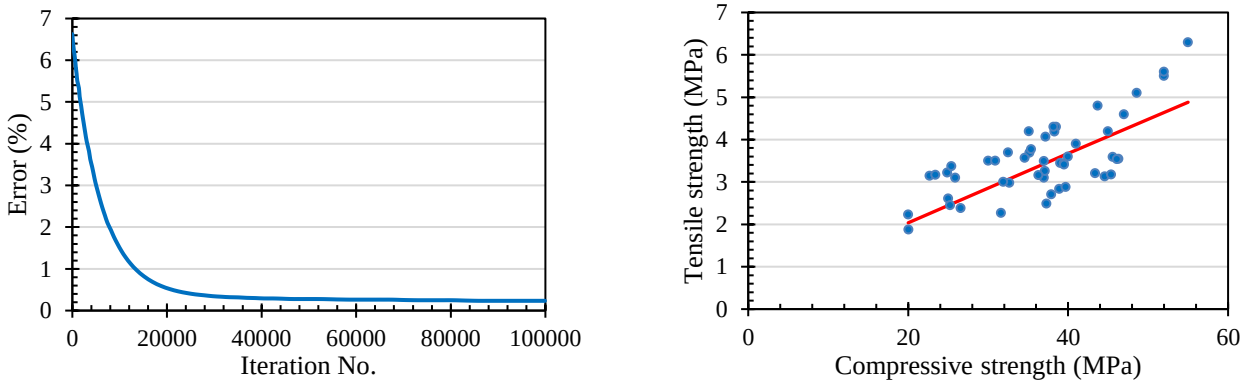



**Figure 10:** (a) Percentage of error vs. iteration plot and (b) Tensile strength and compressive strength dataset from previous studies

### 3.5 Flexural Behavior

The quasi-static flexural strength test data after 28 days of curing are presented in Table 4. The flexural stress initially increases by 5.5% and 6.4% for adding 5% and 10% LSP with cement, respectively. However, an increment of LSP amount decreases the flexural stress aftermath. Flexural stress is the highest for 10% LSP which is 10.36 MPa. The lowest flexural stress was observed for 20% LSP, where flexural stress decreased 1.2% and 9.6% for 15% and 20% LSP, respectively.

When used in place of cement, LSP mostly displays filler and diluting effects, which can densify the concrete microstructure and improve the interfacial transition zone between the cement paste and aggregates (Ratsarahasina *et al.*, 2022; Kępniak *et al.*, 2021; Liu & Yan, 2010). LSP also promotes the heteronucleation of cement hydration products on the limestone particles, further enhancing the cement matrix (Kępniak *et al.*, 2021). Hence, the use of LSP in place of up to 10% cement improves the flexural strength of concrete. Similar result is also observed by W. Li *et al.* (2015). When higher LSP content is used to replace more than 10% of cement, the cementing material content decreases, and the non-cementing component

**Table 4** Flexural strength test results at 28 days.

| Mix ID | First crack load (kN) | Maximum load (kN) | Deflection at maximum load (mm) | Flexural stress at maximum load (MPa) | Toughness (kN-mm) |
|---|---|---|---|---|---|
| C100L0 | 18.82 | 21.64 | 0.349 | 6.49 | 3.42 |
| C95L5 | 20.72 | 22.83 | 0.398 | 6.85 | 4.31 |
| C90L10 | 15.88 | 23.02 | 0.549 | 6.91 | 6.53 |
| C85L15 | 16.33 | 21.37 | 0.616 | 6.41 | 5.40 |
| C80L20 | 16.95 | 19.55 | 0.683 | 5.86 | 5.37 |

increases, which is responsible for the reduction of concrete flexural strength (D. Wang *et al.*, 2018b). There are residual LSP after filling up the spaces between aggregate particles. This governs the dilution effect, because of which the cement matrix becomes less dense, the hydration rate decelerates, which significantly lowers the amount of C-S-H formation (A. H. Ahmed *et al.*, 2023). This indicates that the volume of cement can be lowered up to 10% to increase the dimensional stability of concrete and reduce the risk of cracking without affecting strength. This is attributed to the filler effect of the LSP.

Figure 12 illustrates the Load-Deflection curves of the specimens. All the curves have the same pattern. Each curve is separated into three phases. The first stage begins at the loading point and finishes at the point where the slope of the curve first begins to vary. The first crack appears at this stage. At this point, the load-deflection curve seems to be linear, representing the uncracked beam. After increasing the load, the curve rises linearly to the highest point. The load vs deflection curve shows that the control specimen with 0% LSP has a straight elastic region up to the first crack load (18.82 kN), followed by a very short hardening region up to peak load (21.64 kN), indicating that it does not take much load after the first crack load appears. Adding LSP increases the elastic region and for this reason, it takes more time to fail compared to the control specimen. Following that, the beam bears no more stress, and an abrupt falling segment is visible. The concrete beam then fails like a brittle material. The deflection capacity also increases with higher LSP, as seen from Table 4. It is to be noted that although the 10% LSP level has the lowest first crack load among all the mixes (15.88 kN), failure load capacity of this mix is the highest (23.02 kN). This indicates that 10% LSP makes the concrete more brittle, allowing it to carry more flexural stress even after the first crack appears.

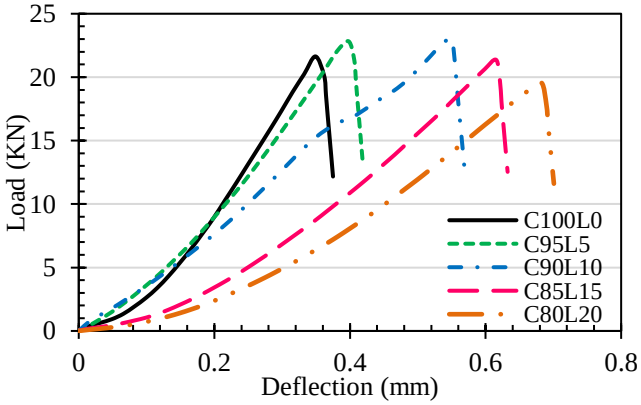



**Figure 12:** Load-deflection curves of concrete

The toughness index of each sample is determined using the load-deflection curves. From Table 4, it is seen that all the mixes containing LSP has a greater toughness value than the control mixes. The toughness index first starts to increase and is the highest for 10% LSP. After that, the toughness index starts to decrease with higher LSP amounts. The variation of toughness index is 26%, 90%, 58% and 57% respectively for 5%, 10%, 15% and 20% LSP compared to the control specimen. Therefore, it indicates that concrete with 10% LSP requires the most energy to fracture, and the control specimen requires the lowest energy to fracture. As the fracture toughness of a component with a specific length decreases, so does the component's capacity to bear load before cracking. For a given stress, however, when fracture toughness improves, a component may endure a longer crack before fracturing.

### 3.6 Chloride Ion Penetrability Test

The study of chloride permeability is an important factor that influences the durability of concrete. Figure 13 shows the surface resistivity of cylinders at different ages. These data are correlated to the penetrability standard according to AASHTO TP 95 (2011). Specific resistance values less than 12 are classified as high penetrability, and 12 KΩ-cm to 24 KΩ-cm are classified as moderate penetrability by this test method.

After 7 days of curing, all the samples have high penetrability, which migrates to a moderate level after 28 and 56 days of curing. The surface resistivity is the highest for specimens with 5% LSP and the lowest for 15% LSP content. Then the resistivity gradually decreases for 10% and 15% LSP. Surface resistivity increases by 8%, 4% and 3% for 5% LSP content after 7, 28, and 56 days of curing, respectively. According to D. Wang *et al.* (2018a), when a little quantity of fine LSP is used to substitute cement, it mostly works as a filler and reduces the chloride

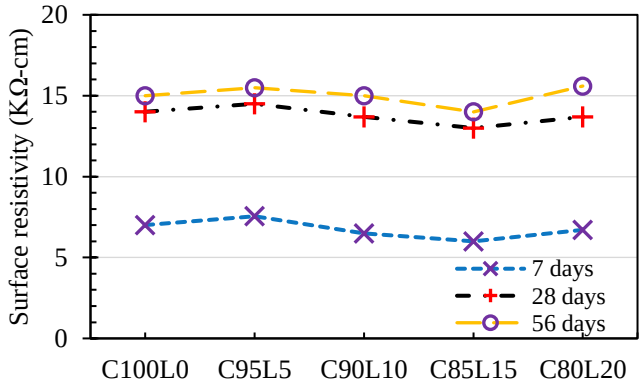



**Figure 13:** Chloride penetration of concrete with LSP

permeability of the concrete. This is why the samples with 5% LSP have the highest surface resistivity. With a longer curing period, concrete cylinders become more compacted and denser, and thus the surface resistivity increases for 28 and 56 days. The surface resistivity decreases by up to 14% for higher LSP content, which indicates higher chloride ion penetrability. A similar result was also observed by Hornain *et al.* (1995). Chloride ion penetrability is contingent upon the quantity and distribution of the pores. LSP refines the pore structure of concrete due to its filler and nucleation activities, and hence the chloride diffusion coefficient reduces as LSP concentration increases (D. Wang *et al.*, 2018a). Thus, the surface resistivity increases as well as the chloride ion penetrability decreases for the presence of LSP to an optimum level. Notably, at 56 days, a 4% increase in surface resistivity for 20% LSP is observed. This is attributed to the long-term pore refinement and matrix densification (Liu & Yan, 2010). This influences the surface resistivity at a higher replacement level of LSP.

### 3.7 Water Permeability Test

Figure 14 represents the permeability depth of concrete specimens under hydrostatic pressure and Figure 15 shows the depth of water in samples after the test. The permeability of the control specimen is 25 mm. Increasing the percentage of LSP reduces permeability. Similar trend was observed by L. G. Li and Kwan (2015) when cement was replaced by LSP. The water permeability is the highest for the control specimen. Then for all the combinations, permeability is lesser and the lowest for 20% LSP. The decrement variation is 12%, 24%, 28% and 36% respectively for 5%, 10%, 15% and 20% LSP compared to the control specimen. LSP improves the particle packing density of the concrete mix, which enhances compaction and reduces porosity (Ratsarahasina *et al.*, 2022). This densification results in a compact, less permeable microstructure, which in turn enhances the water permeability as well as the overall strength and performance of the concrete. The reduction in permeability also suggests a denser interfacial transition zone (ITZ), which narrows down the pathways for water ingress (Liu & Yan, 2010). This suggests that the inclusion of LSP not only reduces permeability but may also improve durability under aggressive environmental conditions.

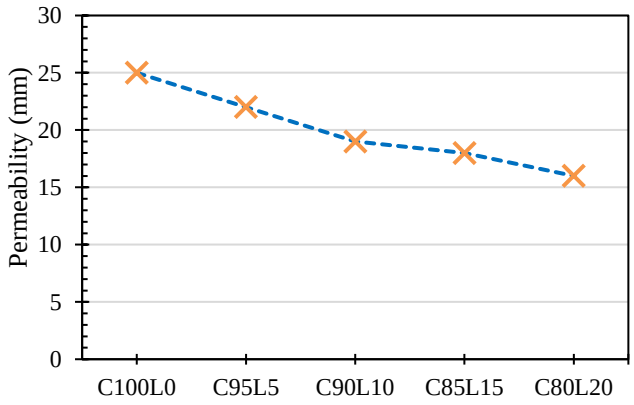



**Figure 14:** Water permeability of concrete with LSP

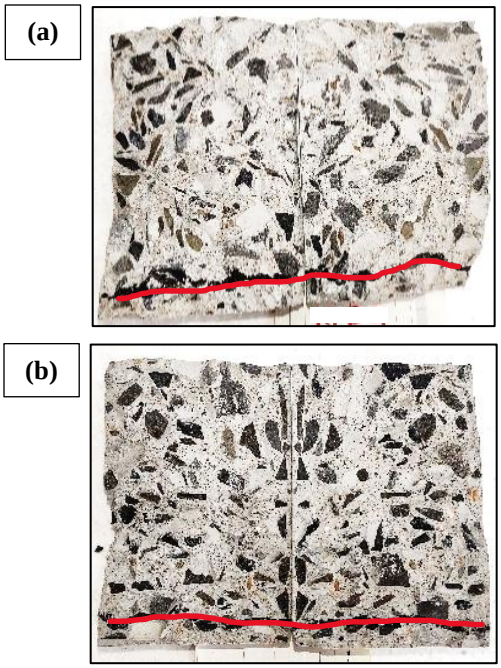



**Figure 15:** Samples after water penetration test (a)C100L0, (b) C80L20

## 4. CONCLUSIONS

The physical, mechanical, and durability features of LSP blended concrete are extensively investigated in this study. The findings may be best summed up:

i. Slump increases linearly with higher content of LSP. The filler effect of LSP makes the concrete flowable and thus increases workability.

ii. With the increasing percentage of LSP replacements, the compressive strength decreases initially and reaches a maximum of 10% LSP replaced concrete, 39.45 MPa, and 44.28 MPa at 28 and 56 days, respectively, due to the nucleation effect. The dilution effect caused by a higher percentage of LSP offsets the hydration process which reduces compressive strength for 15% and 20% LSP.

iii. With the addition of LSP, the splitting tensile strength does not vary significantly up to 10% replacement. After both 28 and 56 days of curing, the splitting tensile strength of the 10% LSP sample and the control sample are almost similar. Afterwards, tensile strength decreases. A smaller dosage of LSP optimizes the pore structure and facilitates the early hydration, which does not disadvantage the tensile strength. An equation has been proposed to predict the tensile strength of LSP mixed concrete using a machine learning approach.

iv. Maximum flexural strength is obtained for 10% percent LSP, which is 6.4% higher than the control specimen. The toughness index also has a similar trend, which increases by 90% for 10% LSP. Higher LSP content gradually reduces flexural strength. This happens because there are residual LSP after the optimum amount, which governs the dilution effect.

v. The water permeability and chloride ion penetrability gradually reduce with the addition of LSP. For 5% LSP content, the surface resistivity is the highest because a smaller amount of LSP works mostly as filler and produces a compact, less permeable microstructure, which enhances the water permeability and chloride ion penetrability of concrete. 10% LSP content gives a similar surface resistivity as the control specimen.

LSP blended concrete gives better mechanical and durability properties up to an optimum level. From the experimental results, it is consistent that 10% LSP has the best outcome in terms of mechanical and durability properties. Thus, 10% LSP can be considered as the optimum level to substitute Portland cement.

**ACKNOWLEDGMENTS**

The authors would like to thank MIST for providing the necessary facilities and technical support required to successfully conduct the experimental investigations of this study.

**DATA AVAILABILITY STATEMENT**

Datasets generated during the current study are available from the corresponding author upon reasonable request.

**FUNDING DECLARATION**

This research was financially supported by a start-up fund provided by the authors. Special thanks to Seven Rings Cement for partnering with the project.

**ETHICS APPROVAL**

This study is an engineering experimental investigation. The MIJST Research Ethics Committee has confirmed that formal ethical approval was not required.

**ETHICS, CONSENT TO PARTICIPATE, AND CONSENT TO PUBLISH**

Not applicable.

**COMPETING INTERESTS**

The authors declare that they have no competing interests.

**AUTHOR CONTRIBUTIONS**

Author 1: Md. Jahidul Islam- Writing – review & editing, Supervision, Methodology, Conceptualization, Funding acquisition, Formal analysis.

Author 2: Tasnia Ahmed- Data curation, Formal analysis, Software, Writing – original draft.

Author 3: Nishat Naila Meghna- Investigation, Data curation, Formal analysis, Writing – original draft.

Author 4: Ismat Abida- Investigation, Data curation.

Author 5: Nayeem Mohammad Mashfiq- Investigation, Data curation

**ARTIFICIAL INTELLIGENCE ASSISTANCE STATEMENT**

Portions of this manuscript were assisted by an artificial intelligence language model (ChatGPT, OpenAI). The tool was used solely for language editing, text refinement, and clarity improvement. All content, data interpretation, analysis, conclusions, and final decisions were generated, verified, and approved by the authors. The authors take full responsibility for the accuracy and integrity of the manuscript.

**CONFLICT OF INTEREST DECLARATION**

The authors declare that they have no conflicts of interest.

**REFERENCES**

AASHTO TP 95. (2011). Standard Method of Test for Surface Resistivity of Concrete's Ability to Resist Chloride Ion Penetration. *American Association of State Highway and Transportation Officials, Washington, DC*.

ACI 211.1. (1991). Standard Practive for Selecting Proportions for Normal, Heavyweight, and Mass Concrete. *American Concrete Institute, Farmington Hills, MI*.

ACI 211.7R-15. (2015). Guide For Proportioning Concrete Mixtures With Ground Limestone and Other Mineral Fillers. *American Concrete Institute, Farmington Hills, MI*.

ACI 318-14. (2014). Building Code Requirements for Structural Concrete and Commentary. *American Concrete Institute, Farmington Hills, MI*.

Adel Mohammed, Z., Burhan Abdurrahman, R., & Abdul Hakeem Hamed Ahmad, D. (2010). Influence of Limestone Powder as Partial Replacement of Cement on Concrete and the Effect of High Temperature on It. *Al-Rafidain Engineering Journal (AREJ), 18*(5), 24-34. doi:10.33899/rengj.2010.32863

Ahmad, I., Shen, D., Khan, K. A., Jan, A., & Ahmad, T. (2022). Evaluation of mechanical properties and environmental impact of using limestone powder in high-performance concrete. *Magazine of Concrete Research, 74*(24), 1280-1295. doi:10.1680/jmacr.21.00199

Ahmed, A. H., Nune, S., Liebscher, M., Köberle, T., Willomitzer, A., Noack, I., Butler, M., & Mechtcherine, V. (2023). Exploring the role of dilutive effects on microstructural development and hydration kinetics of limestone calcined clay cement (LC3) made of low-grade raw materials. *Journal of Cleaner Production, 428*, 139438. doi:https://doi.org/10.1016/j.jclepro.2023.139438

Ahmed, T., Bediwy, A., Azzam, A., Elhadary, R., El-Salakawy, E., & Bassuoni, M. T. (2024). Utilization of Novel Basalt Fiber Pellets from Micro- to Macro-Scale, and from Basic to Applied Fields: A Review on Recent Contributions. *Fibers, 12*(2), 17. doi:https://doi.org/10.3390/fib12020017

Ahmed, T., Bediwy, A., & Islam, M. J. (2025). Durable and sustainable nano-modified basalt fiber-reinforced composites for elevated temperature

applications. *Journal of Building Engineering, 108*, 112865. doi:https://doi.org/10.1016/j.jobe.2025.112865

Amran, M., Makul, N., Fediuk, R., Lee, Y. H., Vatin, N. I., Lee, Y. Y., & Mohammed, K. (2022). Global carbon recoverability experiences from the cement industry. *Case Studies in Construction Materials, 17*, e01439. doi:https://doi.org/10.1016/j.cscm.2022.e01439

Araf, S., Shahjalal, M., Ahmed, T., Juthi, S., Rahman, S., & Islam, M. (2023). *Mechanical and Durability Properties of Induction Furnace Slag and Recycled Aggregate Concrete.* Paper presented at the 2nd International Conference on Advances in Civil Infrastructure and Construction Materials, 26-28 July 2023, MIST, Dhaka, Bangladesh.

ASTM C33. (2023). *Standard Specification for Concrete Aggregates*. Paper presented at the ASTM International, West Conshohocken, PA.

ASTM C39. (2021). Standard Test Method for Compressive Strength of Cylindrical Concrete Specimens. *ASTM International, West Conshohocken, PA*.

ASTM C78. (2022). Standard Test Method for Flexural Strength of Concrete (Using Simple Beam with Third-Point Loading). *ASTM International, West Conshohocken, PA*.

ASTM C150. (2022). Standard Specification for Portland Cement. *ASTM International, West Conshohocken, PA*.

ASTM C187. (2023). Standard Test Method for Amount of Water Required for Normal Consistency of Hydraulic Cement Paste. *ASTM International, West Conshohocken, PA*.

ASTM C188. (2023). Standard Test Method for Density of Hydraulic Cement. *ASTM International, West Conshohocken, PA*.

ASTM C191. (2021). Standard Test Method for Time of Setting of Hydraulic Cement by Vicat Needle. *ASTM International, West Conshohocken, PA*.

ASTM C204. (2024). Standard Test Methods for Fineness of Hydraulic Cement by Air-Permeability Apparatus. *ASTM International, West Conshohocken, PA*.

ASTM C496. (2017). Standard Test Method for Splitting Tensile Strength of Cylindrical Concrete Specimens. *ASTM International, West Conshohocken, PA*.

Barbhuiya, S., Kanavaris, F., Das, B. B., & Idrees, M. (2024). Decarbonising cement and concrete production: Strategies, challenges and pathways for sustainable development. *Journal of Building Engineering, 86*, 108861. doi:https://doi.org/10.1016/j.jobe.2024.108861

Barbhuiya, S., Nepal, J., & Das, B. B. (2023). Properties, compatibility, environmental benefits and future directions of limestone calcined clay cement (LC3) concrete: A review. *Journal of Building Engineering, 79*, 107794. doi:https://doi.org/10.1016/j.jobe.2023.107794

Benachour, Y., Davy, C. A., Skoczylas, F., & Houari, H. (2008). Effect of a high calcite filler addition upon microstructural, mechanical, shrinkage and transport properties of a mortar. *Cement and Concrete Research, 38*(6), 727-736. doi:https://doi.org/10.1016/j.cemconres.2008.02.007

Bonavetti, V., Donza, H., Menéndez, G., Cabrera, O., & Irassar, E. F. (2003). Limestone filler cement in low w/c concrete: A rational use of energy. *Cement and Concrete Research, 33*(6), 865-871. doi:https://doi.org/10.1016/S0008-8846(02)01087-6

BS EN 12390–8:2009. (2009). The Standard for Testing hardened concrete - Depth of Penetration of Water under pressure. *British Standards Institution, UK*.

Celik, K., Hay, R., Hargis, C. W., & Moon, J. (2019). Effect of volcanic ash pozzolan or limestone replacement on hydration of Portland cement. *Construction and Building Materials, 197*, 803-812. doi:https://doi.org/10.1016/j.conbuildmat.2018.11.193

Chen, J., Kwan, A., & Jiang, Y. (2014). Adding limestone fines as cement paste replacement to reduce water permeability and sorptivity of concrete. *Construction and Building Materials, 56*, 87-93.

Chen, J., Kwan, A., & Jiang, Y. (2014). Adding limestone fines as cement paste replacement to reduce water permeability and sorptivity of concrete. *Construction and Building Materials, 56*, 87–93. doi:10.1016/j.conbuildmat.2014.01.066

Demirhan, S., Turk, K., & Ulugerger, K. (2019). Fresh and hardened properties of self consolidating Portland limestone cement mortars: Effect of high volume limestone powder replaced by cement. *Construction and Building Materials, 196*, 115-125. doi:https://doi.org/10.1016/j.conbuildmat.2018.11.111

Dhir, R., Limbachiya, M., McCarthy, M., & Chaipanich, A. (2007). Evaluation of Portland limestone cements for use in concrete construction. *Materials and structures, 40*(5), 459-473. doi:https://doi.org/10.1617/s11527-006-9143-7

Diab, A. M., Abd Elmoaty, A. E. M., & Aly, A. A. (2016). Long term study of mechanical properties, durability and environmental impact of limestone cement concrete. *Alexandria Engineering Journal, 55*(2), 1465-1482. doi:https://doi.org/10.1016/j.aej.2016.01.031

EN, B. S. (2000). 197-1, Cement-Part 1: Composition, specifications and conformity criteria for common cements. *British Standards Institution*.

Eurocode 2. (2005). EN 1992-1-1, Design of Concrete Structures – Part 1–1: General Rules and Rules for Buildings. *Thomas Telford, London, UK*.

fib 2010. (2010). fib Model Code for Concrete Structures. *International Fedaration for Structural Concrete*.

Gesoğlu, M., Güneyisi, E., Kocabağ, M. E., Bayram, V., & Mermerdaş, K. (2012). Fresh and hardened characteristics of self compacting concretes made with combined use of marble powder, limestone filler, and fly ash. *Construction and Building Materials, 37*, 160-170.

Hornain, H., Marchand, J., Duhot, V., & Moranville-Regourd, M. (1995). Diffusion of chloride ions in limestone filler blended cement pastes and mortars. *Cement and Concrete Research, 25*(8), 1667-1678. doi:https://doi.org/10.1016/0008-8846(95)00163-8

Hyun, J. H., Lee, B. Y., & Kim, Y. Y. (2018). Composite Properties and Micromechanical Analysis of Highly Ductile Cement Composite Incorporating Limestone Powder. *Applied Sciences, 8*(2), 151. doi:https://doi.org/10.3390/app8020151

Islam, M. J., Ahmed, T., Imam, S. M. F. B., Islam, H., & Shaikh, F. U. A. (2023a). Comparative study of carbon fiber and galvanized iron textile reinforced concrete. *Construction and Building Materials, 374*, 130928. doi:https://doi.org/10.1016/j.conbuildmat.2023.130928

Islam, M. J., Ahmed, T., Salehin, M. R., Sakib, M. S., Shariar, M. S., & Hossain, M. (2023b). Physical, Mechanical, and Durability Properties of Concrete with Class F Fly Ash. *MIST INTERNATIONAL JOURNAL OF SCIENCE AND TECHNOLOGY, 11*(2). doi:10.47981/j.mijst.11(02)2023.430(27-41)

Kępniak, M., Woyciechowski, P., & Franus, W. (2021). Transition Zone Enhancement with Waste Limestone Powder as a Reason for Concrete Compressive Strength Increase. *Materials, 14*, 7254. doi:10.3390/ma14237254

Kim, Y.-J., Leeuwen, R. v., Cho, B.-Y., Sriraman, V., & Torres, A. (2018). Evaluation of the Efficiency of Limestone Powder in Concrete and the Effects on the Environment. *Sustainability, 10*(2), 550. doi:https://doi.org/10.3390/su10020550

Li, L. G., & Kwan, A. K. (2015). Adding limestone fines as cementitious paste replacement to improve tensile strength, stiffness and durability of concrete. *Cement and Concrete Composites, 60*, 17-24. doi:https://doi.org/10.1016/j.cemconcomp.2015.02.006

Li, P. P., Brouwers, H. J. H., Chen, W., & Yu, Q. (2020). Optimization and characterization of high-volume limestone powder in sustainable ultra-high performance concrete. *Construction and Building Materials, 242*, 118112. doi:https://doi.org/10.1016/j.conbuildmat.2020.118112

Li, V. C. (2003). On engineered cementitious composites (ECC) a review of the material and its applications. *Journal of Advanced Concrete Technology, 1*(3), 215-230.

Li, W., Huang, Z., Cao, F., Sun, Z., & Shah, S. P. (2015). Effects of nano-silica and nano-limestone on flowability and mechanical properties of ultra-high-performance concrete matrix. *Construction and Building Materials, 95*, 366-374. doi:https://doi.org/10.1016/j.conbuildmat.2015.05.137

Lin, W.-T., Cheng, A., & Černý, R. (2020). Effect of limestone powder on strength and permeability of cementitious mortars. *MATEC Web of Conferences, 322*, 01009. doi:10.1051/matecconf/202032201009

Liu, S., & Yan, P. (2010). Effect of limestone powder on microstructure of concrete. *Journal of Wuhan University of Technology-Mater. Sci. Ed., 25*(2), 328-331. doi:10.1007/s11595-010-2328-5

Lothenbach, B., Le Saout, G., Gallucci, E., & Scrivener, K. (2008). Influence of limestone on the hydration of Portland cements. *Cement and Concrete Research, 38*(6), 848-860. doi:https://doi.org/10.1016/j.cemconres.2008.01.002

Mahi, M. S. H., Ridoy, T., Faiag, M., & Sheikh, M. (2025). Limestone Powder in Concrete Mixes: A Review of Mechanical Enhancements. *Smart and Green Materials, 2*, 11-21. doi:10.70028/sgm.v2i1.25

Meddah, M. S., Lmbachiya, M. C., & Dhir, R. K. (2014). Potential use of binary and composite limestone cements in concrete production. *Construction and Building Materials, 58*, 193-205.

Meghna, N. N., Abida, I., Mashfiq, N. M., Ahmed, T., Karim, M. R., & Islam, M. J. (2025, 2025//). *Influence of Mechanical and Durability Properties of Concrete with Limestone Powder.* Paper presented at the Proceedings of the Canadian Society for Civil Engineering Annual Conference 2023, Volume 6, Cham.

Mohammed, B. K., & Al-Numan, B. S. (2024). Effectiveness of Limestone Powder as a Partial Replacement of Cement on the Punching Shear Behavior of Normal- and High-Strength Concrete Flat Slabs. *Sustainability, 16*(5), 2151. doi:https://doi.org/10.3390/su16052151

Nikbin, I. M., Beygi, M. H. A., Kazemi, M. T., Vaseghi Amiri, J., Rabbanifar, S., Rahmani, E., & Rahimi, S. (2014). A comprehensive investigation into the effect of water to cement ratio and powder content on mechanical properties of self-compacting concrete. *Construction and Building Materials, 57*, 69-80. doi:https://doi.org/10.1016/j.conbuildmat.2014.01.098

Pliya, P., & Cree, D. (2015). Limestone derived eggshell powder as a replacement in Portland cement mortar. *Construction and Building Materials, 95*, 1-9.

Ratsarahasina, D. M., Ratsimbazafy, H. M., Robisonarison,

G. J., Randrianirainy, H. P. B., & Ramaroson, J. D. D. (2022). Etudes Des Influences Du Filler Calcaire Sur La Maniabilité Et Le Retrait Du Béton. *International Journal of Progressive Sciences and Technologies, 31*(1), 11. doi:10.52155/ijpsat.v31.1.4088

Sezer, G. İ. (2012). Compressive strength and sulfate resistance of limestone and/or silica fume mortars. *Construction and Building Materials, 26*(1), 613-618.

Shi, J., Wu, Z., Zhuang, J., Zhang, F., Zhu, T., & Li, H. (2023). Synergistic Effects of SAP, Limestone Powder and White Cement on the Aesthetic and Mechanical Properties of Fair-Faced Concrete. *Materials, 16*(21), 7058.

Vance, K., Kumar, A., Sant, G., & Neithalath, N. (2013). The rheological properties of ternary binders containing Portland cement, limestone, and metakaolin or fly ash. *Cement and Concrete Research, 52*, 196-207. doi:https://doi.org/10.1016/j.cemconres.2013.07.007

Wang, D., Shi, C., Farzadnia, N., Shi, Z., & Jia, H. (2018a). A review on effects of limestone powder on the properties of concrete. *Construction and Building Materials, 192*, 153-166. doi:https://doi.org/10.1016/j.conbuildmat.2018.10.119

Wang, D., Shi, C., Farzadnia, N., Shi, Z., Jia, H., & Ou, Z. (2018b). A review on use of limestone powder in cement-based materials: Mechanism, hydration and microstructures. *Construction and Building Materials, 181*, 659-672. doi:https://doi.org/10.1016/j.conbuildmat.2018.06.075

Wang, Q., Yang, J., & Chen, H. (2017). Long-term properties of concrete containing limestone powder. *Materials and Structures, 50*(3), 168. doi:10.1617/s11527-017-1040-8

Wang, X.-Y. (2020). Optimal mix design of low-CO2 blended concrete with limestone powder. *Construction and Building Materials, 263*, 121006. doi:https://doi.org/10.1016/j.conbuildmat.2020.121006

Yu, R., Spiesz, P., & Brouwers, H. J. H. (2014). Effect of nano-silica on the hydration and microstructure development of Ultra-High Performance Concrete (UHPC) with a low binder amount. *Construction and Building Materials, 65*, 140-150. doi:https://doi.org/10.1016/j.conbuildmat.2014.04.063

Zhao, L., He, T., Niu, M., Chang, X., Wang, L., & Wang, Y. (2024). Effect of Limestone Powder Mixing Methods on the Performance of Mass Concrete. *17*(3), 617.

Zhou, J., Qian, S., Beltran, M. G. S., Ye, G., van Breugel, K., & Li, V. C. (2010). Development of engineered cementitious composites with limestone powder and blast furnace slag. *Materials and structures, 43*(6), 803-814. doi:https://doi.org/10.1617/s11527-009-9549-0

MIJST
MIST International Journal of Science and Technology

# Potential Health Impacts from Radioactive Releases at Rooppur Nuclear Power Plant Under Hypothetical Accident Scenario

**Md Rosaidul Mawla[1,*], Radmim Ryean[1], Anisur Rahman[2], Abdus Sattar Mollah[3], Md. Shafiqul Islam[4], Kazi Imtiaz Kabir[5]**

[1]Department of Electrical, Electronic and Communication Engineering, Military Institute of Science and Technology, Mirpur 1216, Dhaka, Bangladesh
[2]Center for Research Reactor, Atomic Energy Research Establishment, Savar 1349, Bangladesh
[3]Department of Nuclear Science and Engineering, Military Institute of Science and Technology, Mirpur 1216, Dhaka, Bangladesh
[4]Department of Nuclear Engineering, University of Dhaka, Dhaka 1000, Bangladesh
[5]Research and Development Wing, Military Institute of Science and Technology, Mirpur 1216, Dhaka, Bangladesh

***Corresponding Email:** *mawla71@yahoo.com*

**ARTICLE INFO**

**Article History:**

*Received: 04th July 2025*
*Revised: 08th May 2025*
*Accepted: 12th May 2025*
*Published: 30th December 2025*

**Keywords**:

*Total Effective Dose*
*Committed Effective Dose*
*Thyroid Dose*
*Radiological Health Risk*
*Nuclear Accident*

**ABSTRACT**

This study presents a comprehensive assessment of radiological dose consequences from potential severe accident scenarios at the Rooppur Nuclear Power Plant (NPP), focusing on health impacts from radioactive releases. Utilizing HotSpot 3.1.2 and ORIGEN 2.2, the research estimates Total Effective Dose Equivalent (TEDE) and Committed Effective Dose Equivalent (CEDE) to critical organs, including the thyroid, skin, lungs, surface bone, red marrow, and liver, under seasonal meteorological conditions. The thyroid, due to its high affinity for radioactive iodine (particularly 131I), showed maximum CEDE values of 8.0 × 105 Sv and 4.4 × 105 Sv during the autumn and rainy seasons, respectively, at 30 meters from the source. These values, along with other organ doses, exceeded public and occupational dose limits up to 15 km in the rainy season and 30 km in the autumn season, primarily influenced by wind speed and precipitation. The study underscores the need for emergency protective measures such as sheltering, evacuation, and the administration of potassium iodide (KI), especially for populations within high-risk zones. It further recommends the integration of dose modeling findings into the National Nuclear and Radiological Emergency Preparedness and Response Plan (NNREPRP) to enhance response strategies and protect public health in the event of nuclear accidents.

This work is licensed under a *Creative Commons Attribution-Non-commercial 4.0 International License.*

## 1. INTRODUCTION

Nuclear energy plays a pivotal role in supporting the sustainable development goals by delivering low-carbon, high-capacity power that enhances both energy security and environmental sustainability. Achieving sustainable development necessitates a reliable and affordable energy infrastructure capable of minimizing greenhouse gas emissions, supporting healthcare and education systems, fostering industrialization, and reducing poverty. Nuclear power, when integrated with other advanced energy technologies, can meet these demands while promoting long-term economic resilience and environmental protection (Rogner, 2001; Sattar et al., 2016). In alignment with these goals, Bangladesh is commissioning the Rooppur Nuclear Power Plant (NPP), comprising two VVER-1200 units designed under the Generation III+ ASE-2006 specifications. These reactors are expected to become operational by 2025/2026 and are equipped with enhanced passive and active safety systems, offering increased resistance to severe accidents (Fairuz and Sahadath, 2020). Nevertheless, the possibility of a low-probability, high-consequence event cannot be entirely dismissed and warrants thorough risk assessment and emergency preparedness planning.

The International Atomic Energy Agency (IAEA) defines a nuclear accident as an event involving the release of radioactive materials that has significant consequences for the environment, the public, and the nuclear facility where it occurs (IAEA, 2013). When safety systems fail to operate as designed, such events can escalate into severe accidents with profound impacts on human health (Aliyu et al., 2015) and the surrounding environment. During a

nuclear accident, radionuclides such as iodine-131 ($^{131}$I), cesium-137 ($^{137}$Cs), and strontium-90 ($^{90}$Sr) may be released, emitting gamma rays, beta particles, and alpha particles. These forms of radiation vary in their penetration capabilities and biological effects. The severity of health outcomes depends on the type and amount of radiation, duration of exposure, and individual susceptibility. Short-term effects may include acute radiation syndrome, nausea, burns, and immune suppression, while long-term effects can involve cancer, organ damage, reproductive issues, and hereditary mutations.

Historical nuclear accidents provide critical insight into the nature and consequences of radioactive releases. The Chernobyl disaster in 1986 resulted in the release of a wide range of radionuclides, with iodine-131 ($^{131}$I) and cesium-137 ($^{137}$Cs) having the most significant impact on public health and the environment due to their radiological properties and biological uptake (Sihver and Yasuda, 2018). Similarly, the Fukushima Daiichi accident in 2011 led to the release of several volatile fission products, including noble gases like krypton-85 ($^{85}$Kr) and xenon-133 ($^{133}$Xe), as well as isotopes of iodine ($^{131}$I, $^{132}$I), cesium ($^{134}$Cs, $^{136}$Cs, $^{137}$Cs), and tellurium ($^{132}$Te) (Faith and Kim, 2020). Studies on previous nuclear power plant accidents confirm that these radionuclides, particularly noble gases (xenon and krypton), iodine, cesium, strontium, tellurium, and rubidium are among the most likely to be released during a severe event (ICRU, 2015; Faith and Kim, 2020). These substances vary in terms of their physical and chemical properties, environmental mobility, and biological effects, making them critical indicators for dose assessment and emergency planning. These past incidents highlight the necessity of understanding the behavior and health implications of specific radionuclides in order to enhance preparedness and response strategies for nuclear facilities, including the Rooppur NPP in Bangladesh.

Radioactive releases during nuclear accidents pose serious health risks, with iodine-131 ($^{131}$I) and cesium-137 ($^{137}$Cs) being the most critical radionuclides. $^{131}$I has a short half-life of about eight days and accumulates in the thyroid gland when inhaled or ingested, increasing the risk of thyroid cancer (Walsh et al., 2014, Faith and Kim, 2020), particularly in children. In contrast, $^{137}$Cs, with a 30-year half-life, contaminates soil and food supplies, leading to long-term exposure and impacts on agriculture (Yasunari et al., 2011), livestock, and human health (Hoeve and Jacobson, 2012; Aliyu et al., 2015).

Assessing radiation dose is essential for understanding these risks. Dose assessment considers external, inhalation, and ingestion pathways to estimate the Total Effective Dose Equivalent (TEDE) and Committed Effective Dose Equivalent (CEDE). The thyroid gland receives special attention due to its sensitivity to radioiodine. Based on dose assessments, protective measures such as sheltering, evacuation, food restrictions, and potassium iodide distribution are used to minimize health effects.

This research focuses on a hypothetical major radioactive release at the Rooppur NPP, which houses Generation III+ VVER-1200 reactors. While limited studies exist globally on VVER-1200 accident scenarios, few integrate detailed source term modeling, meteorological analysis, and radiation dispersion together. This study bridges that gap by combining source term estimation using ORIGEN 2.2 (Croff, 1980; Croff, 1983), wind pattern simulation via wind rose analysis, and atmospheric dispersion and dose modeling with HotSpot Health Physics software (Homann and Aluzzi, 2013).

This study aims to estimate potential radiation doses to **human organs** and the **environment** under a severe accident scenario at Rooppur NPP using a **site-specific** and **seasonally** differentiated approach. By integrating reactor source term modeling (**ORIGEN 2.2**) with atmospheric dispersion analysis (**HotSpot 3.1.2**), it provides a detailed assessment of **TEDE** and **organ-specific CEDE**, particularly highlighting **thyroid vulnerability**. A novel aspect of this research is the use of **localized meteorological data** to simulate real-world seasonal variations in radiological impact zones, thereby offering tailored recommendations for emergency preparedness and radiological protection planning in Bangladesh.

## 2. MATERIALS AND METHODS

### 2.1 Overview

This study employs a combined approach using ORIGEN 2.2 and HotSpot 3.1.2 to assess the radiological impact of a hypothetical accident at the Rooppur NPP. The ORIGEN 2.2 code is used to estimate the radionuclide inventory based on operational parameters of the VVER-1200 reactor, including thermal power, fuel enrichment, and burnup data. The calculated source term, representing the types and quantities of radionuclides released during an accident, is then input into the HotSpot code to simulate atmospheric dispersion and dose distribution.

Site-specific meteorological data, such as wind speed, direction, atmospheric stability class, and mixing height, are collected from the Bangladesh Meteorological Department (BMD) and used in the simulation. The general plume model within HotSpot is applied to evaluate airborne dispersion under two seasonal scenarios: rainy and autumn. These conditions reflect varying atmospheric behaviors that can influence the spread and deposition of radioactive materials.

This section outlines the use of dispersion modeling, seasonally variable weather conditions, and validated simulation tools to estimate TEDE and CEDE to the public. The integrated methodology aims to support emergency planning and radiological risk assessment for the Rooppur NPP. The flowchart presented in Figure 1 illustrates the structured methodology adopted in this study to evaluate the health impacts of potential radioactive releases from the Rooppur NPP. The process begins with the identification of the study area, focusing on the Rooppur NPP, which hosts two VVER-1200 pressurized water reactors. Subsequently, reactor core specifications and meteorological data such as wind speed, direction, temperature, and rainfall are collected from the BMD. Radionuclide inventories are calculated using the ORIGEN 2.2 code, while atmospheric dispersion modeling is

conducted with HotSpot 3.1.2. The final phase involves radiation dose estimation and health impact analysis, incorporating both TEDE and organ-specific CEDE, under varying seasonal and spatial conditions.

### 2.2 Study Area

The study focuses on the Rooppur NPP as shown in Figure 2, located in Ishwardi Upazila of the Pabna District, on the eastern bank of the Padma River in Bangladesh. Geographically, the plant is positioned at approximately 24.068° N latitude and 89.032° E longitude. As Bangladesh's first nuclear power facility, Rooppur NPP consists of two VVER-1200 pressurized water reactors, each with a capacity of 1,200 MWe, developed to address the country's increasing energy demands.

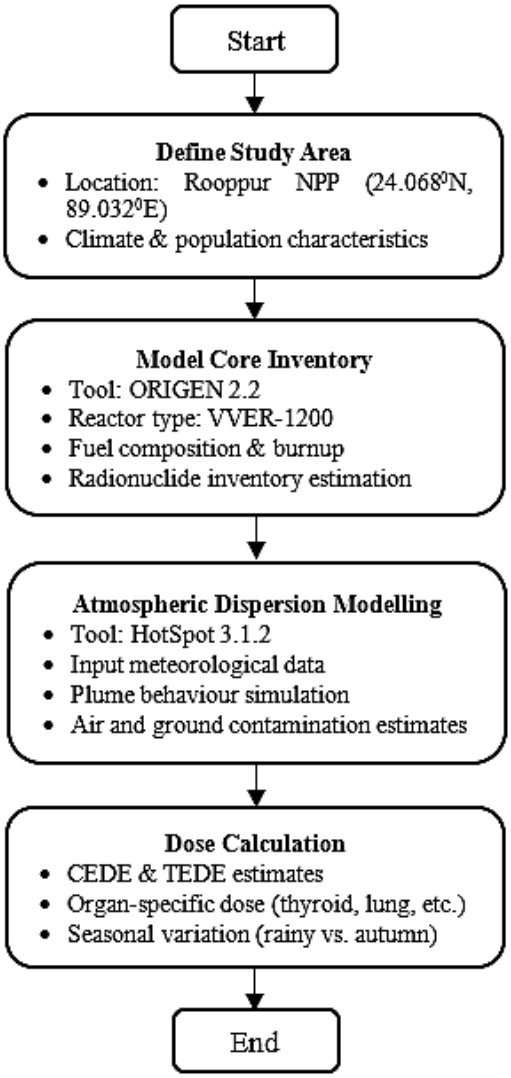



**Figure 1**: Overview of methodological framework.

Site selection for the plant was guided by detailed feasibility assessments, which considered geological stability, the availability of water resources for reactor cooling, and the relative remoteness from densely populated areas to minimize public risk. The surrounding region is primarily rural, comprising agricultural lands, small settlements, and ecologically sensitive zones, which underscores the critical importance of ensuring public and environmental safety in the event of a radiological incident.

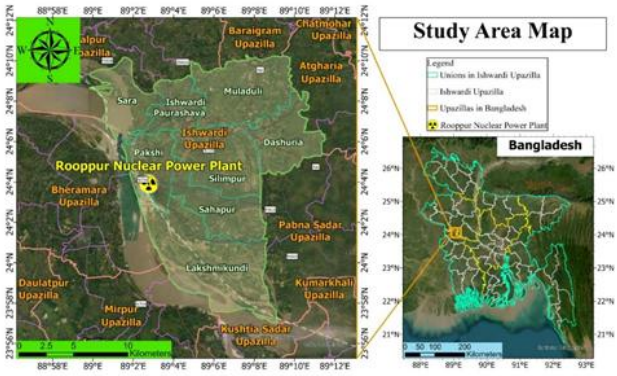



**Figure 2**: Study area of the Rooppur NPP site.

The area falls under a subtropical monsoon climate, characterized by distinct seasonal variability in meteorological conditions. High precipitation during the rainy season contributes to increased wet deposition of airborne radionuclides, while lower wind speeds in autumn can lead to elevated ground-level concentrations near the release point. These meteorological parameters significantly influence the dispersion behavior of radioactive materials and are therefore central to assessing their potential health impacts.

For this study, site-specific meteorological data, including wind speed, wind direction, temperature, and rainfall, were obtained from the BMD. This data served as input for modeling dispersion and dose assessment using the HotSpot 3.1.2 and ORIGEN 2.2 software tools. The analysis considered a radial distance of up to 40 kilometers from the reactor site, covering zones that may be impacted during a severe nuclear accident.

The selection of this study area allows for a comprehensive assessment of potential radiological health risks to nearby populations and provides a basis for recommending protective measures and emergency response strategies tailored to the specific geographical and climatic conditions of the Rooppur NPP vicinity.

### 2.3 ORIGEN2.2 Code

ORIGEN2.2 (Croff, 1980; Croff, 1983), developed by Oak Ridge National Laboratory, USA, is a computer code designed to calculate the isotopic composition and associated radiological characteristics of nuclear fuel over time. It models the production and depletion of nuclides due to fission, radioactive decay, neutron capture, and transmutation, making it an essential tool for evaluating source terms in nuclear safety analyses.

The code uses the matrix exponential method to solve a large system of coupled, first-order linear differential equations that describe the time evolution of nuclide concentrations. These equations are based on a point reactor model, assuming a homogeneous system where neutron flux and cross-section values are averaged over space and energy.

The time-dependent concentration of a nuclide $X_i$ is expressed by the following equation (1):

$$\frac{dX_i}{dt} = \sum_{j=1}^{N} l_{ij}\lambda_j X_j + \bar{\Phi}\sum_{k=1}^{N} f_{ik}\sigma_k X_k - X_i(\lambda_i + \bar{\Phi}\sigma_i) \quad (1)$$

Where:

$\bar{\Phi}$: average neutron flux (spatial and energy),
$\lambda_i$: decay constant of nuclide i,
$\sigma_i$: neutron absorption cross-section of nuclide i,
$l_{ij}$: fraction of radioactive decay from nuclide j to i,
$f_{ik}$: fraction of neutron absorption by nuclide k leading to formation of i,
$X_i$: atomic concentration of nuclide i.

In this study, ORIGEN2.2 was applied to simulate the fission product inventory of the VVER-1200 reactor at Rooppur NPP, using plant-specific data such as core power level, enrichment, burnup, and operational history. The resulting radionuclide inventory serves as the source term input for atmospheric dispersion modeling using the HotSpot code.

### 2.4 HotSpot Simulation Model

HotSpot 3.1.2 (Homann and Aluzzi, 2013), developed by Lawrence Livermore National Laboratory, is a user-friendly health physics code designed to support emergency planners and first responders in evaluating the radiological consequences of incidents involving radioactive material releases. It employs Gaussian plume atmospheric dispersion models to provide rapid, first-order approximations of radiation impacts due to short-term, short-range, and near-surface radioactive emissions under relatively simple meteorological conditions.

HotSpot is particularly effective in field applications due to its portability, fast computation, and validated performance. Its global recognition and integration into nuclear emergency preparedness tools make it a valuable asset for safety analysis (Malizia et al., 2021). In this study, HotSpot was applied to model a hypothetical radioactive release from the VVER-1200 reactor at Rooppur NPP. The simulation process involved the following key inputs:

- **Source term data** from ORIGEN2.2, which provided the radionuclide inventory and activity,
- **Site-specific meteorological data** such as wind speed, direction, atmospheric stability class, and mixing height (collected from the Bangladesh Meteorological Department),
- **Release conditions**, including release height, duration, and deposition velocity.

Two seasonal scenarios, rainy and autumn, were chosen to reflect different atmospheric dispersion patterns. The primary outputs from the HotSpot simulation included:

- TEDE,
- CEDE due to inhalation of radioactive materials,
- Organ dose for specific human organs exposed to the radiation.

These outputs help determine potential health effects, inform protective actions, and support emergency response planning for hypothetical accident scenarios.

The flowchart of the HotSpot simulation process is illustrated in Figure 3 below.

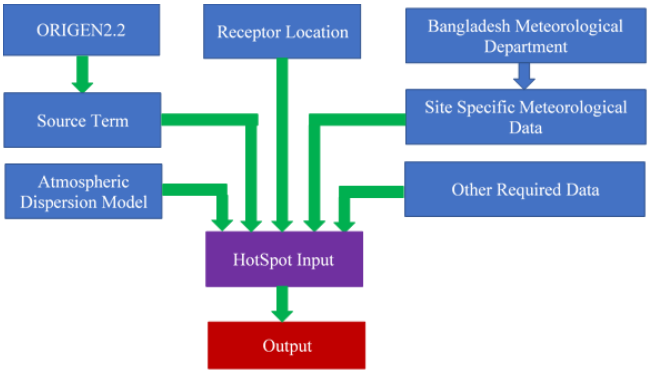



**Figure 3:** Flowchart illustrating the simulation process of HotSpot (Mawla et al., 2024).

### 2.5 Meteorological Conditions

Bangladesh has six traditional seasons; however, for the purpose of this study, four primary seasons have been considered due to their meteorological significance: winter (December–February), summer (March–May), rainy season (June–September), and autumn (October–November) (Ayesha et al., 2016). The country experiences a tropical monsoon climate, marked by notable variations in temperature, humidity, and rainfall across these seasons.

During the summer, long sunny days and high temperatures dominate. The rainy season is characterized by heavy cloud cover and frequent, intense rainfall. The autumn season generally features lower rainfall and slightly cooler temperatures, while winter brings the lowest temperatures of the year.

Meteorological conditions at the Rooppur NPP site are particularly important for both routine operations and emergency preparedness. Wind speed, direction, temperature gradients, and atmospheric stability significantly influence the dispersion of radioactive materials in the event of an accidental release. This study specifically focuses on two representative seasons, rainy and autumn, to evaluate atmospheric dispersion behavior and radiological impacts under varying weather conditions.

#### 2.5.1 Rainy Season

The rainy season, also known as the southwest monsoon, spans June through September and is characterized by persistent cloud cover, frequent rainfall, and high humidity (Ayesha et al., 2016). During this period, wind predominantly flows from the east, with occasional movement from the south.

The wind rose analysis of the last thirty-two years, presented in Figure 4, illustrates the seasonal wind direction and frequency patterns for the Rooppur region. Based on this long-term data, the average wind speed during the rainy season is 1.64 m/s, while the calm wind frequency stands at 30.7%. Wind speeds ranging from 0.50–2.10 m/s occur 27.3% of the time, 2.10–3.60 m/s occur 22.5%, and 3.60–5.70 m/s occur 7.9%.

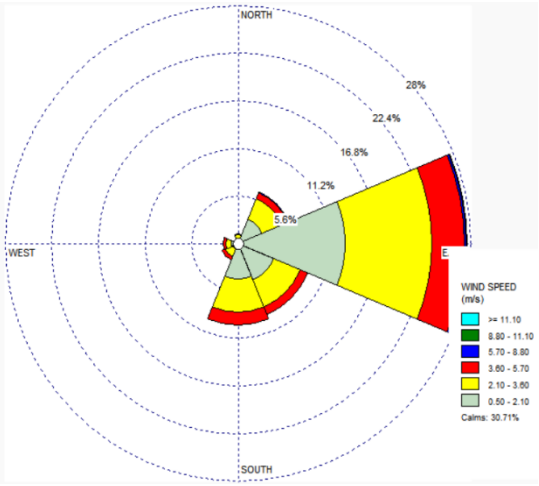



**Figure 4**: The wind rose for the average wind speed of the rainy season.

Relative humidity is generally high throughout the season, often exceeding 80%, which can significantly affect atmospheric dispersion. According to the BMD, the average rainfall during this period is approximately 0.65 mm/hr. Wind conditions are typically light to moderate (Ayesha et al., 2016), influencing the surface-level concentration and movement of airborne radioactive materials in the event of a nuclear release.

### 2.5.2 Autumn Season

The autumn season, also referred to as the post-monsoon period, encompasses the months of October and November (Ayesha et al., 2016). During this season, the prevailing wind direction is primarily from the east, with occasional flows from the northeast and west.

The wind rose analysis over the past thirty-two years, shown in Figure 5, illustrates the seasonal wind patterns specific to this period. The average wind speed during autumn is 0.95 m/s, the lowest among all four seasons, indicating reduced atmospheric dispersion capacity. The calm wind frequency is notably high at 53.2%. Wind speeds between 0.50–2.10 m/s occur 19.5% of the time, 2.10–3.60 m/s occur 12.5%, and 3.60–5.70 m/s occur only 3.4%.

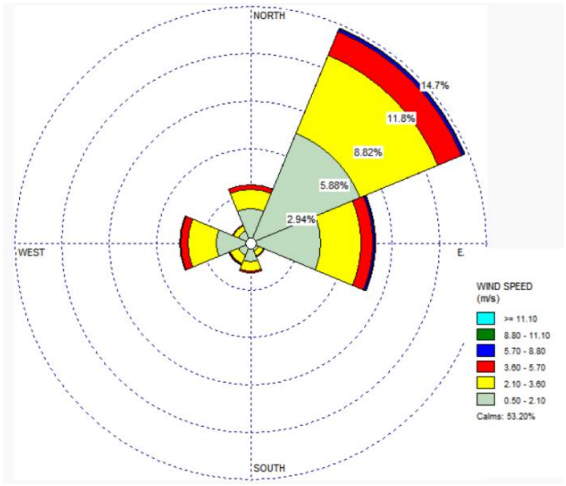



**Figure 5**: The wind rose for the average wind speed of the autumn season

Meteorological data from the BMD show that the average rainfall during autumn is 0.15 mm/hr, indicating relatively dry conditions compared to the rainy season. Additionally, the month of November records the lowest average wind speed of 0.89 m/s and the highest calm wind frequency of 55.21%.

### 2.5.3 Atmospheric Stability

Atmospheric stability refers to the behavior of an air parcel when it is slightly displaced vertically, determining whether it will rise, sink, or remain in equilibrium. This property is crucial in assessing how radioactive materials released during a nuclear incident disperse in the atmosphere. Factors such as temperature gradients, wind speed, and wind direction significantly influence atmospheric stability and, consequently, the dispersion patterns of radioactive plumes (Hussain et al., 2023). Accurate characterization of atmospheric stability is essential for predicting the spread and concentration of radionuclides, which directly impacts the radiological risk to the environment and public health. The Pasquill stability classification is commonly used to categorize atmospheric conditions into six classes: A (very unstable), B (moderately unstable), C (slightly unstable), D (neutral), E (slightly stable), and F (moderately stable) (Foudil et al., 2017; Ned Xoubi, 2020). These classifications are critical inputs for dispersion models like HotSpot, which use them to simulate the transport and deposition of radioactive substances under various meteorological scenarios.

## 3. RESULTS AND DISCUSSIONS

### 3.1 Overview

In this study, the worst-case scenario is modeled based on current meteorological data, where Stability Class A, representing very unstable atmospheric conditions, is assumed to produce the highest radiological impact. For the sake of conservative assessment, the effective release height is considered to be zero meters, simulating a containment failure with ground-level discharge. Several human organs are susceptible to radiation exposure during a severe nuclear accident; however, this analysis focuses on the thyroid, skin, lungs, surface bone, red bone marrow, and liver due to their radiosensitivity and relevance to dose assessment. To simplify calculations in the HotSpot code, an effective population of 50 individuals is assumed within the exposure zone. Distances from the source are defined arbitrarily within the model to evaluate plume dispersion and resulting organ doses.

### 3.2 Calculation of the Source Term

The core inventory of radionuclides was assessed using the ORIGEN 2.2 code, which calculates the time-dependent activity of each nuclide based on fuel composition, burnup history, and operational parameters. To estimate the source term released during a hypothetical accident, group-specific release fractions were applied to the core inventory. The radionuclides were categorized into chemical groups, namely noble gases, halogens, alkali metals, tellurium, and lanthanides. The distribution of radionuclides by group is presented in Table 1, while Table 2 lists the individual radionuclides along with their

corresponding activity values in Becquerels (Bq).

**Table 1:** Formation of source term with different groups

| Nuclide Group | Species | Total Activity (Bq) | Percentage (%) |
|---|---|---|---|
| Noble Gas | Kr, Xe | $1.81 \times 10^{19}$ | 62.60 |
| Halogen | I | $7.81 \times 10^{18}$ | 26.94 |
| Alkali metal | Ba, Cs | $2.34 \times 10^{18}$ | 8.06 |
| Tellurium | Te | $6.93 \times 10^{17}$ | 2.39 |
| Lanthanide | Y | $3.22 \times 10^{15}$ | 0.01 |

Among the groups, noble gases and halogens represent the most significant contributors to the total inventory, with activities of approximately $1.81 \times 10^{19}$ Bq and $7.81 \times 10^{18}$ Bq, respectively. These high activity levels are attributed to their volatility and low retention in containment systems. Figure 6 visualizes the activity levels of each radionuclide group in the reactor core following a postulated accident scenario at the Rooppur NPP, highlighting the dominant role of noble gases and halogens in defining the source term.

To evaluate the environmental impact and associated health risks of various radionuclide groups, ground-level deposition was computed independently for each chemical category. Radioisotopes were selected as representative source terms, grouped into three primary classes. Table 2 provides a detailed overview of each isotope's core inventory, applied release fraction, and corresponding released activity. These findings were benchmarked against international data from multiple nuclear reactors, demonstrating consistency with previous studies conducted by the IAEA (2008), Anvari (2012) and Foudil et al. (2017). The observed variations across datasets are attributed to differences in reactor types, fuel compositions, burnup levels, and radionuclide inventories (Ned Xoubi, 2022).

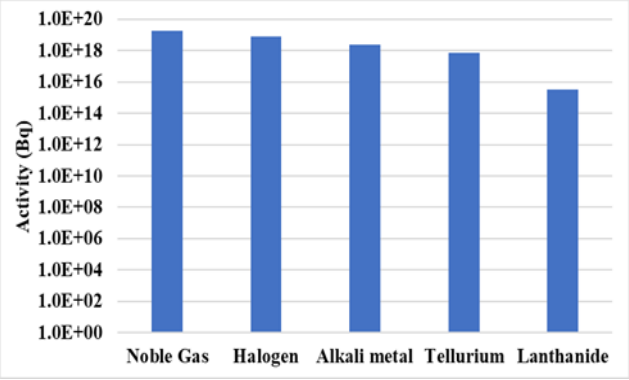



**Figure 6**: Groupwise core inventory.

Each radionuclide poses distinct health hazards depending on its radiological properties and biological uptake mechanisms. For example, the core inventory of Iodine-131 ($^{131}$I) was estimated at $2.97 \times 10^{18}$ Bq, with $1.19 \times 10^{18}$ Bq released into the environment. In comparison, Cesium-137 ($^{137}$Cs) had a core inventory of $3.27 \times 10^{17}$ Bq, of which $9.81 \times 10^{16}$ Bq was released. These estimates are based on a hypothetical worst-case scenario involving complete core exposure and a full containment breach at the Rooppur NPP.

**Table 2**: Source Term of VVER-1200 Reactor Core

| Nuclide | Core Inventory (Bq) | Release Fraction (NRC 1.183) | Release to Environment (Bq) |
|---|---|---|---|
| $^{83m}$Kr | $4.11 \times 10^{17}$ | 1 | $4.11 \times 10^{17}$ |
| $^{85}$Kr | $3.19 \times 10^{16}$ | 1 | $3.19 \times 10^{16}$ |
| $^{85m}$Kr | $8.99 \times 10^{17}$ | 1 | $8.99 \times 10^{17}$ |
| $^{87}$Kr | $1.75 \times 10^{18}$ | 1 | $1.75 \times 10^{18}$ |
| $^{88}$Kr | $2.47 \times 10^{18}$ | 1 | $2.47 \times 10^{18}$ |
| $^{89}$Kr | $3.06 \times 10^{18}$ | 1 | $3.06 \times 10^{18}$ |
| $^{133}$Xe | $6.23 \times 10^{18}$ | 1 | $6.23 \times 10^{18}$ |
| $^{133m}$Xe | $1.92 \times 10^{17}$ | 1 | $1.92 \times 10^{17}$ |
| $^{128}$I | $2.81 \times 10^{16}$ | 0.4 | $1.12 \times 10^{16}$ |
| $^{130}$I | $8.79 \times 10^{16}$ | 0.4 | $3.52 \times 10^{16}$ |
| $^{131}$I | $2.97 \times 10^{18}$ | 0.4 | $1.19 \times 10^{18}$ |
| $^{132}$I | $4.32 \times 10^{18}$ | 0.4 | $1.73 \times 10^{18}$ |
| $^{133}$I | $6.25 \times 10^{18}$ | 0.4 | $2.50 \times 10^{18}$ |
| $^{135}$I | $5.85 \times 10^{18}$ | 0.4 | $2.34 \times 10^{18}$ |
| $^{139}$Ba | $5.69 \times 10^{18}$ | 0.02 | $1.14 \times 10^{17}$ |
| $^{140}$Ba | $5.48 \times 10^{18}$ | 0.02 | $1.09 \times 10^{17}$ |
| $^{134}$Cs | $4.87 \times 10^{17}$ | 0.3 | $1.46 \times 10^{17}$ |
| $^{134m}$Cs | $1.30 \times 10^{17}$ | 0.3 | $3.90 \times 10^{16}$ |
| $^{135m}$Cs | $7.66 \times 10^{16}$ | 0.3 | $2.30 \times 10^{16}$ |
| $^{136}$Cs | $1.53 \times 10^{17}$ | 0.3 | $4.59 \times 10^{16}$ |
| $^{137}$Cs | $3.27 \times 10^{17}$ | 0.3 | $9.81 \times 10^{16}$ |
| $^{138}$Cs | $5.85 \times 10^{18}$ | 0.3 | $1.76 \times 10^{18}$ |
| $^{90}$Y | $2.63 \times 10^{17}$ | 0.0002 | $5.26 \times 10^{13}$ |
| $^{91}$Y | $4.23 \times 10^{18}$ | 0.0002 | $8.26 \times 10^{14}$ |
| $^{91m}$Y | $2.38 \times 10^{18}$ | 0.0002 | $4.76 \times 10^{14}$ |
| $^{92}$Y | $4.38 \times 10^{18}$ | 0.0002 | $8.76 \times 10^{14}$ |
| $^{93}$Y | $4.96 \times 10^{18}$ | 0.0002 | $9.92 \times 10^{14}$ |
| $^{127}$Te | $2.83 \times 10^{17}$ | 0.05 | $1.42 \times 10^{16}$ |
| $^{127m}$Te | $3.75 \times 10^{16}$ | 0.05 | $1.88 \times 10^{15}$ |
| $^{129}$Te | $8.91 \times 10^{17}$ | 0.05 | $4.46 \times 10^{16}$ |
| $^{129m}$Te | $1.33 \times 10^{17}$ | 0.05 | $6.65 \times 10^{15}$ |
| $^{131m}$Te | $4.19 \times 10^{17}$ | 0.05 | $2.10 \times 10^{16}$ |
| $^{132}$Te | $4.26 \times 10^{18}$ | 0.05 | $2.13 \times 10^{17}$ |
| $^{133m}$Te | $2.39 \times 10^{18}$ | 0.05 | $1.19 \times 10^{17}$ |
| $^{134}$Te | $5.43 \times 10^{18}$ | 0.05 | $2.72 \times 10^{17}$ |

To ensure a conservative and safety-focused approach, standard release fractions were applied based on established guidelines and previous literature, including NRC Regulatory Guide 1.183 (2000). Under these assumptions, the total source term released into the environment from the Rooppur NPP, as modeled using the HotSpot code, is estimated at $2.90 \times 10^{19}$ Bq. Among the selected radionuclides, Iodine-131 ($^{131}$I) and Cesium-137 ($^{137}$Cs) emerged as key contributors due to their high radioactivity and environmental persistence, which make them significant threats through contamination of air, water, soil, and food chains. Additionally, Iodine-133 ($^{133}$I) showed the highest individual release at $2.50 \times 10^{18}$ Bq, followed by Xenon-133 ($^{133}$Xe) at $6.23 \times 10^{18}$ Bq highlighting the critical roles of halogens and noble gases in the overall radiological impact. These results closely align with global data from similar reactor studies, accounting for differences in fuel design and operating conditions. Subsequent sections further examine the

HotSpot simulation outputs under the prevailing meteorological conditions to assess the potential dose impacts on human organs and the surrounding environment.

### 3.3 Description of TEDE

#### 3.3.1 TEDE in rainy season

During the rainy season, the highest recorded TEDE along the plume center line was 3.80 × $10^4$ Sv, observed within 30 meters of the reactor core. This value decreased rapidly by two orders of magnitude within six minutes, reaching 9.40 × $10^2$ Sv at 300 meters from the source. The dose continued to drop by another order of magnitude, measuring 2.20 × $10^1$ Sv at 3 kilometers after approximately one hour and two minutes. The declining trend persisted over time and distance, reducing to 1.60 × $10^{-5}$ Sv at 30 kilometers after ten hours and twenty-eight minutes. At a distance of 70 kilometers, the TEDE further declined to 1.30 × $10^{-13}$ Sv, occurring more than twenty-four hours post-release. The variation of dose and activity with distance for both the rainy and autumn seasons is illustrated in Figure 7.

#### 3.3.2 TEDE in Autumn Season

During the autumn season, the peak TEDE at the plume centerline was recorded as 5.5 × $10^4$ Sv at a distance of 30 meters from the reactor core, occurring within less than one minute of the release. This value decreased by two orders of magnitude to 7.8 × $10^2$ Sv at 300 meters from the source within approximately five minutes. The dose continued to diminish, reaching 2.1 × $10^1$ Sv at 3 kilometers after fifty-eight minutes. At a distance of 30 kilometers, the TEDE further dropped to 1.4 × $10^{-2}$ Sv after nine hours and forty-nine minutes. Eventually, at 70 kilometers, the dose declined to 4.5 × $10^{-6}$ Sv within twenty-two hours and fifty-four minutes. The variation of dose with distance across different seasons is illustrated in Figure 7.

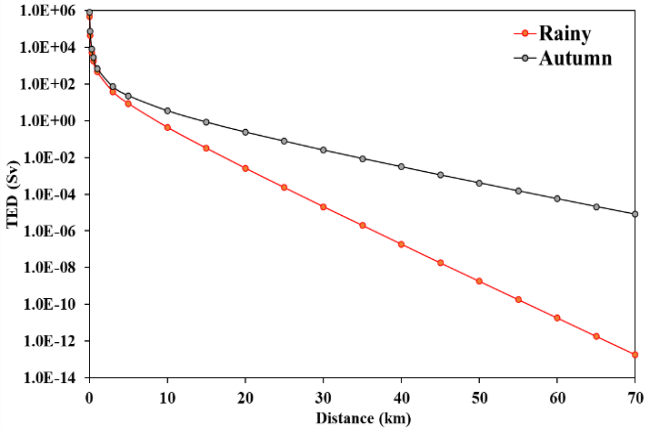



**Figure 7**: TEDE Vs Distance in rainy and autumn seasons.

#### 3.3.3 Comparison of TEDE

The maximum TEDE values for the rainy and autumn seasons were observed at a distance of 0.030 km (30 meters) from the reactor site, registering 3.8 × $10^4$ Sv and 5.5 × $10^4$ Sv, respectively (Figure 7). This variation is primarily attributed to differences in wind speed between the two seasons: the autumn season experiences the lowest average wind speed at 0.95 m/s, while the rainy season records the highest at 1.64 m/s. From the source, TEDE values exhibit a steep decline within the first 300 meters, after which the decrease becomes more gradual over time and distance. These findings are consistent with those of Hussain et al., (2023), which similarly concluded that higher wind speeds contribute to lower peak TEDE values due to enhanced dispersion. Importantly, the doses measured during the first hour of exposure significantly exceed public dose limits established by regulatory authorities.

### 3.4 Individual Organ Dose

The impact of radiation on human health and the environment was assessed using site-specific meteorological data and radionuclide profiles relevant for plume dose estimation. The HotSpot code was employed to calculate the CEDE, which integrates committed dose equivalents over a 50-year period for various body organs, weighted by appropriate tissue weighting factors (Henry et al., 2021). In the event of a severe nuclear accident, radiation exposure can affect human organs, including the skin, lungs, thyroid, surface bone, red marrow, liver, spleen, adrenal glands, ovaries, breasts, stomach wall, small intestine wall, upper and lower large intestine walls, bladder wall, thymus, esophagus, muscle, kidneys, testes, uterus, pancreas, and brain. However, the subsequent discussion focuses on the most radiosensitive organs and compares their responses under different seasonal conditions.

#### 3.4.1 Individual Organ Dose in Rainy Season

Figure 8 presents the CEDE distribution across critical organs, including the thyroid, skin, lungs, surface bone, red marrow, and liver, as a function of downwind distance during the rainy season. Among these, the thyroid exhibits the highest sensitivity, receiving the most significant dose of CEDE. The maximum dose for the thyroid is estimated at 4.7×$10^5$ Sv at a distance of 0.03 km from the reactor, occurring within the first minute of release.

Following the thyroid, the organs with the highest CEDE values at 30 meters include the skin (5.7×$10^4$ Sv), lungs (1.5×$10^4$ Sv), surface bone (2.1×$10^4$ Sv), red marrow (1.4 × $10^4$ Sv), and liver (1.3×$10^4$ Sv). These doses decline sharply with increasing distance and time. At 300 meters, within approximately three minutes, the CEDE values reduce to 5.0×$10^3$ Sv (thyroid), 3.1 × $10^3$ Sv (skin), 7.0×$10^2$ Sv (lungs), 1.0×$10^3$ Sv (surface bone), 7.1 × $10^2$ Sv (red marrow), and 6.6 × $10^2$ Sv (liver).

The trend of dose reduction continues at greater distances. At 3 km, within thirty-four minutes post-release, the thyroid receives 3.9×$10^1$ Sv, followed by the skin (9.2 × $10^1$ Sv), lungs (2.0×$10^1$ Sv), surface bone (2.9 × $10^1$ Sv), red marrow (2.1×$10^1$ Sv), and liver (1.9×$10^1$ Sv). At 20 km, after three hours and forty-seven minutes, the CEDE values further decline to 2.6 × $10^{-3}$ Sv (thyroid), 8.7 × $10^{-3}$ Sv (skin), 1.8×$10^{-3}$ Sv (lungs), 2.7×$10^{-3}$ Sv (surface bone), 1.9×$10^{-3}$ Sv (red marrow), and 1.7×$10^{-3}$ Sv (liver). These observations highlight the rapid attenuation of organ doses

with increasing distance and time after the release.

### 3.4.2 Individual organ dose in the autumn season

Figure 9 illustrates the distribution of CEDE across key human organs, specifically the thyroid, skin, lung, surface bone, red marrow, and liver, as a function of downwind distance during the autumn season. Among these, the thyroid is identified as particularly sensitive, receiving the highest CEDE values shortly after release. The maximum CEDE for the thyroid was observed at 0.030 km from the release point, estimated at $8.0 \times 10^5$ Sv within the first minute. Other organs also exhibited elevated doses at this distance: the skin ($5.4 \times 10^4$ Sv), lung ($1.6 \times 10^4$ Sv), surface bone ($2.2 \times 10^4$ Sv), red marrow ($1.5 \times 10^4$ Sv), and liver ($1.4 \times 10^4$ Sv).

Doses decrease significantly with increasing distance and time. At 300 meters, within approximately three minutes of release, CEDE values dropped to: thyroid ($8.0 \times 10^3$ Sv), skin ($1.6 \times 10^3$ Sv), lung ($3.9 \times 10^2$ Sv), surface bone ($5.6 \times 10^2$ Sv), red marrow ($3.9 \times 10^2$ Sv), and liver ($3.6 \times 10^2$ Sv).

By the time the plume reached 3 km, roughly fifty-eight minutes post-release, organ doses further declined: thyroid ($7.2 \times 10^1$ Sv), skin ($7.9 \times 10^1$ Sv), lung ($1.7 \times 10^1$ Sv), surface bone ($2.5 \times 10^1$ Sv), red marrow ($1.8 \times 10^1$ Sv), and liver ($1.6 \times 10^1$ Sv).

At 35 km, nearly eleven and a half hours after the release, the CEDE levels were significantly reduced but still measurable: thyroid ($8.7 \times 10^{-3}$ Sv), skin ($2.3 \times 10^{-2}$ Sv), lung ($4.6 \times 10^{-3}$ Sv), surface bone ($6.9 \times 10^{-3}$ Sv), red marrow ($4.7 \times 10^{-3}$ Sv), and liver ($4.4 \times 10^{-3}$ Sv).

### 3.4.3 Analysis on Individual Organ Dose

The CEDE is highest near the reactor in both seasons and decreases with time and distance due to plume dispersion and dilution. Lower wind speeds result in higher CEDE values; thus, the autumn season, with an average wind speed of 0.95 m/s, shows greater doses than the rainy season (1.64 m/s), as illustrated in Figures 8 and 9.

At 0.030 km, CEDE values peak for all organs, especially the thyroid ($8.0 \times 10^5$ Sv in autumn). Other affected organs in descending order are skin ($5.4 \times 10^4$ Sv), surface bone ($2.2 \times 10^4$ Sv), lung ($1.6 \times 10^4$ Sv), red marrow ($1.5 \times 10^4$ Sv), and liver ($1.4 \times 10^4$ Sv). These six organs are the most vulnerable to radiation in severe accident scenarios at Rooppur NPP.

In the rainy season, CEDE declines more sharply beyond 10 km, becoming negligible by 20 km due to atmospheric washout from rainfall (0.65 mm/hr). In contrast, the autumn season maintains significant CEDE levels up to 30 km due to minimal precipitation.

Exposures above 0.1 Sv increase cancer risk by 0.5%, per ICRP guidelines (ICRP, 2007). In autumn, CEDE exceeds this threshold up to 20 km, posing health risks to the public. Occupational exposure limits set by the USNRC (50 mSv/year) are exceeded up to 17 km in the rainy season and 30 km in autumn, indicating extended risk zones for workers.

To mitigate internal exposure from inhaled or ingested radionuclides, emergency measures such as evacuation, sheltering, and stable iodine prophylaxis are essential, especially for protecting sensitive organs like the thyroid (Henry et al., 2021).

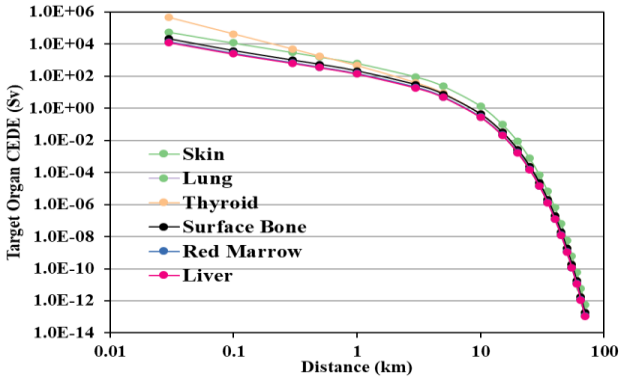



**Figure 8**: Organ CEDE versus downwind distance in the rainy season.

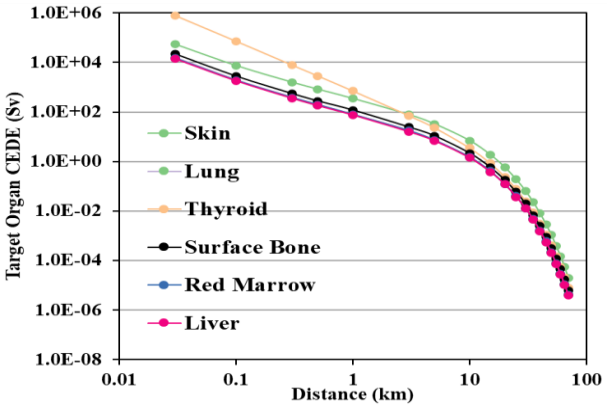



**Figure 9:** Organ CEDE versus downwind distance in the autumn season.

### 3.5 Thyroid Committed Dose Equivalent

Radioactive iodine released during a nuclear power plant accident poses a significant health risk, particularly to the thyroid gland. Due to its natural affinity for iodine, the thyroid readily absorbs radioactive isotopes, making it highly susceptible to radiation damage. This can result in both immediate and long-term health effects, including an increased risk of thyroid disorders and cancer.

### 3.5.1 Thyroid CEDE in Rainy Season.

According to NNREPRP guidelines, the permissible thyroid dose is 50 mSv within the first 7 days following a nuclear incident (NNREPRP, 2020). During the rainy season, thyroid CEDE levels vary significantly with distance from the reactor, as illustrated in Figure 10. The highest doses are observed near the reactor site, gradually decreasing with increasing distance and time. For atmospheric stability class A, individuals within a 15 km radius are likely to receive thyroid doses exceeding the regulatory limit. Beyond this distance, radiation exposure drops to negligible levels. Consequently, emergency protective actions, including relocation to nearby shelters, are strongly recommended for populations residing within the 15 km zone.

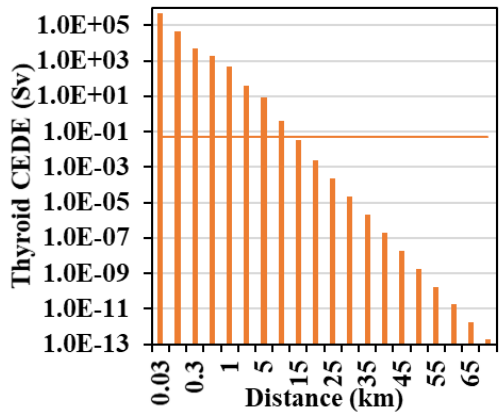



**Figure 10:** Comparison of radiation doses for the thyroid with the generic criteria of IAEA in the rainy season

### 3.5.2 Thyroid CEDE in Autumn Season

As specified by the NNREPRP, the permissible thyroid dose is 50 mSv over the first 7 days following a radiological incident (NNREPRP, 2020). In the autumn season, the distribution of thyroid CEDE varies notably with distance from the reactor site, as illustrated in Figure 11. Radiation exposure is highest in close proximity to the reactor and gradually declines with both time and increasing distance. Under stability class A conditions, individuals within a 27.5 km radius are likely to receive thyroid doses exceeding the allowable limit. Beyond this range, the exposure is considered minimal. Consequently, populations within the 27.5 km zone should be promptly relocated to appropriate shelters as part of emergency protective measures.

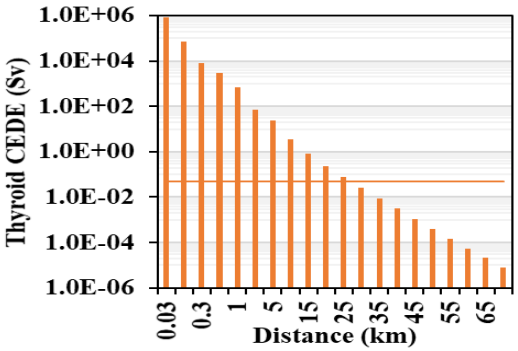



**Figure 11:** Comparison of radiation doses for thyroid with generic criteria of IAEA in the autumn season

### 3.5.3 Analysis of Thyroid CEDE

The highest thyroid CEDE values recorded were 4.48 × $10^5$ Sv during the rainy season and 7.18 × $10^5$ Sv during the autumn season at a distance of 30 meters from the source (Figures 9 and 10). Although radiation exposure declines with distance, elevated doses remain a concern. CEDE values exceeded the safety threshold of 50 mSv up to 15 km in the rainy season and 27.5 km in the autumn season. Beyond these distances, the measured thyroid doses dropped to levels considered negligible, largely due to the dispersive effects of wind and precipitation.

In situations where thyroid dose limits are surpassed, the administration of stable iodine, specifically potassium iodide (KI), is essential as a protective countermeasure. KI effectively saturates the thyroid with non-radioactive iodine, thereby reducing the uptake of radioactive iodine isotopes. The U.S. Food and Drug Administration (FDA) bases KI dosing guidelines (NRC000075, 2001) on findings from the Chernobyl nuclear accident, emphasizing early administration, especially for children and pregnant women. The most conservative intervention level is an internal thyroid exposure exceeding 0.05 Sv (50 mSv), which warrants the use of KI for all age groups, as shown in Table 3.

**Table 3:** Recommended doses of KI for the thyroid gland (NRC000075, 2001)

| **Thyroid dose (mSv)** | KI concentration dose (mg) | Risk group age |
|---|---|---|
| ≥5000 | 130 | Over 40 yr |
| ≥10000 | 130 | Over 18 to 40 yr |
| ≥50 | 130<br>16–65 (with consideration of different weight) | Pregnant women<br>Infants within 1 month to adolescents with 18 yr |

## 4. CONCLUSIONS

This study provided a detailed evaluation of radiological dose consequences, specifically TEDE and CEDE, for individual human organs in the event of a severe nuclear accident scenario at the Rooppur NPP. The analysis was carried out for different atmospheric stability conditions across two representative seasons: the rainy and autumn periods. Using atmospheric dispersion modeling and dose estimation tools, the study assessed radiation exposure as a function of distance, time, and meteorological variability.

In terms of TEDE, which incorporates both external and internal exposure pathways, the results showed similarly elevated dose values near the release point. TEDE assessments reinforce that radiation doses within the first 15 km (rainy season) and 27.5 km (autumn season) surpass the allowable exposure limits for the general public and even exceed occupational safety thresholds in certain cases. For instance:

- The ICRP recommended dose limit of 100 mSv (ICRP, 2007) for cancer risk becomes relevant within 20 km in autumn.
- The USNRC annual occupational TEDE limit of 50 mSv is exceeded up to 17 km in the rainy season and 30 km in the autumn season.

The results indicate that the thyroid gland is the most critically exposed organ, with maximum CEDE values reaching 8.0 × $10^5$ Sv at 0.03 km during the autumn season. The elevated exposure is attributed to the thyroid's high biological affinity for radioactive iodine and the season's low wind speed (0.95 m/s), which limits plume dispersion. In comparison, the rainy season showed lower thyroid CEDE values (4.7 × $10^5$ Sv at 0.03 km), influenced by higher wind speed (1.64 m/s) and rainfall (0.65 mm/hr), which contributed to faster dilution and deposition of radioactive particles.

CEDE to other organs such as the skin, lung, surface bone, red marrow, and liver also showed elevated levels in close

proximity to the reactor, with doses decreasing significantly over time and distance. These organs demonstrated radiation sensitivity, with implications for both deterministic and stochastic health effects. Maximum CEDE values at 30 meters exceeded internationally recommended dose thresholds, warranting urgent protective measures.

These findings emphasize the necessity of both CEDE and TEDE metrics in comprehensive radiological risk evaluation and emergency planning.

To mitigate thyroid exposure specifically, the use of KI as a thyroid-blocking agent is strongly recommended when thyroid CEDE exceeds 50 mSv. Based on FDA guidance, KI administration should be prioritized for vulnerable groups such as infants, children, adolescents, and pregnant women. Dose-specific intervention levels must be tailored based on estimated thyroid CEDE, as outlined in KI dosage guidelines (Table 3 of this study).

Based on these findings, the following conclusions and recommendations are proposed:

- emergency planning zones (EPZs) must be established, considering variations in CEDE and TEDE distributions.
- Evacuation, sheltering, and stable iodine administration should be promptly implemented within 15–30 km of the reactor depending on the season and real-time atmospheric conditions.
- First responders and reactor personnel must be equipped with appropriate protective gear and dosimetry, given the exceedance of occupational TEDE limits in key zones.
- Integration of CEDE and TEDE modeling into national nuclear emergency preparedness frameworks like NNREPRP is essential for realistic response planning.
- Continuous training, simulation, and meteorological monitoring must be maintained to enhance response effectiveness under variable scenarios.

In conclusion, this study highlights that both CEDE and TEDE are critical indicators of radiation risk following a nuclear accident. A multi-organ and multi-seasonal dose evaluation approach is vital for informed decision-making. The results strongly support the enhancement of public health protection protocols and emergency preparedness plans for Rooppur NPP and other nuclear facilities in similar settings.

## DATA AVAILABILITY STATEMENT

Datasets generated during the current study are available from the corresponding author upon reasonable request.

## FUNDING DECLARATION

This research was self-funded.

## ETHICS APPROVAL

This study is an engineering experimental investigation. The MIJST Research Ethics Committee has confirmed that formal ethical approval was not required.

## ETHICS, CONSENT TO PARTICIPATE, AND CONSENT TO PUBLISH

Not applicable.

## COMPETING INTERESTS

The authors declare that they have no competing interests.

## AUTHOR CONTRIBUTIONS

Author 1: Md Rosaidul Mawla1 – Methodology, Investigation, Writing manuscript

Author 2: Radmim Ryean – Investigation, Data curation

Author 3: Anisur Rahman - Validation, manuscript revision

Author 4: Abdus Sattar Mollah - Resources, manuscript revision

Author 5: Md. Shafiqul Islam - Visualization, manuscript revision

Author 6: Kazi Imtiaz Kabir – Visualization, manuscript revision

## ARTIFICIAL INTELLIGENCE ASSISTANCE STATEMENT

Portions of this manuscript were assisted by an artificial intelligence language model (ChatGPT, OpenAI). The tool was used solely for language editing, text refinement, and clarity improvement. All content, data interpretation, analysis, conclusions, and final decisions were generated, verified, and approved by the authors. The authors take full responsibility for the accuracy and integrity of the manuscript.

## CONFLICT OF INTEREST DECLARATION

The authors declare that they have no conflicts of interest.

## REFERENCES

Aliyu, A. S., Ramli, A. T., Saleh, M. A. (2015). Assessment of potential human health and environmental impacts of a nuclear power plant (NPP) based on atmospheric dispersion modeling, Atmósfera 28(1), 13-26, https://doi.org/10.1016/S0187-6236(15)72156-9

Anvari, A., Safarzadeh, L. (2012). Assessment of the total effective dose equivalent for accidental release from the Tehran Research Reactor, Annals of Nuclear Energy, 50, 251-255. https://doi.org/10.1016/j.anucene.2012.07.002

Ayesha, M. K., Rashid, M. B., Hygen, H. O. (2016). MET report on Climate of Bangladesh no. 08/2016, ISSN 2387-4201, https://live6.bmd.gov.bd/file/2016/08/17/pdf/21827.pdf

Croff, A. G., & Oak Ridge National Lab., TN (USA). (1980). User's manual for the ORIGEN2 computer code, ORNL/TM-7175.

Croff, A. G. (1983). ORIGEN2: A versatile computer code for calculating the nuclide compositions and

characteristics of nuclear materials. Nucl. Technol., 62(3), 335–352.

Fairuz, A., Sahadath M. H. (2020). Characterization of Atmospheric Radiological Dispersion alongside Risky Location Designation and Shelter House Proposition around the Planned Rooppur Nuclear Power Plant (RNPP)", Journal of Nuclear Engineering and Radiation Science, 6(4), 042003, https://doi.org/10.1115/1.4046670

Faith, R., Kim, J. (2020). Assessment of Lifetime Attributable Risk for Public Health Sustainability from the Fukushima Accident, Science and Technology of Nuclear Installations, 2020(2020), 1-6, 8873031, https://doi.org/10.1155/2020/8873031

Foudil, Z., Mohamed, B., Tahar, Z. (2017). Estimating of core inventory, source term and doses results for the NUR research reactor under a hypothetical severe accident, Progress in Nuclear Energy, 100, 365–372. https://doi.org/10.1016/j.pnucene.2017.07.013

Henry, K. O., Sylvester, A. B., Gyamfi, K., Simon, A., Andrew, N. (2021), Assessment of radiological consequence of a hypothetical accident at the Ghana Research Reactor-1 facility based on terrorist attack. Science Progress, 104(4), 1-24. doi:10.1177/00368504211054986

Hoeve J. E. T., Jacobson M. Z. (2012). Worldwide health effects of the Fukushima Daiichi nuclear accident. Energ. Environ. Sci. 5(9), 8743-8757, https://doi.org/10.1039/C2EE22019A

Homann, S. G., Aluzzi, F. (2013). HOTSPOT Health Physics Codes Version 3.0 User's Guide, National Atmospheric Release Advisory Center, Lawrence Livermore National Laboratory, LLNL-SM-636474.

Hussain, M., Mehboob, K., Ilyas S. Z., Shaheen S. (2023). Implications of Local Scale Meteorological Data on Radioactive Plume Dispersion and Dose Delivery for a Hypothetical Severe Accident at PARR-1. Arab J Sci Eng 48, 739–755. https://doi.org/10.1007/s13369-022-06998-w

IAEA, (2008). Derivation of the source term and analysis of the radiological consequences of research reactor accidents. Safety reports series No. 53, International Atomic Energy Agency, Vienna, Austria.

IAEA, (2013). Actions to Protect the Public in an Emergency due to Severe Conditions at a Light Water Reactor, Emergency preparedness and response, EPR-NPP-PPA, International Atomic Energy Agency, Vienna, Austria.

ICRP, (2007). ICRP Publication 103: The 2007 Recommendations of the International Commission on Radiological Protection, Ann. ICRP, 37(2.4), p. 2.

ICRU, 2015. Major releases of radionuclides to the environment, Journal of the International Commission on Radiation Units and Measurements, 15(1-2), 4–36, https://doi.org/10.1093/jicru_ndy01

Malizia, A., Chierici, A., Sergio, B., Marco, D., Ludovici, G. M., Francesco, d., Guglielmo, M., Fabio M. (2021). The HotSpot Code as a Tool to Improve Risk Analysis During Emergencies: Predicting I-131 and CS-137 Dispersion in the Fukushima Nuclear Accident, International Journal of Safety and Security Engineering, 11(4), 473-486, https://doi.org/10.18280/ijsse.110421

Mawla, M. R., Rahman, A., Mollah, A. S., Ryean, R., Islam, M. S. (2024). Assessment of radiological consequences to a hypothetical accident of the 3-MW TRIGA Mark-II nuclear research reactor of Bangladesh, Nuclear Engineering and Design, 424, https://doi.org/10.1016/j.nucengdes.2024.113255

Mollah, A. S., Sattar, S., Hossain, A., Salahuddin, M., Khan, A. Z., Hossain, M. S. (2016). Review and analysis of environmental impacts of different energy technologies: clean environment from nuclear energy, MIST Journal of Science and Technology, Vol. 4(1), 1-13, ISSN 2224-2007

Ned Xoubi. (2020). Assessment of environmental radioactive surface contamination from a hypothetical nuclear research reactor accident. Heliyon, 6(9), 1-8, https://doi.org/10.1016/j.heliyon.2020.e04968

NNREPRP (2020). National Nuclear and Radiological Emergency Preparedness and Response Plan (NNREPRP). Ministry of Science and Technology, Government of the People's Republic of Bangladesh.

NRC000075, (2001). Potassium Iodide as a Thyroid Blocking Agent in Radiation Emergencies, U.S. Department of Health and Human Services, Food and Drug Administration, Center for Drug Evaluation and Research (CDER).

NRC 1.183, (2000). Alternative Radiological Source Terms for Evaluating Design Basis Accidents at Nuclear Power Reactors, U.S. Nuclear Regulatory Commission Regulatory Guide.

Rogner, H.-H. (2001). Nuclear Power and Sustainable Energy Development. The Journal of Energy and Development, 26(2), 235–258. http://www.jstor.org/stable/24808916

Sihver, L., Yasuda, N. (2018). Causes and Radiological Consequences of the Chernobyl and Fukushima Nuclear Accidents, Journal of Nuclear Engineering and Radiation Science, NERS-16-1166, 4(2), 020914, https://doi.org/10.1115/1.4037116

Walsh, L., Zhang, W., Shore, R. E., Auvinen, A., Laurier, D., Wakeford, R., Jacob, P., Gent, N., Anspaugh, L. R., Schüz, J., Kesminiene, A., van Deventer, E., Tritscher, A., del Rosarion Pérez, M. (2014). A framework for estimating radiation-related cancer risks in Japan from the 2011 Fukushima nuclear accident, Radiation Research, 182(5), 556-572, https://doi.org/10.1667/RR13779.1

Yasunari, T. J., Stohl, A., Hayano, R. S., Burkhart, J. Eckhardt, F., S., Yasunari, T. (2011). Cesium-137 deposition and contamination of Japanese soils due to the Fukushima nuclear accident. P. Natl. Acad. Sci. USA, 108(49), 19530-19534, https://doi.org/10.1073/pnas.1112058108

MIJST
*MIST International Journal of Science and Technology*

# Agar from Red Algae *(Gracilaria tenuistipitata)* as a Valuable Biopolymer: Extraction and Characterization

**Fawzia Afrin Rimpy[1], Md Enamul Hoque[1*], Quazi Farsheed Mahmud[1], Itmam Nowroj[1], Sazedur Rahman[2], Tarek El-Bialy[3], M. Azam Ali[4]**

[1] Department of Biomedical Engineering, Military Institute of Science and Technology, Dhaka, Bangladesh
[2] Department of Mechanical, Aerospace, and Nuclear Engineering, Rensselaer Polytechnic Institute, Troy, NY, USA 12180
[3] Mike Petryk School of Dentistry, Faculty of Medicine and Dentistry, University of Alberta, Edmonton, Alberta T6G 2E1, Canada
[4] Centre for Bioengineering and Nanomedicine, University of Otago, Dunedin 9016, New Zealand

***Corresponding Email:** *enamul1973@gmail.com*

**ARTICLE INFO**

**Article History:**

*Received: 28th April 2025*
*Revised: 25th December 2025*
*Accepted: 25th December 2025*
*Published: 30th December 2025*

**Keywords**:

*Agar*
*Red Algae*
*Gracilaria tenuistipitata*
*Cox'z Bazar*
*Biomedical Application*

**ABSTRACT**

Agar, a natural biopolymer extracted from red algae, holds immense potential for revolutionizing healthcare, including biomedical engineering. This study explores the extraction feasibility of agar from red algae (*Gracilaria tenuistipitata)* abundantly available in the coastal area of Cox's Bazar, Bangladesh. Five extraction methods were investigated, including a control group and treatments with water and NaOH solutions at concentrations of 2%, 4%, and 6%. The extraction of agar from algae was characterized through Fourier-transform infrared spectroscopy (FTIR), gel strength testing, melting and gelling temperature assessments, pH value measurement, and sulfate content analysis. Statistical analysis, including ANOVA and Tukey's HSD test, was utilized to assess the impact of the pre-treatment process on the yield and characteristics of agar. The test revealed significant variations among the different extraction methods ($p < 0.05$), highlighting the crucial role that pre-treatment plays in influencing agar yield and its physicochemical properties. While the control group achieved the highest agar yield (16.67 ± 1.44%), the 2% NaOH pre-treatment showed superior physicochemical attributes. Specifically, this treatment resulted in agar with optimal gel strength (3.25 ± 0.67 N/cm²), melting temperature (84.20 ± 0.80°C), gelling temperature (36.13 ± 1.21°C), pH (7.49 ± 0.26), and sulfate content (3.67 ± 0.58 mg/L), all of which are comparable to those of commercial agar. This preliminary study suggests that the red algae (*Gracilaria tenuistipitata)* found in Bangladesh is a promising source of agar for wider applications, including biomedical engineering. The agar extracted from abundant local sources in this country could unlock its potential for advancing healthcare solutions and sustainable national economic growth.

This work is licensed under a *Creative Commons Attribution-Non-commercial 4.0 International License.*

## 1. INTRODUCTION

The marine algal diversity of Bangladesh contains at least 200 documented seaweed types that grow along its 710 km coastline, especially in the southeastern areas, including Cox's Bazar and Saint Martin's Island (Hossain et al., 2021). Three types of algae exist in Bangladesh: green (Chlorophyta), brown (Phaeophyta), and red (Rhodophyta). The red algae of Gracilaria establish their dominant position in the scientific field due to their ability to produce high-value hydrocolloids. The algal species found in the country present a significant opportunity to extract sustainable biopolymers from renewable sources (A & G, 2024; El-Beltagi et al., 2022; Hossain et al., 2021; Mohibbullah et al., 2023). Biopolymers have wider applications across the packaging, agricultural, pharmaceutical, and biomedical engineering fields (Hoque et al., 2023; Rahmati et al., 2019; Rashid et al., 2023; Tatrishvili, 2025; Vijayan et al., 2016).

Agar, a natural polysaccharide predominantly extracted from red algae (Gracilaria), comprises two primary components: agarose (a linear polymer of repeating β-D-galactose and 3,6-anhydro-α-L-galactopyranose units) and agaropectin (a sulfated, branched polymer). While agarose provides structural neutrality, agaropectin enables gelation through sulfate-mediated interactions (Madadi et

al., 2021; Padmesh & Singh, 2021; Rhein-Knudsen et al., 2017). The application of agar in different products depends on its qualities and physicochemical conditions (sulfate content, gel strength, pH, melting temperature, and gelling temperature) (Zhang et al., 2020, Mohibbullah et al., 2023). The food industry, microbiological media, cosmetics and biotechnology use agar because it creates thermo-reversible gels, has clarity, and operates at higher melting and gelling temperatures (Graham et al., 2019; Martínez-Sanz et al., 2019). In healthcare, agar-based materials have garnered interest for their advantageous properties in wound dressing, tissue engineering scaffold development, diagnostic devices, and drug delivery platforms (Armisén, 1991; Dhivya et al., 2015; Khandwal et al., 2025; Lam et al., 2015). Furthermore, Agar's characteristics, which resemble those of extracellular matrices and its ability to encapsulate cells, make it particularly suitable for biomedical applications. Developers utilize agar hydrogel membranes derived from Gracilaria species to create promising controlled drug delivery systems and regenerative medicine solutions, owing to their biocompatibility, biodegradability, and mechanical strength (Kazimierczak et al., 2019; Park et al., 2020; Sudhakar et al., 2024; Vieira et al., 2025).

Research on agar is progressing globally; however, studies focusing on local algal biopolymers from Bangladesh are still limited. The red algae species *Gracilaria tenuistipitata*, abundant in Cox's Bazar's coastal waters, presents a promising sustainable agar source due to its rapid growth, environmental resilience, and high polysaccharide content (Hossain et al., 2021). However, optimized extraction protocols are crucial for maximizing yield and enhancing agar quality. A critical step is alkali pretreatment, which chemically converts L-galactose-6-sulfate into 3,6-anhydro-L-galactose. This structural modification directly improves agar's gelling capacity by reducing sulfate group interference with polymer network formation (Xiao et al., 2021). Although alkali pretreatment is crucial for obtaining high-quality agar, it can also dramatically reduce the extraction yield (Mohibbullah et al.). To unlock the full industrial potential of *G. tenuistipitata*, a systematic investigation is needed to refine alkali treatment parameters—including concentration, temperature, duration, and seaweed-to-alkali ratio. Such optimization will establish a scalable, efficient extraction methodology tailored to this underutilized local resource, ensuring consistent quality for high-value applications such as edible coatings for fruits/vegetables, tissue engineering scaffolds, and controlled drug delivery systems.

This study aims to examine the extraction feasibility of agar from red algae (*Gracilaria tenuistipitata*), which is abundantly available in the coastal area of Cox's Bazar, Bangladesh. This research involves assessing the pretreatment effects of different NaOH concentrations (2%, 4%, and 6%) in comparison to a control group and a water-treated group, with the goal of identifying optimal extraction conditions that not only maximize agar yield but also improve its gelling properties and overall quality. Ultimately, this study aims to promote the sustainable utilization of local marine resources in Bangladesh, thereby driving progress in both food and biomedical applications, while also contributing to economic growth.

## 2. MATERIALS AND METHODS

### 2.1 Materials and Instrumentation

This study used a range of high-grade chemicals and advanced equipment. The red sea algae (*Gracilaria tenuistipitata*) were collected from Nuniarchara Sea Beach, Cox's Bazar. Analytical-grade Sodium Hydroxide and Acetic Acid, sourced from Sigma-Aldrich, were employed for the pretreatment and analysis of the algae samples. The gel strength of the extracted agar was evaluated using a Zwick Roell Z010 Universal Testing Machine (UTM), which applied controlled force through a perforated plate onto cylindrical gel samples. For the drying procedure, a Witeg FD-8 bench-top freeze dryer was utilized. Sample preparation involved a Biobase MS7-H550-Pro magnetic stirrer for precise mixing and heating, while sulfate concentrations were analyzed with a DR 6000 UV-Vis Spectrophotometer (Hach). Additionally, functional group identification in the agar samples was performed using a PerkinElmer Spectrum Two FTIR Spectrometer with a ZnSe system.

### 2.2 Extraction Procedure of Agar

The overall methodology of the work is illustrated in the following flowchart (Fig. 1).

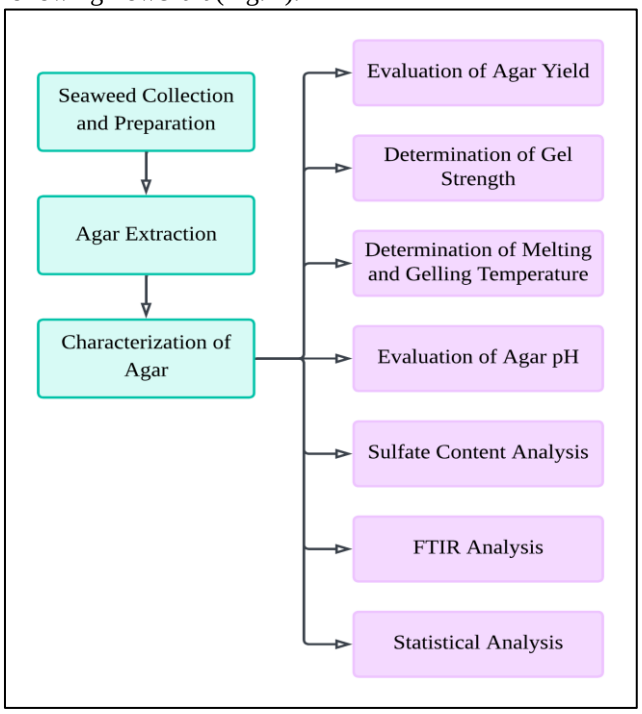



**Figure 1:** Flow diagram for the extraction and characterization of agar

#### 2.2.1 Collection and Preparation of Algae

Algae samples of the *Gracilaria tenuistipitata* species were collected randomly from the shore and subtidal regions of Cox's Bazar Nuniarchara Sea Beach (21°28′27″ N and 91°57′52″ E). These samples, cultivated by local farmers during the summer season, were placed in poly bags and

transported in a large sack to the Biomaterials Lab at the Department of Biomedical Engineering at MIST (Military Institute of Science and Technology). Upon arrival, the samples were thoroughly washed with tap water to remove any sand and debris. After cleaning, samples were stored in a cold and dark environment in the laboratory for further observation and experimentation.

### 2.2.2 Extraction of Agar

The extraction process was divided into five distinct pretreatment groups: control, water treatment, and alkali treatments with 2%, 4%, and 6% sodium hydroxide (NaOH). Each group included three replicates, resulting in a total of fifteen extractions. For all extractions, 4 grams of dried algae were accurately weighed and used per sample.

In the control group, the algae samples were boiled directly in distilled water without any pretreatment. For the water treatment group, the seaweed samples were soaked in 200 mL of distilled water at room temperature for two hours, maintaining a seaweed-to-water ratio of 1:50. For the alkali treatments, analytical-grade NaOH was dissolved in distilled water to prepare 2%, 4%, and 6% (w/v) solutions, with corresponding pH values of 12.8, 13.2, and 13.5, respectively. The algae samples were submerged in 200 mL of each alkali solution at room temperature for two hours. Afterward, the samples were neutralized by soaking them in 200 mL of a 0.5% acetic acid solution for 10 minutes followed by thorough rinsing with distilled water to eliminate residual chemicals.

Following pretreatment, all samples, including the controls, were transferred to 500 mL containers filled with distilled water and boiled at 100°C for three hours. This process disintegrated the algae and released the agar content. The hot extracts were filtered through a cotton towel to separate solid residues. The filtrates were poured into plastic containers and allowed to cool at room temperature, where gelation occurred naturally. The gels were subsequently frozen at -20°C for 24 hours. After freezing, the gels were thawed, and excess water was carefully removed by decanting. The gels were then placed on Whatman filter paper for additional drying before being transferred to petri plates and freeze-dried using a Witeg FD-8 bench-top freeze dryer. The yield of each sample was calculated based on the final dried weight. Representative figures of the dried agar samples are shown in Figure 2.




**Figure 2:** (a) A single dried agar sample, and (b) A collection showcasing all the dried agar samples

### 2.3 Characterization of Agar

### 2.3.1 Yield Evaluation

The samples were extracted and poured into 500 mL polypropylene containers after being filtered through two layers of cotton towels. After the filtrate had been subjected to another night of freezing, it was thawed for four hours at room temperature. It was freeze-dried at -80°C using the Bench-top freeze drier FD-8 made by the German manufacturer Witeg. This process continued until no moisture was detected in the filtrate. Agar yield was used to calculate the quantity of agar recovered. It was calculated using the formula below and expressed as a percentage:

$$\%\text{Yield} = \frac{\text{Amount of Dried Extracted Agar}}{\text{Amount of Dried Algae Used}} \times 100\%$$

### 2.3.2 Gel Strength Measurement

Agar gel was homogenized by heating in a 50 mL beaker. Approximately 20 cc of agar sample was homogenized and poured into cylindrical molds (diameter: 5 cm) to prepare test samples. The gels were allowed to set at room temperature for at least 2 hours. The final gel samples had a thickness of approximately 2.5 cm.

Agar gel strength was tested using a Universal Testing Machine (UTM) at a penetration rate of $1\ \text{mm}\ \text{min}^{-1}$. A perforated disc plate with a diameter of 3.8 cm was placed on top of each gel. A plunger was used to push the disc into the gel, causing the gel to extrude through the perforations. The peak force (in Newton) required for penetration was recorded. Gel strength was calculated by dividing the peak force by the area of the disc and expressed in Newton per square centimeter ($N/cm^2$).

### 2.3.3 Melting and Gelling Temperature Measurement

The agar gels were placed in a beaker and heated on a hot plate to increase their temperature gradually. The melting point of the agar was determined using glass beads. The temperature at which the glass beads, placed on the surface of the agar, began to sink into the jelly was recorded as the melting point. The gelling point, on the other hand, was identified as the temperature at which the glass beads ceased to move within the molten agar as it solidified.

### 2.3.4 pH Measurement

The pH measurement of agar is crucial in scientific and industrial applications, as it influences microbial growth, gel strength, nutrient availability, and the quality control of food and pharmaceutical products (A & G, 2024; El-Beltagi et al., 2022; Hossain et al., 2021; Mohibbullah et al., 2023). Accurate pH determination enables the formulation of customized culture media and the creation of optimal environments for biotechnological and biomedical applications, thus driving advancements in research, technology, and product development. In this study, the pH of agar samples was measured using a calibrated pH and temperature meter (Adma AD8000). All pH measurements were taken while the agar was in its molten state to ensure consistency and accuracy.

### 2.3.5 Sulfate Content Measurement

The sulfate content in agar, an important indicator of its purity, was measured using a DR 6000 UV-Vis Spectrophotometer (Hach). The presence of sulfate is critical as it reflects the degree of polysaccharide extraction from algae cell walls and can influence the gelation, stability, and biological activity of agar (Sasuga et al., 2017; Xiao et al., 2021). To determine the sulfate content, agar samples were first dissolved in distilled water. Each liquid sample was prepared by taking 10 mL of the dissolved agar solution, and approximately 1 mL of each sample was transferred into UV cells for analysis. A specific reagent, SULFAVER-4, was added to the solutions to chemically react with the sulfate ions and form a colored complex. The solutions were vigorously shaken for approximately three minutes to ensure thorough mixing, followed by a 10-minute period for complete color development. After the reaction, the absorbance of each sample was measured at a wavelength of 420 nm using the UV-Vis spectrophotometer. The sulfate concentration in the solutions was directly quantified and expressed in milligrams per liter (mg/L).

### 2.3.6 FTIR Analysis

The FTIR analysis aimed to identify and characterize the functional groups present in the agar samples. This analysis was conducted using a Perkin-Elmer Spectrum Two machine. Initially, the agar samples were dried and ground into a fine powder, which was then mixed with potassium bromide to form circular pellets. These pellets were exposed to infrared radiation, inducing molecular vibrations that resulted in the absorption or emission of infrared radiation. The resulting spectral patterns were quantified, enabling the identification of specific functional groups and chemical bonds within the samples. FTIR analysis was performed on control, water-treated, and alkali-treated samples at concentrations of 2%, 4%, and 6%. For each sample, a graph was generated, and the peaks and troughs were compared to those of the standard agar sample to assess their similarities. The functional groups present in the samples were estimated based on the wavenumbers identified in the spectral graphs.

### 2.3.7 Statistical Analysis

The physicochemical properties of the samples were statistically evaluated using one-way ANOVA, with the support of the Statistical Package for the Social Sciences (SPSS) software. Statistical significance will be determined based on p values predetermined to be less than or equal to 0.05.

## 3. RESULTS AND DISCUSSIONS

### 3.1 FTIR Analysis

Agar consists primarily of agarose and agaropectin, two components with distinct properties and roles. These constituents contribute to the versatility and wide-ranging utility of agar. (Hossain et al., 2021; Mohibbullah et al., 2023). The chemical structure of agar is shown in Figure 3. The Fourier-transform infrared (FTIR) spectroscopy analysis of agar samples provides a comprehensive understanding of their chemical structure and composition, revealing distinctive functional groups within the polysaccharide matrix. This study thoroughly analyzed the FTIR band spectra of several agar samples within the range of 4000 $cm^{-1}$ to 400 $cm^{-1}$. The purpose was to get insights into their molecular structure and possible uses.

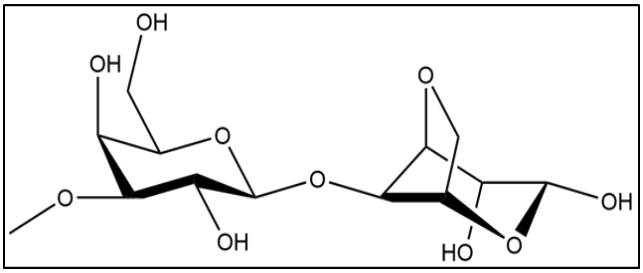



**Figure 3:** Chemical Structure of Agar

According to the studies, the identification of characteristic peaks at specific wavenumbers in the FTIR spectra suggests the presence of functional groups in the agar samples. The presence of sulfate groups at the C-4 position in D-galactose units, C-6 of L-galactose units, and 3,6-anhydro-D-galactose C-O linkages is indicated by bands at around 820 $cm^{-1}$, 845 $cm^{-1}$, and 931 $cm^{-1}$, respectively (Gómez-Ordóñez & Rupérez, 2011; Souza et al., 2012). Furthermore, the peaks observed at 1026.3 $cm^{-1}$ and 1067.5 $cm^{-1}$ are attributed to the stretching of the C–O bond in primary alcohols (Sobuj et al., 2021). Additionally, the bands within the range of 990 $cm^{-1}$ to 1150 $cm^{-1}$ indicate the presence of glucose (Rhein-Knudsen et al., 2017; Sukhikh et al., 2022; Thombare et al., 2023). Table 1 concisely presents the functional groups detected in agar by FTIR peaks, providing an overview of their chemical composition and importance. Furthermore, Figures 4 to 10 exhibit graphical illustrations of the FTIR study, demonstrating a comparative view of the spectra acquired from various agar samples belonging to distinct treatment groups.

**Table 1:** Functional groups identified by FTIR peaks in agar

| Wavenumbers ($cm^{-1}$) | Functional Group |
|---|---|
| 3391 | O-H stretching; vibration of water and hydroxyl groups |
| 2932 | C-H stretching; vibration of methyl and methylene groups |
| 1629 | C=O stretching; vibration of carboxylic acids and esters |
| 1370 | C-H bend |
| 1250 | C-O-C stretching; vibration of ether linkages |
| 1072 | C-O stretch |
| 931 | C-O stretching; vibration of 3,6-anhydrogalactose units, which are unique to agar |
| 845 | C-O-C bending; vibration of pyranose rings |
| 820 | Sulfate group |

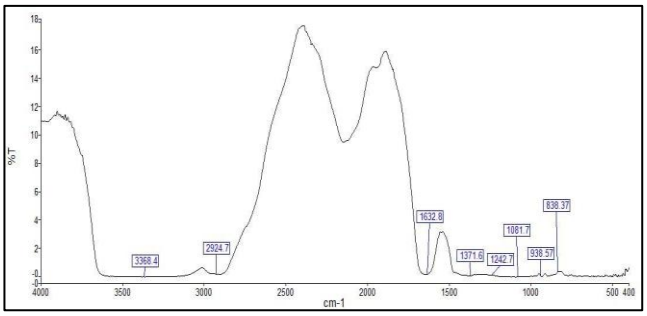



**Figure 4:** Fourier-Transform Infrared (FTIR) analysis of commercial Agar-Agar

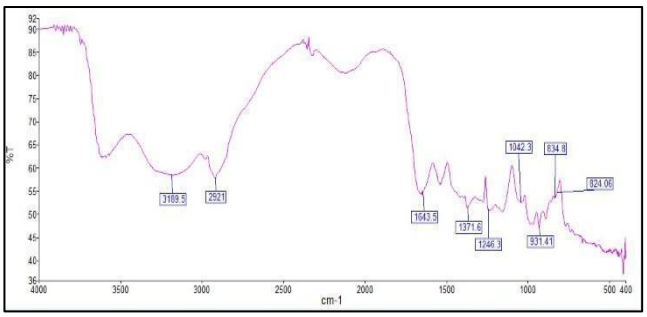



**Figure 5:** Fourier-Transform Infrared (FTIR) analysis of control sample

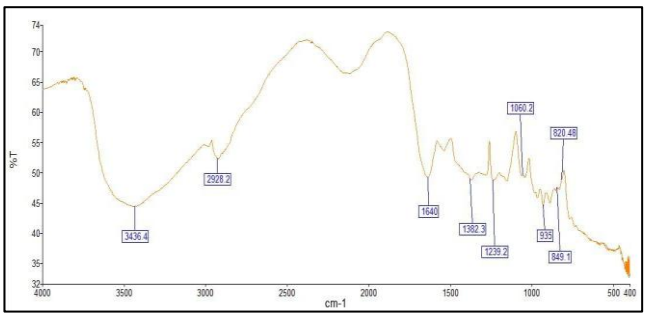



**Figure 6:** Fourier-Transform Infrared (FTIR) analysis of water-treated sample

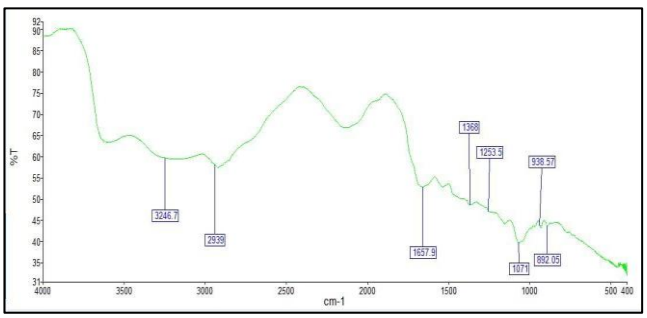



**Figure 7:** Fourier-Transform Infrared (FTIR) analysis of 2% NaOH-treated sample

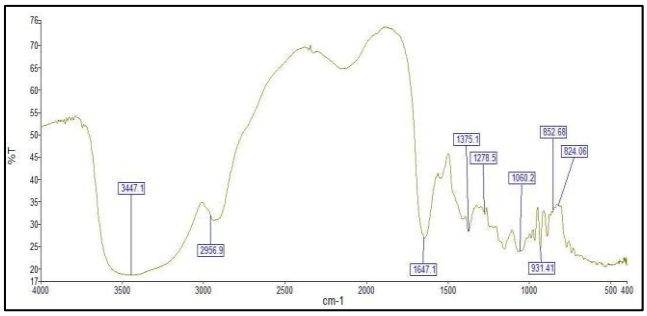



**Figure 8:** Fourier-Transform Infrared (FTIR) analysis of 4% NaOH-treated sample

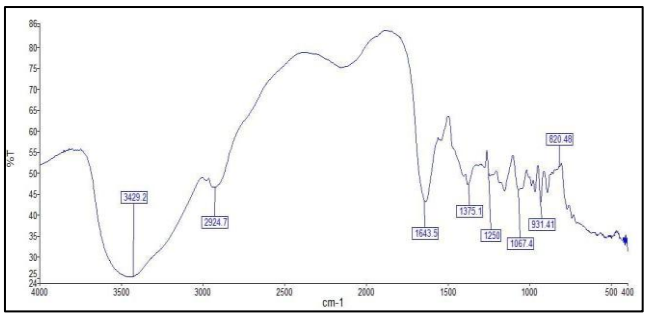



**Figure 9:** Fourier-Transform Infrared (FTIR) analysis of 6% NaOH-treated sample

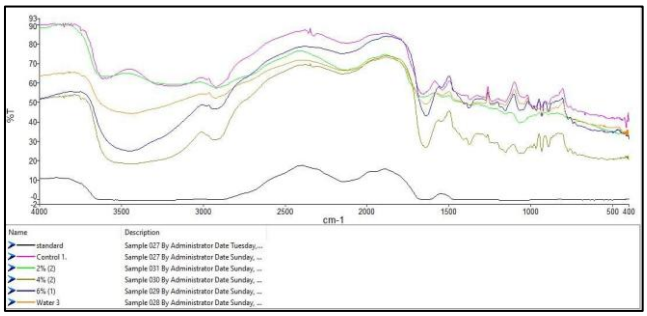



**Figure 10:** Fourier-Transform Infrared (FTIR) analysis of all samples

Based on the FTIR spectra, the control sample shows stronger and additional absorption bands, including a distinct peak at 845 $cm^{-1}$, which may indicate the presence of residual impurities. In contrast, the spectrum of commercial food-grade agar-agar appears broader with fewer sharp peaks, likely due to the inclusion of additives or preservatives. Differences in peak sharpness and intensity among samples suggest variations in chemical composition and purity. The water-treated sample exhibits elevated baseline absorbance but less defined peaks, indicating inefficient impurity removal. NaOH-treated samples exhibit more pronounced spectral differences: the 2% NaOH treatment yields fewer sharp peaks, suggesting effective yet gentle purification, while the 4% NaOH treatment provides more distinct peaks, indicating improved clarity and purity. However, the 6% NaOH treatment, despite higher absorbance, may lead to structural degradation due to the harshness of the treatment. FTIR analysis thus provides insight into the

chemical structure and quality of extracted agar (Fujiwara et al., 2023). The presence of similar functional groups in both the extracted and commercial agar samples supports the potential for industrial and biomedical applications (Qari & Haider, 2021).

### 3.2 Determination of Yield Percentage

The extraction yield percentage is a vital metric that indicates the efficiency of agar extraction and the influence of various pre-treatment conditions on the yield obtained from red algae (*Gracilaria tenuistipitata*). Table 2 presents a summary of the yield percentages for each group.

**Table 2:** Yield percentage of agar extracted from red sea algae (*Gracilaria tenuistipitata*)

| Treatment Groups | Agar Yield (% DW) | | | Mean ± Standard Deviation |
|---|---|---|---|---|
| | Extraction 1 | Extraction 2 | Extraction 3 | |
| Control | 15.00 | 17.50 | 17.50 | 16.67 ± 1.44 |
| Water | 12.50 | 15.00 | 15.00 | 14.17 ± 1.44 |
| 2% NaOH | 12.50 | 12.50 | 10.00 | 11.67 ± 1.44 |
| 4% NaOH | 10.00 | 12.50 | 7.50 | 10.00 ± 2.50 |
| 6% NaOH | 7.50 | 10.00 | 7.50 | 8.33 ± 1.44 |

The results demonstrate a significant decrease in yield for the treated agar samples compared to the control group, which exhibited a yield of 16.67 ± 1.44%. This decline can be attributed to structural modifications induced by the pre-treatment processes, as well as the presence of impurities in the control samples that may have artificially inflated their yield measurement. The control group retained its native polysaccharide structure, along with potential contaminants. In contrast, the water treatment yielded 14.17 ± 1.44%, likely resulting in the partial dissolution of some agar components, although it also removed some impurities. The alkali treatments, utilizing concentrations of 2% to 6% NaOH, showed progressively lower yields, ranging from 11.67 ± 1.44% to 8.33 ± 1.44%. This reduction can be attributed to several key factors. Firstly, the alkaline hydrolysis of glycosidic bonds in agarose results in the breakdown of polymer chains. Additionally, the excessive removal of sulfate groups, which are crucial for the gel-forming properties of agar, contributes to the decline in yield. Furthermore, the more thorough elimination of non-agar impurities, which were present in the control group and contributed to its higher yield, also plays a significant role in this reduction. The lowest yield recorded in the 6% NaOH treatment (8.33 ± 1.44%) is particularly noteworthy, as illustrated in Table 2. This reduction is a consequence of the harsh alkaline conditions, which caused significant degradation of polysaccharides, loss of smaller fragments during filtration, and the complete removal of impurities. These findings are consistent with previous studies indicating that higher alkali concentrations can substantially reduce agar yield while enhancing purity and gel strength (Sasuga et al., 2017; Xiao et al., 2021; Mohibbullah et al.,2023). The one-way analysis of variance (ANOVA) confirmed that the pretreatment significantly affected agar yield ($F(4, 10) = 11.29$, $p = 0.0001$). Post-hoc analysis indicated significant differences between the control and treatment groups. The trends are illustrated in the bar chart in Figure 11, which shows the control group with the highest yield, followed closely by the water treatment group. Conversely, the yields for the 2%, 4%, and 6% NaOH treatment groups progressively declined, reaching a minimum in the 6% NaOH group.

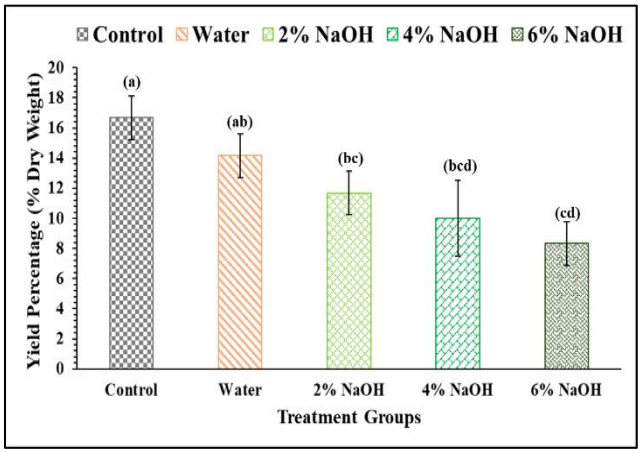



**Figure 11:** A bar chart illustrating descriptive statistics (mean ± standard deviation) of agar yield percentage and Tukey HSD post-hoc comparisons for each pretreatment group

### 3.3 Determination of Gel Strength

The gel strength of agar extracted from *Gracilaria tenuistipitata* was evaluated to determine the influence of different pre-treatment conditions on its physical properties. The results, summarized in Table 3, revealed significant variations in gel strength across the treatment groups. The control group exhibited the highest gel strength at 4.67 ± 0.64 N/cm², indicating the retention of a robust gelling network structure. In contrast, the water-treated samples showed the lowest gel strength at 1.44 ± 0.66 N/cm², suggesting that water pretreatment disrupts the agar's gelling network. Among the NaOH-treated groups, agar extracted with 2% NaOH demonstrated optimal gel strength (3.25 ± 0.67 N/cm²), comparable to commercial agar standards (3.38 ± 0.26 N/cm²). This finding highlights the suitability of 2% NaOH treatment for producing agar with industrially relevant gelling properties. However, higher NaOH concentrations led to a progressive decline in gel strength, with values of 3.16 ± 0.38 N/cm² for 4% NaOH and 2.34 ± 0.42 N/cm² for 6% NaOH. The reduction in gel strength at higher NaOH concentrations can be attributed to excessive sulfate group removal and polymer degradation, as supported by previous studies (Sasuga et al., 2017; Xiao et al., 2021; Mohibbullah et al.,2023).

**Table 3:** Gel strength of agar extracted under different pre-treatment conditions

| Treatment Groups | Gel Strength (N/cm²) | | | Mean ± Standard Deviation |
|---|---|---|---|---|
| | Extraction 1 | Extraction 2 | Extraction 3 | |
| Control | 5.40 | 4.45 | 4.17 | 4.67 ± 0.64 |
| Water | 1.12 | 0.99 | 2.20 | 1.44 ± 0.66 |
| 2% NaOH | 2.48 | 3.71 | 3.55 | 3.25 ± 0.67 |
| 4% NaOH | 3.59 | 2.86 | 3.03 | 3.16 ± 0.38 |
| 6% NaOH | 2.78 | 1.94 | 2.30 | 2.34 ± 0.42 |

The one-way ANOVA confirmed that pretreatment significantly influenced agar gel strength ($F(5, 12) = 12.53$, $p = 0.0002$). Tukey HSD post-hoc comparisons further highlighted the significant differences among groups. The 2% NaOH group ranked third in gel strength, statistically similar to the commercial agar and 4% NaOH groups, but significantly higher than the water treatment group. The 4% NaOH-treated group showed the fourth-highest gel strength, significantly exceeding the water-treated group but not differing substantially from the 6% NaOH group. The 6% NaOH group exhibited the fifth-highest gel strength, reflecting the detrimental effects of excessive alkali treatment on gelling properties. Figure 12 provides a graphical representation of the gel strength data, emphasizing the significant variations across groups. The results demonstrate that while alkali pretreatment reduces agar yield (as shown in Table 1), moderate NaOH concentrations, particularly 2%, optimize gelling properties, making the extracted agar suitable for applications requiring specific textural characteristics. These applications include food preservation (as coatings for fruits and vegetables) and pharmaceutical uses, such as stabilizing drug solutions to enhance shelf life.

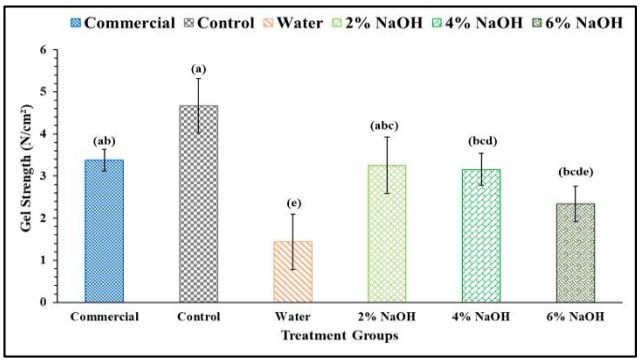



**Figure 12:** A bar chart illustrating descriptive statistics (mean ± standard deviation) of agar gel strength and Tukey HSD post-hoc comparisons for each pre-treatment group

### 3.4 Determination of Melting Temperature

The melting temperature of the extracted agar was determined to assess the influence of various pretreatment conditions. The melting temperature was measured for each of the 15 extractions, as well as for three commercial agar samples, and the results are summarized in Table 4.

**Table 4:** Melting temperature of agar extracted under different pre-treatment conditions

| Treatment Groups | Melting Temperature (°C) | | | Mean ± Standard Deviation |
|---|---|---|---|---|
| | Extraction 1 | Extraction 2 | Extraction 3 | |
| Control | 92.50 | 90.60 | 90.80 | 91.30 ± 1.04 |
| Water | 81.20 | 80.50 | 79.20 | 80.30 ± 1.01 |
| 2% NaOH | 83.40 | 84.20 | 85.00 | 84.20 ± 0.80 |
| 4% NaOH | 79.20 | 80.10 | 82.30 | 80.53 ± 1.59 |
| 6% NaOH | 80.10 | 81.00 | 79.40 | 80.17 ± 0.80 |

The melting temperature reflects the structural integrity and purity of agar, both of which are influenced by pretreatment conditions. The findings revealed significant differences in melting temperatures among the groups. The control group exhibited the highest melting temperature at 91.30 ± 1.04°C, indicating the presence of impurities that increased the melting point. In contrast, the water-treated group showed the lowest melting temperature at 80.30 ± 1.01°C, suggesting that water treatment may have disrupted the agar's structure and reduced its thermal stability. Similarly, the 4% NaOH- and 6% NaOH-treated groups had melting temperatures of 80.53 ± 1.59°C and 80.17 ± 0.80°C, respectively, reflecting a slight decrease in thermal stability due to the excessive removal of structural components, consistent with the observed trends in gel strength. The 2% NaOH-treated group demonstrated a melting temperature of 84.20 ± 0.80°C, which was comparable to that of commercial agar 85.03 ± 0.21°C. This indicates that mild alkali treatment effectively removes impurities while maintaining the structural integrity of agar, making it well-suited for applications demanding high thermal stability, such as in the food industry, microbiological media, cosmetics, and biotechnology. The one-way ANOVA confirmed that pretreatment significantly influenced the melting temperature of agar ($F (5, 12) = 56.37$, $p = 6.45E-08$). Tukey HSD post-hoc comparisons highlighted significant differences among the groups. The control group had a significantly higher melting temperature compared to all other groups, including the commercial, water-treated, and NaOH-treated groups. The commercial agar group exhibited a higher melting temperature than the water, 4% NaOH, and 6% NaOH groups, but was statistically similar to the 2% NaOH group. The melting temperatures of the water, 4% NaOH, and 6% NaOH groups were statistically identical, indicating a similar level of structural disruption across these treatments. Figure 13 illustrates the descriptive statistics (mean ± standard deviation) for the melting temperature of agar under each pretreatment condition, along with Tukey HSD post-hoc comparisons.

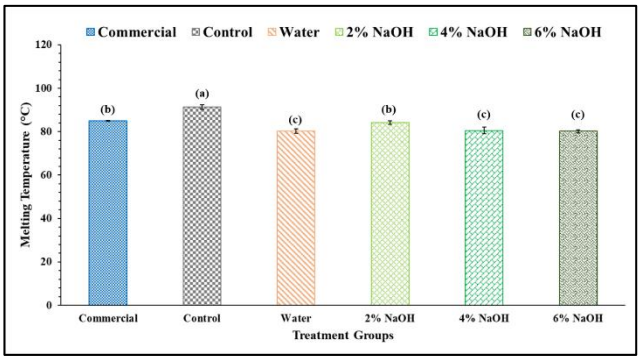



**Figure 13:** A bar chart illustrating descriptive statistics (mean ± standard deviation) of melting temperature and Tukey HSD post-hoc comparisons for each pretreatment group

### 3.5 Determination of Gelling Temperature

The gelling temperature of agar, a critical parameter influencing its application in various industries, was measured for samples extracted under different pretreatment conditions and compared to commercial agar. The gelling temperature was determined by monitoring the point at which the agar solution transitioned into a gel. A detailed summary of the gelling temperatures for all groups is provided in Table 5.

**Table 5:** Gelling temperature of agar extracted under different pretreatment conditions

| Treatment Groups | Gelling Temperature (°C) | | | Mean ± Standard Deviation |
|---|---|---|---|---|
| | Extraction 1 | Extraction 2 | Extraction 3 | |
| Control | 39.50 | 36.00 | 39.10 | 38.20 ± 1.91 |
| Water | 35.00 | 35.80 | 33.40 | 34.73 ± 1.22 |
| 2% NaOH | 37.40 | 36.00 | 35.00 | 36.13 ± 1.21 |
| 4% NaOH | 37.50 | 37.80 | 36.00 | 37.10 ± 0.96 |
| 6% NaOH | 35.80 | 33.40 | 34.60 | 34.60 ± 1.20 |

The results revealed that pretreatment conditions significantly influenced the gelling temperature of the extracted agar ($F(5, 12) = 3.38$, $p = 0.0388$). The control group exhibited the highest gelling temperature at 38.20 ± 1.91°C, indicating that impurities may have contributed to the higher value. The water-treated group showed a slightly lower gelling temperature of 34.73 ± 1.22°C, reflecting the impact of water pretreatment on the agar's gel-forming properties. Among the NaOH-treated groups, the 2% NaOH treatment yielded a gelling temperature of 36.13 ± 1.21°C, which closely aligns with the gelling temperature of commercial agar (36.17 ± 1.07 °C). The 4% NaOH treatment slightly increased the gelling temperature to 37.10 ± 0.96°C, whereas the 6% NaOH treatment resulted in the lowest gelling temperature at 34.60 ± 1.20°C, indicating that excessive alkali treatment may negatively impact gelling properties. Figure 14 graphically presents the descriptive data, including the mean and standard deviation, for the gelling temperature of agar in each group, alongside the Tukey HSD post-hoc comparisons. The analysis revealed that the 6% NaOH treatment group exhibited a significantly lower gelling temperature compared to the control group, indicating that harsh alkali conditions disrupt the structural integrity necessary for gelling. However, no significant differences were observed between the control group and the water, 2% NaOH, 4% NaOH, or commercial agar groups. Similarly, the gelling temperatures of the water-treated group and the NaOH-treated groups (2%, 4%, and 6%) were statistically comparable to that of commercial agar, except for the 6% NaOH group.

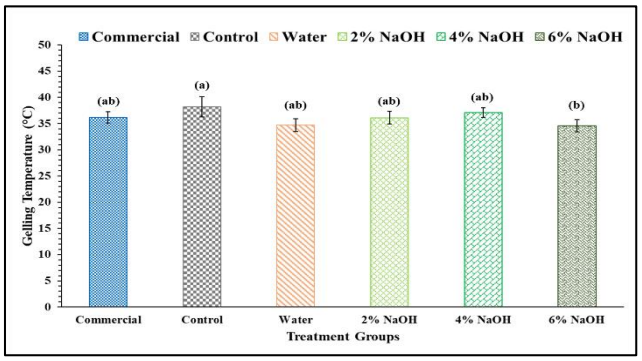



**Figure 14:** A bar chart illustrating descriptive statistics (mean ± standard deviation) of gelling temperature and Tukey HSD post-hoc comparisons for each pre-treatment group

### 3.6 Determination of pH

The pH of agar is a crucial parameter that determines its quality, stability, and suitability for various applications. In this study, the pH of extracted agar samples was measured using a digital pH meter calibrated with standard buffer solutions to ensure accuracy. The pH values of the samples, subjected to different pretreatment conditions, are summarized in Table 6.

**Table 6:** pH of agar extracted under different pre-treatment conditions

| Treatment Groups | pH | | | Mean ± Standard Deviation |
|---|---|---|---|---|
| | Extraction 1 | Extraction 2 | Extraction 3 | |
| Control | 6.80 | 6.75 | 6.82 | 6.79 ± 0.04 |
| Water | 7.90 | 8.00 | 8.10 | 8.00 ± 0.10 |
| 2% NaOH | 7.20 | 7.58 | 7.70 | 7.49 ± 0.26 |
| 4% NaOH | 7.20 | 7.03 | 7.23 | 7.15 ± 0.11 |
| 6% NaOH | 7.44 | 7.74 | 7.58 | 7.59 ± 0.15 |

The results revealed that the pretreatment conditions significantly influenced the pH of the extracted agar ($F(5, 12) = 26.03$, $p = 4.74E\text{-}06$). Agar derived in the control

group exhibited a slightly acidic pH of 6.79 ± 0.04, indicating the natural acidity of the algae. In contrast, the water-treated group had the highest pH value at 8.00 ± 0.10, reflecting a shift toward alkalinity due to the removal of specific acidic components during water pretreatment. The NaOH-treated groups exhibited intermediate pH values, with the 2% NaOH treatment yielding a pH of 7.49 ± 0.26, the 4% NaOH treatment producing a pH of 7.15 ± 0.11, and the 6% NaOH treatment resulting in a pH of 7.59 ± 0.15. These values indicate that the concentration of alkali used during pretreatment directly affects the pH of the resulting agar. The pH of the commercial agar sample (7.51 ± 0.06) closely aligned with that of the 2% NaOH treatment group, suggesting that mild alkali treatment is likely employed during commercial agar production. This consistency highlights the suitability of 2% NaOH pretreatment for producing agar with a pH similar to commercial standards, balancing both quality and functionality. Figure 15 presents a bar chart illustrating the descriptive statistics for the pH values, including the mean and standard deviation for each group, alongside Tukey HSD post-hoc comparisons. The statistical analysis revealed significant differences among groups. The water-treated group had a significantly higher pH than all other groups. In contrast, the 6% NaOH group exhibited the second-highest pH, considerably higher than the control and 4% NaOH groups, but not statistically different from the 2% NaOH and commercial groups. The commercial group's pH was significantly higher than the control group, but not substantially different from the 2% NaOH and 4% NaOH groups. No significant differences were observed between the 2% NaOH and 4% NaOH groups, although the 2% NaOH group had a significantly higher pH than the control group.

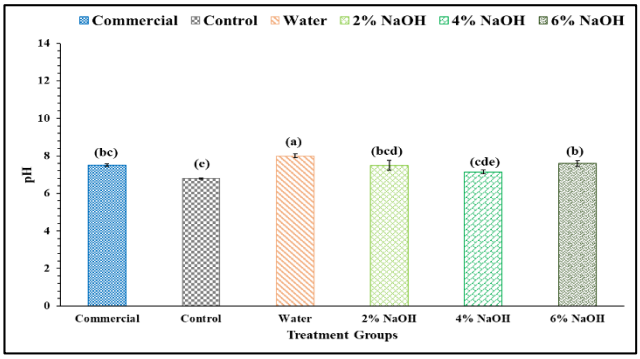



**Figure 15:** A bar chart illustrating descriptive statistics (mean ± standard deviation) of pH and Tukey HSD post-hoc comparisons for each pre-treatment group

### 3.7 Determination of Sulfate Concentration

The sulfate content in agar is a critical parameter that reflects its purity and significantly impacts its gelling capacity, stability, and biological activity (Sasuga et al., 2017; Xiao et al., 2021). This study evaluated the sulfate concentration in agar extracted from *Gracilaria tenuistipitata* under different pretreatment conditions, with results summarized in Table 7. The findings revealed that pretreatment had a significant influence on the sulfate concentration of the extracted agar ($F(5, 12) = 517.18$, $p = 1.54E-11$). The control group exhibited the highest sulfate content at 24.00 ± 1.00 mg/L, similar to the water-treated group, which had a sulfate concentration of 23.00 ± 1.00 mg/L. The marginal reduction in the water-treated group may be attributed to the mechanical agitation during the process, which likely removed some surface contaminants and salts. In contrast, the NaOH-treated groups demonstrated a substantial reduction in sulfate content, confirming the effectiveness of alkali treatment in improving agar purity.

**Table 7:** Sulfate concentration of agar extracted under different pre-treatment conditions

| Treatment Groups | Sulfate Concentration (mg/L) | | | Mean ± Standard Deviation |
|---|---|---|---|---|
| | Extraction 1 | Extraction 2 | Extraction 3 | |
| Control | 25.00 | 23.00 | 24.00 | 24.00 ± 1.00 |
| Water | 23.00 | 22.00 | 24.00 | 23.00 ± 1.00 |
| 2% NaOH | 3.00 | 4.00 | 4.00 | 3.67 ± 0.58 |
| 4% NaOH | 3.00 | 4.00 | 2.00 | 3.00 ± 1.00 |
| 6% NaOH | 2.00 | 3.00 | 2.00 | 2.33 ± 0.58 |

Precisely, agar treated with 2% NaOH showed a significant reduction in sulfate concentration, measuring 3.67 ± 0.58 mg/L. Further reductions were observed with higher concentrations of NaOH, as the 4% NaOH-treated group had a sulfate content of 3.00 ± 1.00 mg/L, and the 6% NaOH-treated group exhibited the lowest sulfate concentration at 2.33 ± 0.58 mg/L. Notably, there was no statistically significant difference in sulfate concentrations among the NaOH-treated groups, suggesting that even mild alkali treatment is highly effective in sulfate removal. Figure 16 illustrates a bar chart of the sulfate concentrations, including mean values, standard deviations, and Tukey HSD post-hoc comparisons. The chart highlights the stark contrast between the control and water treatment groups, which had the highest sulfate levels, and the NaOH-treated groups, which exhibited significantly lower levels. Therefore, the results emphasize the role of NaOH pretreatment in enhancing the quality of extracted agar by reducing sulfate content, thereby improving its gelling characteristics and overall performance.

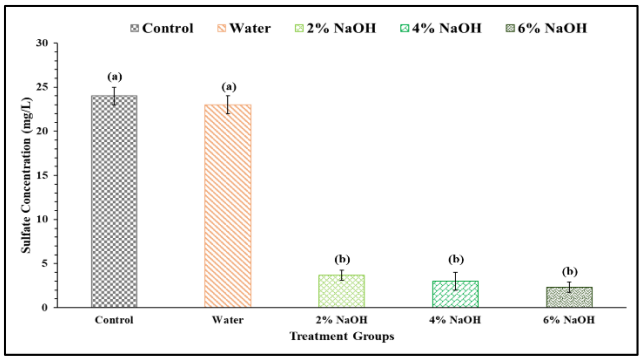



**Figure 16:** A bar chart illustrating descriptive statistics (mean ± standard deviation) of sulfate concentration and Tukey HSD post-hoc comparisons for each pre-treatment

group

## 9. CONCLUSIONS

Bangladesh, being endowed with extensive marine biodiversity, offers a sustainable avenue for extracting valuable biopolymer agar from red algae (*Gracilaria tenuistipitata)* abundantly available on Cox's Bazar beach. The preliminary results of this work recognize the high potential of red algae as a promising source of agar. The comparative evaluation of different extraction processes indicates that pre-treatment conditions greatly influence the yield, and physicochemical characteristics and overall quality of the extracted agar. Among all methods studied, the 2% NaOH pre-treatment yielded the most favorable results—producing agar with high gel strength, desirable melting and gelling temperatures, and physicochemical properties (such as pH and sulfate content) comparable to those of commercial-grade agar. Furthermore, the FTIR spectroscopy confirmed the structural integrity and the presence of characteristic functional groups (e.g., sulfate esters, hydroxyl, and glycosidic linkages), which are essential for the agar's performance in various biomedical applications. Overall, these findings suggest that the extracted agar possesses the necessary characteristics for potential use in biomedical fields such as edible coatings for fruits and vegetables, tissue engineering scaffolds, and drug delivery systems.

Through the optimization of the extraction process and the utilization of local marine resources, this work not only creates a greater scope for biomedical advancements but also promotes environmental sustainability and economic benefits. The agar derived from this abundant local source in Bangladesh has the potential to revolutionize healthcare solutions while contributing to sustainable national economic growth.

## ACKNOWLEDGMENTS

The authors would like to thank the Department of Biomedical Engineering, Military Institute of Science and Technology, Bangladesh, for providing laboratory facilities and technical support for this study.

## DATA AVAILABILITY STATEMENT

Datasets generated during the current study are available from the corresponding author upon reasonable request.

## FUNDING DECLARATION

This research was self-funded.

## ETHICS APPROVAL

This study is an engineering experimental investigation. The MIJST Research Ethics Committee has confirmed that formal ethical approval was not required.

## ETHICS, CONSENT TO PARTICIPATE, AND CONSENT TO PUBLISH

Not applicable.

## COMPETING INTERESTS

The authors declare that they have no competing interests.

## AUTHOR CONTRIBUTIONS

Author 1: Fawzia Afrin Rimpy- Methodology, Investigation, Writing manuscript

Author 2: Md Enamul Hoque- Conceptualization, Project Administration, Supervision, Manuscript revision

Author 3: Quazi Farsheed Mahmud- Investigation, Data curation, Writing manuscrip

Author 4: Itmam Nowroj- Methodology, Analysis, Writing Manuscript

Author 5: Sazedur Rahman- Validation, Manuscript revision

Author 6: Tarek El-Bialy- Resources, Manuscript revision

Author 7: M. Azam Ali- Visualization, Manuscript revision

## ARTIFICIAL INTELLIGENCE ASSISTANCE STATEMENT

Portions of this manuscript were assisted by an artificial intelligence language model (ChatGPT, OpenAI). The tool was used solely for language editing, text refinement, and clarity improvement. All content, data interpretation, analysis, conclusions, and final decisions were generated, verified, and approved by the authors. The authors take full responsibility for the accuracy and integrity of the manuscript.

## CONFLICT OF INTEREST DECLARATION

The authors declare that they have no conflicts of interest.

## REFERENCES

A, A. D., & G, K. (2024). Microalgae: An emerging source of bioplastics production. *Discover Environment*, *2*(1), 10. https://doi.org/10.1007/s44274-024-00038-0

Armisén, R. (1991). Agar and agarose biotechnological applications. In J. A. Juanes, B. Santelices, & J. L. McLachlan (Eds.), *International Workshop on Gelidium* (pp. 157–166). Springer Netherlands. https://doi.org/10.1007/978-94-011-3610-5_15

Beaumont, M., Tran, R., Vera, G., Niedrist, D., Rousset, A., Pierre, R., Shastri, V. P., & Forget, A. (2021). Hydrogel-Forming Algae Polysaccharides: From Seaweed to Biomedical Applications. *Biomacromolecules*, *22*(3), 1027–1052. https://doi.org/10.1021/acs.biomac.0c01406

Curvello, R., Raghuwanshi, V. S., & Garnier, G. (2019). Engineering nanocellulose hydrogels for biomedical applications. *Advances in Colloid and Interface Science*, *267*, 47–61. https://doi.org/10.1016/j.cis.2019.03.002

Dhivya, S., Padma, V. V., & Santhini, E. (2015). Wound dressings – a review. *BioMedicine*, *5*(4), 22.

https://doi.org/10.7603/s40681-015-0022-9

El-Beltagi, H. S., Mohamed, A. A., Mohamed, H. I., Ramadan, K. M. A., Barqawi, A. A., & Mansour, A. T. (2022). Phytochemical and Potential Properties of Seaweeds and Their Recent Applications: A Review. *Marine Drugs*, *20*(6), 342. https://doi.org/10.3390/md20060342

Fujiwara, E., Rosa, L. O., Oku, H., & Cordeiro, C. M. B. (2023). Agar-based optical sensors for electric current measurements. *Scientific Reports*, *13*(1), 13517. https://doi.org/10.1038/s41598-023-40749-7

Gómez-Ordóñez, E., & Rupérez, P. (2011). FTIR-ATR spectroscopy as a tool for polysaccharide identification in edible brown and red seaweeds. *Food Hydrocolloids*, *25*(6), 1514–1520. https://doi.org/10.1016/j.foodhyd.2011.02.009

Graham, S., Marina, P. F., & Blencowe, A. (2019). Thermoresponsive polysaccharides and their thermoreversible physical hydrogel networks. *Carbohydrate Polymers*, *207*, 143–159. https://doi.org/10.1016/j.carbpol.2018.11.053

Hoque, M. E., Sarker, M. A., Arif, K., Ali, M. A., & El-Bialy, T. (2023). Antibacterial/Antiviral Face Masks: Processing, Characteristics, Challenges, and Sustainability. MIST INTERNATIONAL JOURNAL OF SCIENCE AND TECHNOLOGY, 11, 61–79. https://doi.org/10.47981/j.mijst.11(02)2023.421(61-79)

Hossain, Md. T., Sohag, A. A. M., Haque, Md. N., Tahjib-Ul-Arif, Md., Dash, R., Chowdhury, M. T. H., Hossain, Md. A., Moon, I. S., & Hannan, Md. A. (2021). Nutritional Value, Phytochemical Profile, Antioxidant Property and Agar Yielding Potential of Macroalgae from Coasts of Cox's Bazar and St. Martin's Island of Bangladesh. *Journal of Aquatic Food Product Technology*, *30*(2), 217–227. https://doi.org/10.1080/10498850.2020.1869876

Jiang, F., Xu, X.-W., Chen, F.-Q., Weng, H.-F., Chen, J., Ru, Y., Xiao, Q., & Xiao, A.-F. (2023). Extraction, Modification and Biomedical Application of Agarose Hydrogels: A Review. *Marine Drugs*, *21*(5), 299. https://doi.org/10.3390/md21050299

Kazimierczak, P., Palka, K., & Przekora, A. (2019). Development and Optimization of the Novel Fabrication Method of Highly Macroporous Chitosan/Agarose/Nanohydroxyapatite Bone Scaffold for Potential Regenerative Medicine Applications. *Biomolecules*, *9*(9), 434. https://doi.org/10.3390/biom9090434

Khandwal, D., Patel, S., Pandey, A. K., & Mishra, A. (2025). A Comprehensive, Analytical Narrative Review of Polysaccharides from the Red Seaweed Gracilaria: Pharmaceutical Applications and Mechanistic Insights for Human Health. *Nutrients*, *17*(5), 744. https://doi.org/10.3390/nu17050744

Lam, P.-L., Gambari, R., Kok, S. H.-L., Lam, K.-H., Tang, J. C.-O., Bian, Z.-X., Lee, K. K.-H., & Chui, C.-H. (2015). Non-toxic agarose/gelatin-based microencapsulation system containing gallic acid for antifungal application. *International Journal of Molecular Medicine*, *35*(2), 503–510. https://doi.org/10.3892/ijmm.2014.2027

Liao, Y.-C., Chang, C.-C., Nagarajan, D., Chen, C.-Y., & Chang, J.-S. (2021). Algae-derived hydrocolloids in foods: Applications and health-related issues. *Bioengineered*, *12*(1), 3787–3801. https://doi.org/10.1080/21655979.2021.1946359

Madadi, R., Maljaee, H., Serafim, L. S., & Ventura, S. P. M. (2021). Microalgae as Contributors to Produce Biopolymers. *Marine Drugs*, *19*(8), 466. https://doi.org/10.3390/md19080466

Martínez-Sanz, M., Gómez-Mascaraque, L. G., Ballester, A. R., Martínez-Abad, A., Brodkorb, A., & López-Rubio, A. (2019). Production of unpurified agar-based extracts from red seaweed Gelidium sesquipedale by means of simplified extraction protocols. *Algal Research*, *38*, 101420. https://doi.org/10.1016/j.algal.2019.101420

Mohibbullah, Md., Talha, Md. A., Baten, Md. A., Newaz, A. W., & Choi, J. (2023). Yield optimization, physicochemical characterizations, and antioxidant properties of food grade agar from *Gracilaria tenuistipitata* of Cox's Bazar coast, Bangladesh. *Food Science & Nutrition*, *11*(6), 2852–2863. https://doi.org/10.1002/fsn3.3265

Padmesh, S., & Singh, A. (2021). Agars: Properties and Applications. In Inamuddin, M. I. Ahamed, R. Boddula, & T. Altalhi (Eds.), *Polysaccharides* (1st ed., pp. 75–93). Wiley. https://doi.org/10.1002/9781119711414.ch5

Park, S. H., Lee, C.-R., & Hong, S.-K. (2020). Implications of agar and agarase in industrial applications of sustainable marine biomass. *Applied Microbiology and Biotechnology*, *104*(7), 2815–2832. https://doi.org/10.1007/s00253-020-10412-6

Qari, R., & Haider, S. (2021). Agar Extraction, Physical Properties, FTIR Analysis and Biochemical Composition of Three Edible Species of Red Seaweeds Gracilaria corticata (J. Agardh), Gracilaria dentata (J. Agardh) and Gracilariopsis longissima (S. G. Gmelin)..... *Biological Sciences - PJSIR*, *64*(3), 263–273. https://doi.org/10.52763/PJSIR.BIOL.SCI.64.3.2021.263.273

Rahmati, M., Alipanahi, Z., & Mozafari, M. (2019). Emerging Biomedical Applications of Algal Polysaccharides. *Current Pharmaceutical Design*, *25*(11), 1335–1344. https://doi.org/10.2174/1381612825666190423160357

Rashid, A.B.; Hoque, M.E.; Kabir, N.; Rifat, F.F.; Ishrak, H.; Alqahtani, A.; Chowdhury, M.E.H. Synthesis, Properties, Applications, and Future Prospective of Cellulose Nanocrystals. Polymers 2023, 15, 4070. https://doi.org/10.3390/polym15204070

Rhein-Knudsen, N., Ale, M. T., Ajalloueian, F., Yu, L., &

Meyer, A. S. (2017). Rheological properties of agar and carrageenan from Ghanaian red seaweeds. *Food Hydrocolloids*, *63*, 50–58. https://doi.org/10.1016/j.foodhyd.2016.08.023

Sasuga, K., Yamanashi, T., Nakayama, S., Ono, S., & Mikami, K. (2017). Optimization of yield and quality of agar polysaccharide isolated from the marine red macroalga Pyropia yezoensis. *Algal Research*, *26*, 123–130. https://doi.org/10.1016/j.algal.2017.07.010

Sobuj, M. K. A., Islam, Md. A., Islam, Md. S., Islam, Md. M., Mahmud, Y., & Rafiquzzaman, S. M. (2021). Effect of solvents on bioactive compounds and antioxidant activity of Padina tetrastromatica and Gracilaria tenuistipitata seaweeds collected from Bangladesh. *Scientific Reports*, *11*(1), 19082. https://doi.org/10.1038/s41598-021-98461-3

Souza, B. W. S., Cerqueira, M. A., Bourbon, A. I., Pinheiro, A. C., Martins, J. T., Teixeira, J. A., Coimbra, M. A., & Vicente, A. A. (2012). Chemical characterization and antioxidant activity of sulfated polysaccharide from the red seaweed Gracilaria birdiae. *Food Hydrocolloids*, *27*(2), 287–292. https://doi.org/10.1016/j.foodhyd.2011.10.005

Sudhakar, M. P., Nived, S. A., & Dharani, G. (2024). Fabrication and Characterization of Agar- and Seaweed-Derived Biomembrane Films for Biomedical and Other Applications. *Biopolymers*, e23643. https://doi.org/10.1002/bip.23643

Sukhikh, S., Prosekov, A., Ivanova, S., Maslennikov, P., Andreeva, A., Budenkova, E., Kashirskikh, E., Tcibulnikova, A., Zemliakova, E., Samusev, I., & Babich, O. (2022). Identification of Metabolites with Antibacterial Activities by Analyzing the FTIR Spectra of Microalgae. *Life*, *12*(9), 1395. https://doi.org/10.3390/life12091395

Tatrishvili, T. (Ed.). (2025). *Sustainability in Polymer Technology and Plastic Engineering: Concepts, Strategies, and Opportunities* (First edition). Apple Academic Press.

Thombare, N., Mahto, A., Singh, D., Chowdhury, A. R., & Ansari, M. F. (2023). Comparative FTIR Characterization of Various Natural Gums: A Criterion for Their Identification. *Journal of Polymers and the Environment*, *31*(8), 3372–3380. https://doi.org/10.1007/s10924-023-02821-1

Vieira, C. B., Sousa, J. R., Do Vale, D. A., Guimarães, C. P., De Sousa, K. C., Mattos, A. L. A., Silva, A. L. C., De Sá Moreira Souza Filho, M., & Souza, B. W. S. (2025). Edible films based on sulfated polysaccharides from the seaweed Gracilaria birdiae: Physicochemical, optical and mechanical properties. *Carbohydrate Research*, *552*, 109473. https://doi.org/10.1016/j.carres.2025.109473

Vijayan, S. R., Santhiyagu, P., Ramasamy, R., Arivalagan, P., Kumar, G., Ethiraj, K., & Ramaswamy, B. R. (2016). Seaweeds: A resource for marine bionanotechnology. *Enzyme and Microbial Technology*, *95*, 45–57. https://doi.org/10.1016/j.enzmictec.2016.06.009

Xiao, Q., Wang, X., Zhang, J., Zhang, Y., Chen, J., Chen, F., & Xiao, A. (2021). Pretreatment Techniques and Green Extraction Technologies for Agar from Gracilaria lemaneiformis. *Marine Drugs*, *19*(11), 617. https://doi.org/10.3390/md19110617

Zhang, C., An, D., Xiao, Q., Weng, H., Zhang, Y., Yang, Q., & Xiao, A. (2020). Preparation, characterization, and modification mechanism of agar treated with hydrogen peroxide at different temperatures. Food Hydrocolloids, 101, 105527. https://doi.org/10.1016/j.foodhyd.2019.105527

MIJST
*MIST International Journal of Science and Technology*

# Numerical Investigation for Flexural Response of Stainless-Steel Reinforced Concrete Beams

**Nusrat Tabassum[1], Abdullah Al-Moneim[1,*], Said Razu[1], Aziz Ahmed[2], Khondaker Sakil Ahmed[1]**

[1]Department of Civil Engineering, Military Institute of Science and Technology, Dhaka, Bangladesh
[2]School of Civil, Mining, Environmental and Architectural Engineering, University of Wollongong, Australia

***Corresponding Email:** *moneim@ce.mist.ac.bd*

**ARTICLE INFO**

**Article History:**

*Received: 2th July 2025*
*Revised: 4th July 2025*
*Accepted: 06th October 2025*
*Published: 30th December 2025*

**Keywords**:

*Stainless steel rebar*
*Finite element analysis*
*Flexural response*
*Ultimate capacity*

**ABSTRACT**

Stainless steel (SS) is becoming increasingly popular as reinforcement across the globe, owing to its superior mechanical and durability properties. This study numerically investigates the flexural behavior of concrete beams reinforced with stainless steel. Primarily, the experimental results are validated by developing 3D finite element (FE) models with stainless steel rebars, considering the actual test data. In the modelling process, 8-node brick element for concrete and 2-node beam element for reinforcement were employed in the finite element model. The numerical results are presented in terms of load displacement response, yield, and ultimate capacity with respective deformation, ductility, etc. The numerical results depicted reasonably good precision in predicting the load deformation response and ultimate load of the concrete beam reinforced with stainless-steel. The models have been regenerated for concrete beams with conventional mild steel to investigate the comparative behaviour in terms of significant changes in their load-carrying capacity and the corresponding ultimate deformation. Results revealed that the peak loads remained approximately the same for 30 MPa and 40 MPa concrete strengths, although the stainless-steel reinforced beams showed greater deformability and ductility. In addition, a parametric study of reinforced concrete beam models consisting of Grade 201 stainless steel rebars and 60-grade mild steel rebars with varying concrete grades of 30 MPa, 40 MPa, and 50 MPa was also performed to inspect their influence on the initial stiffness, ductility, and ultimate load-carrying capability of the concrete beams. The numerical response rendered that beam reinforced with stainless steel provide similar ultimate flexural capacity with improved stiffness and ductility in contrast to that of the mild steel rebars.

This work is licensed under a *Creative Commons Attribution-Non-commercial 4.0 International License.*

## 1. INTRODUCTION

Reinforced concrete is the outcome of the process where the limitations of concrete, such as minimal tensile strength, brittle nature, are excluded with the addition of reinforcing steel in concrete. Since the late nineteenth century, high tensile strength steel has been used to reinforce concrete, mainly in areas where concrete's minimal tensile strength would limit the member's load-carrying capacity. The reinforcing steel in reinforced concrete provides ductility and strength by bonding and anchoring to the concrete. The deterioration of steel, concrete, or both can severely diminish this bond, compromising the concrete structure's durability. The concrete must be of adequate durability to resist any chemical and physical variables that may influence the structure while also protecting the reinforcing steel embedded in it (Kapasny & Zembo, 1993). Steel deterioration is typically caused by corrosion, which is one of the key reasons of reinforced concrete's low durability (Fu & Chung, 1997). Given that steel is corrosive and less fire-resistant, engineers faced a novel challenge in obtaining a specific steel composition that met all of the requirements. One of the study's breakthroughs was the use of stainless steel (SS). SS is versatile and can be used for aesthetics and structural stability (Baddoo, 2008; Corradi, Di Schino, Borri, & Rufini, 2018; Rossi, 2014). Studies demonstrate that SS is more ductile than mild steel (MS) and reasonably more plastic in its characteristics between the yield and ultimate tensile stress, also has an outstanding toughness at low temperatures, and a degree of anisotropy (Farzana & Ahmed, 2020; Gardner, 2005; Gedge, 2008). High-strength stainless steel offers sufficient structural strength and is highly corrosion-resistant. The corrosive behaviour of three low-cost stainless steels with low nickel content demonstrated that the samples remained in a passive state even under the

maximum chloride contamination level that is naturally found in the environment (Gedge, 2008). Stainless steel demonstrated the best corrosion resistance among a range of galvanized reinforcing bars tested (Gedge, 2008). Furthermore, for any construction, ductility is a crucial problem because it is directly related to energy dissipation and structural endurance during any seismic event. Hot-rolled austenitic and duplex SS are about three times more ductile compared to conventional carbon steel (Saraswathy & Song, 2005). However, stainless steel is a difficult material to work with owing to its diverse alloy composition. This research conducts a comparative investigation of MS and SS reinforced concrete.

Extensive experiments to determine the bond behavior of steel and concrete, stress generation at each point, and various properties such as ductility and corrosion resistance capacity, under different loading patterns are tedious, time-consuming, and expensive due to the complex setup. To address all of these restrictions, numerical modeling was performed. The task of designing and analyzing any structural member with variable material properties, boundary conditions, and loading patterns became very simple with the aid of numerical modelling, which required no significant setup. In a numerical study, a cross-section layer model and the stiffness matrix method are used to simulate the deflection of beams that failed in bending at any load level. To accurately predict the force-midspan deformation relationship in the tested beams, this numerical strategy utilized the material properties obtained from experimental tests. This showed that the approach is adequate for simulating the behaviour of RC beams reinforced by the near surface mounted (NSM) strengthening procedure using carbon fibre reinforced polymer (CFRP) laminate strips (Barros & Fortes, 2005). The dynamic response of RC beams under varying rates of point loading was studied using LS-DYNA, an explicit finite element program. The test program yielded a significant amount of test data, including load vs. mid-span deformation, crack profiles, strain at the mid-point of longitudinal tensile reinforcement acceleration at many sites along the specimens (Adhikary, Li, & Fujikake, 2012).

This paper examined mild steel and concrete beams reinforced with stainless steel using finite element analysis. Primarily, the numerical models of both MS and SS reinforced concrete beams have been validated with existing experimental data (Ahmed, Habib, & Asef, 2021; Saatci & Vecchio, 2009). Results are extracted in terms of load deformation response, stress distribution, and failure pattern. In addition, a parametric analysis was carried out to determine the impact of various concrete grades on both MS and SS.

## 2. METHODOLOGY

In experimental testing of beams, stress transfer occurs at the steel-concrete interface after the load application. Fine fractures form as a result of an imbalanced stress distribution. These cracks develop over time and eventually cause the structural member to disintegrate. Finite element models were developed to facilitate the determination of failure loads and displacements, stress generation, load deflection curves, and failure patterns. Two-step validation was done using numerical models for separate experimental test beams. Firstly, an experimental simply supported RC beam with no shear reinforcement was validated (Saatci & Vecchio, 2009). Later, from another study, both SS reinforced beams and MS reinforced beams were validated (Ahmed et al., 2021). Lastly, using the numerical models for both SS and MS reinforced beams, a parametric study for varying concrete strength was carried out.

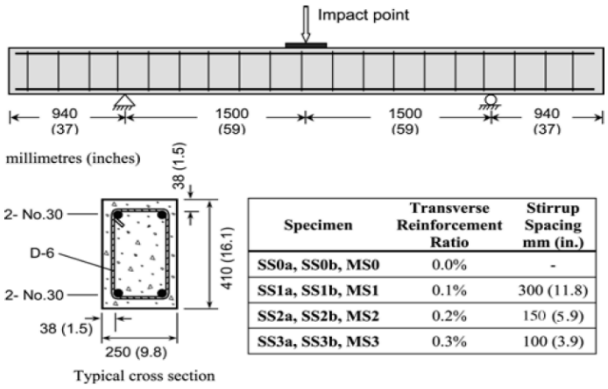
### 2.1 SPECIMEN DETAILS

#### 2.1.1 FE MODEL FOR VALIDATION OF EXPERIMENTAL TEST RESULTS

This section's static analysis replicates the experiments on RC beams conducted by Saatci (2007) (Saatci & Vecchio, 2009). The outcomes of the study were compared against the experimental test results after the static beam was modelled in ABAQUS (2012) using the FE technique. To gain a better understanding of how shear reinforcement affects failure behaviour, the experimental test was carried out on four simply supported RC beams. These beams were supplied with same longitudinal reinforcement and varying shear reinforcement. This study's validation used the beam specimen MS0, which had no shear reinforcement. The RC beam tested in the previous analysis is shown in **Figure 1**.

#### 2.1.2 EXPERIMENTAL TEST OF STAINLESS AND MILD STEEL REBAR REINFORCED BEAMS

The current investigation modelled a mild steel reinforced and another SS reinforced concrete beam with a cross-sectional area of 150 mm x 200 mm and a length of 1500 mm (Ahmed et al., 2021). A loading plate of cross-sectional area 150 mm x 50 mm and length of 500 mm was also modelled, and the displacement was placed on top of it. Two cylinders with a diameter of 100 mm and a length of 150 mm were positioned beneath the beam, with two more cylinders of identical geometry inserted between the RC beam and the loading plate. The load vs. displacement graphs were acquired for the beams' mid-span section.




| Specimen | Transverse Reinforcement Ratio | Stirrup Spacing mm (in.) |
|---|---|---|
| SS0a, SS0b, MS0 | 0.0% | - |
| SS1a, SS1b, MS1 | 0.1% | 300 (11.8) |
| SS2a, SS2b, MS2 | 0.2% | 150 (5.9) |
| SS3a, SS3b, MS3 | 0.3% | 100 (3.9) |

**Figure 1**: Experimental test setup (Saatci & Vecchio, 2009)

### 2.2 MATERIAL MODELLING

The beam model's concrete compressive strength was around 50 MPa during validation testing, and mild steel rebars of Grade 60 were used. Later, beams reinforced with stainless steel and mild steel were modelled and validated using previously conducted experimental tests. A comparative investigation of beams reinforced with stainless steel and mild steel was conducted. Furthermore, a parametric investigation of these beams reinforced with stainless and mild steel for varied concrete strengths was carried out. **Figure 2** provides information on the material properties of SS adopted in this study.

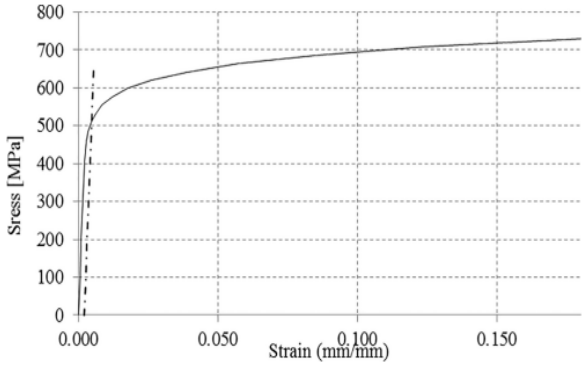



**Figure 2:** Typical mechanical properties of the 201 grade plain SS rebar

The elastic properties of concrete of varying compressive strength are presented in Table 1.

**Table 1:** Elastic property of varying concrete strength (Hafezolghorani, Hejazi, Vaghei, Jaafar, & Karimzade, 2017)

| Concrete Strength (MPa) | Young's Modulus (MPa) | Poisson's Ratio |
|---|---|---|
| 30 | 25918.92 | 0.2 |
| 40 | 30000 | 0.2 |
| 50 | 32795.2 | 0.182 |

Similarly, the plastic properties of varying concrete grades are provided in Table 2.

**Table 2:** Plastic properties of concrete of varying concrete strength (Hafezolghorani et al., 2017)

| Concrete Strength (MPa) | Dilation Angle | Eccentricity | fb0/fc0 | K | Viscosity Parameter |
|---|---|---|---|---|---|
| 30 | 31 | 0.1 | 1.16 | 0.67 | 0 |
| 40 | 31 | 0.1 | 1.16 | 0.67 | 0 |
| 50 | 38 | 0.1 | 1.16 | 0.66 | 0 |

Finally, the tensile properties of various concrete grades adopted in the study are presented in Table 3.

**Table 3:** Tensile behaviour of concrete of varying concrete strength (Hafezolghorani et al., 2017)

| Concrete Strength (MPa) | Yield Stress (MPa) | Inelastic Strain |
|---|---|---|
| 30 | 3 | 0 |
| | 0.03 | 0.001167315 |
| 40 | 4 | 0 |
| | 0.04 | 0.001333333 |
| 50 | 5 | 0 |
| | 0.05 | 0.001494322 |

Additionally, the material properties of 60-grade mild steel are presented in Table 4.

**Table 4:** Mild (MS) and stainless steel (SS) properties

| Type | Density (tonne / mm$^3$) | Elasticity | | Plasticity | |
|---|---|---|---|---|---|
| | | Young's Modulus (MPa) | Poisson's Ratio | Yield Stress (MPa) | Plastic Strain (mm/mm) |
| MS | 7.85E-9 | 200000 | 0.3 | 420 | 0 |
| | | | | 532 | 0.00271 |
| | | | | 551 | 0.0224 |
| | | | | 655 | 0.114 |
| | | | | 447 | 0.218 |
| SS | 7.8E-9 | 190000 | 0.28 | 420 | 0 |
| | | | | 450 | 0.051 |
| | | | | 500 | 0.152 |
| | | | | 550 | 0.352 |

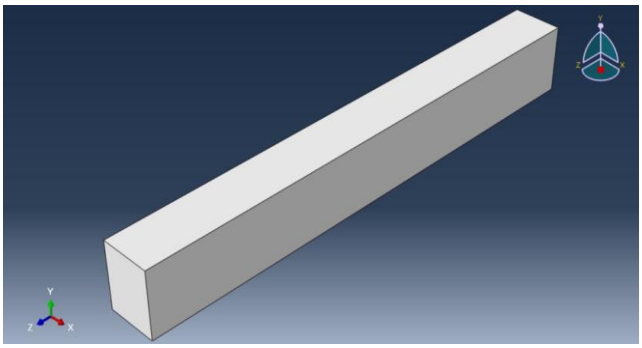
## 2.3 NUMERICAL MODELLING

The bending and shear reinforcements were coupled to the surrounding concrete utilizing the embedded model technique at each place where the concrete and reinforcing sections cross. The employment of embedded components implied the perfect bond between the reinforcement and the concrete. The CDP model aids in visualizing the pattern of damage of concrete sections as tension and compression damage. The reinforcements were simulated using simple elastic-plastic materials based on existing research. The beam was simulated at full scale to ensure the actual test behaviour, as illustrated in **Figure 3**. **Table 5** presents detailed data for numerical modelling.

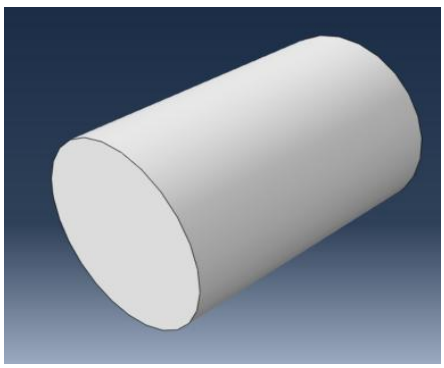
**Table 5:** Numerical modelling details overview

| | | |
|---|---|---|
| **Material Modelling** | • | Concrete: Concrete Damage Plasticity |
| | • | Steel: Elasto Plastic Steel |
| **Element** | • | Concrete: C3D8R |

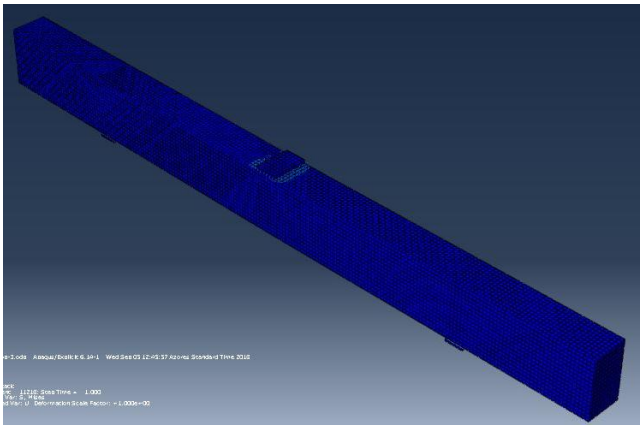
| | |
|---|---|
| **Type** | • Steel: B31 |
| **Element Interface** | • Embedded Model |
| **Contact Algorithms** | • Mechanical Constraint Formulation: Penalty Contact Method<br>• Contact Property: Coulomb Friction<br>• Method: Tangential Behavior - Friction Coefficient (0.25)<br>• Normal Behavior: Pressure over-closure- "Hard" contact. |
| **Mesh Size** | • 25 mm for validation test beam by Saatci (2007).<br>• 20 mm for comparative and parametric study test beam reinforced with stainless steel and mild steel rebars. |
| **Loading Protocol** | • Displacement control.<br>• A supporting steel plate with 1-inch thickness was used for the validation test beam by Saatci (2007).<br>• For the beams modelled for comparative and parametric study, a downward displacement of 30mm was applied to the upper surface of the plate placed over the cylinders. |
| **Boundary Conditions** | • The lower outer surfaces of two of the beams are made encastred.<br>• The plate and cylinders' x-directional and z-directional movements are restrained. |



(a)



(b)



(c)

**Figure 3:** (a)-(b) Model development using parts in Abaqus CAE, (c) Meshing of the developed model.

## 3. RESULTS AND DISCUSSIONS

### 3.1 NUMERICAL VALIDATION OF TEST BEAM BY SAATCI (2007)

The schematic view of the numerical model of the test beam (Saatci & Vecchio, 2009) is illustrated in Fig. 3(c). The load deformation curve of the beam MS0 is presented in **Figure 4**. The load was applied to the beam at midspan by a bearing plate, and the analysis was performed using the explicit approach of ABAQUS (2012). As a result, the stiffness, or static load, of the beam has been calculated using the reaction force between the beam's contact surface and the loading plate. Data fluctuation was detected during testing because of non-linear complex deformation when the load increased, and crack propagation occurred.

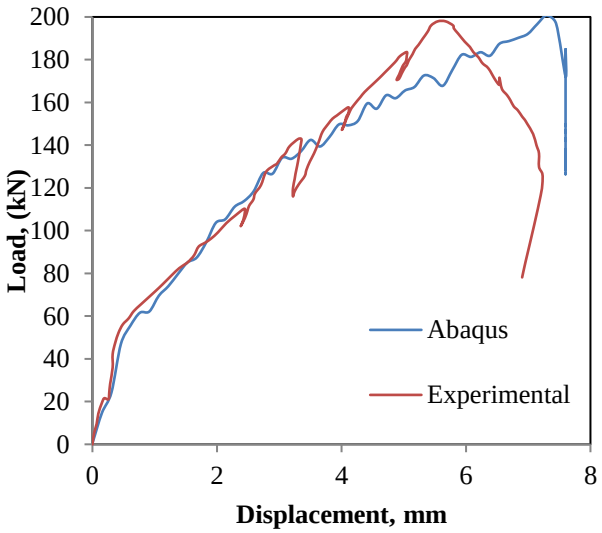



**Figure 4:** Comparison of load deformation response between numerically analysed beam (MS0) with experimental test result obtained by (Saatci & Vecchio, 2009)

This phenomenon is also noticed during flexural tests on RC beams. MS0's response via FE analysis was determined to be relatively comparable to the actual response obtained in the experiment. The beam was estimated by ABAQUS

(2012) to be somewhat more flexible than the response that was seen in the experiment. Once the peak load was reached, the main behavioral discrepancy between the expected and observed results became apparent. Using ABAQUS (2012), it was found that the beam could withstand loads up to 197.86 kN before losing its capacity at a maximum load of 200.7 kN. This implies that the numerical model was successfully developed and accurately simulated real circumstances, with a peak load prediction accuracy of 98.58%.

### 3.2 NUMERICAL VALIDATION FOR SS REINFORCED CONCRETE BEAM

SS reinforced concrete beams have been previously tested experimentally by Ahmed et al. (Ahmed et al., 2021). **Figure 5** depicts the deflected shape of the tested beam with stress distribution.

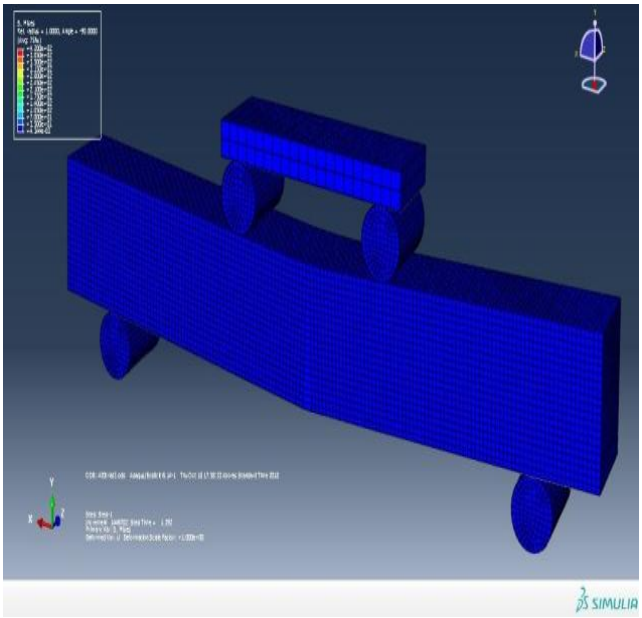


**Figure 5:** FE model of the tested RC beam (Ahmed et al., 2021)

For validation, a comparative analysis between experimental and numerical data for both SS reinforced concrete beams and MS reinforced concrete beams was done. In **Figure 6**, the load deformation responses of both experimental results and numerical outcomes are presented. The results indicate that the beams' ultimate flexural capacity is in good accord. The ultimate flexural capacity of the beam derived from the computational model was 72.85 kN, while the maximum load obtained for the experimental beam was 72.5 kN. The experimental curve demonstrates that the peak load is attained with a higher displacement than the numerical model curve. The experimental beam's increased displacement is owing to the incorporation of a softer material between the beam and the support. In addition, there is an initial set between the beam and support that creates a larger displacement on its own, resulting in more displacement than the ABAQUS numerical model curve.

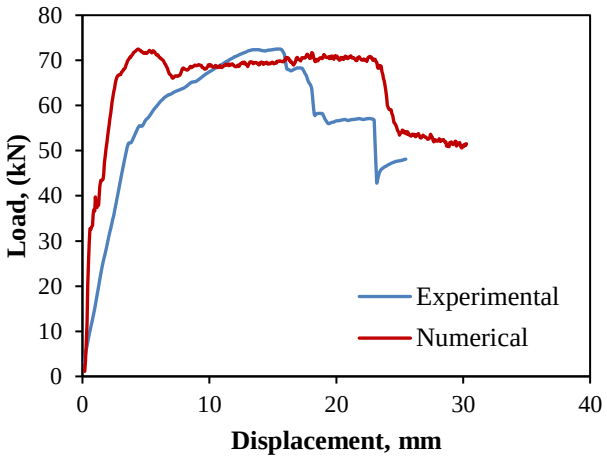



**Figure 6:** Load displacement response of the experimental (B50) (Saatci & Vecchio, 2009) and the numerical model of the mild steel reinforced concrete beam (MSL-2)

In the experimental and numerical curves, as shown in **Figure 7**, the peak loads are predicted satisfactorily, but the displacement of the experimental beam is more than the numerical model. The maximum load obtained for the numerical beam modelled was 71.93 kN with a corresponding displacement of 3mm, and the maximum load obtained for the experimental beam was 72.42 kN with a corresponding displacement of 18.77 mm. This phenomenon is due to the fact that the bars used in the experiment are plain stainless steel. When a load was applied, there was a slip in the contact surface, resulting in more displacement than the deformed bars. In the numerical model, the bars are embedded into the concrete surface and function as an integral part. The slip characteristics were not incorporated into the model; hence, the load vs. displacement curves vary.

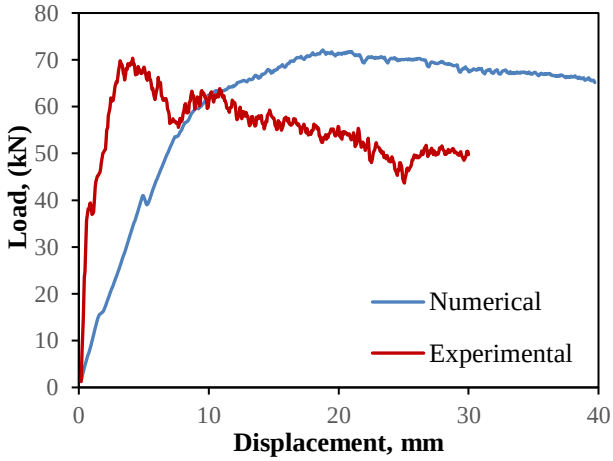
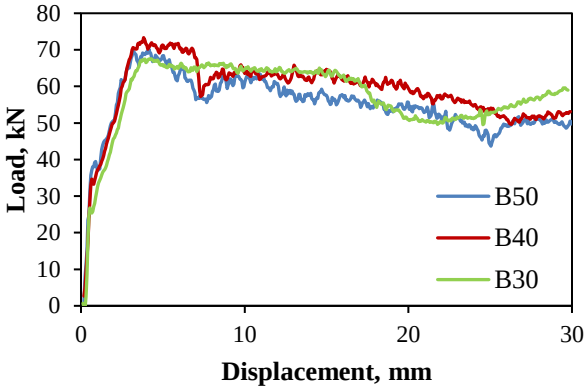



**Figure 7:** The load-deformation response of experimental (B50) and numerical model of stainless steel reinforced concrete beam (SSL-1)

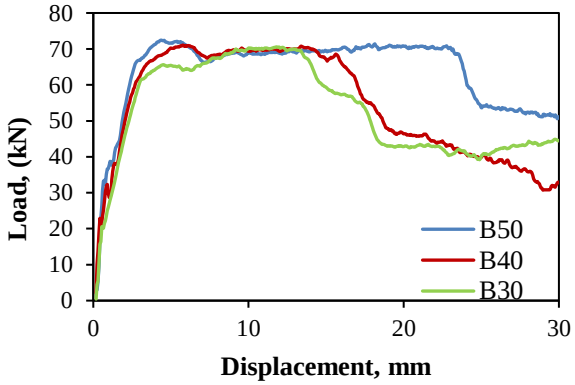
### 3.3 PARAMETRIC STUDY FOR VARYING CONCRETE STRENGTHS

**Figure 8** compares numerical model beams with varied concrete grades (30 MPa, 40 MPa, and 50 MPa) reinforced

with stainless steel. **Table 6** demonstrates that the SS reinforced RC beam with concrete strength 40MPa has the highest load carrying capability of 74.89 kN with a displacement of 3.65 mm. This occurs because stainless steel reinforced beams with higher-grade concrete break early due to the high ductility of SS reinforcement and lower cracking strains of higher-grade concrete, which happen before the ultimate strength of SS.




(a)




(b)

**Figure 8**: The load-deformation response of concrete beams reinforced with (a) stainless rebar, (b) mild steel rebar

**Table 6**: Peak loads for SS reinforced RC beams with varying concrete strength

| Concrete Strength (MPa) | Peak Load (kN) |
|---|---|
| 30 | 68.82 |
| 40 | 74.89 |
| 50 | 72.61 |

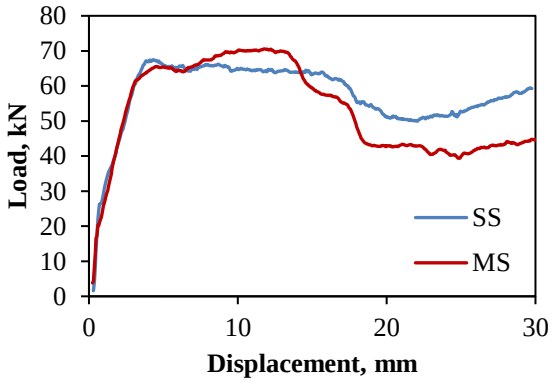
In **Figure 9**, numerical model beams with varying concrete grades (30 MPa, 40 MPa, and 50 MPa) reinforced with stainless steel are compared. From **Table 7**, it is observed that the MS reinforced RC beam with concrete strength 50 MPa has the highest load carrying capacity of 72.85 kN with corresponding displacement 4.33 mm.

**Table 7:** Peak loads for MS reinforced RC beams with varying concrete strength

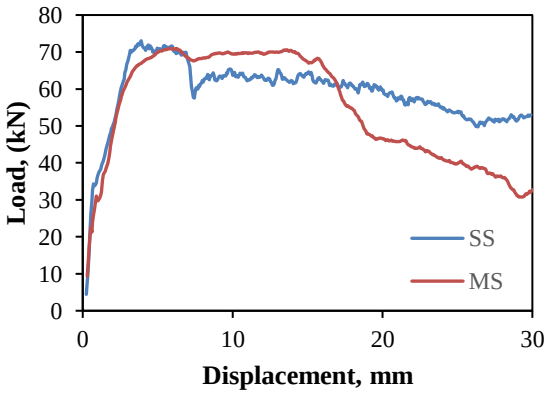
| Concrete Strength (MPa) | Peak Load (kN) |
|---|---|
| 30 | 65.7 |
| 40 | 71.37 |
| 50 | 72.85 |

### 3.4 COMPARATIVE STUDY BETWEEN STAINLESS STEEL REINFORCED BEAM AND MILD STEEL REINFORCED BEAM

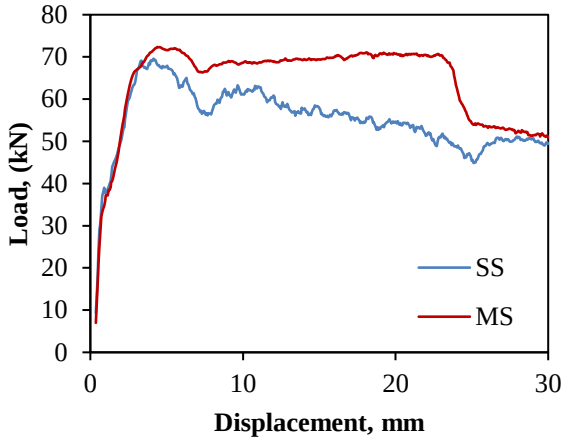
The load deformation response of MS and SS reinforced beams developed with three different concrete grades is generated as part of the parametric analysis using the numerical models shown in **Figure 9** (a), (b), and (c). The statistics show that stainless steel has equivalent or larger peak loads than mild steel. At 30 MPa concrete strength, MS has a greater peak load than SS. This is owing to the fact that the findings are dependent on concrete modelling and confinement. When the beam was modelled, the connection between concrete and stainless steel was not adequately characterized. This resulted in a minor divergence. This could possibly be related to the fact that stainless steel reinforced beams break earlier due to high ductility cracking strain, which occurs before the ultimate strength of SS.




(a)




(b)




(c)

**Figure 9:** Comparison of Load - Load-displacement responses SS and MS reinforced concrete beams with (a) 30, (b) 40, and (c) 50 MPa Concrete Strength.

In **Table 8**, the peak loads for MS reinforced concrete beams and SS reinforced concrete beams with varying concrete grades are tabulated. From this table, it is observed that SS reinforced beams show a greater load-carrying capacity than mild steel reinforced beams.

**Table 8:** Peak Loads for MS reinforced concrete beam vs. SS reinforced concrete beam with varying concrete grade

| Concrete Strength (MPa) | Peak Load (SS bar) (kN) | Peak Load (MS bar) (kN) |
|---|---|---|
| 30 | 68.58 | 70.95 |
| 40 | 74.89 | 71.37 |
| 50 | 72.61 | 72.85 |

## 4. CONCLUSIONS

In this study, the finite element technique was used to analyze the flexural response of concrete beams reinforced stainless steel. Numerical models were evaluated against experimental data for both MS and SS. The influence of the concrete grade on the flexural response was also observed using numerical simulations. Based on the analyses, the following conclusions can be derived:

1. The numerical model for mild steel reinforced concrete beams demonstrated good agreement with the test results claimed by Saatci (2007), with an accuracy of 98.58% in predicting ultimate flexural capacity. In the instance of a mild steel reinforced concrete beam, the peak value of the numerical analysis is 0.48% higher than the experimental result. In contrast, the initial stiffness of numerical analysis is greater. This is because geometric nonlinearities were not incorporated, as well as certain test setup shortcomings.
2. In the case of stainless steel reinforced concrete beams, the numerical models also predicted the ultimate load quite precisely with an accuracy of 99.32%. However, the initial stiffness of the experimental analysis was found to be lower due to test setup shortcomings.
3. In the instance of SS reinforced concrete beams with variable concrete strength, peak values, stiffness, and ductility were accurately predicted and proved to be almost identical for all B30, B40, and B50 concrete strengths. This is because flexural failure occurs at the reinforcing ends; therefore, increasing concrete strength does not improve the flexural capacity of beams.
4. In comparison with the SS reinforced concrete beam and the MS reinforced concrete beam with 30 and 40 MPa concrete, the ductility of the SS reinforced concrete beam was found to be higher than the conventional MS rebar.
5. The validated model prepared in this study can provide the basis for subsequent experimental and numerical studies planned by the authors on the properties of concrete reinforced with stainless steel rebars.

## ACKNOWLEDGMENTS

The authors gratefully recognize the support provided by the Concrete lab and the Structural Mechanics lab of the Civil Engineering department of MIST during the preparation and testing of the experimentally investigated beams.

## DATA AVAILABILITY STATEMENT

Datasets generated during the current study are available from the corresponding author upon reasonable request.

## FUNDING DECLARATION

This research was self-funded.

## ETHICS APPROVAL

This study is an engineering experimental investigation. The MIJST Research Ethics Committee has confirmed that formal ethical approval was not required.

## ETHICS, CONSENT TO PARTICIPATE, AND CONSENT TO PUBLISH

Not applicable.

## COMPETING INTERESTS

The authors declare that they have no competing interests.

## AUTHOR CONTRIBUTIONS

Author 1: Nusrat Tabassum - Writing: Original draft, Formal analysis, Software, Validation

Author 2: Abdullah Al Moneim - Writing: Review and editing, Visualization

Author 3: Aziz Ahmed - Writing: Review and editing

Author 4: Khondaker Sakil Ahmed - Writing: Review and editing, Supervision

## ARTIFICIAL INTELLIGENCE ASSISTANCE STATEMENT

Portions of this manuscript were assisted by an artificial intelligence language model (ChatGPT, OpenAI). The tool was used solely for language editing, text refinement, and clarity improvement. All content, data interpretation, analysis, conclusions, and final decisions were generated, verified, and approved by the authors. The authors take full responsibility for the accuracy and integrity of the manuscript.

## CONFLICT OF INTEREST DECLARATION

The authors declare that they have no conflicts of interest.

## REFERENCES

Adhikary, S. D., Li, B., & Fujikake, K. (2012). Dynamic behavior of reinforced concrete beams under varying rates of concentrated loading. *International Journal of Impact Engineering*, *47*, 24-38.

Ahmed, K. S., Habib, M. A., & Asef, M. F. (2021). *Flexural response of stainless steel reinforced concrete beam.* Paper presented at the Structures.

Baddoo, N. (2008). Stainless steel in construction: A review of research, applications, challenges and opportunities. *Journal of constructional steel research*, *64*(11), 1199-1206.

Barros, J. A., & Fortes, A. (2005). Flexural strengthening of concrete beams with CFRP laminates bonded into slits. *Cement and Concrete Composites*, *27*(4), 471-480.

Corradi, M., Di Schino, A., Borri, A., & Rufini, R. (2018). A review of the use of stainless steel for masonry repair and reinforcement. *Construction and Building Materials*, *181*, 335-346.

Farzana, K., & Ahmed, K. (2020). *Performance based seismic analysis of stainless steel reinforced concrete bridge pier using damping ductility relationship.* Paper presented at the IABSE-JSCE Joint Conference on Advances in Bridge Engineering-IV August.

Fu, X., & Chung, D. (1997). Effect of corrosion on the bond between concrete and steel rebar. *Cement and Concrete Research*, *27*(12), 1811-1815.

Gardner, L. (2005). The use of stainless steel in structures. *Progress in Structural Engineering and Materials*, *7*(2), 45-55.

Gedge, G. (2008). Structural uses of stainless steel—buildings and civil engineering. *Journal of constructional steel research*, *64*(11), 1194-1198.

Hafezolghorani, M., Hejazi, F., Vaghei, R., Jaafar, M. S. B., & Karimzade, K. (2017). Simplified damage plasticity model for concrete. *Structural engineering international*, *27*(1), 68-78.

Kapasny, L., & Zembo, S. (1993). *The influence of the reinforcement corrosion on the load-bearing capacity of the reinforced concrete structures.* Paper presented at the Proc. Int. Conf. RILEM. Bratislava.

Rossi, B. (2014). Discussion on the use of stainless steel in constructions in view of sustainability. *Thin-Walled Structures*, *83*, 182-189.

Saatci, S., & Vecchio, F. J. (2009). Effects of shear mechanisms on impact behavior of reinforced concrete beams. *ACI structural Journal*, *106*(1), 78.

Saraswathy, V., & Song, H. W. (2005). Performance of galvanized and stainless steel rebars in concrete under macrocell corrosion conditions. *Materials and Corrosion*, *56*(10), 685-691.

MIJST
MIST International Journal of Science and Technology

# Decentralized LRM System Architecture with Biometric Authentication and Digital Certificate Verification through Blockchain Technology

**Shakil Mosharrof[1], Farhan Nasif Nizami[1], Mahdi Mohtasim[1], Mahdi Adib[1], M. Akhtaruzzaman[*2], Md Shofiqul Islam[3], Muhammad Towfiqur Rahman[4], and Hosney Jahan[5]**

[1]Department of Computer Science and Engineering, Military Institute of Science and Technology, Dhaka, Bangladesh
[2]Department of Computer Science and Engineering, Daffodil International University, Savar, Dhake-1216, Bangladesh
[3]Institute for Intelligent Systems Research and Innovation (IISRI), Deakin University, Warun Ponds, Victoria, Australia
[4]Department of Computer Science and Engineering, University of Asia Pacific (UAP), Dhaka, Bangladesh
[5]Department of Computer Science and Engineering, East West University, Aftabnagar, Dhaka-1212, Bangladesh

***Corresponding Email:** *akhtaruzzaman.cse@diu.edu.bd*

**ARTICLE INFO**

**Article History:**

*Received: 11th April 2025*
*Revised: 29th October 2025*
*Accepted: 03rd November 2025*
*Published:30th December 2025*

**Keywords**:

*Blockchain-based LRM,*
*Land record management,*
*Ethereum,*
*Biometric,*
*Fingerprint authentication,*
*Smart-contracts,*
*Decentralized architecture*

**ABSTRACT**

Managing land records is a fundamental duty of a government, ensuring the accuracy, consistency, integrity of ownership, and reliable transaction of data. Conventional paper-based or centralized digital technology-based land record systems are unable to hold the system trust, efficiency, and consistency, thus mostly demonstrate errors, fraud, and corruptions. On the other hand, blockchain technology presents a transformative solution. It offers transparent, tamper-proof, secure, and reliable approach for Land Record Management (LRM) system. In this study a blockchain-driven LRM system architecture with distributed ledger technology is presented. The proposed strategy enhances security and trust by ensuring transparency, acceptance, and accountability. The study also designs the smart-contracts algorithm in detail that facilitates land registration, ownership transfers, verification, and streamlining processes. The proposed architecture ensures automated functionalities with little human intervention, uplifting the system security. Moreover, the proposed blockchain architecture integrates finger-print biometric authentication that boosts the system strength in terms of security through identity verification. This mitigates the risks of errors, fraud, illegal modification, and unauthorized access. This article outlines a blockchain-based LRM framework and verified through implementation and testing, reflecting the potentiality of viable adoption of this advanced technology.

This work is licensed under a *Creative Commons Attribution-Non-commercial 4.0 International License.*

## 1. INTRODUCTION

Land ownership records and registry are one of the common and essential activities for a society. Traditional centralized land registry and management is mostly overwhelmed with opaqueness, inefficiency, unauthorized transactions, and identity falsification, which often result in property disputes, financial losses, erosion of property rights, and sometimes life threatens. Such consequences not only affect legitimate landowners, but also exacerbates socio-economic inequalities. To address these issues, modern technology-based well-architecture system is undoubtedly essential to ensure a secure, transparent, equitable, and reliable conduction of these important activities.

Promising solution to the structural and functional insufficiencies of the existing LRM system can be proposed through decentralized networks (*Hasan, Alam, and Tanha, 2022*). Blockchain technology has the decentralized and unalterable nature and sufficient to ensure the secure, transparent, trustworthy management of land documents and records (*Beuria et al., 2020; Singh et al., 2020*). Cryptographic validation of the technology ensures the integrity of record transactions, resistant to fraudulent and unauthorized access (*Bouraga, 2025*). Moreover, the smart-contract algorithm of the blockchain network ensures seamless functionalities of land registry workflow, automating traditional processes of deed authentication, transferring title, performing registration, etc. (*Nandi et al., 2020*). The integration of biometric authentication; for example, finger-print verification, facial recognition, iris scans, etc.; in the blockchain-based distributed LRM boosts and reinforces the trust in managing property transactions (*Aquib et al., 2020*). Traditional verification is vulnerable to manipulation (*Khan et al., 2020*), while biometric

authentication-based decentralized immutable architecture of the technology ensures super secure framework for access control and transaction verification.

To enhance transparency, security, and automation in LRM process, this manuscript presents a blockchain network-based LRM system framework with detail design of smart-contracts algorithm. By conducting a comprehensive analysis, the study identifies existing gaps and key challenges that leads to inefficiencies and security vulnerabilities in the traditional land registry models. The key contribution of this study is to propose a decentralized LRM system architectural workflow encapsulating cryptographic security, smart-contracts algorithm, consensus mechanisms, and fingerprint based biometric authentication within a decentralized network of blockchain technology. The study also implements the proposed architecture and examines the prototype through testing and result analysis, reflecting a resilient, tamper-proof, and efficient LRM system. Advanced registration, reliable owner transfer, immutable audit, and robust access control are the significant features of the proposed framework.

## 2. RELATED WORKS

Now a days, blockchain applications are lingering beyond the digital currencies with smart-contract enabled systems influencing various domains including the LRM. Among several attempts over the last decade, Bangladesh launched the first digital LRM system in 2011 as a pilot project (*Hasan, Alam, and Tanha, 2022*). Even with some advancements, the project is still not mature enough to be a completely successful digitization endeavor. While online application submissions continue to be the major method of digital contact, current initiatives are mostly focused on digitizing archive materials, like Manchitra (maps), Khatiyan (ledger), and daag number (serial number) (*Hasan, Alam, and Tanha, 2022*). A double layer hybrid blockchain structure was also proposed in the country where Ethereum smart-contacts was incorporated to improve transparency, synchronization, and accessibility in land record management. A study conducted by Beuria et al. (*Beuria et al., 2020*) highlighted the decentralized architecture of blockchain network. The study emphasized the role of distributed automated ledger mechanism to record the transactions across multiple nodes to confirm any changes with permission from all the dependent blocks. The integrity and security of land register systems are reinforced by this unalterable structure.

Various approaches including formal verification, runtime monitoring, static analysis, etc. were explored in a study conducted by Singh et al. (*Singh et al., 2020*). The authors tried to improve contract reliability by formulating the blockchain smart-contracts to overcome the security vulnerabilities. Key challenges like scalability, correctness, and the evolving nature of the blockchain network were also emphasized in this study with some important directions like interdisciplinary research in developing a robust and secured framework for smart-contracts.

Another study by Nandi et al. *(Nandi et al., 2020)* analyzed the uses of Ethereum in blockchain-based systems, demonstrating its relatively low transaction processing time, making it viable for real-life applications. The research also highlighted the vulnerabilities of traditional database systems in maintaining records, highlighting their susceptibility to security breaches. Additionally, the study found that implementing blockchain would cost individuals only $0.36 per transaction, which is about thousand times less than the cost of the conventional system in India. However, the fluctuating nature of Ethereum gas fees shows uncertainty in transaction costs, posing a challenge to the consistent pricing.

*Aquib et al. (2020)* proposed three key stakeholders, the Registrar Department, the Revenue Department, and National Database and Registration Authority (NADRA), to collect data from both buyers and sellers and submit it to the blockchain system, creating an immutable ledger that cannot be modified or altered without authorization. The study suggested a private blockchain architecture for LRM in Pakistan to address the limitations of existing systems. Integration of the registrar, revenue, and national ID departments was the aim of the proposed system to modernize the workflows. To demonstrate the system feasibility, the prototype was implemented on Hyperledger. However, the study failed to address the challenges of scalability and viability of practical adoption. Another recent study conducted by *Khan et al., (2020)* emphasized the advantages of blockchain technology in providing unalterable land records without proper validation and authentication. The study recommended to include cryptocurrency-based land asset liquidation features.

A certificate verification system on blockchain-based network was studied by Suganthe et al. (*Suganthe et al., 2021*) where Ethereum platform with smart-contracts was used. Pereira et al. (*2021*) also introduced similar architectural framework based on blockchain network for land administration in Bangladesh. The architecture accumulated the blockchain features with the functionalities of the Land Administration Systems (LAS) through testing based on an Ethereum prototype with smart-contracts. However, their evaluation was limited to simulations, lacking real-life adoption of the system. Sen, Mukhopadhyay, and Karforma (*2021*) presented a blockchain system for property registration that integrates government entities as peers and utilizes smart contracts for the execution of transactions. The performance evaluation was conducted on Hyperledger Fabric, focused on latency and throughput metrics. Sahai, and Pandey (*2020*) also proposed a blockchain-based framework for land registration that employed smart contracts written in Solidity to automate registration and transfer transactions. They established the process by developing a sample decentralized application called DApp.

Through the above literature studies, it is evident that a sever attempts on designing blockchain-based land registry system framework were conducted. At this stage, it is imperative to determine the gaps of the current focus in improving the advanced framework of the distributed land registry management system based on the blockchain network. A structured summary of the studied literatures is presented in Table 1.

The proposed system architecture presented in this study aims to develop a blockchain-based framework for land registry management systems that enhances transparency, trust, predictive capabilities, reliability, control, security, cost-efficiency, and ease to access. Integration of blockchain features, such as immutability, decentralization, and consensus mechanisms into land registry operations, the proposed framework ensures that all nodes maintain a consistent, verifiable record of land transactions, accessible anytime anywhere. Smart contracts automate the processes like ownership transfer and access control through multi-party authorization. Furthermore, storing historical transaction data enhances predictive analytics, while data duplication across nodes boosts the reliability of the system. The biometric verification and certificate scanning subsystem further strengthens the security, transparency, reliability, and trust. Consensus mechanisms improve control eliminating the need for third-party involvement, while encryption and multi-node storage boost security. The decentralization nature of the system facilitates quick and easy access of land records by the users. Ultimately, the goal is to create a blockchain-based system that provides significant advantages in land administration, such as increased transparency, trust, security, and efficiency.

**Table 1:** Finding the gaps of the studied literatures

| Ref. | Objectives | Outcomes | Limitations |
|---|---|---|---|
| ***Hasan, Alam, and Tanha, (2022)*** | To implement blockchain for LRM in Bangladesh. | Prototype developed using Ethereum for transparency and accessibility. | The project has not reached full maturity. |
| ***Beuria et al., (2020)*** | To highlight decentralized nature of and its role in securing LRM. | Blockchain provides immutable records, improving security and integrity in land registry systems. | No direct application to LRM, focus on blockchain technical nature. |
| ***Singh et al., (2020)*** | To formalize blockchain smart contracts to mitigate vulnerabilities. | Explored formal verification, runtime monitoring, and static analysis to ensure contract reliability. | Challenges in scalability, correctness, and the evolving nature of blockchain. |
| ***Nandi et al., (2020)*** | To evaluate Ethereum for real-world blockchain applications in land records. | Low transaction processing time, making Ethereum suitable for real-world applications. | Ethereum's fluctuating gas fees introduce uncertainty in transaction costs. |
| ***Aquib et al., (2020)*** | To propose a private blockchain architecture for LRM in Pakistan. | Integration of departments like the Registrar, Revenue, and NADRA, using blockchain to create an immutable ledger. | Scalability and real-world adoption challenges remain unaddressed. |
| ***Khan et al., (2020)*** | To explore benefits of blockchain for immutable LRM | A cost-effective solution, with blockchain providing a secure and efficient LRM system. | Lack of detailed implementation or practical deployment. |
| ***Suganthe et al., (2021)*** | To implement a blockchain-based certificate verification system. | Ethereum-based smart contract system for secure and efficient certificate verification. | Limited to certificate verification, not directly related to land records. |
| ***Pereira et al., (2021)*** | To develop an architecture for land administration in Bangladesh. | Ethereum prototype tested for smart contract-based land registration and verification. | Simulated evaluation, no real-world adoption studies. |
| ***Sen, Mukhopadhyay, and Karforma, (2021)*** | To create a blockchain system for property registration with government. | Smart contracts for transaction execution and government entities, evaluated on Hyperledger Fabric for latency and throughput. | Limited evaluation focused on performance metrics, no real-world deployment. |
| **Sahai, and Pandey (*2020*)** | To develop a blockchain framework for LRM with smart contracts in Solidity. | A DApp demonstrated for automating registration and transfer transactions using smart contracts. | Limited scope, no real-world adoption or comprehensive evaluation beyond DApp demonstration. |

## 3. THEORETICAL BACKGROUND

### 3.1 Blockchain Technology and Use Cases

Blockchain technology, a distributed ledger system, was first proposed in 2008. Its primary goal was to enhance security through decentralization of data while creating a comprehensive global index (*Jesus et al., 2018*). Each blockchain consists of multiple blocks, containing a header and a main body. The block header includes a timestamp, a random number (nonce), the current block number, the hash of the previous block, and other metadata (*Yin et al., 2018*). Moreover, the block body stores network data in the form of a Merkle tree. The conceptual diagram of Blockchain and its workflow are presented in Figure 1.

The framework of blockchain proposed by Sen, Mukhopadhyay, and Karforma (*2021*) was for property registration within e-governance systems. They highlighted the key advantages of blockchain technology, including data immutability, decentralization, and transparency, which address challenges in existing electronic property record systems, such as security risks, data integrity issues, and single points of failure. The framework leverages smart bcontracts and a permissioned blockchain network to facilitate secure and efficient property registration and information sharing among government agencies and stakeholders.

Thamrin *et al.* (*2021*) propose a Blockchain-based land certificate management system in Indonesia to address fraud, lack of transparency, and inefficiencies in the existing paper-based system. Their framework follows a three-phase approach, starting with a public blockchain, transitioning to a hybrid model, and ultimately implementing a fully integrated hybrid blockchain. They also present a detailed blueprint for developing smart contracts for the public blockchain phase using Ethereum.

Smart-contracts are independent programs embedded in a blockchain that automatically execute and enforce agreements once predefined conditions are met. By removing the need for intermediaries, they enhance security, transparency, and resistance to tampering, that ensures reliable and efficient transactions (*Buterin et al., 2014; Khan et al., 2020; Khan et al., 2021*). They facilitate network automation and the seamless transition from paper contracts to digital ones. Unlike traditional contracts, smart contracts

encode agreements into codes, confirming trust through automated transactions without central oversight (*Singh et al., 2020; Singh et al., 2022*). To prevent manipulation, the blockchain network replicates the smart contracts among all nodes. In the blockchain platform, smart contracts can reduce human errors and contract disputes. Sahai, and Pandey (*2020*) demonstrated a comprehensive analysis of blockchain and smart-contract applications for property registration system in India addressing the key challenges, including lack of transparency, accountability, and delays.

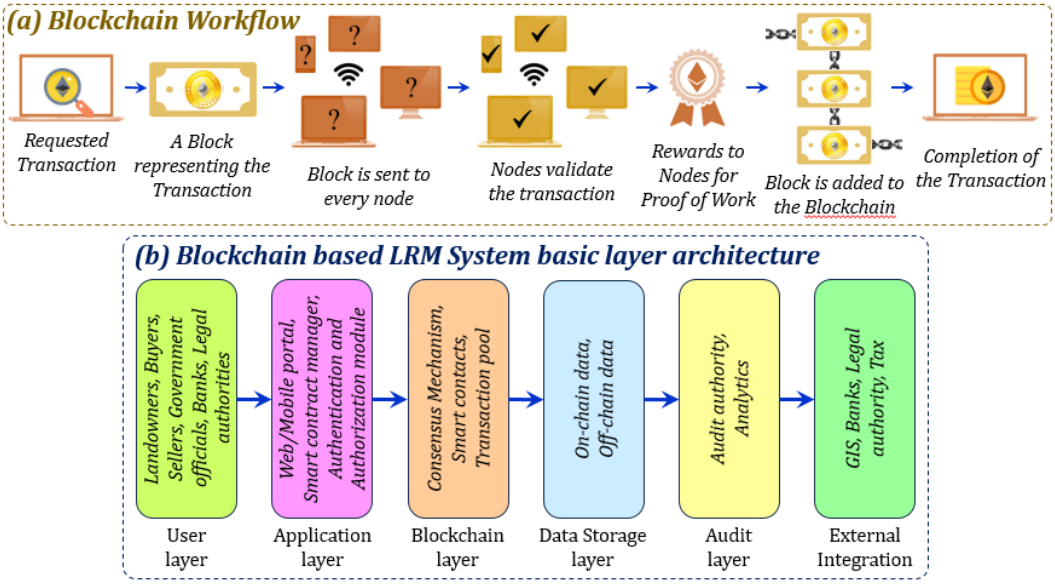



**Figure 1:** Conceptual architecture of Blockchain workflow and Blockchain based LRM system layers

### 3.2 IoT integration with blockchain network

With the ability to handle unauthorized access and privacy issues, blockchain technology can eradicate Internet of Things (IoT) security problems. The aim of the relevant research is to enhance decentralization, simplify interactions, and enable autonomous coordination among IoT devices (*Jesus et al., 2018; Kollu et al., 2022*). Furthermore, blockchain integration may be able to successfully encounter the Stalker Attack, which is recognized as one of the common dangers to any IoT setup.

Blockchain is often recognized for its effectiveness in minimizing the distributed denial of service (DDoS) attacks within the IoT networks. However, some studies have examined existing limitations of blockchain-based systems in rebutting the DDoS threats (*Beuria et al., 2020*). At the same time, some have proposed possible solutions to the security and privacy challenges in IoT interconnections integrated with blockchain technology (*Mohanta et al., 2020*). Along with privacy issues pertaining to data collection and processing in IoT applications, the study examined a number of security threats, including replay, node capture, and man-in-the-middle attacks.

Blockchain helps in developing safe and dependable IoT network especially for memory and power supply management (*Reyna et al., 2018*). At the same time, Dorri, Kanhere, and Jurdak, (*2017*) have seen some additional downsides, like resource restrictions, centralization issues, and maintaining user privacy for data exchange, of a traditional IoT network setup. The authors delineated that the decentralized nature, concealment, and security features make the system promising to overcome the challenges in IoT based systems.

### 3.3 Blockchain with Authentication Systems

Authentication-based systems are evolving with advancements in blockchain technology, decentralized applications, and edge computing. Padrón Núñez (*2021*) examined the legal implications of key platform components, including biometric sensors, OLED displays, and NodeMCU development kits, alongside the Ethereum blockchain, smart contracts, and IPFS. The study proposed a biometric-based work attendance tracking and logging system leveraging blockchain technology. Moreover, quantum-resistant transaction authentication mechanism can be integrated into blockchain systems to eliminate threats from quantum computing (*Yin et al., 2018; Acquah et al., 2020*). This approach employs lattice-based cryptography to improve the security of digital signatures while maintaining efficiency. In solving the tiny integer problem, the bonsai-tree technology based lightweight, non-deterministic wallets with safe proof were designed. Outcomes of the study supported the post-quantum cryptography techniques for the blockchain network architecture, ensuring long-term robustness and safety.

Fingerprint profile protection would enhance safety if the profile is encrypted and stored as a decentralized manner ensuring data integrity and immutability. This can be achieved through blockchain as the technology offers recording of encrypted template hashes. A blockchain application for e-voting system with fingerprint-based biometric authentication was studied by Ibrahim et al. (*2021*) proposing a secure voter verification system. The study reflected data integrity, transparency, access control, and data security, through a central node network-based authentication and transactions. Although, the research highlighted some challenges related to voter privacy,

scalability, and some issues on security risks, it identified some strategies to overcome those challenges.

Similarly, a decentralized biometric authentication system was studied by Lee and Jeong (*2021*) where they have demonstrated that the fragmented and distributes information of biometric signature across nodes truly minimizes the breach risks. The study also examined the performance overhead and scalability, comparing with the traditional methods. The outcomes of the research ensured the viability of the approach having minimal computational impact. It also highlighted the role of the blockchain network in securing the overall system through biometric authentication.

Biometric authentication methods offer significant advantages over password-based systems by providing enhanced security and convenience (*Jain, Bolle, and Pankanti, 2006; Pournaghi et al., 2018*). When a user places their fingerprint on the scanner, an optical sensor captures a digital image, from which distinct biometric features are extracted to generate a mathematical template. This template is then compared to stored templates to verify the user identity within predefined security thresholds, ensuring reliable and accurate authentication. To verify a certificate of land ownership on the blockchain, the certificate identifier or transaction number is required. This unique identifier of the certificate can be utilized as a verification system linked to the blockchain for land records. The verification system uses the certificate ID and retrieves the corresponding blockchain record. The blockchain record includes the land information, the owner's name, date of the transaction, document hashes, and khatiyan (ledger) hashes and daag numbers (serial number assigned to each plot of land). The system checks that the record is on the distributed ledger and that the land registry authority confirms the digital signature. The certificate is authentic and unaltered. The blockchain record also includes the original land certificate hash or digital identifier. This hash can be calculated independently from the displayed certificate document and compared to the hash recorded in the blockchain. This verifies the authenticity of the certificate document. After verifying the certificate's blockchain record and document hash, the system can validate that the presented certificate accurately identifies the land parcel's proprietor based on the blockchain land records.

## 4. DESIGN OF THE INITIAL MODULES

There are five modules or subsystems in the blockchain based Land Record System, as shown in Figure 2. The Stakeholder Management System holds and manages the necessary information about the stakeholders like identity, ownership, etc. The Fingerprint Module ensures that the fingerprints of the users are taken for verification and validation purposes. The Scanner Module converts the land record certificates into digital form and sends to the system. The Hash Generator module generates public and private hashes to identify blocks and transactions uniquely. The Nodes Management System of blockchain ensures the retrieval of the land record information from the blockchain and shown to the users. After each transaction, the system keeps adding nodes accordingly.

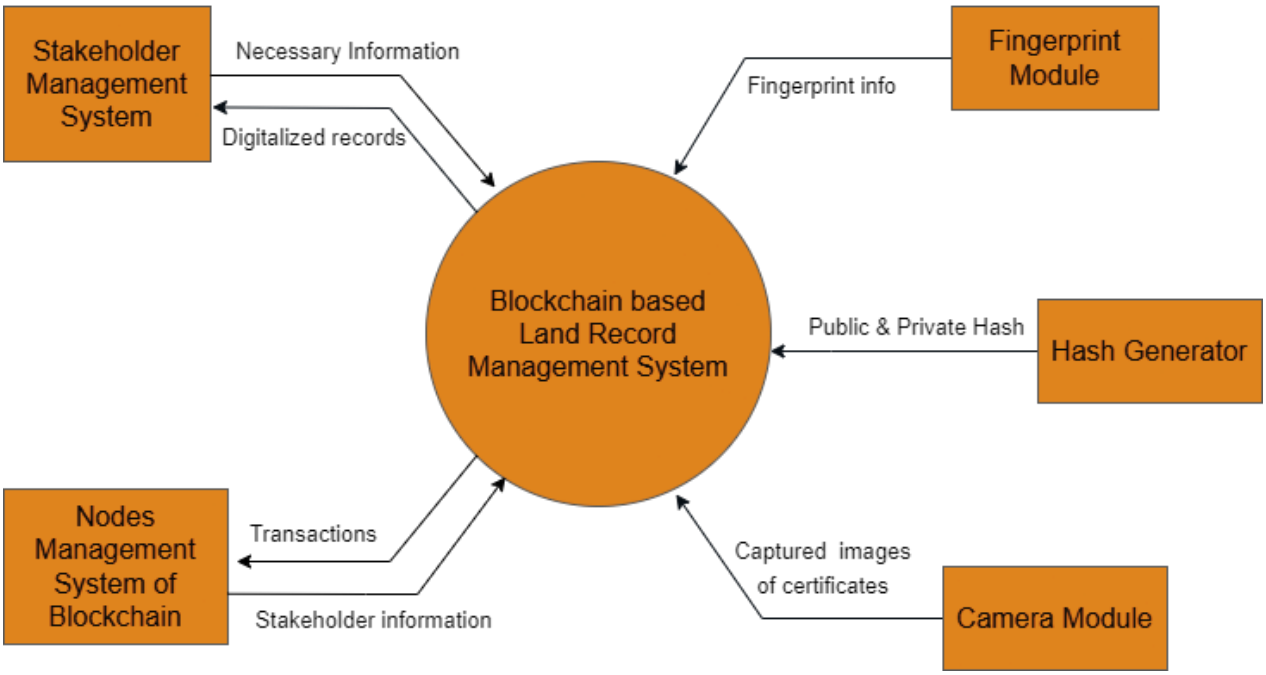



**Figure 2:** Five Subsystems of LRM System

The key features of the user panel are viewing and editing profiles, viewing Khatians, paying taxes, applying for tokens for land registration or ownership transfer, and viewing their transaction history. The user can sign using a valid National Identification (NID) and password if the user owns an account. Otherwise, the user needs to sign up using a valid NID through One-Time Password (OTP) verification. Then the user is able to update the basic information in the profile, apply for a new token for a new land registry or ownership transfer, pay taxes and necessary fees online, and view

certificates and Khatians. The user state diagram is demonstrated in Figure 3.

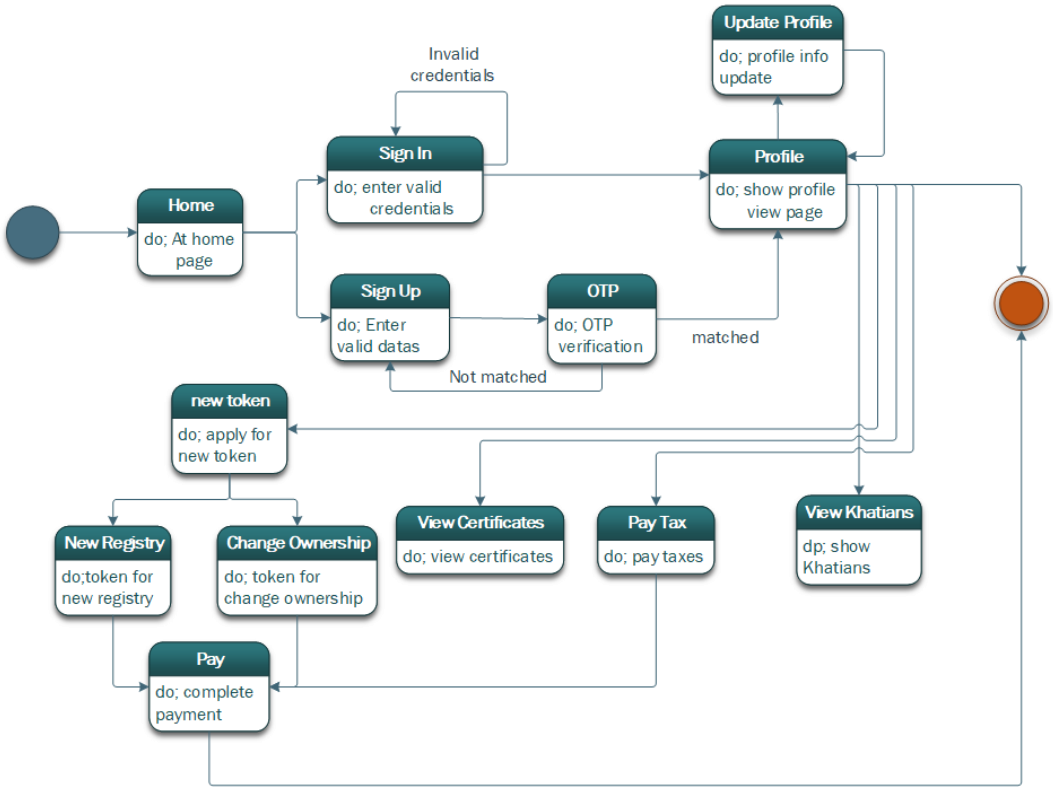



**Figure 3:** User State Diagram

The key features of the admin panel are verifying users through fingerprint data, uploading users' certificates, adding new Khatians, mutating previous Khatians, updating plot information, and viewing all transaction history. The admin can verify a new user by scanning his fingerprint data and saving it in the database. The certificates and the plot information are uploaded by the admin and the user is verified. The admin can perform the ownership update operation by validating all the new stakeholders, processing payment, and uploading the new Khatians. The admin can also view the history of the transactions. The admin state diagram is shown in Figure 4.

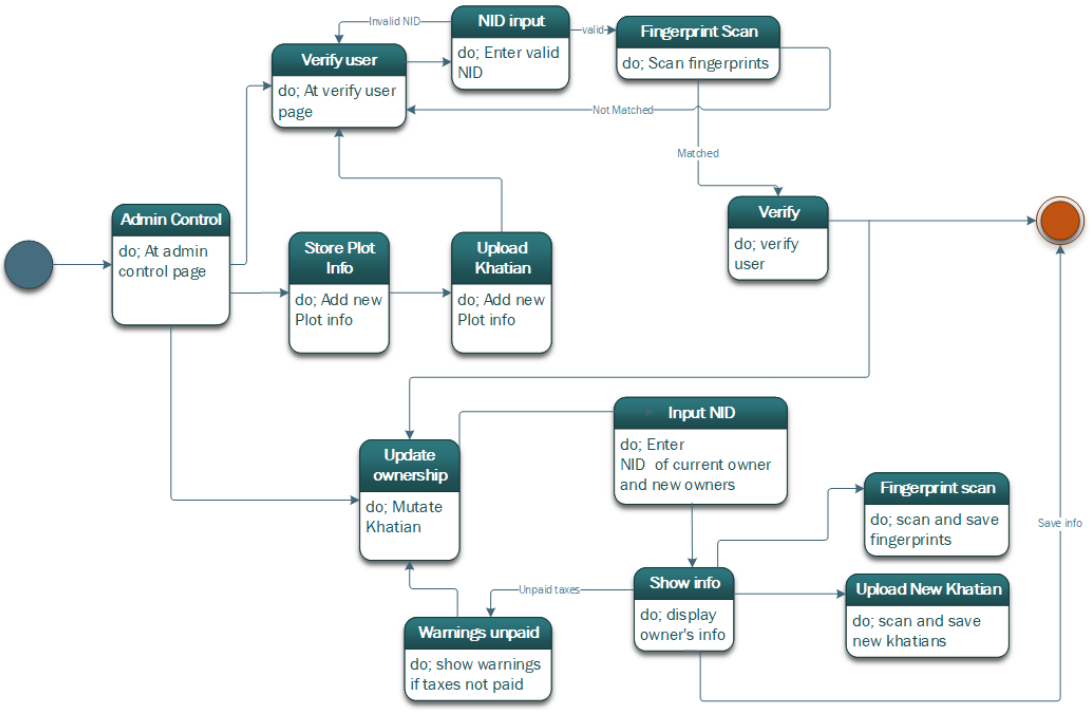



**Figure 4:** Admin State Diagram

The sequence diagrams of the user authentication system, fingerprint sensor, and scanner module demonstrate a detailed insight of user interactions with the authentication system, verification using fingerprint sensor, and scanning and uploading certificates. The user authentication sequence, shown in Figure 5, outlines the process of creation and authentication of a profile on the website. A user signs up and logs in with valid credentials. The system then guides them through entering additional profile information, storing it successfully, and allowing them to view their completed profile page. If login credentials are invalid, the system prompts the user to try again.

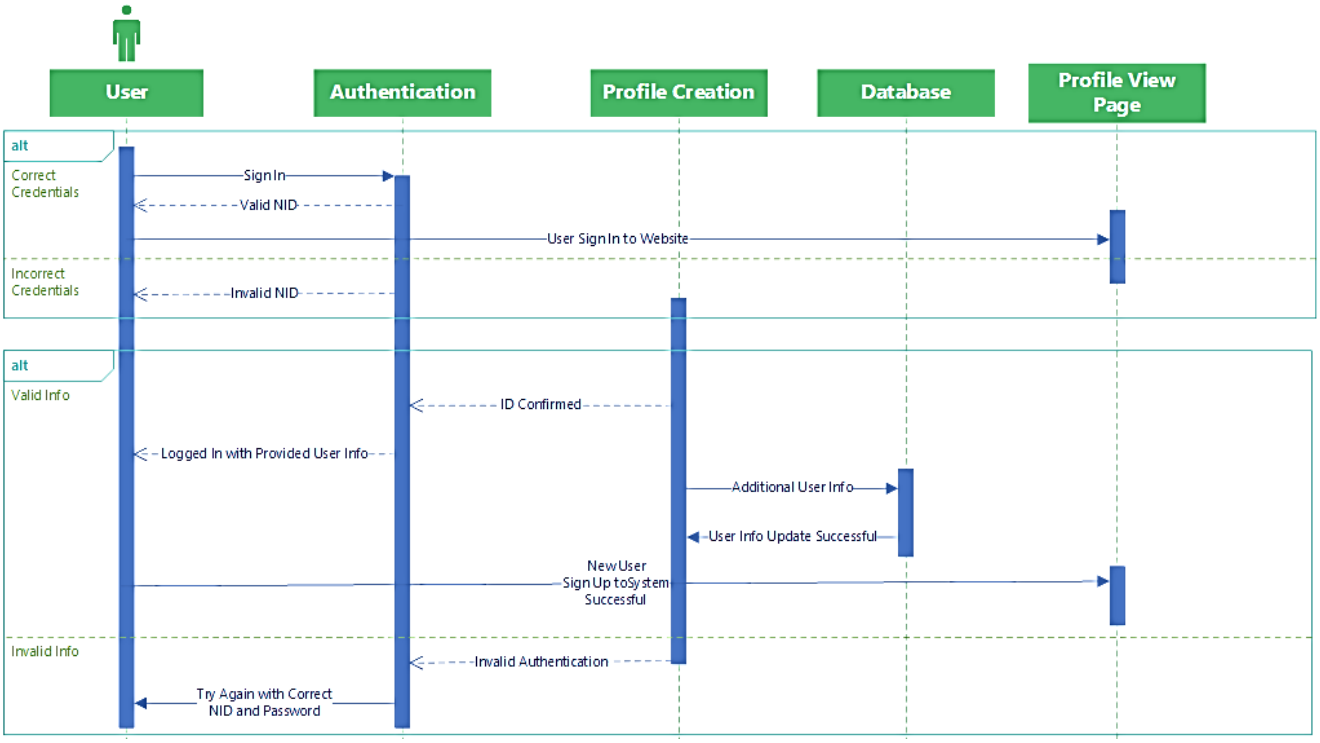



**Figure 5:** User Authentication Sequence

The fingerprint interaction sequence shows the enrolment process of a fingerprint. The user places their finger on the sensor twice. The sensor captures images of the fingerprint and stores them for future identification. Finally, the system returns a unique identifier associated with the enrolled fingerprint. The sequence diagram is presented in Figure 6.

The sequence diagram of the scanner module shows the process of scanning certificates and storing them into the database, potentially on a blockchain for safekeeping. The admin initiates the process through the inputs of certificates. A copy of the scanned data is uploaded to a blockchain for tamper-proof storage. The corresponding sequence diagram is depicted in Figure 7.

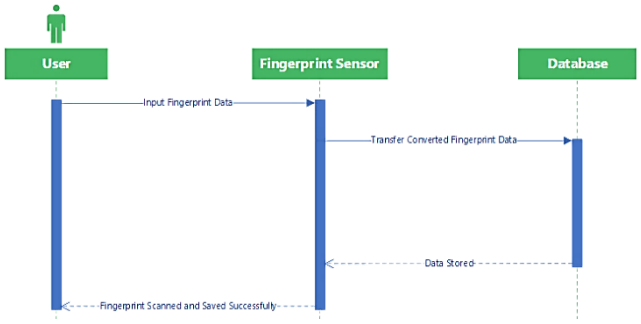



**Figure 6:** Fingerprint Sensor Interaction

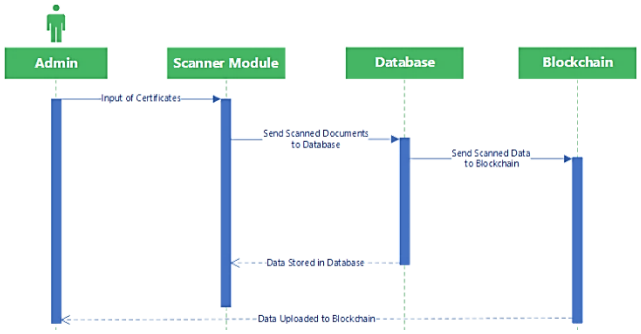



**Figure 7:** Scanner Module Interaction

## 5. DESIGN OF THE PROPOSED ARCHITECTURE

The proposed LRM system is based on blockchain technology which is designed to handle various challenges that arise while managing the land registry and records. This proposed architecture includes various tasks, like authentic registration, reliable transfer of property ownership, production of certificates, etc. The overall architectural workflow diagram is presented in Figure 8.

Initially, landowners begin the procedures of registering their lands within the system by providing their identity and relevant information regarding ownership. Blockchain then stores the information within its distributed network system, establishing a permanent and secure data repository of land ownership.

During the ownership transfer process, the owners complete the registration with the submission of their identification and ownership information to the system. Subsequently, the

system transfers the ownership rights of the land to the newly designated owner, simultaneously updating the nodes on the blockchain. This process establishes a secure and immutable, yet easily accessible record of the transaction, ensuring the transparency of the transfer of ownership.

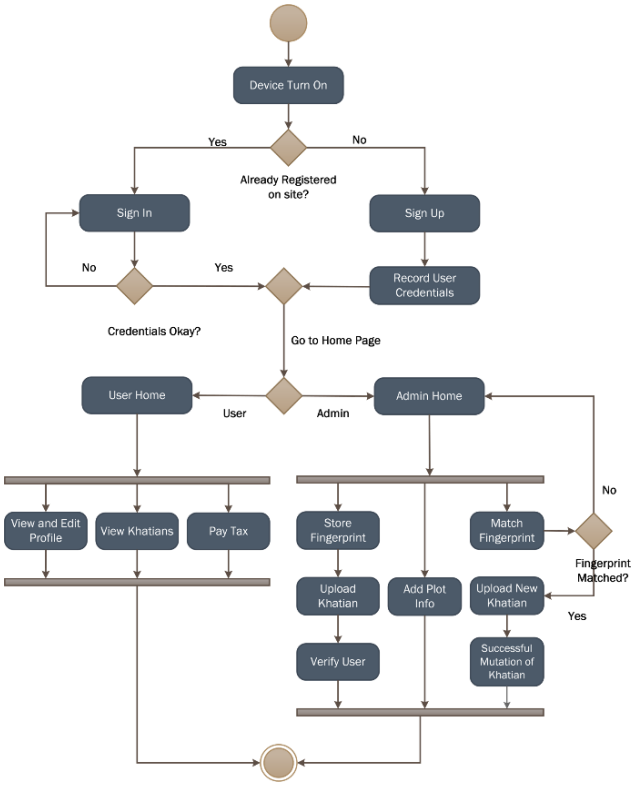



**Figure 8:** Overall architectural workflow of the proposed system

The system is able to produce certificates of land records and stores them securely in the blockchain node-network. Every user has permission to access these certificates. On the other hand, only the authorized users can allow and facilitate the retrieval of the records. The proposed system through the nodes of the blockchain verifies each transaction and guarantee its security and integrity.

The workflow diagram also explains the vital stages of the administration process of land records. It offers a well-defined practice for the land registration, ownership transfer, and protected storage of certificates. The proposed system offers two user options or types, general users and administrative users. The registered users without any administrative permission are considered as general users. They are able to conveniently view land certificates, transactions, and other information related to their own land records.

Access to the administrative users is restricted only to those who have the administrative access permission. These users are not only responsible for enrolling new users in the system, but also use the user ID and fingerprint for identification purposes. They are also responsible for storing and controlling data within the blockchain network as well as executing transactions as per the user requirements. Moreover, the administrator plays a key role in verifying user identity and validity while ensuring proper documentation of any changes.

## 6. INTEGRATION OF SYSTEM HARDWARE

Necessary hardware integration focuses on two key components, a JM-101 fingerprint reader and a LiDE-120 document scanner, which improves the system functionality and security. The fingerprint sensor confirms accurate user identification and verification by capturing fingerprints during registration and authentication. Software drivers and libraries facilitate continuous communication between the sensor and the system. The document scanner enables efficient scanning of land records and certificates. Custom software components were developed to manage scanning operations while ensuring data confidentiality and integrity. Figure 9 shows the basic hardware integration of the development and test environment setup. The JM-101 fingerprint module with Arduino-nano (*Akhtaruzzaman, 2021; Baki et al., 2023*) micro-controller is shown in Figure 10. Algorithm 1 is presenting the code-snippet of Biometric Authentication procedures.




**Figure 9:** Basic environment setup with necessary hardware connections

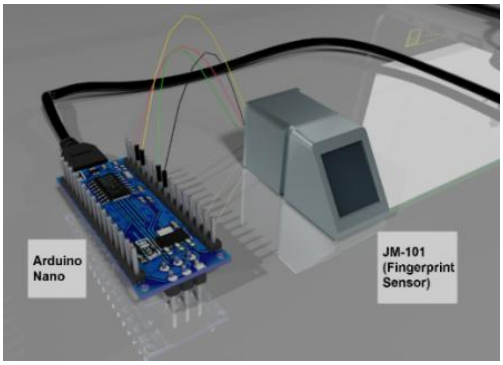



**Figure 10:** JM-101 Fingerprint Module integrated with Arduino-nano

**Algorithm 1: Biometric Authentication**

```
1: getFingerprintEnroll( ):
2: //Create an object of Adafruit Fingerprint
3: finger ← Adafruit Fingerprint(&mySerial)
4: // Give Fingerprint 1st time...
5: temp ← -1
6: while temp != FINGERPRINT_OK do
7:         temp ← finger.getImage()
8: end while
9: finger.image2Tz(1)
10: // Remove Finger...
11: temp ← 0
12: while temp != FINGERPRINT_NOFINGER do
```

```
    temp ← finger.getImage()
end while
// Give Fingerprint 2nd time...
temp ← -1
while temp != FINGERPRINT_OK do
    temp ← finger.getImage()
    finger.image2Tz(2)
end while
// Create and Store Model and return ID of fingerprint
finger.createModel()
finger.storeModel()
return finger.fingerID
Function getFingerprintID():
temp ← finger.getImage()
if temp != FINGERPRINT_OK then
    return -1
end if
temp ← finger.image2Tz()
if temp != FINGERPRINT_OK then
    return -1
end if
temp ← finger.fingerFastSearch()
if temp != FINGERPRINT_OK then
    return -1
end if
return finger.fingerID
```

## 7. ALGORITHM DESIGN AND IMPLEMENTATION

The proposed method for managing the land records registry is a solid foundation that will make the land registry safer and more open. Users can quickly sign up and create legal accounts, adding an additional layer of trust and speed to the LRM process. The user registration process is mainly a three steps process, Providing personal information, Fingerprint verification, and Document scanning.

In the first step, upon accessing the website of the system, individuals are directed through the initial registration procedure where the users are required to enter their personal information. Subsequently, they obtain an OTP by electronic mail. The One-Time Password acts as an essential security mechanism for the purpose of verifying user identities.

The second step is to ensure maximum security. It is necessary for individuals to undergo a verification process at their respective local land register office, whereby they are required to provide their fingerprints and land record certificates. A registrar administrator provides assistance to users. The system employs a matching algorithm to compare and save hexadecimal values derived from fingerprints, providing evidence of user identification. The verified fingerprints are securely stored on the blockchain. Example of fingerprint verification page is displayed in Figure 11.

Third step is required to present their land record certificates to the administrator for the purpose of scanning. The scanned copies are securely preserved within the database of the land registration office, therefore guaranteeing both the accessibility and integrity of crucial documents. An example scanned document is shown in Figure 12.

The user registration system architecture with blockchain attachment is demonstrated in Figure 13. The process algorithm is designed through necessary smart contact functions, as shown in the Algorithm 2.

The *uploadUserInfo()* function is a smart contract method that allows only authorized users to upload personal information linked to a unique NID. It accepts several parameters, including the NID, full name, parents' names, email, date of birth, fingerprint ID, and address. The function first verifies that only the contract owner can execute it and ensures the NID is not already registered to prevent duplicates. If both checks pass, it standardizes certain string inputs by converting them to uppercase and stores the data in a mapping structure indexed by the NID, using bytes32 for efficient blockchain storage. Finally, it marks the user as registered by setting a Boolean flag to true. The function's flowchart is shown in Figure 14.

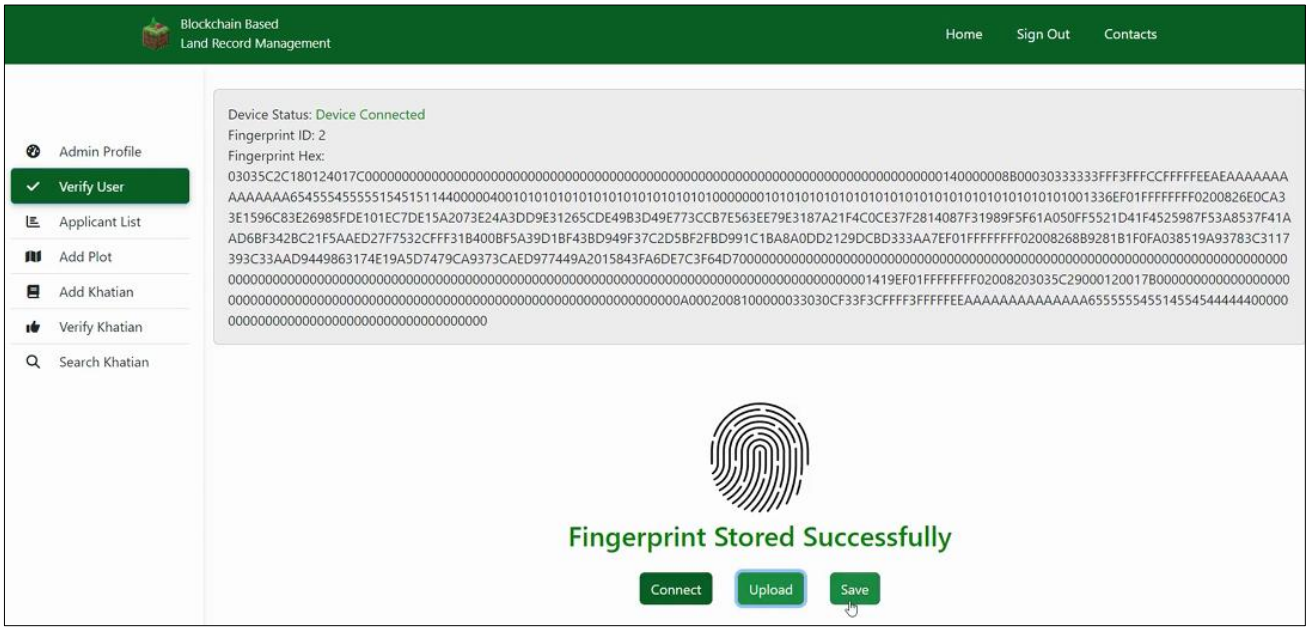
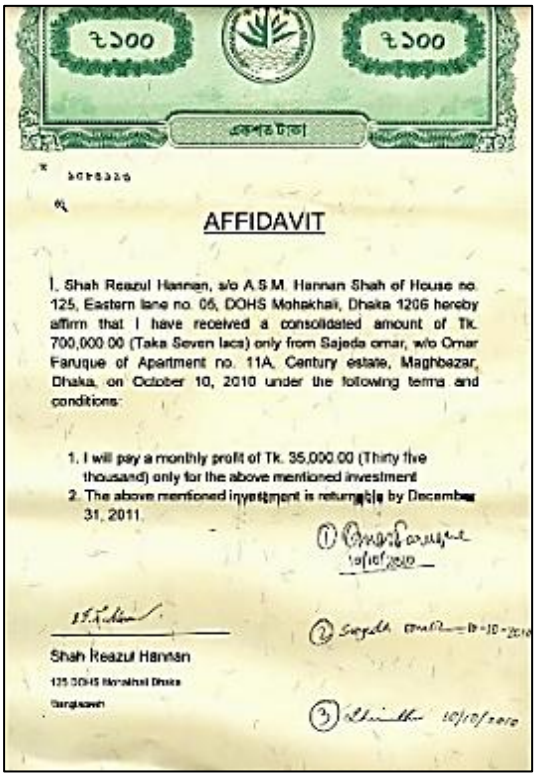



**Figure 11:** An example of fingerprint verification page



AFFIDAVIT

I, Shah Reazul Hannan, s/o A.S.M. Hannan Shah of House no. 125, Eastern lane no. 06, DOHS Mohakhali, Dhaka 1206 hereby affirm that I have received a consolidated amount of Tk. 700,000.00 (Taka Seven lacs) only from Sajeda omar, w/o Omar Faruque of Apartment no. 11A, Century estate, Maghbazar, Dhaka, on October 10, 2010 under the following terms and conditions:

1. I will pay a monthly profit of Tk. 35,000.00 (Thirty five thousand) only for the above mentioned investment
2. The above mentioned investment is returnable by December 31, 2011.

Shah Reazul Hannan

**Figure 12:** Sample of a scanned Certificate for uploading and verification

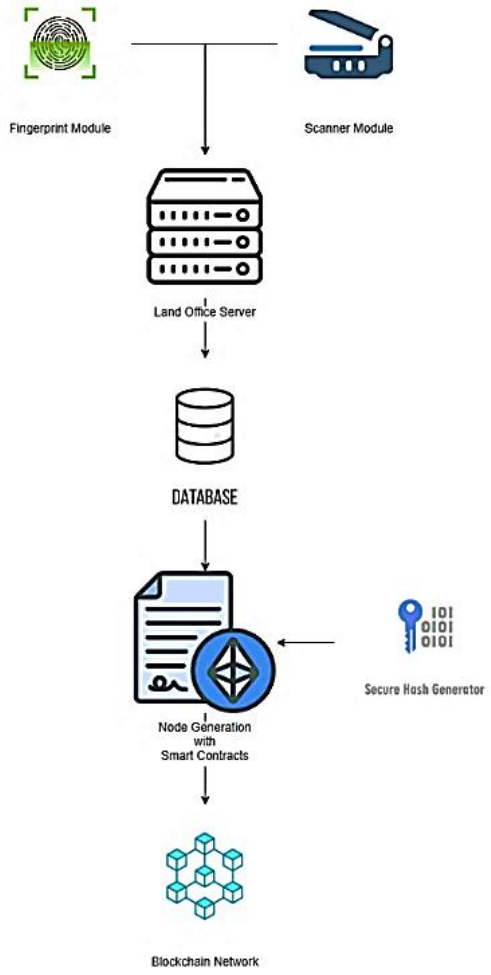



**Figure 13:** User registration system architecture

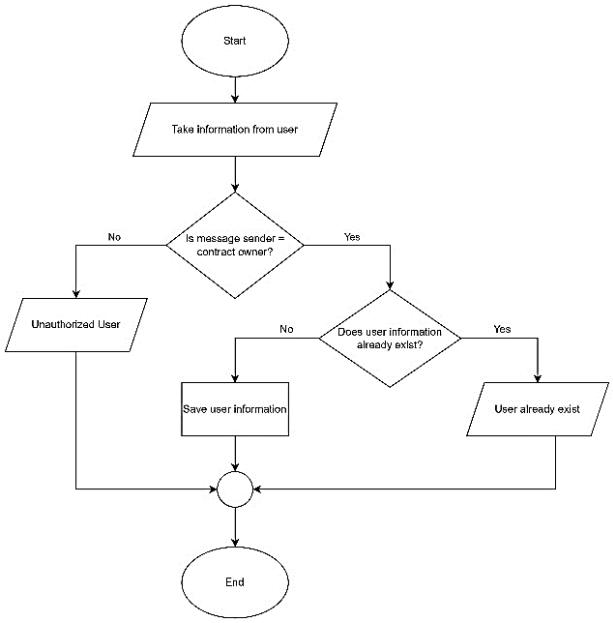



**Figure 14:** Flowchart of *uploadUserInfo( )* function

The *getUserInfo( )* function retrieves user information from the smart contract by querying the blockchain. It allows authorized users to access stored personal data linked to a specific NID if the user is registered. The function's flowchart is shown in Figure 15.

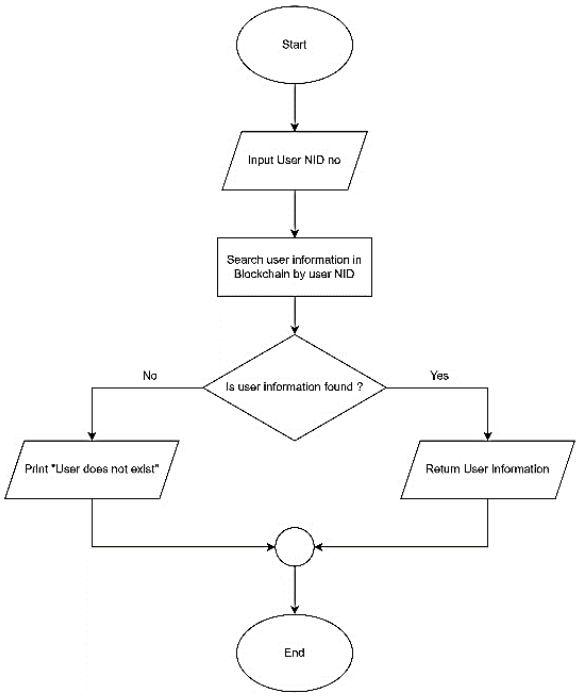



**Figure 15:** Flowchart of *getUserInfo( )* Function

The *addPlotInfo( )* function records plot details in the smart contract. It accepts parameters such as geographical location (Division, District, Thana), numeric identifiers (JLNo, plot number), plot type, and area. The function then generates a plot hash using the keccak256 algorithm for secure identification. The function first ensures that only the contract owner can add plots, reverting with an error if unauthorized. It then converts the Division, District, and Thana strings to uppercase. If the plot is not already

recorded, the function stores the provided details in the plot information mapping, using the plot hash as the key. The flowchart of the function is shown in Figure 16.

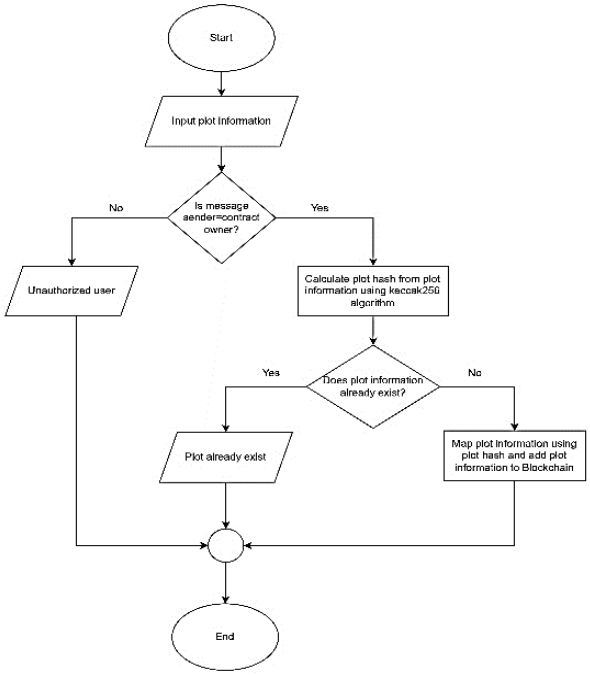



**Figure 16:** Flowchart of *addPlotInfo( )* Function

The *getPlotInfo( )* function retrieves plot details from the smart contract using a unique plot Hash. Before fetching the data, it verifies whether the plot exists. If not, it reverts with an error message. The function's flowchart is shown in Figure 17.

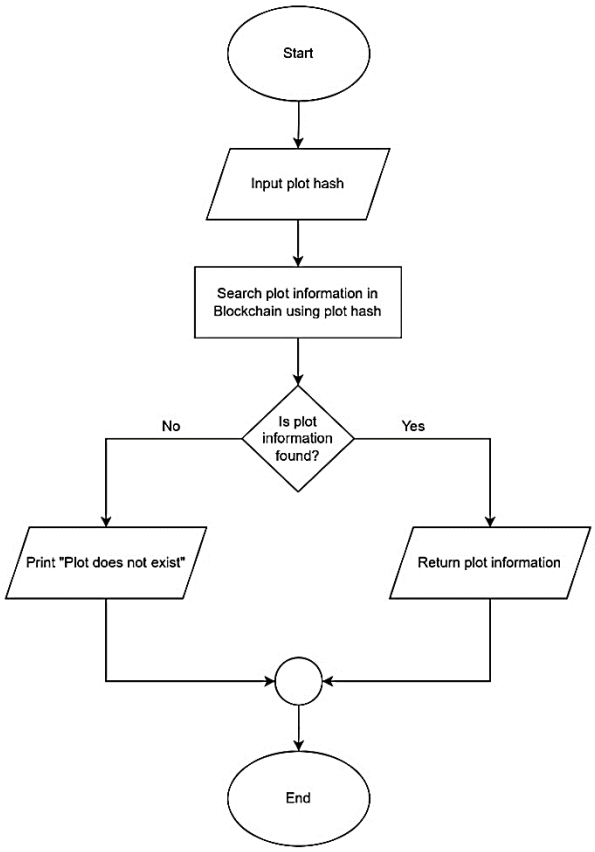



**Figure 17:** Flowchart of *getPlotInfo( )* Function

The *addNewKhatianInfo( )* function records khatian details in the smart contract. It accepts parameters such as khatian ID, plot hash, owner NIDs, land area, and ownership percentages. The function first ensures that only the contract owner can execute it. If the plot hash is valid, it generates a khatian hash using the keccak256 algorithm based on the plot hash and khatian ID. It then verifies that the khatian hash does not already exist and checks the validity of each owner's NID, converting them to bytes32 format. Finally, it stores the khatian details in the khatianInfo mapping, using the khatian hash as the key. The flowchart is shown in Figure 18.

The *addKhatianInfoFromOld( )* function is designed to add Khatian entries, similar to the *addNewKhatianInfo( )* function. However, this function includes additional functionality to handle the transfer or sale of land from one owner to another.

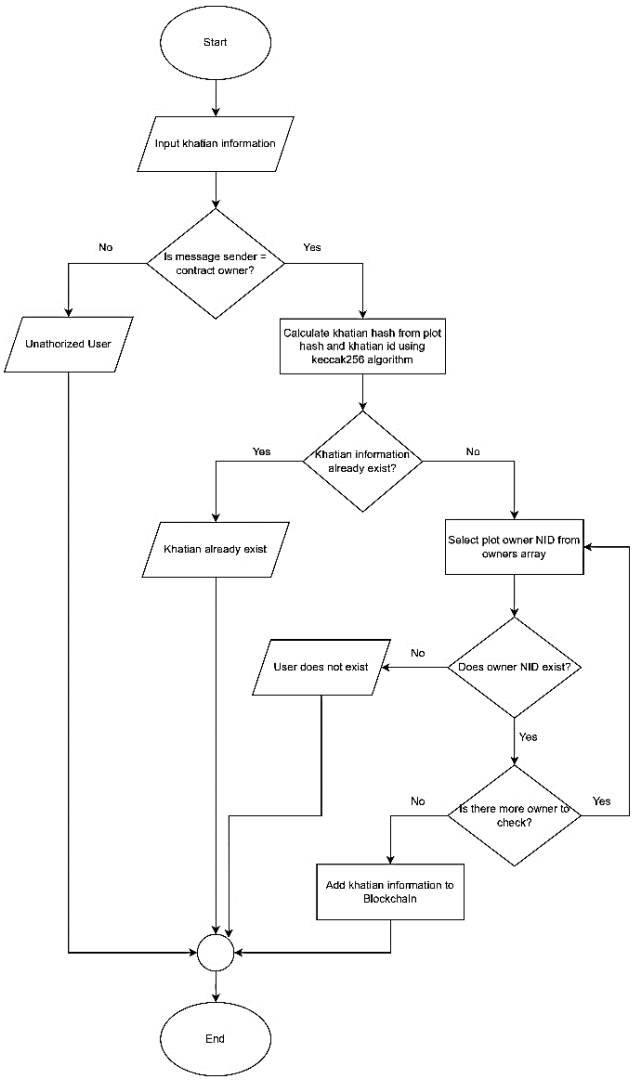



**Figure 18:** Flowchart of *addNewKhatianInfo( )* Function

Similar to the *addNewKhatianInfo( )* function, this function authorizes the contract owner, calculates khatian hash, and validates the owners' NIDs. It also checks if the buying land area is less or equal to the land area mentioned in the previous khatian. If every requirement is fulfilled, the

owners of the land are updated according to the new khatian. The flowchart is given in Figure 19.

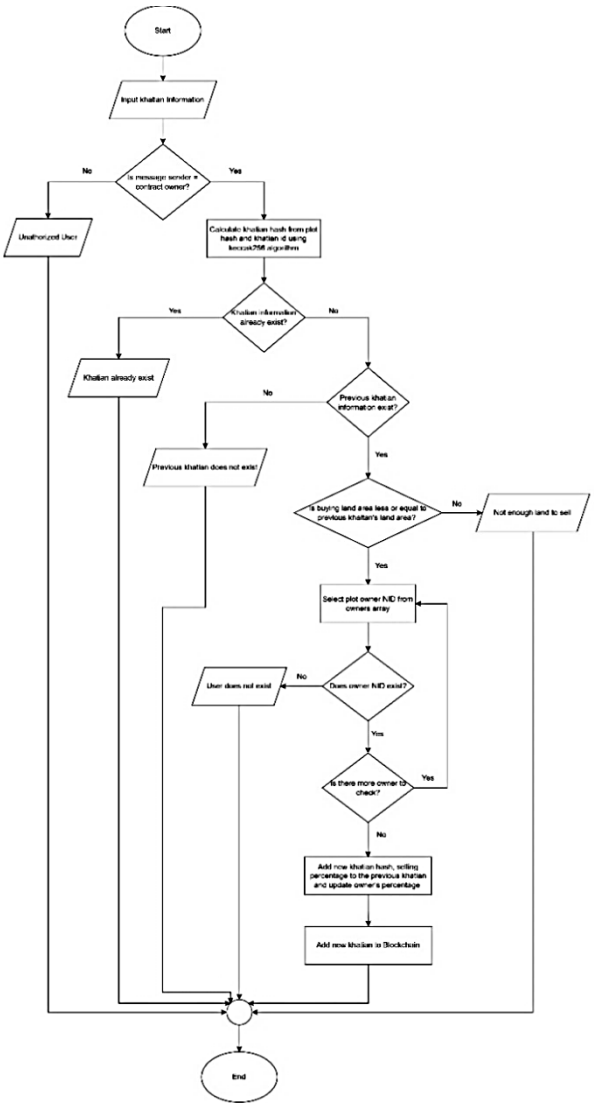



**Figure 19:** Flowchart of *addKhatianInfoFromOld( )* Function

Next, the *getKhatianInfo( )* function retrieves information about a specific khatian using the khatian hash, which is a unique identifier for each khatian. If the khatian hash exists in the system, the function returns the khatian information associated with the khatian hash. The corresponding flowchart is given in Figure 20.

**Algorithm 2: Smart Contract**

```
1:  Function uploadUserInfo(user):
2:  if msg.sender == contractOwner then
3:          if user info[nid].isExists==false then
4:                  user info[nid] = user
5:          else
6.                  User already exists
7:  else
8:          Sender is not authorized
9:  end if
10: Function getUserInfo(nid):
11: if user info[ nidbyte].isExist == true then
12:         return user info[nid]
13: else
14:         User does not exist
15: end if
16: Function addPlot(plot):
17: if msg.sender == contractOwner then
18:         if plot info[plothash].isExists== false then
19:                 plot info[plothash] = plot
20:                 plot array.push(plot)
21:         else
22:                 Plot already exists
23:         end if
24: else
25:         Sender is not authorized
26: end if
27: Function addKhatianNew(khatian):
28: if msg.sender == contractOwner then
29:         khatian info[khatianhash] = khatian
30:         for owner in owners list
31:                 khatian of users[owner].push(khatianhash)
32:         end
33:         khatian array.push(khatianhash)
34: else
35:         Sender is not authorized
36: end if
37: Function addKhatianFromOld(khatian):
38: if msg.sender == contractOwner then
39:         khatianinfo[buy from].sellTo.push(khatianhash)
40:         khatianinfo[buyFrom].sellPercentage.push(percentOwn)
41:         khatian info[buyFrom].percentOwn == percentOwn;
42:         khatian info[khatianhash] = khatian
43:         for owner in owners list
44:                 khatians of users[owner].push(khatianhash)
45:         end
46:         khatian array.push(khatianhash)
47: else
48:         Sender is not authorized
49: end if
50: Function getKhatianInfo(khatianhash):
51: if khatian info[khatianhash].isExist == true then
52:         return khatian info[khatianhash]
53: else
54:         Khatian does not exist
55: end if
```

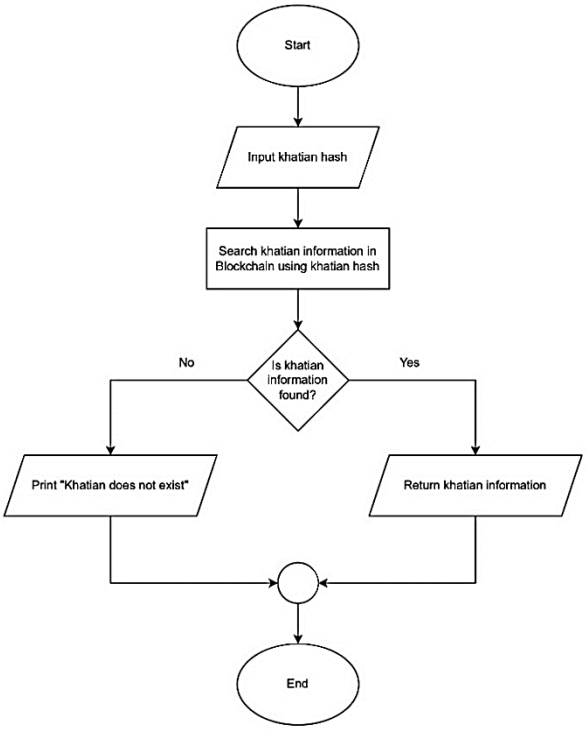



**Figure 20:** Flowchart of *getKhatianInfo()* function

The smart contract provides several functions for interaction. The *uploadUserInfo()* function stores user details such as

name, parents' names, date of birth, address, email, and fingerprint hash in a mapping, using the NID as the key. The *getUserInfo()* function retrieves user data if the NID exists in the system. The *addPlot()* function records plot details, including plot number, JL number, plot type, and address. The *getPlot()* function retrieves plot information if a matching plot hash exists. For khatian management, *addKhatianNew()* adds new khatian records, while *addKhatianFromOld()* transfers ownership from a previous owner. The *getKhatianInfo()* function retrieves stored khatian details.

The interface of the system is designed to prioritize user-friendliness and simplicity, enhancing the efficiency of property transactions. The provided screenshots of the designed interface, Figure 21 to Figure 34, demonstrate improvements in accessibility for land management.

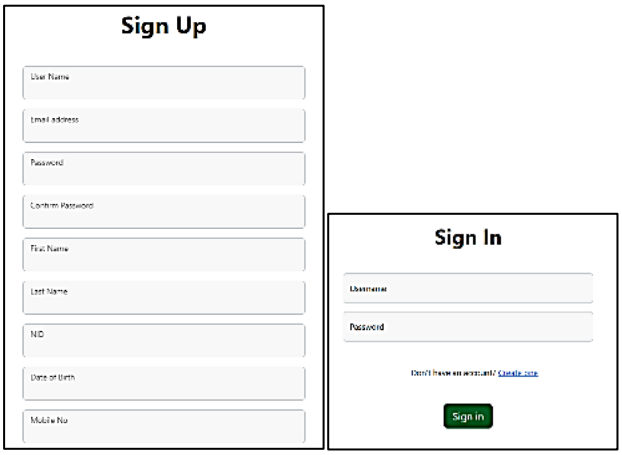



**Figure 21:** Signup and Login interface

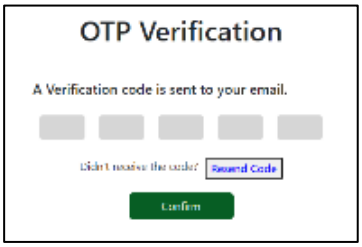



**Figure 22:** OTP verification interface

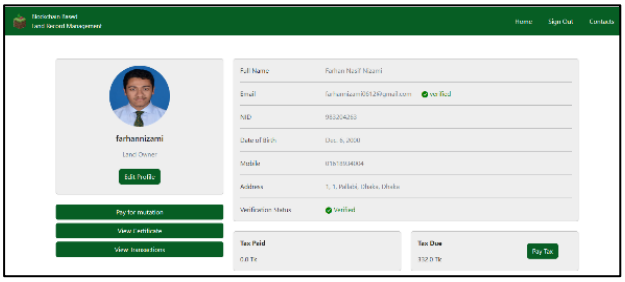



**Figure 23:** Customer Profile view

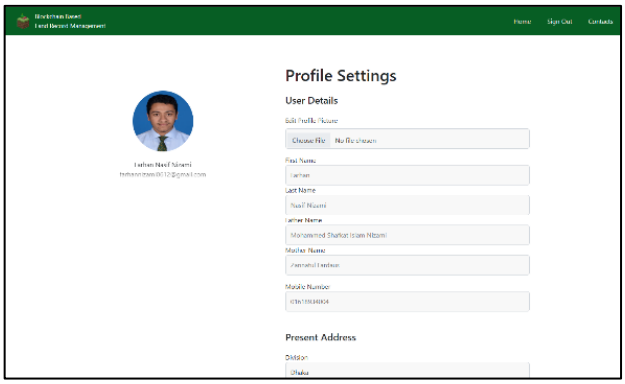



**Figure 24:** Customer Profile Setting Interface

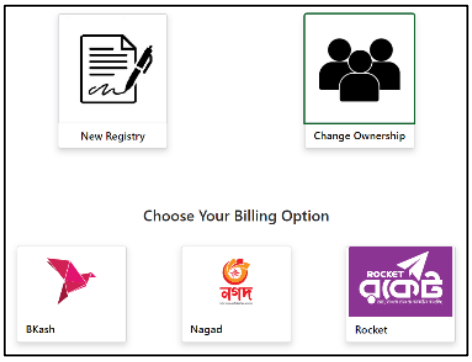



**Figure 25:** Customer Tax Payment options page

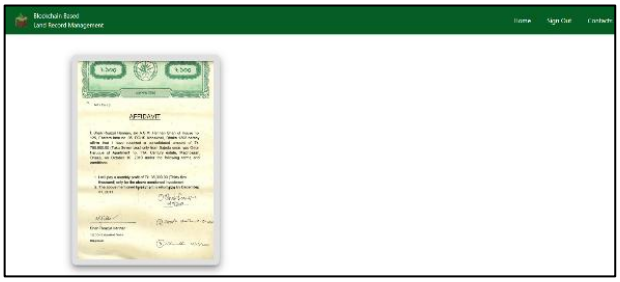


**Figure 26:** Customer View Certificate Page

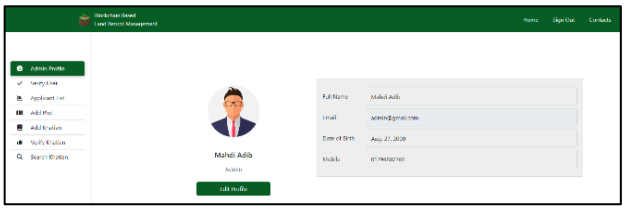



**Figure 27:** Admin Profile Page

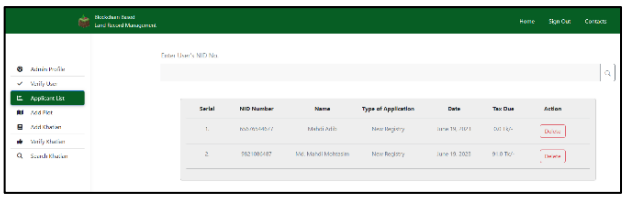


**Figure 28:** Admin Applicant List Page

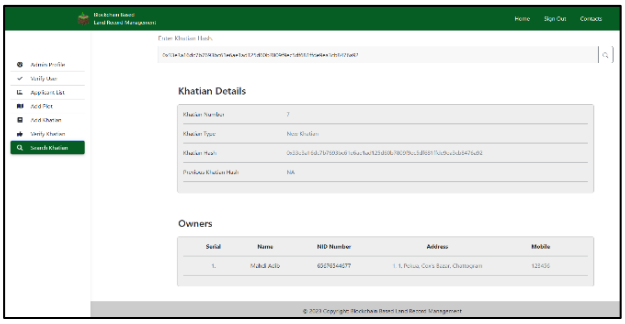



**Figure 29:** Admin Search Khatian interface

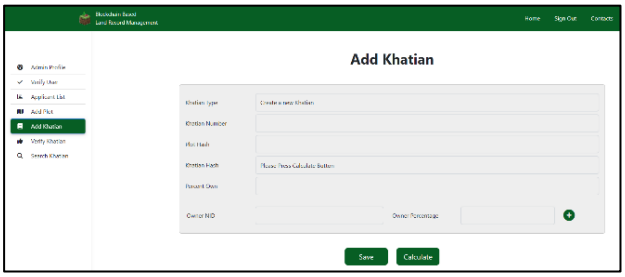



**Figure 30:** Admin Add Khatian interface

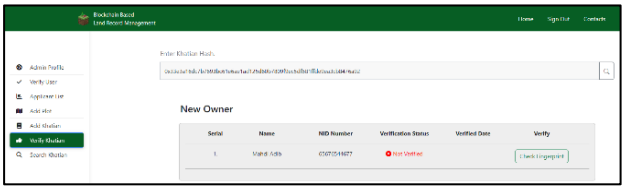



**Figure 31:** Admin Verify Khatian page

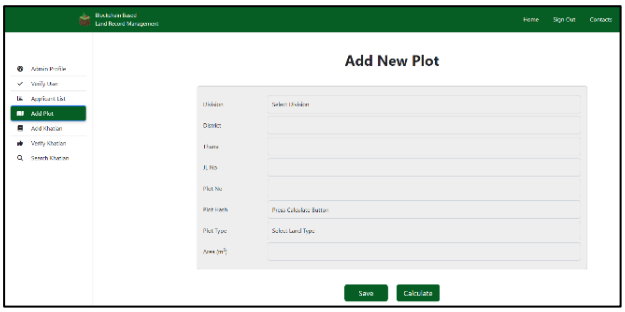



**Figure 32:** Admin Add Plot interface

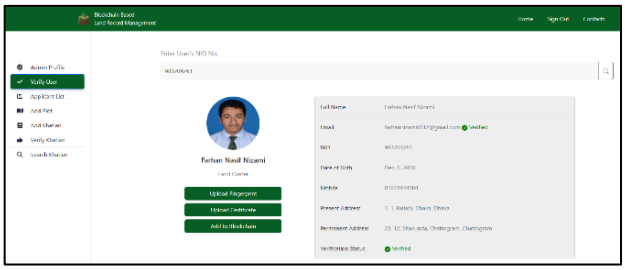



**Figure 33:** Admin Verify User Page

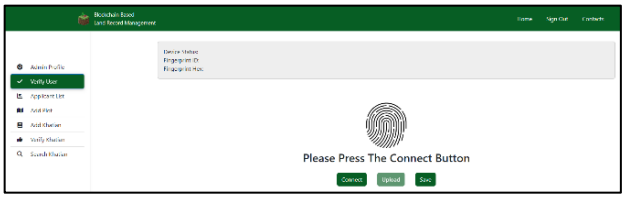



**Figure 34:** Admin Verify User Fingerprint Page

## 8. RESULTS AND DISCUSSIONS

When a smart contract is deployed on Ethereum and an event is triggered, a block is generated. Mining and verifying this block, before adding it to the chain, require computational power, quantified as gas fees. Additionally, a specific amount of Ether is needed for transactions (*Kollu et al., 2022; Hobeck et al., 2024*). The computational cost has been calculated for five fundamental operations in the system: deploying the migration function, deploying the smart contract, constructing land, acquiring land, and listing land for sale. Figures 35 and 36 display histograms illustrating gas consumption and Ethereum costs for each function, with color codes assigned to each function for clarity. These figures provide a visual representation of the computational requirements for different operations.

Table 2 presents a feature comparison with existing works. All transactions were conducted on an ASUS laptop running Windows 10 (Version 1803), equipped with a 6-core 2.40GHz Intel Core i7 processor and 16GB RAM. Interaction between the user interface and the Ethereum test network was facilitated using the Web3 framework.

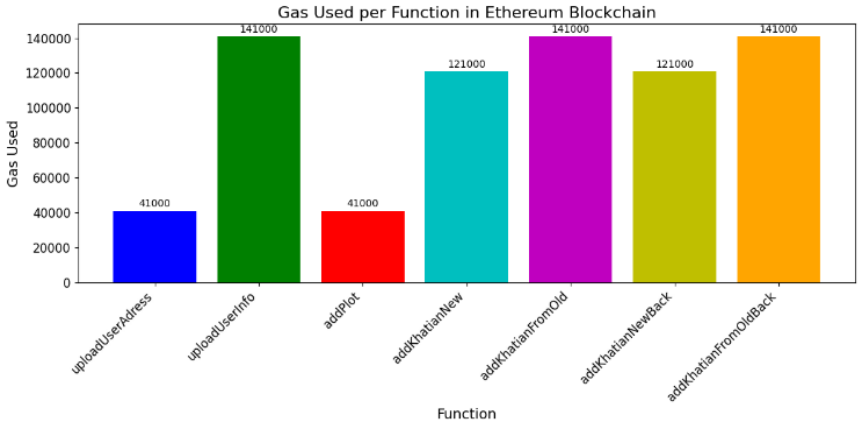



**Figure 35:** Gas Used per Function

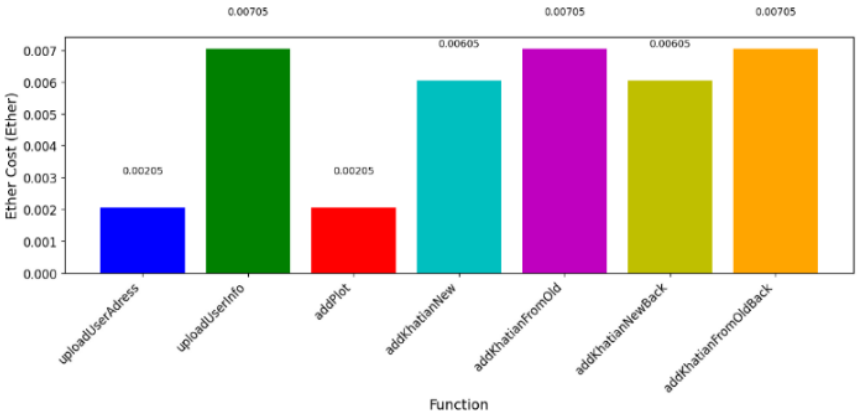



**Figure 36:** Ether cost per function

**Table 2:** Feature Comparison of developed system vs. existing systems

| Features | Hasan, Alam, and Tanha, (2022) | Nandi et al. (2020) | Thamrin et al. (2021) | Aquib et al. (2020) | Proposed System |
|---|---|---|---|---|---|
| **Country** | Bangladesh | India | Indonesia | Pakistan | Bangladesh |
| **Challenge** | Increase efficiency, improve accessibility to land records | Maintaining proper land ownership/transfer records, including fraud, disputes, and inefficiencies in the current paper-based system | Ease the complexity around project and execution control | Address limitations of traditional land record system | Ensure transparency, and prevent corruption while decentralizing the recording process |
| **Digitization level** | Varies across different phases of the system | Publicly-verifiable ledger system | Land database available | Not fully digitized | Varies across different phases of the system |
| **Proposed model** | Incremental three-phase permissioned blockchain | Incremental two-phase hybrid blockchain with consensus mechanism | Single phase public blockchain | Incremental private blockchain | Single phase hybrid blockchain |
| **Hardware Integration** | N/A | N/A | N/A | Biometric scanners | Fingerprint sensor, Document scanner |
| **Land division and Ownership transfer& Land division and transfer** | Land division and transfer | Ownership transfer | Ownership transfer | Land division and transfer | Plot division, fractional ownership transfer |
| **Project Implementation** | Ethereum as prototype | Ethereum as conceptual study | Ethereum as prototype | Hyperledger Fabric and Hyperledger Composer Government Initiated Seek feedback from real deployments | Ethereum based blockchain network |
| **Experimental Result** | Reduces the number of required travels, improves data accessibility, cost of operations | Improves cost of transactions, and time complexity | NA | Satisfactory feedback from test users | Satisfactory feedback from test users |

## 9. CONCLUSION

This study introduces an efficient and secured approach in tracking land records using Blockchain technology. In contrast to traditional centralized registry systems, the proposed framework offers absolute transparency, automation, and security. The method incorporates biometric fingerprint authentication, digital land certificates verification, and a blockchain network to record immutable transactions. A comprehensive architecture is presented, including user and administrator interfaces, hardware integration of sensors and scanners, smart contracts for operations, and user interfaces. This approach demonstrates blockchain-based processing strategies, like decentralization, cryptographic security, and consensus mechanisms that will transform traditional land record management process into an advanced technological improvement. By recording land transactions in a distributed and tamper-proof ledger, the system reduces the risk of fraud and delays compared to paper-based and centralized digital systems. The integration of sensory tools, e.g. biometrics authentication and document automation further strengthen the credibility of the proposed architecture. Overall, this system represents a significant advancement in the application of blockchain technology that reforms traditional land record management through a state-of-the-art technological application.

To ensure the scalability of the proposed system,

- Modular Blockchain architecture can be design for dynamic scaling of the increasing number of land

transactions with ensuring the data integrity and consensus efficiency.

- Integration of Layer-2 protocol, like sidechain or rollups, for offloading transaction processing from the principal Blockchain may improve throughput while reducing latency.
- Using AI driven data optimization and machine learning (*Islam et al., 2024; Akhtaruzzaman et al., 2025*) will help to predict transaction pattern and may optimize data storage, caching, and retrieval ensuring faster integration of blocks.
- Implementing upgradable smart contact for land transactions in supporting the evolving policies as well as regulatory requirements while keeping the existing records safe and secure.
- Implementation of Decentralized Identity (DID) can be considered to authenticate landowners and officials preventing identity fraud in transactions.
- Adopting post-quantum cryptographic method would provide the system extra strength against advanced security threats.
- Investigating the relation and existence of Phi ($\Phi$) the Golden Ratio (*Akhtaruzzaman, and Shafie, 2011; Akhtaruzzaman et al., 2024*) could open another dimension of the relevant research.

## ACKNOWLEDGMENTS

Authors also would like to express their gratitude to the Department of Computer Science and Engineering, Military Institute of Science and Technology (MIST), Department of Computer Science and Engineering, Daffodil International University (DIU), and Quantum Robotics and Automation Research Group (QRARG), Dhaka, Bangladesh for their support and guidelines in conducting the project and improving the content of the article.

## DATA AVAILABILITY STATEMENT

Datasets generated during the current study are available from the corresponding author upon reasonable request.

## FUNDING DECLARATION

This research was self-funded.

## ETHICS APPROVAL

This study is an engineering experimental investigation. The MIJST Research Ethics Committee has confirmed that formal ethical approval was not required.

## ETHICS, CONSENT TO PARTICIPATE, AND CONSENT TO PUBLISH

Not applicable.

## COMPETING INTERESTS

The authors declare that they have no competing interests.

## AUTHOR CONTRIBUTIONS

Author 1: Shakil Mosharrof - Conceptualization, Design, Analysis, Implementation, Testing, writing initial draft;

Author 2: Farhan Nasif Nizami - Implementation, Testing, Analysis, Editing;

Author 3: Mahdi Mohtasim - Analysis, Implementation, Testing, Editing;

Author 4: Mahdi Adib - Analysis, Implementation, Testing, Review and editing;

Author 5: M. Akhtaruzzaman - Conceptualization, Design, Analysis, writing original draft, Supervision;

Author 6: Md Shofiqul Islam - Mentoring, Analysis, Review and editing;

Author 7: Muhammad Towfiqur Rahman - Mentoring, Review and editing;

Author 8: Hosney Jahan - Mentoring, Review and editing;

## ARTIFICIAL INTELLIGENCE ASSISTANCE STATEMENT

No AI tools were used. The authors take full responsibility for the accuracy and integrity of the manuscript.

## CONFLICT OF INTEREST DECLARATION

The authors declare that they have no conflicts of interest.

## REFERENCES

Acquah, M. A., Chen, N., Pan, J.-S., Yang, H.-M., & Yan, B. (2020). *Securing fingerprint template using blockchain and distributed storage system. Symmetry, 12*(6), 951. https://doi.org/10.3390/sym12060951

Akhtaruzzaman, M. (2021). *Force-sensitive classic toothbrush: System analysis, design, and simulation. Electrica, 21*(2).

Akhtaruzzaman, M., & Shafie, A. A. (2011). Geometrical substantiation of Phi, the golden ratio and the baroque of nature, architecture, design and engineering. *International Journal of Arts*, 1(1), 1-22

Akhtaruzzaman, M., Shahryer, F., Halder, S., & Tanvin, J. U. (2025). Modeling a fuzzy expert system for predicting customers' behavioral intention for restaurant business through parallel prediction of perceived values and satisfactions. International Journal of Information Technology, 17(2), 1007-1014.

Akhtaruzzaman, M., Tanvin, J. U., Shafie, A. A., Shahryer, F., & Haldar, S. (2024). Application of phi (ϕ), the Golden Ratio, in Computing: A Systematic Review. *IEEE Access*.

Aquib, M., Das Dhomeja, L., Dahri, K., & Malkani, Y. A. (2020). *Blockchain-based land record management in Pakistan.* In *Proceedings of the 2020 3rd International Conference on Computing, Mathematics and Engineering Technologies (iCoMET)* (pp. 1–5). IEEE. https://doi.org/10.1109/iCoMET48670.2020.9073992

Baki, R. F., et al. (2023). *Intelligent Head-bot, towards the development of an AI based cognitive platform. MIJST, 11*(2), 1–14.

Beuria, M. K., Sharma, P. K., Dangra, J., Bulla, C. M., & Abadar, K. (2020). *Applicability of blockchain towards mitigation of distributed denial of service attack in IoT*. European Journal of Molecular & Clinical Medicine, 7(10), 3432–3442

Bouraga, S. (2025). CASCADE – Framework for the early-phase development of blockchain-based applications. *Business & Information Systems Engineering*. https://doi.org/10.1007/s12599-024-00912-4

Buterin, V., et al. (2014). *A next-generation smart contract and decentralized application platform* (White paper, Vol. 3, No. 37, pp. 1–2). Ethereum Foundation. https://ethereum.org/en/whitepaper

Dorri, A., Kanhere, S. S., & Jurdak, R. (2017). *Towards an*

*optimized blockchain for IoT.* In *Proceedings of the Second International Conference on Internet-of-Things Design and Implementation* (pp. 173–178). IEEE. https://doi.org/10.1109/IoTDI.2017.7984551

Hasan, M. M. U., Alam, M. M., & Tanha, K. J. (2022). *Decentralized blockchain-based land deed verification and reservation system in Bangladesh*. In 2022 25th International Conference on Computer and Information Technology (ICCIT) (pp. 971–975). IEEE. https://doi.org/10.1109/ICCIT57492.2022.10055779

Hobeck, R., Klinkmüller, C., Bandara, H. M. N. D., et al. (2024). On the suitability of process mining for enhancing transparency of blockchain applications. *Business & Information Systems Engineering.* https://doi.org/10.1007/s12599-024-00903-5

Ibrahim, M., Ravindran, K., Lee, H., Farooqui, O., & Mahmoud, Q. H. (2021). *ElectionBlock: An electronic voting system using blockchain and fingerprint authentication.* In *2021 IEEE 18th International Conference on Software Architecture Companion (ICSA-C)* (pp. 123–129). IEEE. https://doi.org/10.1109/ICSA-C52604.2021.00029

Islam, M. S., Al Farid, F., Shamrat, F. J. M., Islam, M. N., Rashid, M., Bari, B. S., ... & Karim, H. A. (2024). Challenges issues and future recommendations of deep learning techniques for SARS-CoV-2 detection utilising X-ray and CT images: a comprehensive review. *PeerJ Computer Science*, 10, e2517.

Jain, A. K., Bolle, R., & Pankanti, S. (Eds.). (2006). *Biometrics: personal identification in networked society* (Vol. 479). Springer Science & Business Media.

Jesus, E. F., Chicarino, V. R., De Albuquerque, C. V., & Rocha, A. A. D. A. (2018). A survey of how to use blockchain to secure internet of things and the stalker attack. *Security and communication networks*, *2018*(1), 9675050

Khan, S. N., Loukil, F., Ghedira-Guegan, C., Benkhelifa, E., & Bani-Hani, A. (2021). *Blockchain smart contracts: Applications, challenges, and future trends. Peer-to-Peer Networking and Applications, 14*, 2901–2925. https://doi.org/10.1007/s12083-021-01156-0

Khan, R., Ansari, S., Sachdeva, S., & Jain, S. (2020, August). *Blockchain-based land registry system using Ethereum blockchain. Journal of Xi'an University of Architecture & Technology, 12*, 3640–3648

Kollu, P. K., Kumar, K., Kshirsagar, P. R., Islam, S., Naveed, Q. N., Hussain, M. R., & Sundramurthy, V. P. (2022). *Development of advanced artificial intelligence and IoT automation in the crisis of COVID-19 detection. Journal of Healthcare Engineering, 2022*(1), 1987917. https://doi.org/10.1155/2022/1987917

Lee, Y. K., & Jeong, J. (2021). *Securing biometric authentication system using blockchain. ICT Express, 7*(3), 322–326. https://doi.org/10.1016/j.icte.2021.04.004

Mohanta, B. K., Jena, D., Ramasubbareddy, S., Daneshmand, M., & Gandomi, A. H. (2020). *Addressing security and privacy issues of IoT using blockchain technology. IEEE Internet of Things Journal, 8*(2), 881–888. https://doi.org/10.1109/JIOT.2020.2963312

Nandi, M., Bhattacharjee, R. K., Jha, A., & Barbhuiya, F. A. (2020). *A secured land registration framework on blockchain.* In *Proceedings of the 2020 Third ISEA Conference on Security and Privacy (ISEA-ISAP)* (pp. 130–138). IEEE. https://doi.org/10.1109/ISEA-ISAP49340.2020.235432

Padrón Núñez, J. (2021). *Biometric work attendance management and logging with a blockchain system* (Doctoral dissertation, ETSIS_Telecomunicacion)

Pereira, S. N., Tasnim, N., Rizon, R. S., & Islam, M. N. (2021). *Blockchain-based digital record-keeping in land administration system.* In *Proceedings of the International Joint Conference on Advances in Computational Intelligence (IJCACI)* (pp. 431–443). Springer. https://doi.org/10.1007/978-981-16-0961-3_36

Pournaghi, S. M., Zahednejad, B., Bayat, M., & Farjami, Y. (2018). *NECPPA: A novel and efficient conditional privacy-preserving authentication scheme for VANET. Computer Networks, 134*, 78–92. https://doi.org/10.1016/j.comnet.2018.01.019

Reyna, A., Martín, C., Chen, J., Soler, E., & Díaz, M. (2018). *On blockchain and its integration with IoT: Challenges and opportunities. Future Generation Computer Systems, 88*, 173–190. https://doi.org/10.1016/j.future.2018.05.046

Sahai, A., & Pandey, R. (2020). *Smart contract definition for land registry in blockchain.* In *Proceedings of the 2020 IEEE 9th International Conference on Communication Systems and Network Technologies (CSNT)* (pp. 230–235). IEEE. https://doi.org/10.1109/CSNT49383.2020.9150791

Sen, S., Mukhopadhyay, S., & Karforma, S. (2021). A blockchain based framework for property registration system in e-governance. *International Journal of Information Engineering and Electronic Business*, *11*(4), 30

Singh, A., Joshi, K., Shuaib, M., Bharany, S., Alam, S., & Ahmad, S. (2022). *Navigation and speed regulation aimed at travel through immersive virtual environments: A review.* In *2022 IEEE International Conference on Current Development in Engineering and Technology (CCET)* (pp. 1–6). IEEE. https://doi.org/10.1109/CCET55037.2022.9845678

Singh, A., Parizi, R. M., Zhang, Q., Choo, K.-K. R., & Dehghantanha, A. (2020). *Blockchain smart contracts formalization: Approaches and challenges to address vulnerabilities.* Computers & Security, 88, 101654. https://doi.org/10.1016/j.cose.2019.101654

Suganthe, R. C., Shanthi, N., Latha, R. S., Gowtham, K., Deepakkumar, S., & Elango, R. (2021). *Blockchain enabled digitization of land registration.* In *Proceedings of the 2021 International Conference on Computer Communication and Informatics (ICCCI)* (pp. 1–5). IEEE. https://doi.org/10.1109/ICCCI50826.2021.9402475

Thamrin, R. M. H., Harahap, E. P., Khoirunisa, A., Faturahman, A., & Zelina, K. (2021). *Blockchain-based land certificate management in Indonesia. ADI Journal on Recent Innovation, 2*(2), 232–252.

Yin, W., Wen, Q., Li, W., Zhang, H., & Jin, Z. (2018). *An anti-quantum transaction authentication approach in blockchain. IEEE Access, 6*, 5393–5401

MIJST
MIST International Journal of Science and Technology

# Visual Assessment and Genetic Distance Analysis of Gamma-Irradiated Lemon Leaf Mutants Developed Using the Leaf-Cut Method

**Jawata Afnan*[1], Moriom Azad[1], Mokhlesur Rahman[1] and Md Shaheen Sarkar[2]**

[1]Department of Nuclear Science and Engineering, Military Institute of Science and Technology, Dhaka, Bangladesh
[2]Technological University of the Shannon, Moylish, Limerick, Ireland

***Corresponding Email:** *jawataafnan909@gmail.com*

**ARTICLE INFO**

**Article History:**

*Received: 26th May 2025*
*Revised: 07th September 2025*
*Accepted: 28th September 2025*
*Published: 30th December 2025*

**Keywords**:

*Gamma radiation*
*Lemon leaf mutant*
*Leaf-cut propagation*
*Genetic distance*
*Visual inspection*

**ABSTRACT**

Ionizing radiation, particularly gamma rays, is widely used to induce genetic mutations for improving morphological traits and enhancing genetic diversity in plants. In citrus plants, such mutations can be achieved by irradiating leaves and propagating the resulting mutants through vegetative methods. This study was conducted at the BINA research farm with the objective of developing Citrus limon mutants using gamma radiation and analyzing their morphological characteristics through visual inspection, alongside genetic diversity assessment using hierarchical clustering. A total of 400 fresh leaves were collected from the mother plant (BINA Lebu-1) and exposed to different doses of gamma radiation (0, 60, 80, and 100 Gy), divided into four treatment batches. The irradiated samples were planted in unit plots following a Randomized Complete Block Design (RCBD). Root and shoot development were monitored visually after 3 to 4 months. Maximum root length was observed at 100 Gy, the highest root quantity at 60 Gy, and the highest success rate at 80 Gy. After 7–8 months, mature plants were further assessed, and leaves were collected for genomic analysis. Genetic relationships among the different treatment groups were evaluated using a Dendrogram generated through simple hierarchical clustering. The results indicated clear genetic dissimilarities between irradiated (60, 80, and 100 Gy) and non-irradiated (0 Gy) plants, with the 100 Gy group showing the greatest genetic distance from the others. Due to time constraints, fruit production could not be observed. Nonetheless, the study demonstrates the effectiveness of combining visual inspection and genetic distance analysis in evaluating gamma-induced citrus mutants developed via the leaf-cut method.

This work is licensed under a *Creative Commons Attribution-Non-commercial 4.0 International License.*

## 1. INTRODUCTION

Lemon (Citrus limon) is the best source of vitamin C and contains other essential nutrients that are good for human health. Lemon aids in improving human health with countless benefits (Barkley et al., 2006). Citrus fruits like lemon play a vital role in agriculture as their demand is increasing with the growth of the population (Hodgson, 1967). However, conventional breeding techniques of citrus face multiple challenges, such as limited efficiency, climate conditions, etc. Mutation induction techniques such as radiation effectively overcome these challenges, typically arising from extremely low-frequency spontaneous mutations, by increasing variability in plant characteristics (Belele et al., 2001; Çimen et al., 2020). Gamma radiation induces DNA damage and structural and physiological alterations; this can result in new variations like agronomic or molecular differences (Sparrow et al., 1956; Whittwer, 1971). The leaf-cut technique is an asexual propagation method that allows roots and shoots to form at the base of leaves. This method maintains consistency in yield and formation of genetically identical plants (Deependra et al., 2018). Visual inspection is used to observe and record morphological variations from irradiated gamma lemon leaf mutants (Waqar et al., 1992). Cluster analysis is employed to group genetically similar and dissimilar plants into clusters (Gulsen et al., 2001; Sidler et al., 2015). This technique can help us to discover genetic distances or changes in lemon plants at different gamma levels. Genetic distance offers more opportunities for the conservation and evaluation of genetic resources (Taheri et al., 2014). This research aims to screen for better lemon cultivars by examining the impact of gamma radiation on the leaves of lemons formed through leaf-

cutting. This study offers farmers a shorter path to obtain improved lemon plants than traditional breeding (Kumar et al., 2013). This study also has relevance for agricultural biotechnology because it examines a low-cost and scalable method for genetically improved lemon propagation.

## 2. MATERIALS AND METHODS

An experiment was conducted at Horticulture research farm of Bangladesh Institute of Nuclear Agriculture (BINA), Mymensingh, from July 2024 to April 2025, to induce mutation by gamma radiation in *Citrus Limon* using leaf cut propagation technique.

### 2.1 Sample Collection and Separation

Lemon leaves were collected from non-irradiated mother plant (BINA Lebu-1). Four hundred fresh leaves were gathered and separated into 4 batches; each batch consisted of 100 leaves. Then, the samples were labeled according to desired doses (60, 80 and 100 Gy) before exposing them to radiation, shown in Figure 1. One of the batches was labeled as a control batch (0 Gy), which would be unexposed to radiation.

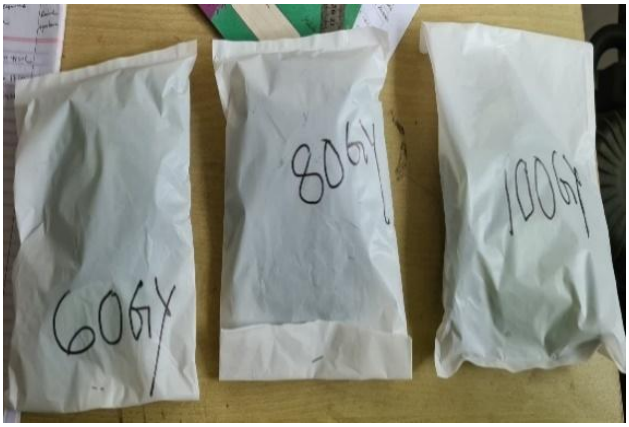



**Figure 1:** Sample (BINA Lebu-1 leaves) separation according to desired radiation doses

### 2.2 Exposure data calculation and Irradiation

Required exposure time was calculated before irradiation of the samples. For radiation exposure on leaves, a shielded gamma irradiation facility, known as a gamma chamber shown in Figure 2, was used. Co-60 used as a radiation source in the gamma chamber. After calculating the required parameters, a single batch of samples each time, totaling 3 batches were placed and irradiated in the chamber.



**Figure 2:** Irradiator Co-60 Gamma Chamber (Model-GC-5000)

### 2.3 Planting and Monitoring

After irradiating the leaves, cutting aid (containing Indole Butyric Acid, Poly Hydroxyl Butyrate and boric acid) was applied as a root promoter to the leaves and planted in the prepared soil at a shade house. The leaves were planted in the RCBD (Randomized Complete Block Design) with 3 replications. After planting all the leaves, a suitable environment (Temperature: 25-35°C and relative humidity: 80-100%) should be provided in the shade house to promote the formation of callus, roots, and shoots.

### 2.4 Morphological Assessment

A few days after planting, the initiation of roots was observed. The length of the roots was measured for three levels of gamma doses at 60, 70, and 90 days after planting. After the formation of shoots, shoot lengths were also measured at 90, 120, and 150 days after planting. Other notable changes were also recorded. Figure 3 shows the formation of roots from the irradiated leaves for different gamma levels.



**Figure 3**: Root formation from irradiated leaves (60,80 and 100 Gy from left to right)

### 2.5 Molecular Data Acquisition

After 7 to 8 months of planting, grown plants were observed. Then, leaves were detached from them to analyze genomic data. To evaluate the plant genomic data, DNA Extraction & Gel Electrophoresis Test were conducted.

#### 2.5.1 DNA Extraction

To extract DNA from plant tissues, the leaves detached from plants grown under radiation treatments (0, 60, 80, 100 Gy) were grinded and mixed with liquid nitrogen and preheated extraction buffer and poured into 4 different micro centrifuge tubes. Then, they were centrifuged at 13,000 rpm for 12 minutes, for 3 times and after discarding the supernatant and drying, concentrated DNA pellet samples for each tube was obtained.

#### 2.5.2 Gel Electrophoresis Testing

Before gel electrophoresis test, DNA pellets were amplified by RAPD-PCR (Random Amplified Polymorphic DNA- Polymerase Chain Reaction) process. The samples were prepared with the mixture of concentrated DNA pellets, RAPD primer (Cp-02), PCR master mix (polymerase, buffer) were placed in PCR Thermal Cycler machine and rotated for 45 cycles to automate DNA amplification. After amplification, Gel electrophoresis or RAPD PCR gel run test, shown in Figure 3, was conducted to separate DNA fragments by applying an electric field to an agarose gel matrix. After running the gel along with a 1 kilo base (kb) DNA ladder as a reference for size estimation of DNA fragments, it was stained with a dye which was Ethidium Bromide (EtBr) and visualized under UV light. The DNA fragments appeared as bands and to observe the band pattern, a gel documentation system or a camera was used to capture an image of the gel, including the ladder.

### 2.6 Cluster Analysis

Analysis of the gel image showed different bands for each sample, representing unique DNA fragments. These bands were noted as "1" (band present) or "0" (band absent) for statistical analysis. Then, a similarity matrix is created, using Jaccard's coefficients to compare band patterns. Based on Jaccard distance between each sample, a simple hierarchical clustering was constructed. The result is visualized as a Dendrogram, where branch lengths represent genetic distance.

## 3. RESULTS AND DISCUSSIONS

### 3.1 Morphological Variation Inspection

For the different levels of gamma irradiation, significant morphological variations were found per leaf cutting. The average time of callus formation, time of root initiation, and time of shoot initiation was recorded for all gamma levels, shown in Figure 4.

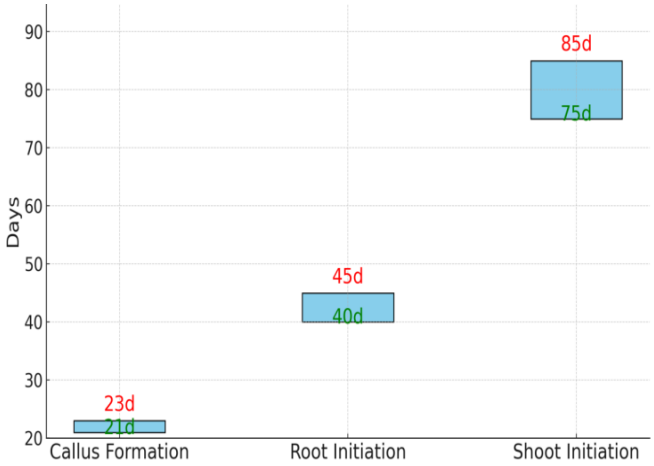



**Figure 4:** Timeline for different stages of plant growth

Figure 4 shows that the timeline for callus formation was 21 to 23 days after planting. So, the average time of callus formation was 22 days. The timeline for root initiation was 40 to 45 days after planting. So, the average time of root initiation was 42 days. And the timeline for shoot initiation was 75 to 85 days after planting. Therefore, the average time of shoot initiation was recorded to be 80 days after planting of leaves. Then, the number and length of roots, length of shoots, plant survivability and success rate were recorded, shown in Table 1.

**Table 1:** Combined morphological variation on different gamma levels

Table 1 shows the rate of success and survivability is higher for low doses, and the success rate decreases as the dose level increases. For the 100 Gy dose, the survivability rate is minimum. And the maximum morphological changes are observed for 100 Gy than for other doses. While the maximum number of roots and minimum length of roots and shoots is found for 60 Gy. And average morphological changes are found for the 80 Gy dose.

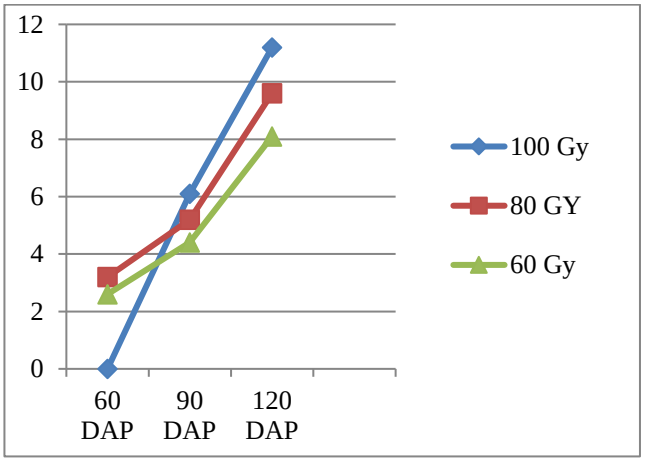



**Figure 5:** Length of roots on different gamma radiation levels

Though the highest length of root (11.2 cm) and shoot (25 cm) was found for the 100 Gy dose, (Figure 5 and Figure 6), the percent survivability and percent success are minimum for 100 Gy. Maximum survivability (43.76) and success rate (39.44) were found for the 60 Gy dose (Figure 7).

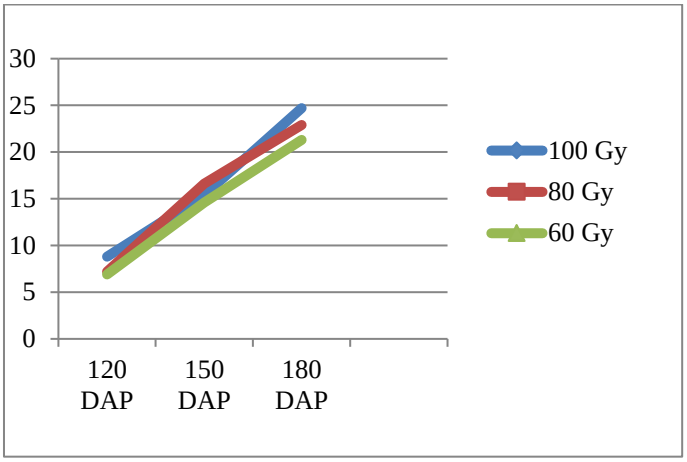



**Figure 6:** Length of shoots on different gamma radiation levels

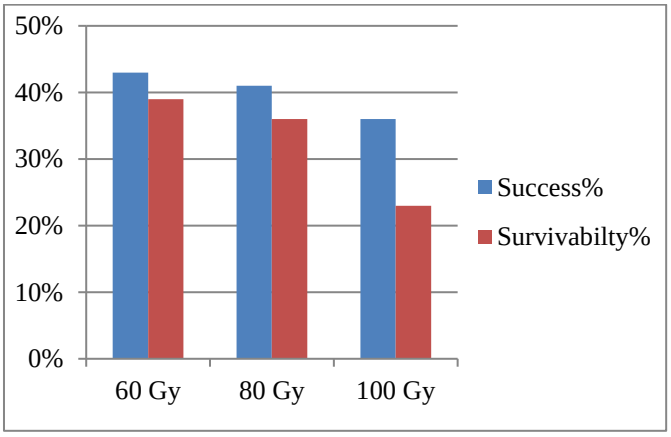



**Figure 7:** Percent success and survivability of propagated lemon leaves on different irradiation level

### 3.2 Genetic distance Measurement

From the gel image, band patterns indicated the degree of band presence and absence for samples of different radiation doses. Table 2 shows the values of band presence and absence obtained for different samples in a range of 2000-100 band pattern(bp).

| Gamma Dose | Number of Roots | | | Length of Roots (cm) | | | Length of Shoots (cm) | | | Survivability (%) | Success (%) |
|---|---|---|---|---|---|---|---|---|---|---|---|
| | 60 DAP | 90 DAP | 120 DAP | 60 DAP | 90 DAP | 120 DAP | 120 DAP | 150 DAP | 180 DAP | | |
| 100 Gy | 3-5 | 4-6 | 6-8 | 0 | 6.1 | 11.2 | 8.8 | 15.4 | 24.7 | 38.21 | 25.78 |
| 80 Gy | 1-3 | 3-4 | 4-7 | 3.2 | 5.2 | 9.6 | 7.2 | 16.6 | 22.9 | 42.33 | 34.96 |
| 60 Gy | 2-4 | 2-6 | 5-10 | 2.6 | 4.4 | 8.1 | 6.9 | 14.6 | 21.3 | 43.76 | 39.44 |

**Table 2:** Binary Matrix (Band Presence/Absence)

| Band (bp) | 100 Gy | 80 Gy | 60 Gy | 0 Gy (control) |
|---|---|---|---|---|
| 2000 | 1 | 0 | 0 | 0 |
| 1000 | 1 | 1 | 1 | 1 |
| 750 | 1 | 1 | 1 | 1 |
| 500 | 1 | 1 | 1 | 0 |
| 250 | 0 | 0 | 0 | 0 |
| 100 | 0 | 0 | 0 | 0 |

Here, 0 = Band absent; 1 = Band present

To determine genetic distances, Jaccard Similarity Coefficients are to be calculated. The Jaccard index measures similarity between samples. Here, it was used to measure genetic similarity between different samples (0,60,80,100 Gy).

The formula for measuring the Jaccard Index,

$$\mathbf{JI} = \frac{\textbf{Shared bands}}{\textbf{Total bands present in the sample}}$$

The Jaccard index is a coefficient, so it is a dimensionless quantity.

Then, the next thing to be measured was the Jaccard distance. It indicated the degree of genetic dissimilarity between different samples.

The formula for measuring Jaccard distance,

**JD = 1- Jaccard index (JI).**

Jaccard distance is also a dimensionless quantity.

Table 3 shows the calculated values of the Jaccard index and the Jaccard distance.

**Table 3:** Calculation of Jaccard index and Jaccard distance

| Sample Pair | Shared Bands | Total Unique Bands | Jaccard Index | Jaccard Distance |
|---|---|---|---|---|
| 100 Gy vs 80 Gy | 3 | 4 | 0.75 | 0.25 |
| 100 Gy vs 60 Gy | 3 | 4 | 0.75 | 0.25 |
| 100 Gy vs 0 Gy | 2 | 4 | 0.50 | 0.50 |
| 80 Gy vs 60 Gy | 3 | 3 | 1.00 | 0.00 |
| 80 Gy vs 0 Gy | 2 | 3 | 0.67 | 0.33 |
| 60 Gy vs 0 Gy | 2 | 3 | 0.67 | 0.33 |

The higher values of Jaccard distance indicate less similarity. Genetic distances are calculated by averaging the Jaccard distances between the most similar samples and clustering them together. As the Jaccard distance between 80 and 60 Gy is lower than that of others, both of them are the most similar samples. So, these two were clustered first. Similarly, the next closest sample was clustered with the previous one and the genetic distance between them was calculated by averaging their individual distances. For a cluster of (100/80) - 60 Gy, the genetic distance will be
(0+0.25+0.25)/2 = 0.25. Similarly, all the given samples were clustered.

Table 4 shows the clustering of samples with their genetic distances, given below:

**Table 4**: Clustering of samples with their genetic distances

| Cluster of samples | Genetic Distance |
|---|---|
| 80 Gy - 60 Gy | 0.00 (~0.01 for visual adjustment) |
| (100/80) - 60 Gy | 0.25 |
| (100/80/60) - 0 Gy | 0.39 |

As the genetic distance between 80 and 60 Gy is almost 0, 0.01 was taken 0.01 instead of 0 for visual adjustment in the illustration of the Dendrogram.
Now, the Dendrogram shows the relationship between Genetic Distances in different samples.

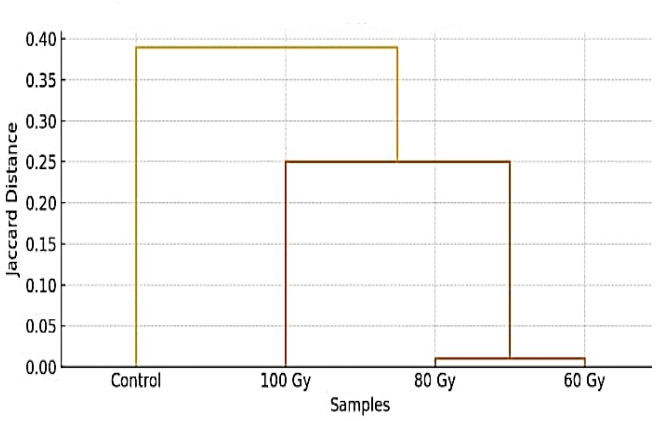



**Figure 8**: A simple Dendrogram Construction

In the above figure, X axis shows the samples to be compared with each other and Y axis shows the height at which clusters merge. Hence, the Dendrogram indicates that control (0 Gy) or non-irradiated samples have large genetic distance with others. It means, gamma radiation successfully produced mutations in samples of doses 100, 80 and 60 Gy. However, if the samples of 100, 80 and 60 Gy doses are compared, 60 and 80 Gy samples are mostly similar and 100 Gy have larger genetic distance with 80 and 60 Gy. Therefore, these results suggest that increasing radiation doses amplifies its genetic distance.

## 4. CONCLUSIONS

This study provides a comprehensive analysis of induced mutations in *Citrus limon* through the combined application of the leaf-cut technique and gamma irradiation. The dual approach—visual inspection of morphological traits and genetic distance analysis—proved effective in identifying and distinguishing mutant lines. Among the gamma radiation doses tested, 60 Gy appeared to be the threshold dose for mutation induction, 80 Gy was found to be the most optimal for successful plant regeneration, and 100 Gy induced the highest degree of genetic variation. These findings demonstrate the potential of gamma irradiation, particularly at controlled doses, for generating genetic diversity in citrus plants for future breeding programs.

## ACKNOWLEDGMENTS

The authors would like to thank the Military Institute of Science and Technology (MIST) and the Bangladesh Institute of Nuclear Agriculture (BINA) for their guidance, support, and provision of laboratory facilities.

## DATA AVAILABILITY STATEMENT

Datasets generated during the current study are available from the corresponding author upon reasonable request.

## FUNDING DECLARATION

This research was self-funded.

## ETHICS APPROVAL

This study is an engineering experimental investigation. The MIJST Research Ethics Committee has confirmed that formal ethical approval was not required.

## ETHICS, CONSENT TO PARTICIPATE, AND CONSENT TO PUBLISH

Not applicable.

## COMPETING INTERESTS

The authors declare that they have no competing interests.

## AUTHOR CONTRIBUTIONS

Author 1: Jawata Afnan - Conceptualization, methodology, experimental investigation, data analysis, visualization, and manuscript writing (original draft).

Author 2: Moriom Azad - Experimental investigation, data collection, data curation, and assistance in analysis.

Author 3: Mokhlesur Rahman - Supervision, resources, review, and editing of the manuscript.

## ARTIFICIAL INTELLIGENCE ASSISTANCE STATEMENT

Portions of this manuscript were assisted by an artificial intelligence language model (ChatGPT, OpenAI). The tool was used solely for language editing, text refinement, and clarity improvement. All content, data interpretation, analysis, conclusions, and final decisions were generated, verified, and approved by the authors. The authors take full responsibility for the accuracy and integrity of the manuscript.

## CONFLICT OF INTEREST DECLARATION

The authors declare that they have no conflicts of interest.

## REFERENCES

Barkley, N.A.; Roose, M.L.; Krueger, R.R. & Federici, C.T. (2006). Assessing genetic diversity and population structure in a citrus germplasm collection utilizing simple sequence repeat markers (SSRs). Theor. Appl. Genet. 112, 1519–1531.

Belele C.L., Vieira G.S. and Goulart L.R. (2001). Effects of gamma radiation of morphological traits and seed storage proteins of bean, Legume Research, 45, 23

Çimen, B., Yeşiloğlu, T., & Aka Kaçar, Y. (2020). Effects of Gamma Irradiation on Seedlessness and Fruit Quality of Ortanique Tangor. *Turkish Journal of Agriculture - Food Science and Technology*

Deependra Yadav and S.P. Singh. (2018). Vegetative methods of plant propagation: I- cutting layering and budding. Journal of Pharmacognosy and Phytochemistry 7(2) 3267- 3273

Gulsen, O. & Roose, M.L. (2001). Lemons: diversity and relationships with selected citrus genotypes as measured with nuclear genome markers. J. Am. Soc. Hort. Sci. 126: 309–317.

Hodgson, R. W. (1967). Horticultural varieties of Citrus. The Citrus Industry (W. Reuther, H. J. Webber, and L. D. Batchelor. eds.). University of California Press. Berkely, 1: 431-591.

Kumar, S., Kumari, R., & Kumar, S. (2013). Plant breeding by mutation induction: Current trends. *Botany Research International*, *6*(2), 41–48

Sidler, C., Li, D. P., Kovalchuk, O., and Kovalchuk, I. (2015). Development dependent expression of DNA repair genes and epigenetic regulators in Arabidopsis plants exposed to ionizing radiation. Radiat. Res. 183, 219–232.

Sparrow, A.H. and Gunckel, J.E. 1956. The effect of plants on chronic exposure to gamma-radiation from radio cobalt. Proc Int Conf Peaceful Uses of Atomic Energy, 17:52-59

Taheri, S., Abdullah, T. L., Ahmad, Z., and Abdullah, N. A. P. (2014). Effect of acute gamma irradiation on Curcuma alismatifolia varieties and detection of DNA polymorphism through SSR Marker. Biomed Res. Int. 2014:631813.

Waqar, A., Wasim, A. Farooqi and Sattar (Jr), A. (1992). Effect of gamma irradiation on the morphology of Kinnow seedlings. Proc First Intl. Seminar on Citriculture in Pakistan, 2-5 Dec, 1992

Whittwer, S.H. (1971). Radiation induced mutation in crop plants. Outlook Agri., 6:205-17

MIJST
MIST International Journal of Science and Technology

# Impact of Inverter Control and Solar Photovoltaic Integration on Small Signal Stability Augmented with Battery: Modal Analysis Approach

**Md. Mahadi Hasan*, Md. Imranul Hasan Emon, Hasan Monir, and Md Ahsan Kabir**

Department of EECE, Military Institute of Science and Technology, Dhaka, Bangladesh

***Corresponding Email:** *mahadi_hasan@eece.mist.ac.bd*

**ARTICLE INFO**

**Article History:**

*Received: 11th April 2025*
*Revised: 18th October 2025*
*Accepted: 19th October 2025*
*Published: 30th December 2025*

**Keywords**:

*Small Signal Stability; Inertia; Battery; Solar Photovoltaic; Modal Analysis; Inverter*

**ABSTRACT**

The increasing penetration of renewable energy sources, particularly solar photovoltaic (PV), poses significant challenges to grid stability due to the reduction in system inertia. This paper evaluates three inverter control strategies—$\boldsymbol{V_{ac}-\Phi}$, $\boldsymbol{V_{ac}-P}$, and $\boldsymbol{P-Q}$ —using modal analysis and participation matrix evaluation to identify the most effective approach for enhancing small signal stability. Among these, the $\boldsymbol{P-Q}$ control strategy emerges as the best-performing technique, with a notable eigenvalue improvement from $\boldsymbol{-0.62+9.607i}$ $(\boldsymbol{V_{ac}-\Phi})$ to $\boldsymbol{-14.79+0.668i}$, achieving an exceptionally high damping ratio of 0.998. The participation matrix analysis highlights the dominance of active power control in stabilizing critical modes, further validating the superior performance of $\boldsymbol{P-Q}$ control. Moreover, the impact of solar PV has been demonstrated and enhancement of system stability utilizing Battery Energy Storage System (BESS) has been shown in this paper.

This work is licensed under a *Creative Commons Attribution-Non-commercial 4.0 International License.*

## 1. INTRODUCTION

### 1.1 State of the Art

The integration of Renewable Energy Sources (RES) into modern power grids has emerged as a critical strategy to address global energy demands while mitigating environmental impact. It plays a pivotal role in decarbonization, aligning with international climate change mitigation goals by reducing reliance on traditional fossil fuel power plants (Kåberger, 2018), (Ram et al., 2018), (International Renewable Energy Agency, 2022). Among the diverse RES technologies—solar photovoltaic (PV), hydropower, wind power, geothermal energy, biomass energy, concentrated solar power, and ocean energy—solar PV has gained unprecedented momentum as the global energy landscape shifts toward renewables. According to the REN21 report, solar PV accounted for 70% of all new renewable capacity additions in 2022, a trend driven by declining costs, modularity, and accessibility compared to alternative resources (Renné,2022), (REN21, 2023), (McGinn et al., 2013). The combination of falling prices and growing demand has established solar PV as the most cost-effective and desirable RES technology (Chong et al., 2024), (Lu et al., 2021), (Wiser et al., 2017), (Roser, 2020). However, integrating solar PV into existing grid infrastructures presents challenges due to its intermittent and unpredictable nature, as well as the nonlinear characteristics of power converters (Tavakoli et al., 2020), (Kiasari et al., 2024), (Hamid et al., 2023), (Aljarrah et al., 2024), (Hamid et al., 2023). These challenges, particularly pronounced at high penetration levels, can affect grid reliability, stability, and power quality, resulting in issues such as voltage sag, flicker, harmonics, and unbalance (Ali et al., 2024), (Pandey & Prasad, 2024). Modern grid codes have been established to mitigate these challenges, requiring features such as dynamic active power regulation, reactive power support, fault ride-through capabilities, harmonic compliance, and cybersecurity measures to ensure the smooth integration of large-scale PV power plants (Boscaino et al., 2024), (Jamal et al., 2017). Battery Energy Storage Systems (BESS) play a critical role in this integration by addressing the variability of PV output. BESS stores excess energy during peak generation and releases it during periods of deficit, enabling optimal system performance and cost- effectiveness (Shivashankar et al., 2016), (Makarov et al., 2008).

### 1.2 Literature Review

Recent research highlights various strategies for integrating PV and BESS into power grids,

emphasizing inverter-based control methods for enhancing stability and power quality. A genetic algorithm-based approach was proposed in (Gali et al., 2023) to optimize BESS sizing, while (Emrani et al., 2024) developed a day-ahead dispatch model for hybrid PV–wind–BESS systems. Rule-based BESS controllers (Teleke et al., 2010) and power management schemes using moving average filtering (Koohi-Kamali et al., 2014) improved PV output regulation, and Hill et al. (Hill et al., 2012) recommended centralized BESS for voltage and frequency support. Daud et al. (Daud et al., 2012) demonstrated the superiority of lithium-ion batteries for grid-tied PV systems. Other studies (Teng et al., 2012; Akatsuka et al., 2010) applied optimization and hybrid control to minimize losses and stabilize converter outputs. Research in (Zeng et al., 2006; Biroon et al., 2020) analyzed advanced BESS control loops for improved dynamic stability, and (Das & Aliprantis, 2008), (Alias & Singh, 2021), (Iyer et al., 2018), (Muriuki et al., 2016),(Shaw & Kumar, 2016) examined small-signal behavior and damping enhancement through active power, voltage, and reactive power ( $P-Q$ and $V-P$ ) control. Collectively, these works establish the relevance of inverter control strategies—particularly $V_{ac}-\Phi$ , $V_{ac}-\mathrm{P}$ , and $P-Q$ —for small-signal stability improvement in PV- and BESS integrated systems.

### 1.3 Research Gap and Paper Contributions

Despite significant progress in addressing RES integration challenges, the impact of inverter control strategies on system stability remains underexplored. Modal analysis has been widely adopted to evaluate small-signal stability, providing detailed insights into system dynamics and control effectiveness [38–40]. However, systematic comparisons of control strategies like $V_{ac}-\Phi$ , $V_{ac}-\mathrm{P}$ , and $P-Q$ under varying operating conditions are limited especially under scenarios of increasing PV penetration, leaving gaps in understanding their dynamic stability impacts.

This paper addresses these gaps with the following contributions:

- An in-depth comparative study of three key inverter control algorithms—$V_{ac}-\Phi$, $V_{ac}-\mathrm{P}$, and $P-Q$ —using modal analysis to assess their effectiveness in simulating virtual inertia and improving small-signal stability.
- A detailed investigation into the impacts of increasing PV penetration on the stability of a modified 9-bus test system.
- An evaluation of the role of BESS in enhancing system stability, focusing on eigenvalue shifts, participation factors, and their implications for mitigating reduced inertia caused by high-RES penetration.
- An integrated assessment of inverter control strategies and BESS on frequency regulation to provide insights into optimal configurations for grid resiliency.

The paper begins with an introduction in Section 1. Section 2 outlines the methodology adopted for this study, followed by the simulation setup described in Section 3. Section 4 presents the software simulation results, which are discussed in detail in Section 5. Finally, the paper concludes with the key findings summarized in Section 6.

## 2. MATERIALS AND METHODS

### 2.1 Modal analysis

Small-signal stability refers to the ability of a power system to maintain synchronism and return to steady state following small disturbances such as load or generation fluctuations. It primarily depends on the location of eigenvalues of the system's linearized dynamic model. If all eigenvalues possess negative real parts, system modes are stable; eigenvalues near the imaginary axis indicate weak damping and oscillatory behavior. The damping ratio associated with each mode quantifies the rate at which oscillations decay. Participation factors further identify the state variables most responsible for specific modes, linking control loops or devices (e.g., inverters, generators, or BESS) to dominant oscillations.

Therefore, small-signal stability analysis is a powerful tool for understanding the dynamic interactions in converter-based renewable systems and assessing the effectiveness of control strategies such as $V_{ac}-\Phi$, $V_{ac}-\mathrm{P}$, and $P-Q$ control. For small-signal stability analysis the general form of power system mathematical model is linearized (Vetoshkin & Müller, 2021). Hence, the linear form of the model is shown in equation (1).

$$\Delta x = A\Delta x + B\Delta v \tag{1}$$

where $\Delta x$ is the state vector of the power system, $A$ is the system matrix corresponding to devices constants and $B$ is the input matrix that correlates with node voltages. The power flow in the network is described by equation (2):

$$\Delta \mathrm{i} = y_{\mathrm{N}}\Delta v \tag{2}$$

where, $Y_N$ network admittance matrix and $\Delta \mathrm{i}$ is the vector of current injections The current injection is defined as equation (3):

$$\Delta \imath = C_{\mathrm{D}}\Delta x + D_{\mathrm{D}}\Delta v \tag{3}$$

where $C_{\mathrm{D}}$ and $D_{\mathrm{D}}$ is matrix corresponding to individual devices. This simplifies to equation (4):

$$Y_{\mathrm{N}}\,\Delta v = C_{\mathrm{D}}\,\Delta x + D_{\mathrm{D}}\,\Delta v \tag{4}$$

Then the solution for the vector of voltages is given as equation (5):

$$\Delta v = (Y_{\mathrm{N}} - D_{\mathrm{D}})^{-1} C_{\mathrm{D}}\,\Delta x \tag{5}$$

Hence, the system of differential-algebraic equations becomes the system of only differential equations as (6):

$$\Delta x = A\,\Delta x + B\,(Y_N - D_D)^{-1} C_D\,\Delta x \quad (6)$$

Consequently, $A_{sys} = A + B\,(Y_N - D_D)^{-1} C_D$ is new system matrix with reduced algebraic equation. Thus, the small-signal stability can be analyzed by finding the eigenvalues of $A_{sys}$. Furthermore, the damping ratio $\zeta_i$ of individual eigenvalues might be evaluated using the following formula-(7):

$$\zeta_i = \frac{\sigma_i}{\sqrt{\sigma_i^2 + w_i^2}} \quad (7)$$

where the assumed form of the $i_{th}$ eigenvalue is $\lambda_i = \sigma_i + j\omega_i$. The eigenvalues of the system matrix obtained by previous computations are then used for comparing the stability of examined strategies. The Lyapunov indirect method provides insights into the system dynamics, where the system's ability to return to steady-state after a disturbance is determined by *max* (Re($\lambda$)). The damping ratio predicts whether oscillations dampen quickly or persist over time. Additionally, the participation factors for individual modes are calculated using equation-(8):

$$P_{k,i} = \frac{|\omega_{k,i}||v_{k,i}|}{\sum_{k=1}^{n}|\omega_{k,i}||v_{k,i}|} \quad (8)$$

where $\omega_{k,i}$ and $v_{k,i}$ are components of left and right eigenvectors corresponding to $i_{th}$ eigenvalue. The sum of all participation factors for individual modes equals unity.

Voltage source converter (VSC)

The VSC operates in either $P-V$ or $P-Q$ control mode. In $P-V$ control mode, the converter regulates active power ($P$) and voltage ($V$), while in $P-Q$ control mode, it manages fixed active power ($P$) and reactive power ($Q$). For this study, the reactive power in $P-Q$ mode is set to zero.

In grid-connected operation, inverter controls are implemented within the VSC framework using the synchronous $\boldsymbol{d-q}$ reference frame. The $\boldsymbol{V_{ac}-\Phi}$ (voltage–phase) control modulates the converter's terminal voltage magnitude to influence the phase angle between converter and grid voltages, thereby regulating active power flow across the coupling reactance—an approach commonly used in weak-grid or microgrid conditions where voltage–angle dynamics dominate power transfer. The $\boldsymbol{V_{ac}-P}$ (voltage–power) control simultaneously regulates voltage and active power, making it suitable for distribution-level PV inverters that must maintain bus voltage while supporting power balancing. In contrast, the $\boldsymbol{P-Q}$ (active–reactive power) control fully decouples real and reactive power through the $\boldsymbol{d-q}$ current components, enabling fast and independent regulation. This approach is most widely used in grid-tied converters and BESS systems, as it ensures compliance with grid-support requirements such as voltage regulation, reactive power injection, and dynamic stability enhancement. The summary of the inputs and outputs of the three control strategies are given in Table 1.

**Table 1:** Comparative Summary of Control Strategies

| Control Mode | Controlled Variables | Inputs | Outputs |
|---|---|---|---|
| $V_{ac}-\Phi$ | Voltage amplitude ($V_{ac}$) & phase angle ($\Phi$) | $V_{ref}$, $\Phi_{ref}$ | Converter voltage magnitude |
| $V_{ac}-P$ | Voltage amplitude & active power | $V_{ref}$, $P_{ref}$ | $V, P$ |
| $P-Q$ | Active and reactive power | $P_{ref}$, $Q_{ref}$ | $i_d, i_q$ |

2.2.1 PV Control

The P-V controller consists of an active power control loop and a voltage control loop. In (DIgSILENT, 2011), the control system as it appears in Power Factory is presented. In the model, the parameters can be varied to tune the converter to present the desired transient response. The active and voltage control loops are modeled as PI controllers in the $d-q$ reference frame, where active power is primarily regulated through the $d$-axis current and voltage magnitude through the q-axis current reference (Jerkø, 2014).

2.2.2 Active power control loop

The active power control loop is based on a PI controller and decides the active power output of the converter. The active power loop is illustrated in Figure 1.

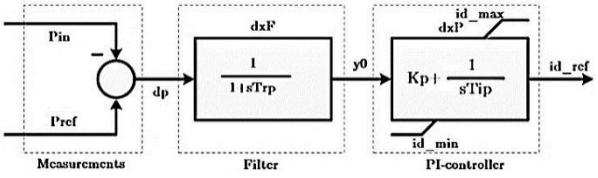



**Figure 1:** Active power control loop.

The first block in the illustration above measures the active power in ($P_{in}$) and computes the error ($d_p = P_{ref}$-$P_{in}$). $P_{ref}$ is the active power reference which can be controlled in per unit. The second block represents a low pass filter with the cut-off frequency as the parameter. $T_{rp}$ is the filter time constant for the active path, and it is a function of the cut-off frequency.

The third block represents a PI controller with defined maximum and minimum limits. This

controller comprises a proportional gain, $k_p$ , and an integrator time constant, $T_{ip}$ . The current in the d-axis, $i_{d,ref}$ , is the parameter limiting the active power. In the simulation events, the active power can be fixed at a desired value by controlling $i_{d,ref}$ . $i_{d,ref}$ is applied to an internal controller which produces the pulse width modulations ($P_{md}$) in the d-axis as show in Figure 2.

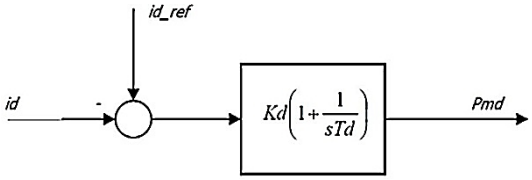



**Figure 2:** Block diagram of the built-in current controller in the d-axis (DIgSILENT, 2011).

The input currents to the controller are the AC-currents expressed in a reference frame defined by an input signal, $cos_{ref}$. The output signal is defined in the same reference frame and transformed back to a global reference using the same $cos_{ref}$. If the built-in current controllers are all set to zero ($k_p$ = 0, $T_{ip}$ = 0, $k_{iq}$ = 0, $T_{iq}$ = 0), the controller is disabled and the converter output current, $i_d$ , is equal to the input variable $i_{d,ref}$. Hence the PWM converter is operating as a current source (DIgSILENT, 2011). The Park Transformation, which describes the conversion from a three-phase sinusoidal signal into quantities in a two-axis reference, is presented in (DIgSILENT, 2011). In steady state analysis, $d_p$ = $i_{d,ref}$ = 0. When the simulation is run with dynamic conditions, these parameters differ from zero, and PI control is performed until $d_p$ is compensated.

2.2.3 Voltage control loop

1. The voltage control loop decides the voltage output of the converter. From the measurement blocks, Vin is measured using a special measuring device. $V_{ref}$ is the controllable reference voltage, while $dV$ is the voltage error. The second block in Figure 3 is the measurement filter, which is a low pass filter dependent on the cut-off frequency. The dead band with offset and limits contains the reactive current support characteristics. The dead band is set to zero in the simulations performed in this work.The last block, in the lower right corner of Figure 4, is a limited non-windup integrator which compensates for the error. This block also soothes out the response of the reactive current for large transients in the input voltage. $i_{q,ref}$ is, just like $i_{d,ref}$, applied to an internal PI controller which produces the q- axis pulse-width-modulations ($P_{mq}$).

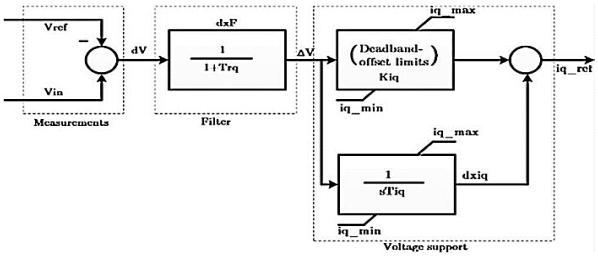



**Figure 3:** Voltage control loop.

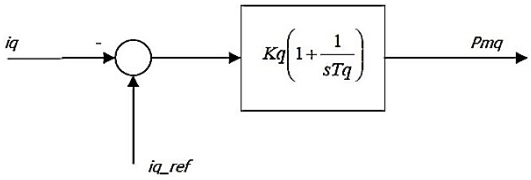



**Figure 4:** Block diagram of the built-in current controller in the q-axis (DIgSILENT, 2011).

where $k_i = sT_d$ which is integral gain and $k_d$ is the proportional gain and $\tau_i$ is the time-constant usually it is in the range of 0.5 to 5 $ms$ depending on the design speed then this can be expanded as shown in equation 9 & 10:

$$k_i = R/\tau_i \quad (9)$$

$$k_d = L/\tau_i \quad (10)$$

The reference frame defined by the input signal for the q- axis is given by $sin_{ref}$ . Setting the built-in controllers to zero will lead to a converter output current, $i_q$ , equal to the input variable $i_{q,ref}$ (Jerkø, 2014; DIgSILENT, 2011).

where $k_i = sT_d$ which is integral gain and $k_d$ is the proportional gain and $\tau_i$ is the time-constant usually it is in the range of 0.5 to 5 $ms$ depending on the design speed then this can be expanded as shown in equation 9 & 10:

$$k_i = R/\tau_i \quad (9)$$

$$k_d = L/\tau_i \quad (10)$$

The reference frame defined by the input signal for the q- axis is given by $sin_{ref}$. Setting the built-in controllers to zero will lead to a converter output current, $i_q$, equal to the input variable $i_{q,ref}$ (Jerkø, 2014; DIgSILENT, 2011).

## 3. RESULTS AND DISCUSSIONS

The simulation setup is based on the standard Western System Coordinating Council (WSCC) 3-machine, 9-bus test system, widely recognized for small-signal stability studies. The network comprises three two-winding transformers, six transmission lines, and three loads, with each synchronous generator modeled to include detailed voltage regulators, exciters, steam turbine–governor dynamics, and excitation systems. The generator operating conditions, which define the steady-state linearization point for modal analysis, are

summarized in Table 2. The negative reactive output of Gen 3 indicates absorption for voltage support, ensuring a realistic operating profile. These dispatch points serve as the initial equilibrium state for eigenvalue-based small-signal analysis. Time-domain simulations were conducted in DIgSILENT PowerFactory, with dynamic models implemented in DIgSILENT Simulation Language (DSL). The overall system configuration is shown in Figure 7.

**Table 2.** Generator operating conditions in the WSCC 9-bus system

| Generator | Active Power (MW) | Reactive Power (MVar) | Rating (MVA) | PF |
|---|---|---|---|---|
| Gen 1 | 71.6 | 27.0 | 247.5 | 0.85 |
| Gen 2 | 163.0 | 6.7 | 192.0 | 0.85 |
| Gen 3 | 128.0 | –10.9 | 128.0 | 0.85 |

## 4. SIMULATION RESULTS

This section presents three case studies on the WSCC 9-bus test system to evaluate its small-signal stability under varying conditions. Small-signal disturbances were introduced as ±5% step changes in the inverter control references—specifically, in the active power ($P_{ref}$) of the d-axis and voltage reference ($V_{ref}$) of the q-axis control loops at Bus 6, where PV and BESS units are integrated. The 0.1–0.5 seconds step duration simulated minor load fluctuations and control adjustments, keeping the system within the linear region for modal analysis. The resulting eigenvalues and participation factors were analyzed to assess damping and stability characteristics.

The first case study compares $V_{ac} - \Phi$, $V_{ac} - \mathrm{P}$, and $P - Q$ control modes, evaluating system performance through eigenvalue and damping ratio analysis across 19 modes and associated state variables. The second case study examines the effect of increasing PV penetration, highlighting reduced inertia and its influence on modal stability. The third case study explores BESS integration, showing how varying storage capacities enhance damping and mitigate low-inertia effects. Collectively, these studies provide a comprehensive evaluation of how inverter control, PV penetration, and BESS capacity influence the dynamic stability of the grid.

### *4.1 Case-I: Comparison among inverter control mode (i.e. $V_{ac} - \Phi, V_{ac} - P$ & $P - Q$) with fixed DC voltage source*

In this study, a fixed DC voltage source was applied, followed by an inverter at bus 6, and three control modes— $V_{ac} - \Phi$ , $V_{ac} - \mathrm{P}$ , and $P - Q$ —were successively implemented to observe their impact on the stability of the system. The PV inverter at Bus 6 is modeled as a 60 MVA PWM converter (100 kV DC, 10 kV AC, 10% short-circuit impedance, 1.0 p.u. voltage reference) operating under sinusoidal modulation [Kiasari et al., 2024]. During small-signal disturbances, its $P - Q$ or $V_{ac} - \mathrm{P}$ control loops adjust the d–q current references within the linear modulation range, maintaining stable power injection and voltage support [(Hamid et al., 2023), (Aljarrah et al., 2024)]. Although its capacity is smaller than the synchronous generators of the WSCC system (247.5, 192.0, and 128.0 MVA)—approximately 24% of Gen3 and 31% of Gen2—the inverter's fast dynamic response enables it to provide disproportionately high damping and voltage regulation [Hamid et al., 2023]. Thus, the inverter acts as an active stability resource, with its rating and control strategy directly influencing eigenvalue trajectories, damping ratios, and modal participation, thereby enhancing small-signal stability in renewable-integrated power systems [(Ali et al., 2024), (Pandey & Prasad, 2024)]. The resulting eigenvalues, damping ratios, and eigenvalue plots are presented in Table 3 and Figure 5.

**Table 3.** Eigenvalue and damping ratio of different control conditions with constant voltage source

| Mode No. | Control Condition | Eigen Value $\lambda_i = \sigma_i + J\omega_i$ | Damping Ratio |
|---|---|---|---|
| 3 | $V_{ac} - \Phi$ | $-0.62 + 9.607i$ | 0.063 |
| | $V_{ac} - \mathrm{P}$ | $-0.62 + 9.589i$ | 0.064 |
| | $P - Q$ | $-14.79 + 0.668i$ | 0.998 |
| 4 | $V_{ac} - \Phi$ | $-0.62 - 9.607i$ | 0.063 |
| | $V_{ac} - \mathrm{P}$ | $-0.62 - 9.589i$ | 0.064 |
| | $P - Q$ | $-14.79 - 0.668i$ | 0.998 |
| 5 | $V_{ac} - \Phi$ | $-0.52 + 6.195i$ | 0.083 |
| | $V_{ac} - \mathrm{P}$ | $-0.514 + 6.26i$ | 0.082 |
| | $P - Q$ | $-15 + 0.26i$ | 0.99 |
| 6 | $V_{ac} - \Phi$ | $-0.52 - 6.195i$ | 0.083 |
| | $V_{ac} - \mathrm{P}$ | $-0.514 - 6.26i$ | 0.082 |
| | $P - Q$ | $-15 - 0.26i$ | 0.99 |
| 7 | $V_{ac} - \Phi$ | $-14.48 + 0.5i$ | 0.99 |
| | $V_{ac} - \mathrm{P}$ | $-14.48 + 0.515i$ | 0.99 |
| | $P - Q$ | $-15.61 + 0.403i$ | 0.99 |
| 8 | $V_{ac} - \Phi$ | $-14.48 - 0.5i$ | 0.99 |
| | $V_{ac} - \mathrm{P}$ | $-14.48 - 0.515i$ | 0.99 |
| | $P - Q$ | $-15.61 - 0.403i$ | 0.99 |

Table 3 highlights the comparison of eigenvalues and damping ratios for the dominant modes, specifically modes 3, 4, 5, 6, and 8. The analysis reveals that the $V_{ac} - \Phi$ and $V_{ac} - \mathrm{P}$ control modes exhibit similar small-signal stability, as their eigenvalue positions are nearly identical. However, a significant shift in eigenvalues from the right to the left half-plane was

observed when the $P-Q$ control mode was applied, indicating an improvement in the system's inertial response and overall stability. Additionally, the damping ratio, a critical indicator of stability, showed a substantial increase under the P-Q control mode compared to the $V_{ac}-\Phi$ and $V_{ac}-\mathrm{P}$ modes, as summarized in Table 3.

P modes, as summarized in Table 3.

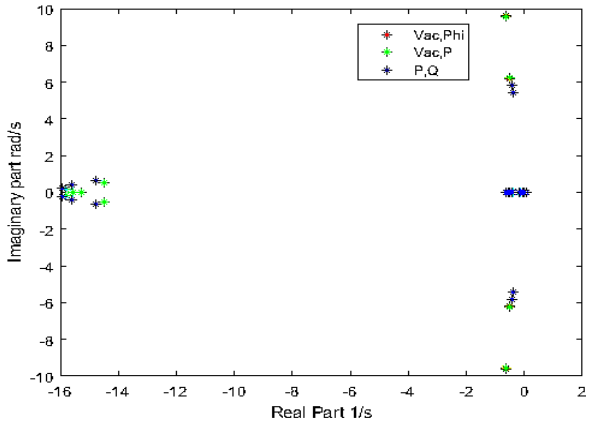
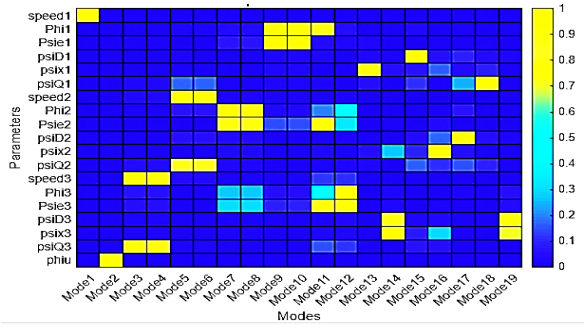
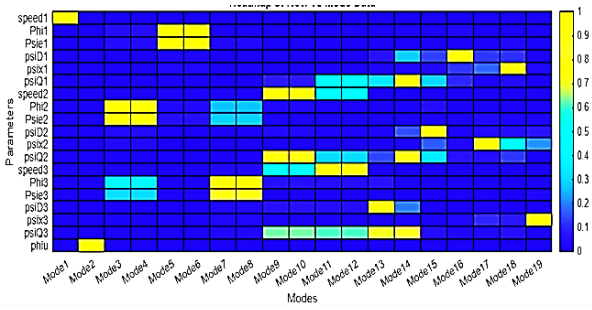



**Figure 5:** Eigenvalues plot in three control conditions with constant voltage source at Bus 6

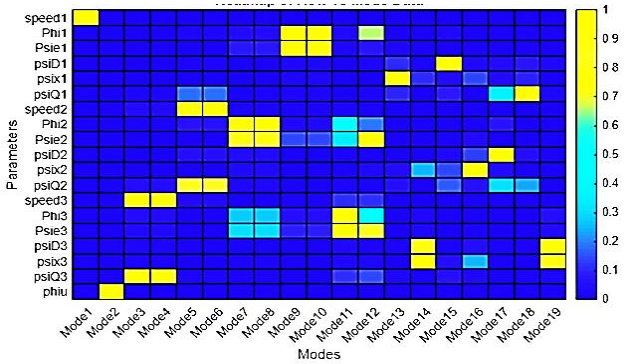
Among the three control strategies, the maximum real part of the eigenvalues (Re(λ)) was observed under the $P-Q$ control mode, demonstrating its superior ability to handle stability challenges more effectively than the other modes. These findings underscore the effectiveness of the $P-Q$ control strategy in enhancing both small-signal stability and overall system performance.




(a)




(b)




(c)

**Figure 6:** Matrix of participation factors under different control conditions with constant Voltage source (a) $V_{ac}-\Phi$ (b) $V_{ac}-\mathrm{P}$ and (c) $P-Q$

The participation matrices, represented in Figure 6 (a) — (c), illustrate the contribution of state variables to different modes under $V_{ac}-\Phi$, $V_{ac}-\mathrm{P}$, and $P-Q$ control conditions, respectively, with a constant voltage source. In the $V_{ac}-\Phi$ control condition (Figure 2), dominant contributions are observed from variables like rotor angle (Φ), flux in D- winding (psiD), and flux in Q-winding (psiQ), particularly in critical modes 3, 4, 5, and 6, highlighting a concentrated influence of generator-related dynamics.

In contrast, the $V_{ac}-\mathrm{P}$ control condition (Figure 2) shows a broader spread of participation across modes, with significant contributions from variables such as flux in x-winding (psix), excitation flux (psie), and speed, reflecting a more distributed interaction between state variables and modes.

Meanwhile, the $P-Q$ control condition (Figure 6(c)) exhibits a much more uniform distribution of participation factors across modes, effectively leveraging a wider range of state variables, including rotor angle, fluxes (psiD, psiQ, psix), and excitation flux, which enhances interaction with both dominant and non-dominant modes. The $P-Q$ control strategy's broader and more balanced participation across modes aligns with its observed superiority in improving small-signal stability, as evidenced by significant eigenvalue shifts and increased damping ratios. This highlights the robustness of $P-Q$ control in addressing stability challenges by engaging a wider spectrum of dynamic variables, offering improved overall system performance compared to $V_{ac}-\Phi$ and$V_{ac}-\mathrm{P}$ control strategies.

### 4.2 Case-II: Variation of solar PV penetration level

In the second case study, a solar PV system has been connected at bus 6, replacing the constant voltage source. The PV system is integrated through an inverter that implements a $P-Q$ control algorithm, known for its superior performance in maintaining system stability. To evaluate the impact of PV penetration on grid stability, the PV penetration level at bus 6 has been varied. A significant observation

from this study is that PV systems inherently lack inertia. As the penetration level of PV increases, the overall system inertia diminishes. This reduction in inertia adversely affects system stability, as evident from the eigenvalue data presented in Table 4. For example, in Mode 14, the real part of the eigenvalue Re(λ) shifts progressively from -0.19 to -0.11 as the PV penetration level increases from 10 MW (6 Mvar) to 100 MW (60 Mvar). A similar trend is observed in Mode 15. This shift of eigenvalues toward the right indicates a reduction in system stability.

Furthermore, the damping ratio decreases with increasing PV penetration. In Mode 14 and Mode 15, the damping ratio declines from 0.825 to 0.756 as PV penetration increases. This behavior is attributed to the diminishing system inertia, which makes the grid more susceptible to instability. The eigenvalue plot (Figure 8) and the participation matrix (Figure 9) corroborate these findings, showing that higher PV penetration levels lead to a less stable system. Therefore, as the level of PV integration increases, it is critical to adopt measures to mitigate the resulting stability challenges.

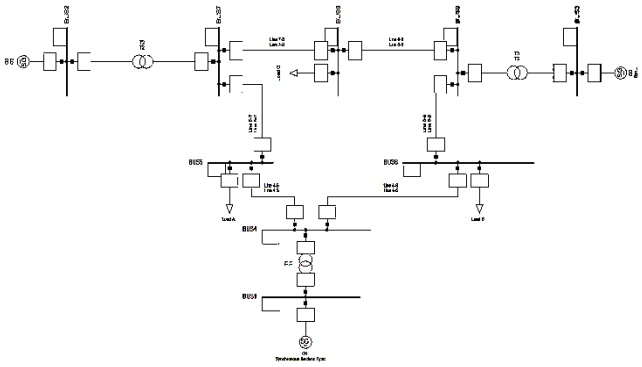


**Figure 7:** Western System Coordinated Council (WSCC) 3- machine, 9-bus system

**Table 4.** Eigenvalue and damping ratio with variable PV penetration level.

| Mode No. | PV Penetration Level | Eigen Value $\lambda_i = \sigma_i + J\omega_i$ | Damping Ratio |
|---|---|---|---|
| 14 | 10 MW, 6 Mvar | $-0.19 + 0.135i$ | 0.825 |
| | 50 MW , 12 Mvar | $-0.17 + 0.118i$ | 0.822 |
| | 100 MW, 60 Mvar | $-0.11 + 0.096i$ | 0.756 |
| 15 | 10 MW, 6 Mvar | $-0.19 - 0.135i$ | 0.825 |
| | 50 MW , 12 Mvar | $-0.17 - 0.118i$ | 0.822 |
| | 100 MW, 60 Mvar | $-0.11 - 0.096i$ | 0.756 |
| 17 | 10 MW, 6 Mvar | $-0.144 + 0i$ | 1 |
| | 50 MW , 12 Mvar | $-0.063 + 0i$ | 1 |
| | 100 MW, 60 Mvar | $-0.094 + 0i$ | 1 |
| 18 | 10 MW, 6 Mvar | $-0.103 + 0i$ | 1 |
| | 50 MW , 12 Mvar | $-0.1004 + 0i$ | 1 |
| | 100 MW, 60 Mvar | $-0.074 + 0i$ | 1 |

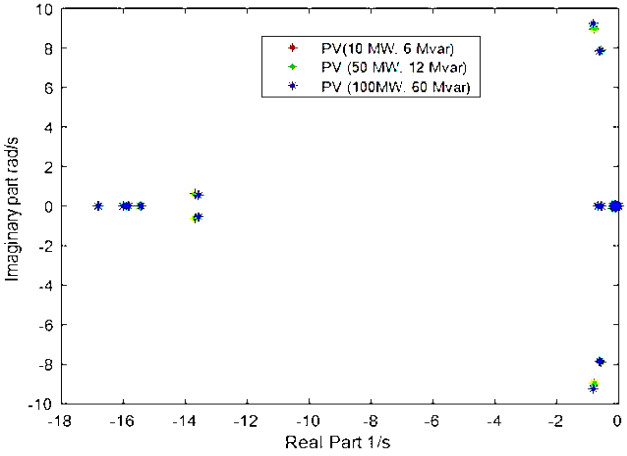
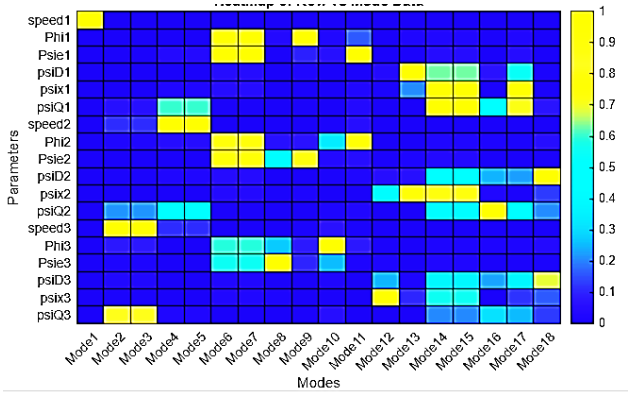
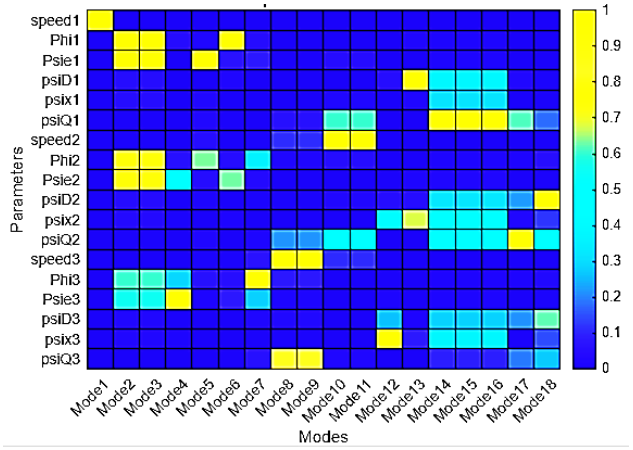



**Figure 8:** Eigenvalues plot for three different PV penetration level at Bus 6.

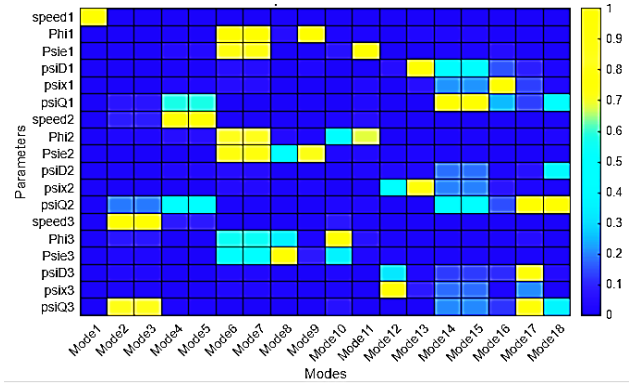
The figures (Fig. 10 (a) — (c)) illustrate the participation factor matrices for various modes under increasing PV penetration levels: 10 MW (6 Mvar), 50 MW (12 Mvar), and 100 MW (60 Mvar), respectively. In Fig. 10 (a), corresponding to 10 MW PV penetration, the participation factors are concentrated in a few modes, with notable activity around Modes 2, 6, and 10. The factors exhibit lower magnitudes overall, primarily under 0.4, suggesting minimal interaction of PV with the system modes at this penetration level.




(a)




(b)




(c)

**Figure 9:** Matrix of participation factors due to PV penetration (a) 10 MW, 6 Mvar (b) 50 MW, 12 Mvar and (c) 100 MW, 60 Mvar.

In Figure 9 (b), at 50 MW penetration, the intensity of participation factors increases significantly, especially in Modes 3, 6, and 14, with magnitudes ranging from 0.5 to 0.7. This indicates an escalation in PV's influence on system dynamics as penetration grows, with a redistribution of dominance across modes.

In Figure 9 (c), at 100 MW penetration, participation factors expand across multiple modes, including Modes 2, 7, 9, and 17, with some values exceeding 0.8. This widespread distribution highlights the profound effect of high PV penetration on system modal dynamics, potentially introducing new stability challenges. These observations underline a clear trend: as PV penetration increases, its impact on the system becomes more extensive and pronounced, emphasizing the need for adaptive control strategies to manage dynamic interactions and maintain system stability effectively.

4.3 Case-III: Solar PV and Variation of integrated BESS size

To address the reduction in system inertia caused by solar PV integration, a BESS has been deployed alongside the solar PV system at bus 6. The BESS in this study is modeled in $P-Q$ control mode using a PWM converter, enabling independent active and reactive power exchange for grid support. Unlike synchronous machines, it does not provide rotational inertia but contributes synthetic inertia via fast control loops that respond to frequency deviations. The low power factor (PF = 0.51) assumption for both PV and BESS represent a stress-test condition, consistent with IEEE 1547-2018 and IEEE P2800 provisions for non-unity PF operation during voltage regulation, weak-grid support, or disturbance events. This deliberate choice allows the analysis to capture system dynamics under reactive-power-dominant operation, providing a rigorous evaluation of stability. In this analysis, the solar PV output is fixed at 100 MW and 60 Mvar, while the BESS size is varied between 20 MW (10 Mvar) and 50 MW (5 Mvar) to assess its impact on system stability.

**Table 5.** Eigenvalues and damping ratio with battery integration with PV at Bus 6.

| Mode No. | Battery Size | Eigen Value $\lambda_i = \sigma_i + J\omega_i$ | Damping Ratio |
|---|---|---|---|
| 6 | 20 MW, 10 Mvar | $-13.55 + 0.516i$ | 0.99 |
| | 50 MW, 5 Mvar | $-13.56 + 0.527i$ | 0.99 |
| 7 | 20 MW, 10 Mvar | $-13.55 - 0.516i$ | 0.99 |
| | 50 MW, 5 Mvar | $-13.56 - 0.527i$ | 0.99 |
| 15 | 20 MW, 10 Mvar | $-0.087 + 0.096i$ | 0.672 |
| | 50 MW, 5 Mvar | $-0.098 - 0.095i$ | 0.72 |
| 16 | 20 MW, 10 Mvar | $-0.087 - 0.096i$ | 0.672 |
| | 50 MW, 5 Mvar | $-0.182 + 0i$ | 1 |

As shown in Table 5, the integration of a larger BESS significantly improves the stability of dominant modes such as 6, 7, 15, and 16. For instance, in mode 15, the real part of the eigenvalue Re(λ) shifts from -0.087 to -0.098 as the BESS size increases. A similar leftward shift is observed in Mode 16, where Re(λ) changes from -0.087 to -0.182. Additionally, the damping ratio improves, indicating enhanced stability.

For example, the damping ratio in mode 15 increases from 0.672 to 0.72 with higher BESS integration, and in Mode 16, it improves from 0.672 to 1. The enhanced performance is attributed to the inertial support provided by the BESS, which compensates for the reduced inertia caused by high PV penetration. Consequently, the stability of the grid improves significantly, as corroborated by the eigenvalue plot in Figure 10. This highlights the importance of BESS in mitigating the adverse effects of renewable energy integration on grid stability.

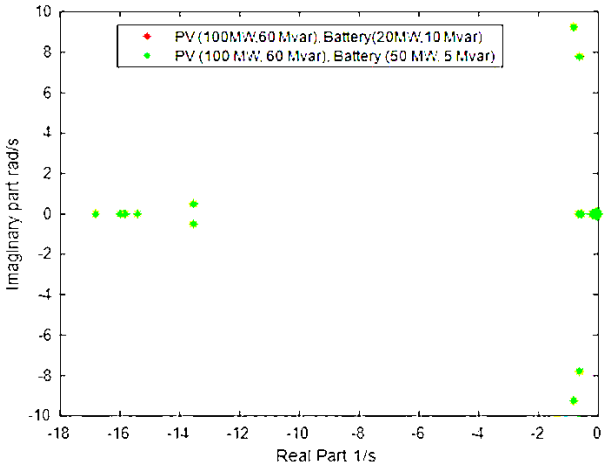
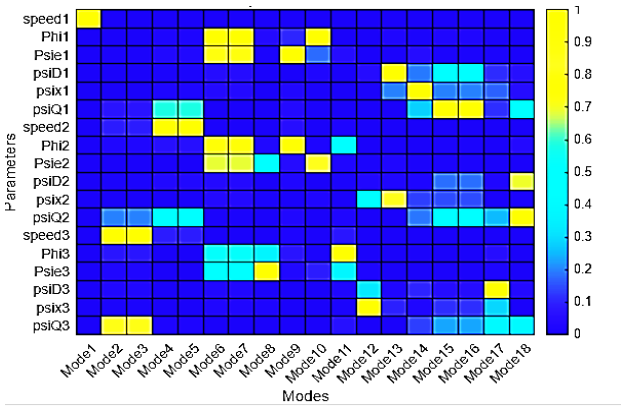


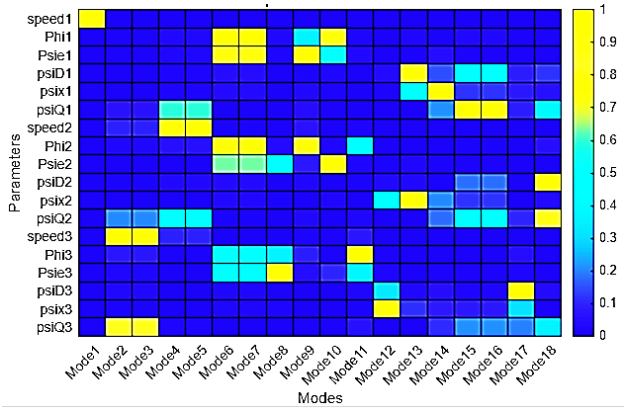

**Figure 10:** Eigenvalues plot due to battery penetration with solar PV at Bus-6

The two figures, Figure 11 (a) and Figure 11 (b), depict the matrices of participation factors for different configurations of a combined PV and BESS.

In both cases, the PV system is rated at 100 MW and 60 Mvar, while the battery capacities differ: 20 MW with 10 Mvar in Figure 11 (a) and 50 MW with 5 Mvar in Figure 11 (b). These matrices show the contributions of various system states (phi, psiD, psiQ, psix, psie, and speed) to the system's dynamic modes (Mode 1 to Mode 18).




(a)




(b)

**Figure 11:** Matrix of participation factors with PV (100 MW, 60 Mvar) & BESS (a) 20 MW, 10 Mvar and (b) 50 MW, 5 Mvar

In Figure. 11 (a), higher participation factors are observed in Modes 3, 6, and 15 for several states, indicating these modes play a critical role in system behavior under this configuration. For instance, the state "phi" shows a strong interaction with Mode 6, while "psiQ" and "psie" exhibit notable contributions to Mode 15. Similarly, "speed" exhibits increased participation in Modes 3 and 6. The distribution of the participation factors is spread across multiple modes, but the intensity is concentrated in specific state-mode pairs, suggesting a dominant influence on those dynamics. In Figure 11 (b), the increased battery capacity (50 MW, 5 Mvar) results in noticeable changes in the distribution of participation factors. Modes 7 and 12 exhibit heightened activity compared to Figure 11 (a), with states such as "psiQ" and "psix" showing significant contributions. For example, the state "psiQ" demonstrates strong interaction with Mode 7, while "psix" and "psie" have more prominent participation in Mode 12. Additionally, "speed" shows altered contributions, with its influence becoming more distributed across Modes 9, 12, and 16 compared to Figure 11 (a).

These changes indicate that increasing the battery capacity significantly impacts the system's modal behavior. The shifts in dominant modes and state contributions underscore the role of battery sizing in modulating system dynamics and enhancing stability. This comparison highlights the critical influence of combined PV and battery systems on participation factors and provides insights into the dynamic interplay between state variables and system modes under varying configurations.

## 5. DISCUSSION

This paper presents three case studies conducted on a standard 9-bus system to evaluate stability issues under varying conditions. The first case study investigates the performance of three inverter control strategies— $P-Q$ control, $V_{ac}-\Phi$ , and $V_{ac}-P$ under small-signal stability analysis.

The results show that the $P-Q$ control strategy outperforms $V_{ac}-\Phi$ and $V_{ac}-\mathrm{P}$ in terms of stability, primarily due to the superior operation of the VSC with built-in current controllers, as discussed in Section 2.4. Analytical evaluation of the control loop constants demonstrates the effectiveness of $P-Q$ control in optimizing proportional gains ($k_p$, $k_{iq}$) and integrator time constants ($T_{ip}$, $T_{iq}$), resulting in a distinct leftward shift in eigenvalues, signifying enhanced damping and system inertia.

The superior performance of the $P-Q$ control strategy can be theoretically attributed to its decoupled control of active ($P$) and reactive ($Q$) power, allowing independent modulation of real and reactive

components through the $d-q$ reference frame. In this configuration, the d-axis current directly influences active power, while the q-axis current controls reactive power. This separation minimizes cross-coupling between voltage and frequency responses, enhancing dynamic stiffness and improving damping of oscillatory modes. In contrast, $V_{ac}-\Phi$ and $V_{ac}-\mathrm{P}$ control depend on voltage-angle or voltage-power coupling, where interactions between voltage magnitude and phase introduce slower dynamic responses and potential instability under weak-grid conditions. Hence, the $P-Q$ strategy results in higher damping ratios and eigenvalue shifts toward the left-half plane, consistent with small-signal stability improvement.

For instance, the eigenvalue of mode 3 for $V_{ac}-\Phi$ control was $-0.62+9.607i$ with a damping ratio of 0.063, while $V_{ac}-\mathrm{P}$ control yielded $-0.62+9.589i$ ($\zeta=0.064$). In contrast, the $P-Q$ inverter control strategy achieved $-14.79+0.668i$ with an exceptionally high damping ratio of 0.998, confirming its superior small-signal performance.

The second case study examines varying solar PV penetration levels. Since PV systems lack mechanical inertia, increasing their penetration reduces overall system inertia and stability. For mode 15, eigenvalues shifted from $-0.19+0.135i$ (10 MW PV) to $-0.11+0.096i$ (100 MW PV), while damping ratios decreased from 0.825 to 0.756—indicating a rightward pole shift and reduced stability as PV penetration increases.

To mitigate these inertia-related stability issues, the third case study integrates a BESS alongside PV. Increasing the BESS size from 20 MW to 50 MW shifted the eigenvalue of mode 16 from $-0.087-0.096i$ to $-0.182+0i$, improving the damping ratio from 0.672 to 1.0, thus confirming its strong stabilizing influence.

The superior performance of BESS arises from its ability to emulate virtual inertia and provide fast frequency and voltage support. The converter-based BESS reacts almost instantaneously to power imbalances by modulating active and reactive power through its control loops, enhancing damping and reducing frequency excursions. The coordinated action of its active/reactive power control loops and PWM converter dynamics allows rapid adjustment to grid disturbances, improving overall dynamic stability. Overall, the findings demonstrate that combining the $P-Q$ control strategy with optimally sized BESS significantly enhances small-signal stability in PV-integrated power systems by compensating for reduced inertia and improving damping performance across dominant modes.

## 6. CONCLUSION

This study investigated the impact of inverter control strategies, solar PV penetration, and Battery Energy Storage System (BESS) integration on the small-signal stability of the WSCC 9-bus system. Three inverter control methods—$V_{ac}-\Phi$, $V_{ac}-\mathrm{P}$, and $P-Q$—were analyzed using modal and participation factor analysis to assess their influence on system damping and dynamic performance. The results revealed that the $P-Q$ control strategy provides the most significant improvement in stability, demonstrating a clear eigenvalue shift from $-0.62+9.607i$ ($V_{ac}-\Phi$) and $-0.62+9.589i$ ($V_{ac}-\mathrm{P}$) to $-14.79+0.668i$ ($P-Q$), with the damping ratio increasing markedly from 0.063 to 0.998. This improvement confirms the effectiveness of $P-Q$ control in enhancing both inertia emulation and oscillation damping under small disturbances.

The study further examined the effect of increasing PV penetration, which led to a progressive rightward shift in eigenvalues (e.g., $-0.19+0.135i$ to $-0.11+0.096i$) and a reduction in damping ratio from 0.825 to 0.756, indicating that higher PV integration weakens system inertia and stability. To counteract this, BESS integration was analyzed, showing that enlarging BESS capacity from 20 MW to 50 MW shifted eigenvalues from $-0.087-0.096i$ to $-0.182+0i$, improving the damping ratio from 0.672 to 1.0. This demonstrates the crucial role of BESS in restoring system stability through fast active–reactive power control and synthetic inertia support.

Overall, the findings highlight that advanced inverter control strategies—particularly $P-Q$ control—combined with appropriately sized BESS can effectively mitigate the stability challenges introduced by high PV penetration. These results provide practical insight into the design of resilient, low-inertia power systems, ensuring improved damping, frequency regulation, and voltage support in future renewable-dominated grids.

## ACKNOWLEDGMENTS

The authors would like to thank MIST for providing the necessary facilities and technical support required to successfully conduct the experimental investigations of this study.

## DATA AVAILABILITY STATEMENT

Datasets generated during the current study are available from the corresponding author upon reasonable request.

## FUNDING DECLARATION

This research was self-funded.

## ETHICS APPROVAL

This study is an engineering experimental investigation. The MIJST Research Ethics Committee has confirmed that formal ethical approval was not required.

## ETHICS, CONSENT TO PARTICIPATE, AND CONSENT TO PUBLISH

Not applicable.

## COMPETING INTERESTS

The authors declare that they have no competing interests.

## AUTHOR CONTRIBUTIONS

Author 1: Md. Mahadi Hasan - visualization, original draft preparation, review and editing of the manuscript and final approval of the manuscript.

Author 2: Md. Imranul Hasan Emon - Formal analysis, experimental investigation, data acquisition, and review and editing of the manuscript, drafting the paper.

Author 3: Hasan Monir - Conceptualization, methodology development, Supervision, project administration, and final approval of the manuscript.

Author 4: Md Ahsan Kabir - Drafting the initial manuscript and critical revision of the manuscript.

## ARTIFICIAL INTELLIGENCE ASSISTANCE STATEMENT

Portions of this manuscript were assisted by an artificial intelligence language model (ChatGPT, OpenAI). The tool was used solely for language editing, text refinement, and clarity improvement. All content, data interpretation, analysis, conclusions, and final decisions were generated, verified, and approved by the authors. The authors take full responsibility for the accuracy and integrity of the manuscript.

## CONFLICT OF INTEREST DECLARATION

The authors declare that they have no conflicts of interest.

## REFERENCES

Ali, Z. M., Ćalasan, M., Jurado, F., & Aleem, S. H. A. (2024). Complexities of power quality and harmonic-induced overheating in modern power grids studies: Challenges and solutions. IEEE Access.

Akatsuka, M., Hara, R., Kita, H., Ito, T., Ueda, Y., & Saito, Y. (2010, June). Estimation of battery capacity for suppression of a PV power plant output fluctuation. In 2010 35th IEEE Photovoltaic Specialists Conference (pp. 000540–000543). IEEE.

Alias, F., & Singh, M. (2021). Damping sensitivity analysis and optimized battery controller for small-signal stability enhancement in wind penetrated networks. Sustainable Energy, Grids and Networks, 26, 100441.

Aljarrah, R., Fawaz, B. B., Salem, Q., Karimi, M., Marzooghi, H., & Azizipanah-Abarghooee, R. (2024). Issues and challenges of grid-following converters interfacing renewable energy sources in low inertia systems: A review. IEEE Access, 12, 5534–5561.

Biroon, R. A., Pisu, P., & Schoenwald, D. (2020, February). Large-scale battery energy storage system dynamic model for power system stability analysis. In 2020 IEEE Texas Power and Energy Conference (TPEC) (pp. 1–5). IEEE.

Boscaino, V., Ditta, V., Marsala, G., Panzavecchia, N., Tinè, G., Cosentino, V., … & Di Cara, D. (2024). Grid-connected photovoltaic inverters: Grid codes, topologies and control techniques. Renewable and Sustainable Energy Reviews, 189, 113903.

Cheah-Mane, M., Egea-Alvarez, A., Prieto-Araujo, E., Mehrjerdi, H., Gomis-Bellmunt, O., & Xu, L. (2023). Modeling and analysis approaches for small-signal stability assessment of power-electronic-dominated systems. Wiley Interdisciplinary Reviews: Energy and Environment, 12(1), e453.

Chen, Q., Bu, S., & Chung, C. Y. (2023). Small-signal stability criteria in power electronics-dominated power systems: A comparative review. Journal of Modern Power Systems and Clean Energy, 12(4), 1003–1018.

Das, T., & Aliprantis, D. C. (2008, November). Small-signal stability analysis of power system integrated with PHEVs. In 2008 IEEE Energy 2030 Conference (pp. 1–4). IEEE.

Daud, M. Z., Mohamed, A., Wanik, M. C., & Hannan, M. A. (2012, December). Performance evaluation of grid-connected photovoltaic system with battery energy storage. In 2012 IEEE International Conference on Power and Energy (PECON) (pp. 337–342). IEEE.

DIgSILENT. (2011). DIgSILENT PowerFactory Technical Reference Documentation: PWMConverter ElmVsc, ElmVscmono. DIgSILENT GmbH.

Emrani, A., Achour, Y., Sanjari, M. J., & Berrada, A. (2024). Adaptive energy management strategy for optimal integration of wind/PV system with hybrid gravity/battery energy storage using forecast models. Journal of Energy Storage, 96(112613), 112613.

Gali, V., Jamwal, P. K., Gupta, N., & Kumar, A. (2023). Multimode control strategy to improve the power quality and autonomy of PV–Wind–BESS-based microgrid using harmonic frequency adaptive observer filter. Electric Power Systems Research, 225, 109786.

Hamid, A. K., Mbungu, N. T., Elnady, A., Bansal, R. C., Ismail, A. A., & AlShabi, M. A. (2023). A systematic review of grid-connected photovoltaic and photovoltaic/thermal systems: Benefits, challenges and mitigation. Energy & Environment, 34(7), 2775–2814.

Hill, C. A., Such, M. C., Chen, D., Gonzalez, J., & Grady, W. M. (2012). Battery energy storage for enabling integration of distributed solar power generation. IEEE Transactions on Smart Grid, 3(2), 850–857.

International Renewable Energy Agency. (2022, July). Renewable power remains cost-competitive amid fossil fuel crisis. https://www.irena.org/...

Iyer, V. M., Gulur, S., & Bhattacharya, S. (2018). Small-signal stability assessment and active stabilization of a bidirectional battery charger. IEEE Transactions on Industry Applications, 55(1), 563–574.

Jamal, T., Urmee, T., Calais, M., Shafiullah, G. M., & Carter, C. (2017). Technical challenges of PV deployment into remote Australian electricity networks: A review. Renewable and Sustainable Energy Reviews, 77, 1309–1325.

Jerkø, A. (2014). Reactive Power and Voltage Control of Offshore Wind Farms (Master's thesis).

Kåberger, T. (2018). Progress of renewable electricity replacing fossil fuels. Global Energy Interconnection, 1(1), 48–52.

Kiasari, M., Ghaffari, M., & Aly, H. H. (2024). A comprehensive review of the current status of smart grid technologies for renewable energies integration

and future trends: The role of machine learning and energy storage systems. Energies, 17(16), 4128.

Koohi-Kamali, S., Rahim, N. A., & Mokhlis, H. (2014). Smart power management algorithm in microgrid consisting of photovoltaic, diesel, and battery storage plants considering variations in sunlight, temperature, and load. Energy Conversion and Management, 84, 562–582.

Lu, Z., Chen, Y., & Fan, Q. (2021). Study on feasibility of photovoltaic power to grid parity in China based on LCOE. Sustainability, 13(22), 12762.

Makarov, Y. V., Lu, S., Ma, J., & Nguyen, T. B. (2008). Assessing the value of regulation resources based on their time response characteristics (No. PNNL-17632). Pacific Northwest National Laboratory.

McGinn, D., Galán, E. M., Green, D., CEC, C. E. C., Junfeng, L., Hinrichs-Rahlwes, R., … & Lins, C. (2013). REN21 Renewables 2013 Global Status Report.

Muriuki, J. K., Muriithi, C. M., Ngoo, L., & Nyakoe, G. N. (2016). Assessment of VSC-HVDC system for transient stability improvement of a power system with large wind power injection.

Powerfactory, D. (2011). Powerfactory user's manual. DIgSILENT GmbH. Powerfactory, D. (2011). Powerfactory user's manual. DIgSILENT GmbH. Milan.

Qiao, L., Xue, Y., Kong, L., & Wang, F. (2024). Small-signal stability analysis for large-scale power electronics-based power systems. IEEE Open Access Journal of Power and Energy, 11, 280–292.

Ali, S. Z., Nahian, M. K., & Hoque, M. E. (2023). Chapter 19—Extraction of cellulose from agro-industrial wastes. In S. Bhawani, A. Khan, & F. Ahmad (Eds.), Extraction of Natural Products from Agro-Industrial Wastes (pp. 319–348). Elsevier. https://doi.org/10.1016/B978-0-12-823349-8.00013-7

Ram, M., Child, M., Aghahosseini, A., Bogdanov, D., Lohrmann, A., & Breyer, C. (2018). A comparative analysis of electricity generation costs from renewable, fossil fuel and nuclear sources in G20 countries for the period 2015–2030. Journal of Cleaner Production, 199, 687–704. \

REN21. (2023). Renewables 2023 Global Status Report. https://www.ren21.net/...

Renné, D. S. (2022, February). The opportunities and challenges for 100% renewable energy. In Sustainable Energy Development and Innovation (pp. 495–503). Springer.

Roser, M. (2020). Why did renewables become so cheap so fast? Our World in Data.

Shaw, P., & Kumar, P. (2016, November). Small signal stability analysis of a battery connected standalone photovoltaic system. In 2016 7th India International Conference on Power Electronics (IICPE) (pp. 1–6). IEEE.

Shivashankar, S., Mekhilef, S., Mokhlis, H., & Karimi, M. (2016). Mitigating methods of power fluctuation of photovoltaic (PV) sources—A review. Renewable and Sustainable Energy Reviews, 59, 1170–1184.

Tavakoli, A., Saha, S., Arif, M. T., Haque, M. E., Mendis, N., & Oo, A. M. (2020). Impacts of grid integration of solar PV and electric vehicle on grid stability, power quality and energy economics: A review. IET Energy Systems Integration, 2(3), 243–260.

Teng, J. H., Luan, S. W., Lee, D. J., & Huang, Y. Q. (2012). Optimal charging/discharging scheduling of battery storage systems for distribution systems interconnected with sizeable PV generation systems. IEEE Transactions on Power Systems, 28(2), 1425–1433.

Vetoshkin, L., & Müller, Z. (2021). A comparative analysis of a power system stability with virtual inertia. Energies, 14(11), 3277.

Wiser, R. H., Mills, A. D., Seel, J., Levin, T., & Botterud, A. (2017). Impacts of variable renewable energy on bulk power system assets, pricing, and costs.

Zeng, J., Zhang, B., Mao, C., & Wang, Y. (2006). Use of battery energy storage system to improve power quality and stability of wind farms. In 2006 International Conference on Power System Technology (pp. 1–6). IEEE.

MIJST
*MIST International Journal of Science and Technology*

# Power Consumption Analysis of UAVs with Varying Payloads for Next Generation Wireless Networks

**Saif Ahmed*, and Nimul Islam Emon**

Department of Electrical and Electronic Engineering, Bangladesh University of Engineering and Technology (BUET), Dhaka-1000, Bangladesh

***Corresponding Email:** *saift6700@gmail.com*

**ARTICLE INFO**

**Article History:**

*Received: 24th January 2024*
*Revised: 27th September 2025*
*Accepted: 28th October 2025*
*Published: 30th December 2025*

**Keywords**:

*Unmanned Aerial Vehicle(UAV)*
*Power Consumption of UAV*
*Payload*
*Wireless Network*
*UAV-enabled communication network*

**ABSTRACT**

Unmanned Aerial Vehicles (UAVs) are emerging as an important component for enhancing the coverage and capacity of next generation wireless networks. However, the use of UAVs is challenging because of crucial power management. The power management becomes more sophisticated for rotary-wing UAVs, the most commonly used ones, which require more energy as payload and flight actions increase. The current study investigates the energy consumption of UAVs with varied payloads during hovering and moving operations. The effects of payloads such as cameras, sensors, GPS modules, communication systems, and flight controllers on UAV power consumption are investigated in this study. It is very much necessary to comprehend these energy dynamics for optimal UAV design and maximizing operational effectiveness. Key findings show how payload configuration and flying conditions affect energy requirements. Two regression-based empirical mathematical models for hovering and moving conditions representing the relationship between the power consumption of UAV and its weight with payloads are proposed. This rigorous analysis of power consumption of UAV provides valuable insights into optimizing UAV design and operation in next-generation wireless networks. The findings of the work, including the proposed mathematical models, are expected to help researchers and engineers develop more energy-efficient UAVs, resulting in extended flight periods and improved operational reliability.

This work is licensed under a *Creative Commons Attribution-Non-commercial 4.0 International License.*

## 1. INTRODUCTION

Unmanned Aerial Vehicles (UAVs), sometimes known as drones, have emerged as critical technologies in a variety of fields such as communication, surveillance, disaster management, and logistics. Their ability to work autonomously, navigate difficult terrain, and deliver cost-effective solutions for a variety of applications makes them important in today's technological environments (Jiang *et al*., 2021). With the emergence of next-generation wireless networks such as 6G, UAVs are being envisioned as a revolutionary instrument for improving communication coverage, maintaining seamless connectivity, and meeting the ever-increasing need for high-speed, low-latency networks (Zeng *et al*., 2016). These UAV-based aerial systems are anticipated to provide support for ultra-reliable low-latency communication (URLLC), massive machine type communication (mMTC), and enhanced mobile broadband (eMBB) services (Horsemanheimo *et al*., 2022). The use of UAV in wireless networks tends to make a dramatic impact in this field. The importance of UAVs in wireless communication has changed dramatically over the previous decade. In fact, integrating UAVs as communication equipment represents a paradigm shift in 6G wireless networks. Traditional communication networks sometimes fail to provide coverage in distant, disaster-prone, or densely populated urban regions. UAVs, which serve as aerial base stations or relays, can bypass these constraints by providing dynamic and adaptable communication platforms, as suggested by (Huang *et al*., 2020) and (Na *et al*., 2020). UAVs' flexibility allows them to address major difficulties like line-of-sight communication, interference mitigation, and network densification, all of which are required for the successful deployment of 6G networks (Huang *et al*., 2020). Another promising use of UAV can be as an aerial base station (Ahmed *et al*., 2020). UAVs can be deployed for remote sensing applications (Bhardwaj *et al*., 2016). However, despite their enormous advantages, significant problems remain in integrating UAVs into next-generation networks. One of the most significant challenges is energy efficiency, which has a direct impact on operating reliability, coverage area, and flight endurance (Chowdhury *et al*., 2020).

Rotary-wing UAVs, such as quadcopters and hexacopters, are extremely useful since they can take advantage of VTOL (vertical take-off and landing) capabilities. Such properties make them appropriate for applications requiring positioning in place, precision maneuvering, or deployment in very limited spaces (Zeng *et al*., 2019). However, these UAVs consume more power than their fixed-wing equivalents, owing to the constant energy demand required to oppose gravity and sustain lift (Gong *et al*., 2023). The addition of payloads such as cameras, sensors, communication modules, and batteries increases energy consumption, reducing the operational endurance (Kottat *et al*., 2023). This involves a thorough examination of the elements that influence power consumption, as well as strategies for optimizing energy usage, particularly under various payload combinations and flight conditions.

Payloads have an important role in defining UAV capability and power requirements. The variety of payloads used in UAV operations reflects the wide range of their applications. Cameras and sensors are essential for surveillance, mapping, and environmental monitoring (Almalki *et al*., 2020). GPS and communication modules provide real-time navigation and data transmission, which is essential for maintaining network connectivity and dependability (Jin *et al*., 2022). Flight controllers and other onboard electronics are required to ensure UAV stability and control, which adds to the total weight and energy needs. The interaction of payload weight, power consumption, and flight dynamics highlights the necessity for a thorough investigation to optimize UAV performance, particularly in scenarios requiring lengthy flight durations and large payload capacity (Mozaffari *et al*. 2016). Apart from energy, meeting sustainable and ecologically friendly solutions concerning both network and technological aspects is simultaneously fostering the growing need for UAV wireless communication. How critical these become factors in enabling a trend like this – that is, solar or hybrid UAVs remain under intensive investigation by authors of related works: Lee *et al*. (2017) and Sun *et al*. (2019). On the other hand, solar-powered UAVs become practical options for extending flight times by exploiting such technologies, and due regard must be given to efficiency in gathering energy and payload limits. According to Huang *et al*. (2020), understanding the complex balance between energy generation, storage, and consumption shall be the key towards developing UAV systems for next-generation wireless networks. Some other challenges related to it were also pointed out by Kathole *et al*. (2022) and Ye *et al*. (2020).

Several studies have acknowledged the critical impact of payload and energy consumption on the operational performance of UAVs. However, the works offered limited insights into detailed power consumption modelling under varying payload conditions. (Chowdhury *et al*., 2020) emphasized the importance of energy efficiency in determining UAV coverage, endurance, and reliability. While this study successfully identified energy consumption as a constraint in UAV-enabled communication networks, it did not provide a deep analysis of how various payload configurations affect power consumption. (Huang *et al*., 2020) emphasized the energy constraints of UAVs as a major technical impediment and concentrated on the integration of UAVs into next-generation wireless networks, particularly 6G. Although their work emphasized the significance of establishing a balance between payload, communication needs, and power, it lacked a thorough examination of the patterns of power consumption related to payloads under various operating situations. Due to the continual energy needed to provide lift, rotary-wing UAVs are inherently energy inefficient, as addressed by (Gong *et al*., 2023). The importance of power consumption characteristics in hovering and maneuvering activities was reaffirmed by this investigation. However, their works did not include any empirical or simulation-based evaluation of various payload scenarios. Kottat *et al*. (2023) explicitly investigated the impact of payload augmentation, such as the addition of sensors and communication modules, on UAV energy consumption and flying time. Although it acknowledged that energy requirements increase with higher payloads, the study lacked quantitative modelling or systematic comparisons of power consumption with various payload settings.

In this paper, an extensive analysis of the power consumption of UAVs has been presented with various payload configurations. The significant contributions of our work are noted below.

i. This analysis examines the power consumption of rotary-wing UAVs with different payload configurations, with a focus on future wireless networks.

ii. A MATLAB simulation model is used to analyze the power consumption of UAVs with various payloads.

iii. Unlike earlier studies that analyze the effect of payload on UAV energy consumption only quantitatively, this paper provides two empirically validated regression models for power consumption in both hovering and movement modes, based on realistic payload configurations and actual component weights.

Such findings will help engineers and researchers to develop energy-efficient UAV systems so that these fulfil the exacting demands of next-generation wireless networks.

## 2. UNMANNED AERIAL VEHICLE (UAV)

Unmanned Aerial Vehicles (UAVs) are remotely piloted or autonomous aircraft for different purposes. Although originally developed for military operations, UAVs nowadays are in wide use for civilian applications like surveillance, disaster management, environmental monitoring, and next-generation wireless networks (Zeng *et al*., 2016). Without an onboard human operator, UAVs are able to accomplish tasks in hazardous or unreachable areas, which enhances safety and efficiency. UAVs have evolved from specialist uses to mainstream technologies, altering industries including logistics, telecommunications, and disaster management. Their ability to adapt to various operational requirements is an important component of their expanding utility. For example, in next-generation wireless networks, UAVs act as aerial base stations,

ensuring continuous connectivity in locations where terrestrial networks are unavailable or insufficient. UAVs can be used for many works, such as aerial base stations and IoT applications. It can be used in mobile crowd sensing, as suggested by (Zhou *et al*., 2018). In crisis events, they provide immediate situational awareness, aiding rescue teams in traversing difficult terrain and locating victims.
The critical factors of energy consumption in UAV operations are linked to the payload weight, flight dynamics, and environmental conditions. Rotary-wing UAVs, especially, need much power for hovering and vertical take-off. Further work in the area is aimed at energy harvesting and lightweight material advancement that might improve flight endurance.

### *2.1 Types of UAV*

UAVs can be broadly divided into two categories based on their structure and working principle. These are:

***A) Rotary-wing UAV:*** A rotary-wing UAV, a drone, or a helicopter type of UAV has lifting and propulsion created by rotating wings. These can be very nimble, taking off and landing vertically, enabling this class to work in minimal areas. Since their rotor system creates their lift force, they also are capable of hovering, omnidirectional flight, and precise translation. Rotary-wing UAVs are widely used in surveillance, aerial photography, search and rescue operations, and environmental monitoring (Zeng *et al*., 2019). They can be equipped with various sensors for performing various specialized tasks. They vary in size, from small hobbyist models to large industrial systems, and offer flexibility for both civilian and military operations. These types are the commonly used UAVs. However, they can be used for various state-of-the-art applications, like aerial base stations and IoT-based functions. In this study, the analysis is carried out with rotary-wing UAVs.

***B) Fixed -wing UAV:*** A fixed-wing UAV is similar to a standard airplane, providing lift through its fixed wings and can't hover or stop in a position like its rotor-wing family since lift generation doesn't occur through stillness and needs forward movement. They come designed for more fuel-efficient long over the distance distances and higher airspeeds, making them ideal candidates for mapping, surveying, environmental monitoring missions and military scout work. The flight endurance and range of fixed-wing UAVs are generally longer than that of rotary-wing drones, and therefore they are more appropriate for area coverage at a large scale (Templin *et al*., 2017). A fixed-wing UAV consists of a fuselage, wings, and a propulsion system that normally includes a small internal combustion or electric engine. Fixed-wing UAVs can take off from runways or catapult systems and land autonomously on prepared surfaces or with parachutes. Fixed-wing UAVs are normally used in applications that require long flight times and large coverage areas due to their effective aerodynamics.

## 3. POWER CONSUMPTION IN UAV

Power consumption in UAVs is a significant element that can influence flying performance, endurance, and operating capabilities. Most UAVs are powered by batteries, fuel cells, or hybrid power systems, which combine multiple sources of energy. A UAV's power consumption is determined by a variety of factors, including its design, weight, flight circumstances, and the activities it performs. Understanding power consumption is critical for increasing flight duration, improving energy efficiency, and achieving mission objectives. It has been already stated that UAVs can play a significant role in wireless communication. However, various applications in this field need to satisfy various requirements and thus require a considerable amount of power (Solyman *et al*., 2021). The main power consumption in rotary-wing UAVs is for the rotation of the rotors and is also enhanced by the use of payloads to some extent. Temperature, altitude, and turbulence are some of the environmental elements that affect battery performance and UAV efficiency. To overcome these issues, UAV developers are looking into advanced solutions such as high-density batteries, solar-powered propulsion, and energy harvesting devices. Flying path optimization and adaptive energy allocation systems, sometimes powered by artificial intelligence, are being used to reduce waste and increase flying time. As UAVs play more intricate roles in industries such as telecommunications, agriculture, and emergency services, understanding their power consumption dynamics is critical to realizing their full potential.

### *3.1 Power Consumption Factors in UAV*

***A. Weight and Payload:*** The UAV's overall weight, including its payload, has a big influence on how much power it uses (Kottat *et al*., 2023). UAVs can be of various sizes and weights. A list of different classes of UAV based on their weights is given in (Lykou *et al*., 2020). Especially when carrying extra gear like cameras, sensors, or communication systems, heavier UAVs need more energy to take off and stay in the air. In addition to increasing drag, larger payloads demand more power to overcome air resistance.

***B. Flight Speed and Altitude:*** Flight speed and altitude determine the energy usage for UAVs. As the speed is increased, more aerodynamic drag is encountered. This results in higher power requirements. At a higher altitude, the energy expenditure is higher as the air becomes denser, leading to reduced lift. Most of the UAVs flying at a lower altitude operate with a greater efficiency of energy usage since there is denser air, making lift easier to sustain.

***C. The Nature of Flight Duration and The Type of Mission:*** In general, power consumption is related to mission and flight duration; long-endurance flights, as it were, to be used in either surveillance or observing the environment sustainably keep UAVs flying, whereas short, intensive missions, such as finding and rescuing a target, may make use of bursts of high power and quick maneuvering.

***D. Aerodynamics:*** It is very important in terms of power consumption; the more a UAV is designed to be aerodynamic, the less drag it produces, hence less use of

energy to maintain flight. Besides, it is in the design of the wings, the fuselage, and rotor systems that together give the general efficiency of the UAV. More efficient UAVs aerodynamically will have longer flight times using the same amount of energy input.

If rotary-wing UAV is considered, the power consumption during hovering can be given by the equation (Dorling *et al*., 2016),

$$P_{hover} = \frac{T^{\frac{3}{2}}}{\sqrt{2 \times \rho \times A_{rotor} \times n}} \quad (1)$$

where,
$P_{hover}$ = Power required for hovering by the UAV
$T$ = Thrust required to keep the UAV in air = Weight of the UAV in Newton
$\rho$ = Air density
$A_{rotor}$ = Area of the rotor of the UAV
$n$ = No. of rotors
The UAV will also need to move when necessary. The power consumption during movement can be calculated by using the equation (Thibbotuwawa *et al.*, 2019),

$$P_{flight} = \frac{1}{2} \times C_D \times A_{rotor} \times \rho \times v^3 + \frac{W^2}{\rho \times b^2 \times v} \quad (2)$$

where,
$P_{flight}$ = Power required during movement by the UAV
$C_D$ = Drag coefficient
$W$ = Weight of the UAV in Newton
$\rho$ = Air density
$A_{rotor}$ = Area of the rotor of the UAV
b = width of the UAV
$v$ = velocity of the UAV

### *3.2 Payloads Used in UAV*

UAV payloads are the equipment carried for special missions in addition to the flight components. These payloads consist of cameras, sensors, communication devices, and delivery systems. They enable UAVs to perform a variety of activities, including airborne photography, surveillance, environmental monitoring, and disaster response. Advanced payloads such as LiDAR and thermal imaging broaden UAV applications to include precision agriculture, infrastructure inspection, and search and rescue operations. The kind and weight of the payload have a considerable impact on the UAV's flight duration, power consumption, and range. Modern UAVs are designed to carry modular payloads, providing flexibility and adaptation across industries and mission needs. In this work, the use of the following five payloads is considered.

***A. Camera:*** UAV cameras can collect photos and videos which can be used in applications including surveillance, mapping, and aerial photography. They range from basic RGB cameras to complex models such as thermal and multispectral cameras. The quality of the camera used is determined by the mission's requirements, with characteristics such as zoom, stabilization, and resolution adapted to individual applications. Lightweight cameras are commonly used in UAV applications to minimize payload weight. For instance, the Raspberry Pi Camera Module v2.1 weighs approximately 3g. However, more advanced cameras can weigh around 75g (Douklias *et al*., 2022).

***B. Sensor:*** Sensors in UAVs gather data for navigation, stability, and environmental awareness. Gyroscopes, accelerometers, barometers, and ultrasonic sensors are among the most common types. Light Detection and Ranging (LiDAR) and infrared sensors provide advanced applications such as obstacle detection, 3D mapping, and environmental monitoring. Different types of sensors are used for performing different types of work. (Sørensen *et al*., 2017) provided the weights of various sensors that are used with UAVs ranging from 2 to 4 gm. A Teensy 3.1 development board, often used in sensor modules, weighs around 30g. Combining such a board to use various sensors can total around 60g.

***C. GPS Module:*** GPS modules offer location data to UAVs, allowing for accurate navigation and flight path execution. They provide autonomous flight, waypoint tracking, and geofencing. This function is of great importance in wireless communications. Advanced GPS systems, such as RTK (Real-Time Kinematics), provide centimetre-level accuracy, which is essential for precision agriculture, surveying, and other jobs that need great positional accuracy. GPS modules designed for UAVs are typically lightweight. GPS modules can weigh from 20g to 30 g (Ukaegbu *et al*., 2021).

***D. Communication Module:*** Communication modules enable data flow between UAVs and ground control stations. Telemetry and command communication are carried out by technologies such as Wi-Fi, Bluetooth, and RF. Advanced modules enable long-distance connection and real-time video streaming, providing effective control and monitoring even in demanding conditions. Modern communication modules enable high data speeds and minimal latency by leveraging modern technologies such as 5G/6G transceivers, software-defined radios, and millimetre-wave communication. These modules, which account for a considerable portion of the UAV's total power consumption, must strike a balance between performance and energy economy. Optimizing their architecture is critical for long-term UAV operation and stable connectivity in next-generation networks. The weight of communication modules can vary greatly depending on their capabilities (Douklias *et al*., 2022). Although the precise weight isn't stated, a total weight of about 200g can be considered for a complete communication setup when taking into account extra parts like antennae and housings.

***E. Flight Controller:*** The flight controller is the UAV's brain, managing stability, navigation, and sensor integration. It processes input from sensors and user commands to control motors and actuators. Modern flight controllers support autonomous features like obstacle avoidance, GPS-based navigation, and real-time adjustments, ensuring efficient and safe UAV operation. Different lightweight flight controllers are suitable for use in a UAV system. Flight controllers typically weigh from 100g to 120g (Unmanned Systems Technology, 2024).

## 4. OVERVIEW OF THE SYSTEM

### *4.1 UAV System Description*

In this work, a rotary-wing UAV is considered for carrying

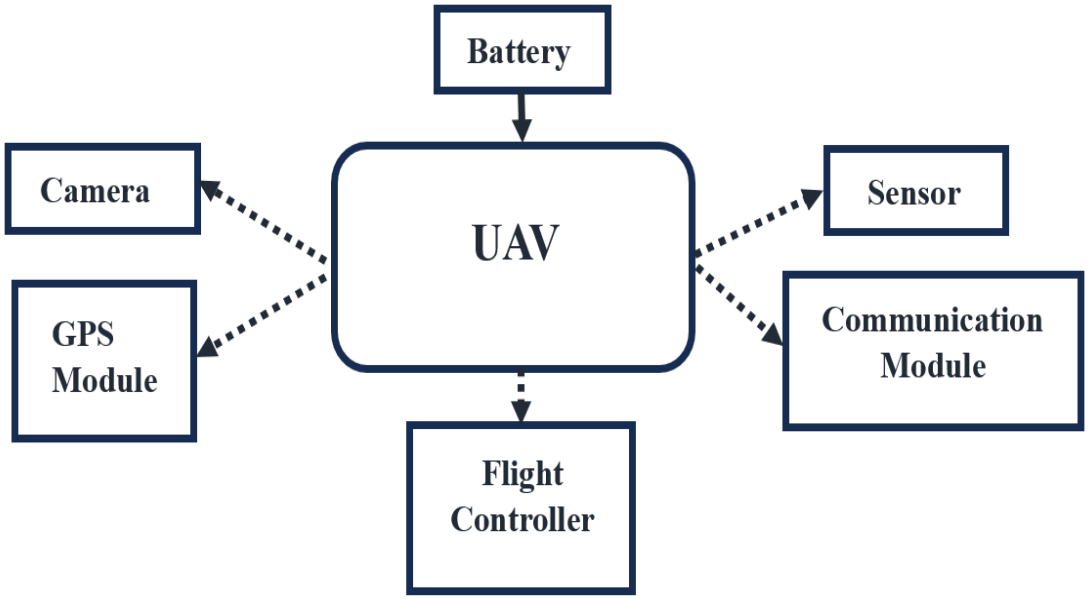



**Figure 1:** Block diagram of the UAV system

out the analysis. The UAV is equipped with some payloads necessary for performing specific tasks. A simple block diagram of the considered system is shown in Figure 1. The simulation and the power consumption analysis of the system are carried out using MATLAB. After that, an empirical model is suggested denoting the relationship between the power consumption of UAV and the payload weights.

### *4.2 Weights of Different Payloads*

In this system, one rotary-wing UAV weighing 1.5 kg (with a battery) and five payloads with different weights are used. The used payloads are a camera, a sensor, a GPS module, a communication module and a flight controller. The weights of these payloads are listed in Table 1 according to (Douklias *et al*., 2022), (Sørensen *et al*., 2017) and (Ukaegbu *et al*., 2021).

**Table 1**
Weights of the components used in the model

| Payload | Weight (g) |
|---|---|
| UAV (with battery) | 1500 |
| Camera | 75 |
| Sensor | 60 |
| GPS Module | 25 |
| Communication module | 200 |
| Flight controller | 110 |

## 5. METHODOLOGY OF WORK

In this paper, the power consumption analysis of UAV is performed in a systematic way. First, a UAV of weight 1.5 kg (with battery) and five different payloads shown in Table 1 are selected. Then simulation of the UAV system is done with different payload configurations. After obtaining the power consumption values from the simulation, a regression-based empirical model is developed to denote the relationship between power consumption and overall weight of UAV. The flow of work is shown in Figure 2.

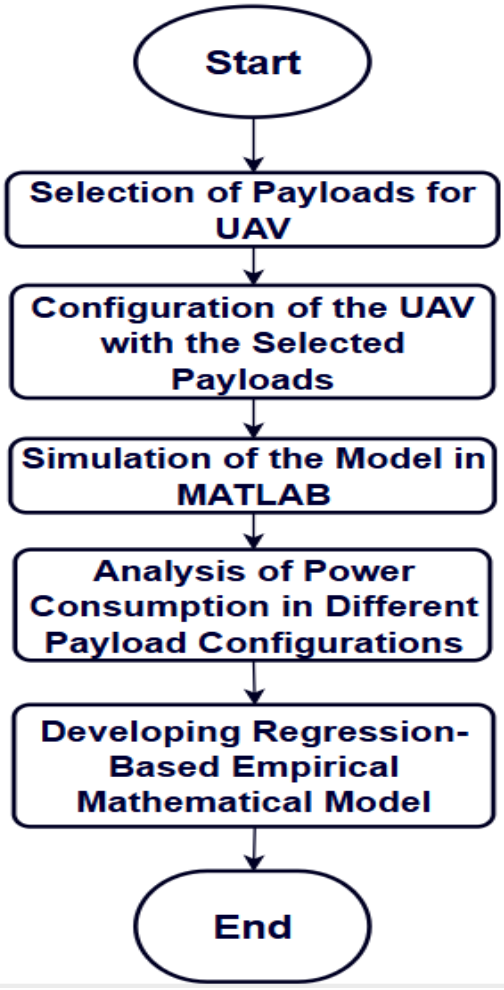



**Figure 2**: Flowchart representing the workflow

## 6. RESULTS AND DISCUSSIONS

### *6.1. Simulation Results of the System:*

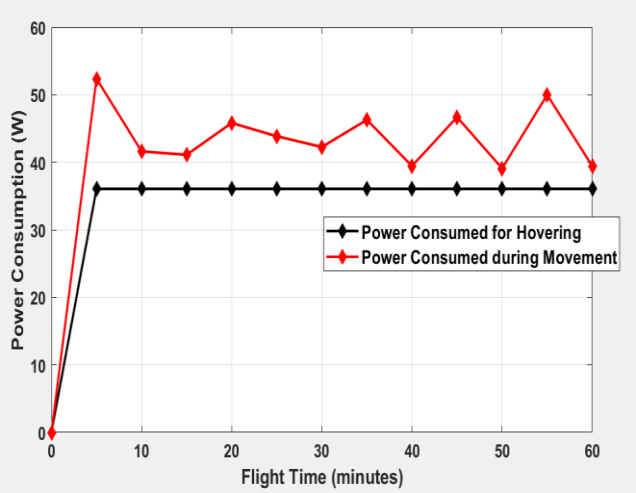



**Figure 3:** Power consumption of UAV without payloads

Figure 3 depicts power consumption in a UAV without payloads. It displays the consumed power without payloads in two scenarios: hovering and movement. Figure 1 shows that the power usage when hovering remains constant throughout the flight time. The UAV's constant power requirements for hovering are 36.06 W. If the UAV is only hovering, it will consume 36.06 W of power during its flight. However, power does not remain constant while moving. The drag constant is the parameter that causes it to vary in our considered system in moving state.

The drag constant varies according to the changing nature of the air and the UAV's movement. When no payload is employed, the UAV's power consumption during movement ranges between 39.10 W and 52.38 W. Figure 1 shows that the largest power consumption while movement occurs during a 5-minute flight time, which is 52.38 W. The power consumed during the 20-minute bout is 45.82 W. The minimum power consumption of 39.1 W occurs during a 50-minute trip. The graph shows that power consumption during movement is always greater than hovering power.

The UAV system used here is equipped with a 14.8 V, 5000 mAh battery. So, the battery has a capacity of 74 Wh or 4,440 watt-minutes. Figure 4 shows the state of the battery with the charge of the battery during both hovering and movement without payloads throughout its flight.

Figure 4 shows that after 60 minutes of hovering in one position, the energy left in the UAV's battery is 2276 watt-minutes (37.93 Wh). If the UAV moves during its flight, the battery will have 1800 watt-minutes, or 30 Wh, left after an hour. This graph verifies results of Figure 1 that power consumption during movement exceeds that during hovering. During hovering, the battery charge is 3358 watt-minutes after 30 minutes, decreasing to 2276 watt-minutes after 60 minutes. The battery charge is 3105 watt-minutes after 30 minutes of movement and reduces to 1800 watt-minutes at the end of an hour of flight.

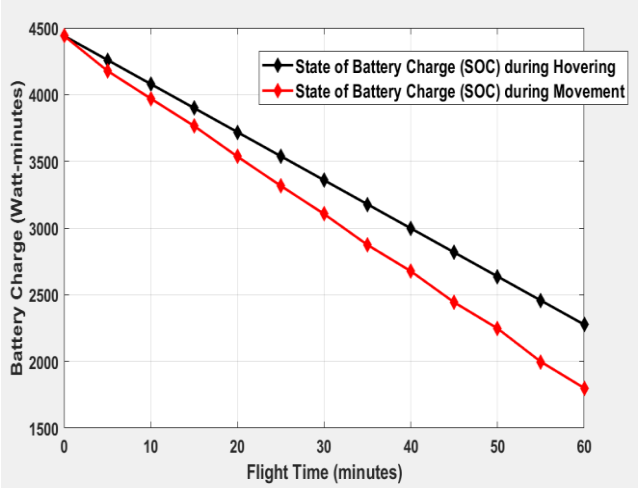



**Figure 4:** State of battery charge (SOC) without using payloads

Now, the analysis of power consumption is carried out by using payloads. The analysis is carried out for hovering and moving conditions separately. The analysis is done for the hovering condition first.

In Figure 5, the consumption of power with and without payloads during hovering is illustrated. It is seen that the power consumption is fixed throughout the flight of the UAV. As seen from Figure 1, the power consumption remains fixed during hovering. The main focus of this graph is to provide a picture of how power consumption increases when payloads are used. When the five payloads, with a total weight of 470 g, are used, the power consumption gets increased. The consumption of power gets increased to 54.28 W, which is 36.06 W when no payload is used. So, an increase in power consumption by 18.22 W can be seen when an additional weight of 470 g is used with the UAV.

Now, an analysis of the state of battery charge is provided for this case. Figure 6 shows the remaining battery charge in the UAV at different times during 1 hour of hovering in the air. It shows a gradual decrease in battery power.

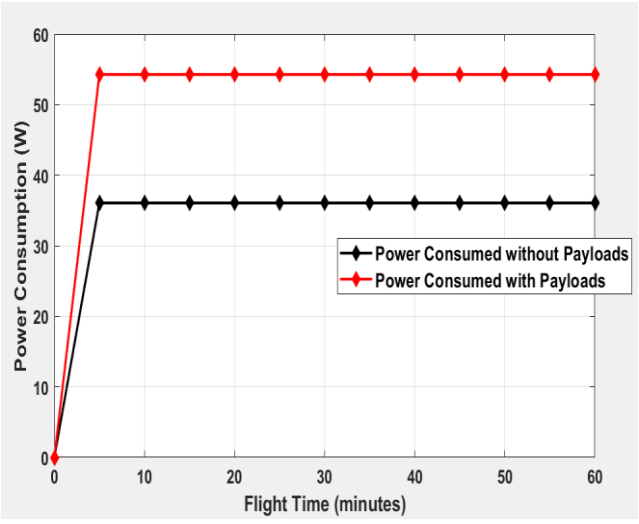



**Figure 5:** Power consumption of UAV during hovering

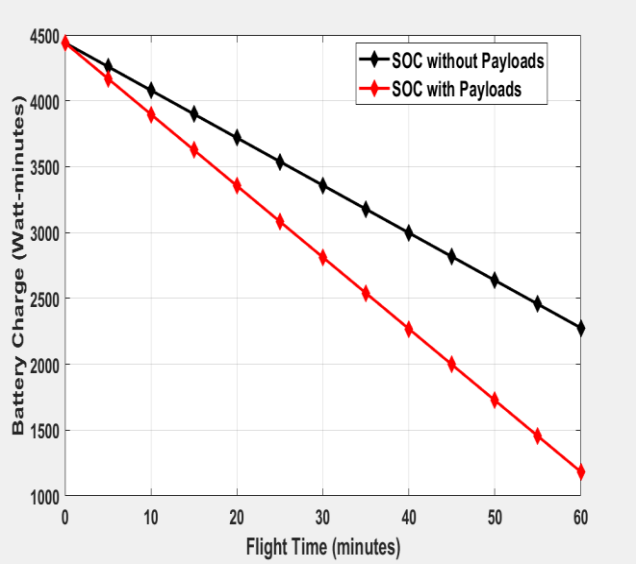



**Figure 6:** State of battery charge (SOC) during hovering

Figure 6 shows that the charge remaining in the UAV's battery after hovering for 60 minutes is 2276 watt-minutes (37.93 Wh). The battery power after 20 minutes of flying is 3719 watt-minutes. After 20 minutes, or 40 minutes of flight, the battery capacity drops to 3538 watt-minutes. After another 20 minutes, or one hour of flight, the power lowers to 2276 watt-minutes (37.93 Wh). When payloads are employed, the battery charge after an hour of hovering is 1183 watt-minutes (19.72 Wh). After 20 minutes of flight, the battery charge level is 3354 watt-minutes. After 40 minutes of flight, the battery power reaches 2269 watt-minutes. When it flies for more than 20 minutes, it drops again, eventually reaching 1183 watt-minutes (or 19.72 Wh).

When payloads are utilized, the remaining battery charge after an hour of hovering is lower than when no payload is used. It is less because more power is required to operate the UAV while carrying payloads. As payloads are employed with UAVs, their weight increases, and they require more thrust to stay in the air by overcoming gravitational force.

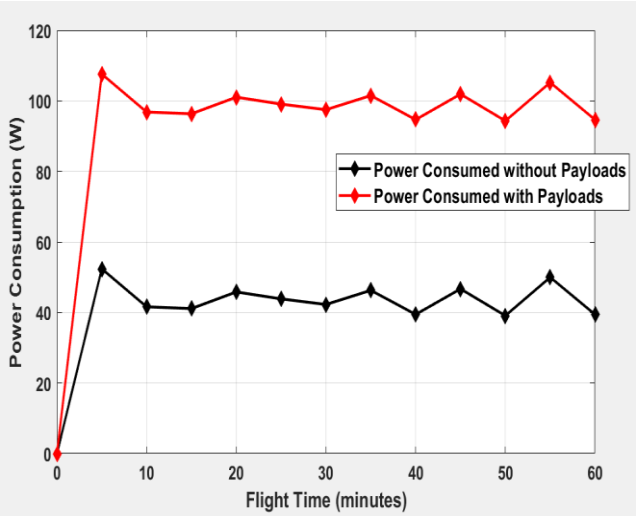



**Figure 7:** Power consumption of UAV in moving condition

In Figure 7, the power consumed by the UAV during movement is illustrated. When the UAV moves without using any payload, the maximum power consumption is 52.38 W, while it increases to 107.6 W when the mentioned payloads are used. So, a significant increase in power consumption is seen when payloads are used. The power consumption increases by 55.22 W. The increase is so high, as the power consumption in moving condition depends on the square of the total weight of the UAV. That means, while moving, payloads play a vital impact on power consumption. So, the weight of the payload needs to be carefully determined by looking at the energy constraints.

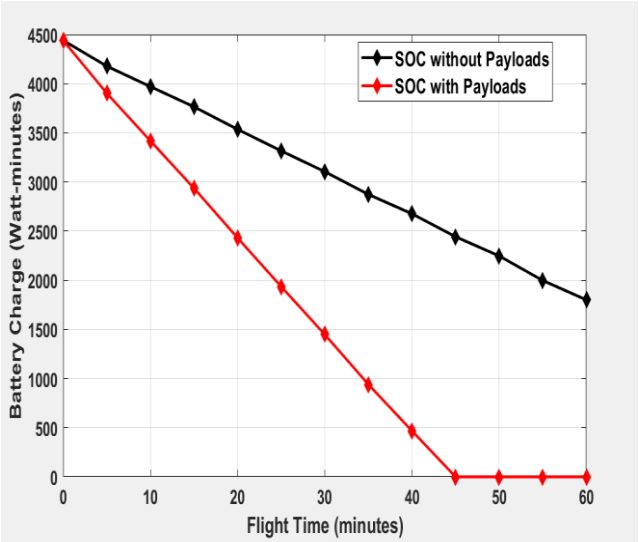



**Figure 8:** State of battery charge (SOC) in moving condition

In Figure 8, the state of battery charge is shown for moving condition. Without payload, after completing a flight of 1 hour, the remaining battery capacity is 1800 watt-minutes or 30 Wh. But when the payloads are used, the battery capacity is 1448 watt-minutes or 24.13 Wh after 30 minutes of flight. So, in this case, a power of 49.87 W has been consumed in 30 minutes. With the remaining power in the battery, it cannot continue to fly for 1 hour. The battery power becomes 0 after 45 minutes of flying. That means, the weight of payloads significantly affects the flight time of UAV. So, while configuring a UAV, the payload weights must be carefully fixed by considering the flight requirements and the availability of power.

Figure 9 illustrates how the weight of the UAV affects its power usage. The payload weight has already been shown to have a substantial impact on the power consumption of UAVs. So, it is very vital to understand the link between weight and power consumption of UAVs.

In this study, the UAV's body weight with battery is 1.5 kg. At a weight of 1.5 kg, the power consumption for hovering is 36.06 W, whereas it is 72.02 when moving. When the UAV's total weight with camera reaches 1.575 kg, the power consumption for hovering and movement is 38.80 W and 77.05 W, respectively. When the sensor module is added with this, the power consumption becomes 41.04 W and 81.25 W, respectively, in hovering and moving conditions.

When the UAV is equipped with a camera, sensor, GPS module, and communication module, the overall weight is 1.86 kg. The power consumption in this case is 49.8 W for hovering, and for movement, the power is 98.41 W. When all the payloads are used, the total weight of the UAV is 1.97 kg. In this case, the consumed power during hovering is 54.28 W, and it is 107.6 W for movement.

Thus, an increase in weight of UAV by 31.33% accounts for an increase in power consumption by 50.53% and 49.40% for hovering and movement respectively. This relationship between power consumption and weight of UAV is summarized in Table 2.

### *6.2. Regression-based Empirical Mathematical Model:*

In this part of the work, regression analysis is employed to establish an empirical connection between the weight of the UAV (with various payloads) and the power it uses for movement and hovering. This model assists in forecasting power requirements for various payload configurations without requiring repeated experiments. The power consumption in both cases shows an apparent linear relation with the weight. However, as payloads increase, the power increase is not always constant. So, the analysis of these obtained data is performed with both linear and 2$^{nd}$-degree polynomial regression to develop the desired relation.

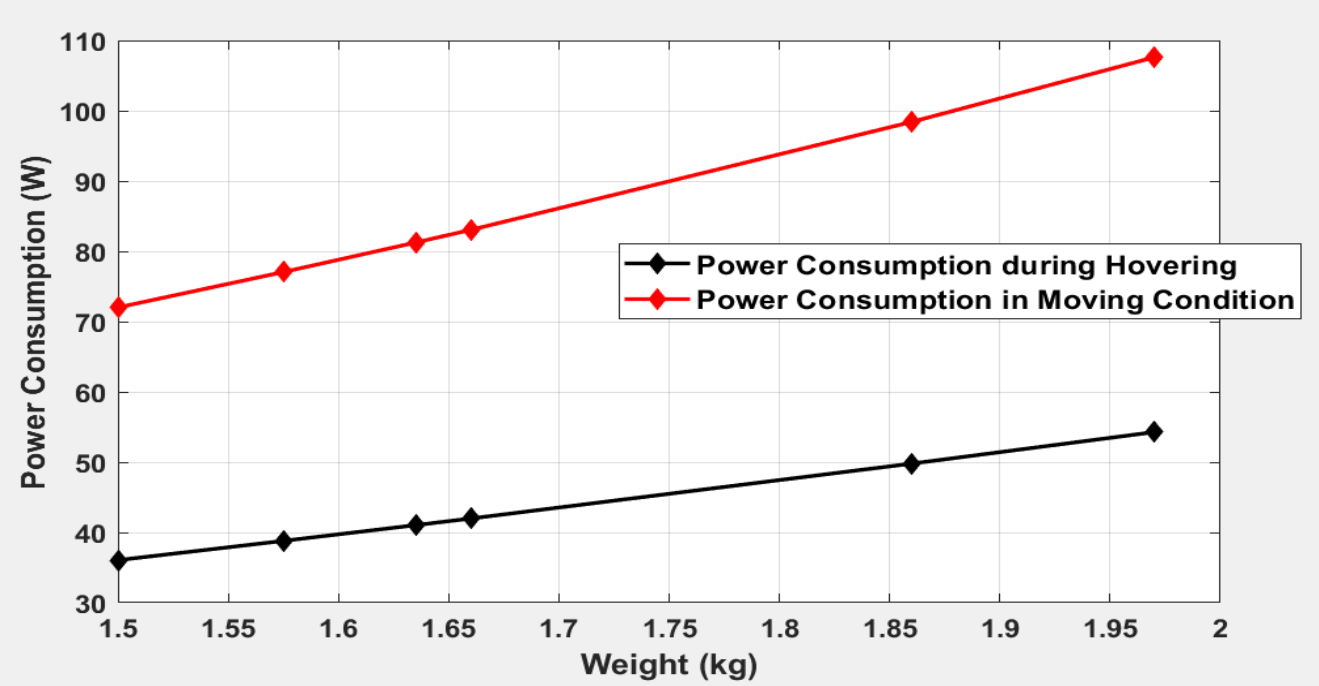



**Figure 9:** Influence of payload weights on power consumption of UAV

**Table 2**
Influence of payload weights on power consumption of UAV

| Component | Weight (kg) | Power Consumption for Hovering (W) | Power Consumption for Movement (W) |
|---|---|---|---|
| UAV | 1.5 | 36.06 | 72.02 |
| UAV + Camera | 1.575 | 38.80 | 77.05 |
| UAV + Camera + Sensor | 1.635 | 41.04 | 81.25 |
| UAV + Camera + Sensor + GPS Module | 1.66 | 41.98 | 83.05 |
| UAV + Camera + Sensor + GPS Module + Communication Module | 1.86 | 49.8 | 98.41 |
| UAV + Camera + Sensor + GPS Module + Communication Module + Flight Controller | 1.97 | 54.28 | 107.60 |

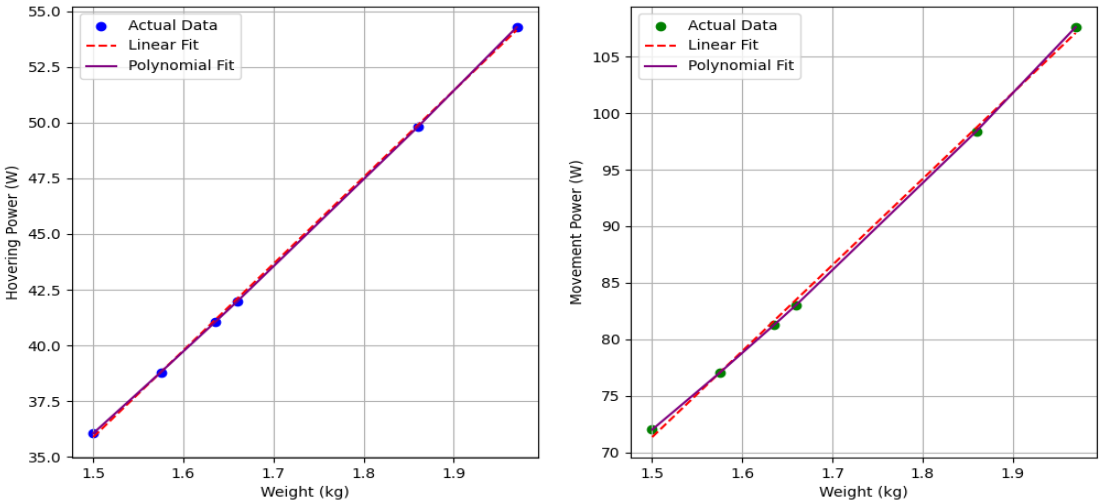



**Figure 10:** Regression analysis to develop an empirical relation between UAV power consumption and its overall weight

In case of linear regression, the models will be:

For hovering power,

$$P_{hover}(W) = a_{hover}W + b_{hover} \quad (3)$$

For movement power,

$$\boldsymbol{P_{move}(W) = a_{move}W + b_{move}} \quad (\mathbf{4})$$

where W is the overall weight of the UAV, a is the coefficient of W or slope, and b is the intercept

In case of 2nd degree polynomial regression, the models will be:

For hovering power,

$$P_{hover}(W) = \alpha_{hover}W^2 + \beta_{hover}W + \delta_{hover} \quad (5)$$

For movement power,

$$\boldsymbol{P_{move}(W) = \alpha_{move}W^2 + \beta_{move}W + \delta_{move}} \quad (\mathbf{6})$$

where α is the coefficient of $W^2$, β is the coefficient of W, and δ is the intercept.

Now, the linear and the 2nd degree polynomial regressions are implemented in Python using the data in Table 2. The results found are shown in Figure 10.

Using linear regression, the $R^2$ values are found to be 0.97 and 0.98 respectively. Although these are good results, better values are obtained with 2nd degree polynomial regression. The $R^2$ values are 1 in both cases, which represents a proper fit. So, the polynomial regression model is used to represent the desired empirical relationship. Using polynomial regression, the values of the coefficients are obtained as follows:

$\alpha_{hover} = 5.61, \beta_{hover} = 19.31, \delta_{hover} = -5.53,$

$\alpha_{move} = 21.83, \beta_{move} = -0.06, \delta_{move} = 22.98,$

Therefore, our desired empirical equations showing the relationships between power consumption and weight of UAV can be written from the equations 5 and 6.

For hovering power, the equation is,

$$P_{hover}(W) = 5.61W^2 + 19.31W - 5.53 \quad (7)$$

For movement power the equation is,

$$P_{move}(W) = 21.83W^2 - 0.06W + 22.98 \quad (8)$$

The equations 7 and 8 describe the desired relation between UAV weight and its power consumption.

## CONCLUSIONS

This paper aims to provide a rigorous analysis of the power consumption of Unmanned Aerial Vehicles (UAVs) with different payload configurations, focusing on the potential use of UAVs in next-generation wireless networks. According to the study, payload weight and type have a significant impact on how much energy is used when hovering and moving - two crucial UAV operating scenarios. Two empirical mathematical models are also proposed in the work which denote how the power consumption depends on the overall weight of UAV. Rotary-wing UAVs, considered in this work, are particularly suitable for applications that require precise positioning and hovering, such as serving as aerial base stations in 6G networks. The findings of this study have significant implications for UAV deployment and design plans. The researchers can optimize UAV design and its deployment to increase flight durations of UAV by utilizing the empirical models provided here. In this work, the environmental factors, such as wind, temperature, and altitude, are not considered, which can have a significant impact on UAV energy consumption. Addressing these factors will be an important direction for future work to enhance this analysis. The analysis performed here is simulation-based. Researchers can conduct analysis by incorporating real UAV systems to increase the credibility of the proposed model. Future studies should focus on creating adaptive scheduling algorithms that take mission needs and real-time energy availability into account. Research on fabricating efficient and lightweight materials for UAVs and for the payloads of UAVs can be very beneficial for developing

next-generation efficient UAVs. By overcoming these obstacles, UAVs can serve the next-generation 6G wireless network in an efficient way. This study serves as a framework for developing energy-efficient UAVs to meet the demands of future wireless technologies.

## ACKNOWLEDGMENTS

The authors would like to thank MIST for providing the necessary facilities and technical support required to successfully conduct the experimental investigations of this study.

## DATA AVAILABILITY STATEMENT

Datasets generated during the current study are available from the corresponding author upon reasonable request.

## FUNDING DECLARATION

This research was self-funded.

## ETHICS APPROVAL

This study is an engineering experimental investigation. The MIJST Research Ethics Committee has confirmed that formal ethical approval was not required.

## ETHICS, CONSENT TO PARTICIPATE, AND CONSENT TO PUBLISH

Not applicable.

## COMPETING INTERESTS

The authors declare that they have no competing interests.

## AUTHOR CONTRIBUTIONS

Author 1: Saif Ahmed - Conducted the literature review, developed the conceptual framework, designed the system and performed the result analysis.

Author 2: Nimul Islam Emon - Contributed to the preparation and writing of the manuscript.

## ARTIFICIAL INTELLIGENCE ASSISTANCE STATEMENT

Portions of this manuscript were assisted by an artificial intelligence language model (ChatGPT, OpenAI). The tool was used solely for language editing, text refinement, and clarity improvement. All content, data interpretation, analysis, conclusions, and final decisions were generated, verified, and approved by the authors. The authors take full responsibility for the accuracy and integrity of the manuscript.

## CONFLICT OF INTEREST DECLARATION

The authors declare that they have no conflicts of interest.

## REFERENCES

Ahmed, S., Chowdhury, M. Z., & Jang, Y. M. (2020). Energy-Efficient UAV relaying communications to serve ground nodes. *IEEE Communications Letters*, *24*(4), 849–852. https://doi.org/10.1109/lcomm.2020.2965120

Almalki, F. A., Soufiene, B. O., Alsamhi, S. H., & Sakli, H. (2021). A Low-Cost platform for environmental smart farming monitoring system based on IoT and UAVs. *Sustainability*, *13*(11), 5908. https://doi.org/10.3390/su13115908

Bhardwaj, A., Sam, L., Akanksha, N., Martín-Torres, F. J., & Kumar, R. (2016). UAVs as remote sensing platform in glaciology: Present applications and future prospects. *Remote Sensing of Environment*, *175*, 196–204. https://doi.org/10.1016/j.rse.2015.12.029

Chowdhury, M. Z., Shahjalal, M., Ahmed, S., & Jang, Y. M. (2020). 6G Wireless Communication Systems: applications, requirements, technologies, challenges, and research directions. *IEEE Open Journal of the Communications Society*, *1*, 957–975. https://doi.org/10.1109/ojcoms.2020.3010270

Dorling, K., Heinrichs, J., Messier, G. G., & Magierowski, S. (2016). Vehicle routing problems for drone delivery. *IEEE Transactions on Systems Man and Cybernetics Systems*, *47*(1), 70–85. https://doi.org/10.1109/tsmc.2016.2582745

Douklias, A., Karagiannidis, L., Misichroni, F., & Amditis, A. (2022). Design and Implementation of a UAV-Based Airborne Computing Platform for Computer Vision and Machine Learning Applications. *Sensors*, *22*(5), 2049. https://doi.org/10.3390/s22052049

Gong, H., Huang, B., Jia, B., & Dai, H. (2023). Modeling power consumptions for multirotor UAVs. *IEEE Transactions on Aerospace and Electronic Systems*, *59*(6), 7409–7422. https://doi.org/10.1109/taes.2023.3288846

Horsmanheimo, S., Tuomimaki, L., Semkin, V., Mehnert, S., Chen, T., Ojennus, M., & Nykanen, L. (2022). 5G Communication QOS measurements for smart City UAV services. *2022 16th European Conference on Antennas and Propagation (EuCAP)*. https://doi.org/10.23919/eucap53622.2022.9769210

Huang, Y., Cui, M., Zhang, G., & Chen, W. (2020). Bandwidth, power and trajectory optimization for UAV base station networks with backhaul and user QOS constraints. *IEEE Access*, *8*, 67625–67634. https://doi.org/10.1109/access.2020.2986075

Jiang, X., Sheng, M., Zhao, N., Xing, C., Lu, W., & Wang, X. (2021). Green UAV communications for 6G: A survey. *Chinese Journal of Aeronautics*, *35*(9), 19–34. https://doi.org/10.1016/j.cja.2021.04.025

Jin, T., Si, X., Liu, J., & Ding, P. (2022). An integrated animal tracking technology combining a GPS tracking system with a UAV. *Methods in Ecology and Evolution*, *14*(2), 505–511. https://doi.org/10.1111/2041-210x.14055

Kathole, A. B., Katti, J., Dhabliya, D., Deshpande, V., Rajawat, A. S., Goyal, S. B., Raboaca, M. S., Mihaltan, T. C., Verma, C., & Suciu, G. (2022). Energy-Aware UAV based on blockchain model using IOE application in 6G Network-Driven CyberTwin. *Energies*, *15*(21), 8304. https://doi.org/10.3390/en15218304

Kottat, A., & Ali, M. E. A. (2023). Effect of number of engines and payload weight on static stability of an

unmanned aerial vehicle. In *Lecture notes in mechanical engineering* (pp. 148–157). https://doi.org/10.1007/978-3-031-49727-8_16

Lee, J., & Yu, K. (2017). Optimal path planning of Solar-Powered UAV using gravitational potential energy. *IEEE Transactions on Aerospace and Electronic Systems*, *53*(3), 1442–1451. https://doi.org/10.1109/taes.2017.2671522

Lykou, G., Moustakas, D., & Gritzalis, D. (2020). Defending Airports from UAS: A Survey on Cyber-Attacks and Counter-Drone Sensing Technologies. *Sensors*, *20*(12), 3537. https://doi.org/10.3390/s20123537

Mozaffari, M., Saad, W., Bennis, M., & Debbah, M. (2016). Unmanned aerial vehicle with underlaid Device-to-Device Communications: Performance and tradeoffs. *IEEE Transactions on Wireless Communications*, *15*(6), 3949–3963. https://doi.org/10.1109/twc.2016.2531652

Na, Z., Liu, Y., Shi, J., Liu, C., & Gao, Z. (2020). UAV-Supported Clustered NOMA for 6G-Enabled Internet of Things: Trajectory Planning and Resource Allocation. *IEEE Internet of Things Journal*, *8*(20), 15041–15048. https://doi.org/10.1109/jiot.2020.3004432

Solyman, A. a. A., & Yahya, K. (2021). Key performance requirement of future next wireless networks (6G). *Bulletin of Electrical Engineering and Informatics*, *10*(6), 3249–3255. https://doi.org/10.11591/eei.v10i6.3176

Sørensen, L. Y., Jacobsen, L. T., & Hansen, J. P. (2017). Low Cost and Flexible UAV Deployment of Sensors. *Sensors*, *17*(1), 154. https://doi.org/10.3390/s17010154

Sun, Y., Xu, D., Ng, D. W. K., Dai, L., & Schober, R. (2019). Optimal 3D-Trajectory design and resource allocation for Solar-Powered UAV communication systems. *IEEE Transactions on Communications*, *67*(6), 4281–4298. https://doi.org/10.1109/tcomm.2019.2900630

Templin, T., Popielarczyk, D., & Kosecki, R. (2017). Application of Low-Cost Fixed-Wing UAV for inland lakes shoreline investigation. *Pure and Applied Geophysics*, *175*(9), 3263–3283. https://doi.org/10.1007/s00024-017-1707-7

Thibbotuwawa, A., Nielsen, P., Zbigniew, B., Bocewicz, G. (2019). Energy Consumption in Unmanned Aerial Vehicles: A Review of Energy Consumption Models and Their Relation to the UAV Routing. In: Świątek, J., Borzemski, L., Wilimowska, Z. (eds) Information Systems Architecture and Technology: Proceedings of 39th International Conference on Information Systems Architecture and Technology – ISAT 2018. ISAT 2018. Advances in Intelligent Systems and Computing, vol 853. Springer, Cham. https://doi.org/10.1007/978-3-319-99996-8_16

Ukaegbu, U. F., Tartibu, L. K., Okwu, M. O., & Olayode, I. O. (2021). Development of a Light-Weight Unmanned Aerial Vehicle for Precision Agriculture. *Sensors*, *21*(13), 4417. https://doi.org/10.3390/s21134417

Unmanned Systems Technology. (2024, November). *Pixhawk 6X flight controller: Modular triple-redundant UAV flight controller*. https://www.unmannedsystemstechnology.com/company/holybro/pixhawk-6x-flight-controller/

Yang, Z., Xu, W., & Shikh-Bahaei, M. (2019). Energy efficient UAV communication with energy harvesting. *IEEE Transactions on Vehicular Technology*, *69*(2), 1913–1927. https://doi.org/10.1109/tvt.2019.2961993

Ye, H., Kang, X., Joung, J., & Liang, Y. (2020). Optimization for Wireless-Powered IoT networks enabled by an Energy-Limited UAV under practical energy consumption model. *IEEE Wireless Communications Letters*, *10*(3), 567–571. https://doi.org/10.1109/lwc.2020.3038079

Zeng, Y., Xu, J., & Zhang, R. (2019). Energy minimization for wireless communication with Rotary-Wing UAV. *IEEE Transactions on Wireless Communications*, *18*(4), 2329–2345. https://doi.org/10.1109/twc.2019.2902559

Zeng, Y., Zhang, R., & Lim, T. J. (2016). Wireless communications with unmanned aerial vehicles: opportunities and challenges. *IEEE Communications Magazine*, *54*(5), 36–42. https://doi.org/10.1109/mcom.2016.7470933

Zhou, Z., Feng, J., Gu, B., Ai, B., Mumtaz, S., Rodriguez, J., & Guizani, M. (2018). When mobile Crowd sensing meets UAV: Energy-Efficient Task Assignment and Route planning. *IEEE Transactions on Communications*, *66*(11), 5526–5538. https://doi.org/10.1109/tcomm.2018.2857461

MIJST
*MIST International Journal of Science and Technology*

# The Dera Heterotopia: Meaning of Home for the Hijra Community

**S. Sameen[1*], A. R. Hossain[2], F. Jerin[1], S. Shreya[1], S. A. Anjum[1], A. Mumtarin[1] and T. Tabassum[1]**

[1]Department of Architecture, Military Institute of Science and Technology, Dhaka, Bangladesh
[2]Native Works, Dhaka, Bangladesh

***Corresponding Email:** *shafinaz@arch.mist.ac.bd*

**ARTICLE INFO**

**Article History:**

*Received: 21th April 2025*
*Revised: 12th October 2025*
*Accepted: 13th October 2025*
*Published: 30th December 2025*

**Keywords**:

*Hijra community*
*Dwelling*
*Home*
*Meaning*
*Dera*

**ABSTRACT**

The *hijra* community, representative of third gender individuals, is one of the most deprived communities in Bangladesh. Not conforming to traditional gender binary identities, they do not embrace the conventional notion of family and home. In this context, the study is exploratory research that delves into the realm of *hijras*, observing their relationship with their dwelling spaces and seeking how they negotiate the meaning of home. By examining *hijra* dwellings called *deras*, it aims to understand the dynamics of the *hijra* lifestyle and ultimately uphold their lived experiences against a dehumanized image of them in the context of Dhaka. For this purpose, the study employs a qualitative approach, drawing on everyday narratives gathered through interviews, group discussions, and observations. Applying Rapoport's framework for linking the built environment with culture and lifestyle, the paper uncovers the meanings of *dera* at three levels: at the lower level, it finds that *dera* provides everyday shelter and a new purpose to these outcasts against the hostile world. At mid-level, the *deras* become a locus of fostering social relations and a spatial manifestation of *hijra* existence. And finally, the higher-level meanings reveal a constant juxtaposition of loss and belonging, colourful appearances with feelings of estrangement, and initiation of *hijra* life with the constant desire for a *normal* one, making *dera* a 'heterotopic space' a manifestation of the *otherness*, as per Foucault's concept of ano*ther* place. The findings of the paper deepen our understanding of how individuals navigate the oppression of stigma and marginality while actively shaping and transforming their identities in adverse circumstances. It uncovers important relationships between (marginal) community and (housing) environment that can contribute to potential future research within the discourse of spatial justice. The study, by upholding marginal voices of *hijra* population around everyday space, advocates for their right to the city.

This work is licensed under a *Creative Commons Attribution-Non-commercial 4.0 International License.*

## 1. INTRODUCTION

As members of the third-gender community, *Hijras* do not conform to the traditional male or female identities. They are perceived as biologically 'defective' (Podder & Shahidullah, 2023; Ghosh, 2018) and consequently, remain ostracized from mainstream society due to a lack of social acceptance. The paper aims to humanize the *hijra* population against the dehumanizing perception of them as 'undesirables', by upholding their lived experiences as outcasts navigating life in Dhaka City. The purpose of adopting the notion of dwelling or home is to enable an insight into their communal and personal space, which is largely overlooked under a stigmatized identity. Not only is home the most personal unit of the built environment and the richest source of personal meanings (Castillo & Corpuz-Mendoza, 2010), but it is also an 'expression of social meanings and identities beyond the physical space that is lived (Wardhaugh, 1999; p 95; cited in Mallett, 2004). Hence, by examining their everyday spaces of dwelling, the *deras*, the study gathers narratives of individual aspirations and communal values amidst their collective struggle as one of the most marginalized groups.

In the scholarly world, the intersection of the built environment and the *hijra* realm remains a significantly unexplored area. Also, most academic research on *hijras* focuses on their socio-economic marginalization, largely influenced by external forces operating outside their dwelling environments (Podder & Shahidullah, 2023). But social relations around gender, class, and race get translated into domestic space, embodied in the home, and represented in the spatiality (Walker, 2002), and hence the relation of space and home is a significant milieu to inform

about a unique culture and marginalization. Researchers have stressed the importance of exploring the concept of home for the *hijras*, as a significant portion of *Hijra* activities takes place within the household environment (Hossain, 2021; Snigdha, 2021; Islam, 2016). Pointing out the significance of 'homemaking' in shaping the *hijra* identity, Podder & Shahidullah (2024; 2023) have shown that their (urban) homemaking can be viewed as a powerful socio-political tool to produce *hijra* identity. The study, building on the scholarship of the meaning of home, explores the personal, communal, and symbolic meanings of their dwelling spaces and uncovers the role of *dera* in the unique context of the everyday lives of *hijras.*

Traditionally, 'home' is imagined both materially and symbolically as belonging to a heterosexual couple who enact particular gendered roles and relationships (Barrett & McIntosh, 1982; cited in Mallett, 2004). However, such concepts leave the non-binary population excluded from the scholarly discourses of home. Feminist and queer theories have extensively criticized the traditional definition of home for its reliance on fixed notions of sex and gender (Mallett, 2004; Butler, 1990, 1993; Grosz, 1994; Young, 1990; Gatens, 1983). Also, concepts and representations of home differ and change over time and place (Walker, 2002). Home today is widely realized as a multidimensional concept and a multi-layered phenomenon (Bowlby et al., 1997; Wardaugh, 1999; Somerville, 1992), needing investigation from varied perspectives. Home, as a social experience, isn't defined by a specific place, but by the emotional meanings we attach to certain social and spatial environments (Boccagni & Duyvendak, 2020). Home as a domestic setting expresses a cultural regime where its members reside (Jackline, 2025). Home, from a cultural perspective, is thus defined by the inhabitants' cultural values and social practices (Ozaki, 2005; Rapoport, 1969). As a semiotic construction, the concept of home guides human meaning-making processes (Märtsin, 2023). Therefore, home is not just a physical dwelling (Mallett, 2004) nor a simple representation of a singular gender binary norm; it is a dynamic and relative phenomenon shaped by the experiences and meanings attached to it.

Furthermore, the experience of home is influenced by factors such as social position (exclusion) and marginalization, which are manifested in location, physical condition, modes of production, and activities that shape the identity and lives of the occupants (Somerville, 1997). Striving for a home in this sense could also mean reclaiming identity, inclusion, and agency in society (Kellett & Moore, 2003). Low-income residents often try to share broader housing norms and experiences, linking personal expressions of desire with collective ones (Kellett & Moore, 2003), and accordingly improve and personalize their spaces, aspiring for participation and belonging in society. Therefore, the concept of dwelling and home provides a significant framework to study the life of *hijras* as spaces representative of their social practices in severe marginalization.

Living outside their biological family, for the *hijras*, hence, the concept of home extends beyond the conventional aspects of culture and the gender binary (Podder & Shahidullah, 2024; 2023). To better understand how the *hijra* individuals negotiate and produce meanings of 'home' out of *dera*, the study explores the realm of *dera* both as their everyday space and a marker of their identity. Toward this end, it seeks to answer the following questions: *What does the spatial and visual organization of dera reveal about the everyday activities of a home? What do their dwellings tell about their social position and relationships? And, what is the relationship between the hijra culture and lifestyle with dera?*

To uncover the complex interplay between the *hijra* realm and their dwelling spaces, the study thus adopts the notion of home as a 'socio-spatial system encompassing cultural norms' (Malett, 2004) and follows Rapoport's framework (1988) that explores the relationship between dwelling (space) and culture (lifestyle) at multiple levels. Both the terms "home" and "dwelling" are used throughout the write-up. The term "dwelling" refers to a physical place of stay, while "home" represents a broader perspective that encompasses the intangible aspects of living. The study, by referring to *dera* as a space of dwelling, explores its experiences as a home and a *hijra* entity. Through this as a whole, the study uncovers how the dwelling spaces of the *hijra* community shape their daily lives, social interactions, and sense of identity.

## 2. UNDERSTANDING THE *HIJRA* REALM

This section delineates the gendered understandings of the *hijra* population and a brief history of the formation of *hijra* identity and culture within the South Asian context. In this region, the concept of a third gender has existed for centuries (Aziz & Azhar, 2020). *Hijra* is a conglomeration of alternative gender identities ranging from hermaphrodite to eunuch (Hossain, 2010). In simple terms, *hijra* refers to a community of third-gender individuals and encompasses a group of gender-nonconforming or non-binary people (Aziz & Azhar, 2020). Hence, *hijra* represents a communal identity and is more of an 'umbrella term' (UNDP, 2010) for gender minority groups, primarily existing in the South Asian region.

The identity and cultural prominence of the *hijra* community evolved considerably during the Delhi Sultanate (1206–1526) and the Mughal Empire (1526– 1707), where they held esteemed positions as servants in elite households, manual laborers, military commanders, political advisors, and guardians of the royal harem (Shroff, 2020). More importantly, during the precolonial era, they were sometimes considered to be transcendental, spiritually powered to bless and curse people (Hossain, 2010), hence, sacred and divine beings (Ghosh, 2018), due to which they were both revered and feared.

However, during British colonial rule, *hijras* faced systematic legal and political oppression (Hamzić, 2019). According to Ahmed (2019; cited in Podder & Shahidullah, 2024), these legal tools meant to suppress the "cultural" identity of the 3rd gender community redefined *hijra* identity as a political construct. The colonial process contributed to the criminalization of *hijra* individuals (Hossain, 2020; Ahmed, 2019), eventually stripping them

of rights and forcing them to 'live outside of mainstream society' (Finzel, 2021).

In the face of social and familial rejection, *hijras* live as a community with those alike. This can be defined as a rudimentarily structured society led by a *guru* with a "relatively undifferentiated comitatus, community, or even communion of equal individuals" (Turner, 1969). The place of dwelling for such a community, primarily a spiritual one, has been known as a *dera* for a long time in this region. "*Dera*" is derived from the Persian word *derah* or *dirah*, meaning a camp, abode, monastery, or convent. In South Asia, it came to denote a settlement or residence, or camp often associated with spiritual leaders or communal living spaces (Encyclopedia MDPI, 2021; Copeman, 2012; Singh, 2010). The term "*dera*" becoming associated with *hijra* communities is thus deeply rooted in South Asian socio-cultural and religious history, particularly within India, Pakistan and Bangladesh.

The *hijra* community has a unique social structure; according to Singh & Kumar (2020), the community is organized into hierarchical groups called gharanas, each led by a *Naayak*, who serves as the primary decision- maker. Under the *Naayak*_are *guru(mas)*, who oversee daily affairs and teach customs to their *chelas* (followers) in their *deras*. Throughout the history of the *hijra* community in this region, the *dera* became associated with their living dynamics within the *guru-chela* (teacher- disciple) organization, which takes place in a communal living environment. Within such a formation, *hijras* rely upon elaborate family structures that delegate various "feminine" roles to different members of the group, such as sister, *guru ma* (mother), *nani (maternal grandmother), and dadi* (paternal grandmother), representing *guru's guru*, etc. (Hall, 1996).

Within mainstream society, being considered an abnormal condition, *hijras* are perceived as 'inferior human beings' (Jami & Kamal, 2017), 'non-humans' (Finzel, 2021), or 'subhuman' (Hossain, 2010). They are mostly conceived as hostile creatures, engaging in anti-social activities that are commonly perceived as 'obscene' (Khan et al., 2009; Hinchy, 2019) by the mainstream urban resident due to the nature of their livelihood (collecting money, begging, or prostitution), appearances, and behavior adopted for survival, often referred to as "*hijragiri"* (Shawkat, 2016). Such *hijragiri, hijraness, or hijraism* have long been associated with *hijra* subjectivity and their performance of gender, visible through the entire set of bodily gestures, sounds, and sartorial choices (Hamzić, 2019). One of the most notable *hijra* expressions is their distinctive hand clapping (*taali*) and colorful female attire (Shawkat, 2016).

The "*hijraness"* not only sets them apart in public spaces but can also be seen as an extension of their physiological identity, reinforcing their visibility and presence in society (Roy, 2015). The community also uses a form of language (*Ulti bhasha*), which serves as a means of communication among *hijra* members (Snigdha, 2021). From a socio-cultural perspective of identity making, *hijraness* is thus essentially a social construct (Vinay, 2022; cited in Podder & Shahidullah, 2024). And, *"hijra*" becomes more of a communal identity than a mere gender identity.

In 2013, Bangladesh officially recognized *hijras* as a third gender, allowing them to use this designation in identity documents and passports, as well as to vote and run for office (McNabb, 2018). However, due to policy gaps and in the face of wider social unacceptance, they face widespread social, economic, and cultural challenges and are among the most deprived communities in Bangladesh (Shuvo, 2018; Aziz &Azhar, 2019). Alienated within society, they have been surviving by supporting each other (Alamgir, A., Brown, S., Gray, E., & Kelly, P., 2025). The everyday narratives of their existence thus disclose the countless ways in which individuals under the most adverse circumstances act as agents in shaping their survival and identity, and negotiating the oppression of stigma, marginality, and poverty (Vanita, 2002).

## 3. CONCEPTUAL FRAMEWORK

"Meaning" is an important mechanism linking environments to people (Rapoport, 1988) and reflecting how people behave in their built environment (Castillo & Corpuz-Mendoza, 2010). Occupants attach meanings to dwelling spaces and features, which, when shared and recognized by others, communicate their identity, status, and values (Coolen & Ozaki 2004). Attached meanings also reflect people's lived experiences, communal identity, and perceptions of the world (Massey, 1994). As the *hijras* live scattered throughout the city, they do not have any designated type of housing; consequently, materiality alone cannot represent their complex realm. Additionally, as *hijras* do not conform to the traditional norms of a 'household' based on a conventional definition of family, their relationship with 'home' is undoubtedly unique. Therefore, for the *hijras*, the relationship between (dwelling) space and beings (individuals and communal) is complex, and the role of home is not straightforward either. By investigating the meanings it conveys, we can better understand the dynamics of *dera* as a home.

Rapoport's theory on the meaning of the built environment (1988) focuses on how individuals and communities assign cultural, social, and personal significance to their living environment. He highlighted that these meanings should be interpreted on multiple levels—from everyday context to cultural symbols and underlying ideologies (Coolen & Ozaki 2004). According to this perspective, a dwelling or house is not just a physical structure but a space that carries symbolic meanings shaped by factors such as tradition, identity, values, social norms, and external influences. It emphasizes that a dwelling serves as a reflection of the occupants' personal and collective identity, offering a sense of belonging and continuity. Overall, Rapoport's framework for studying the built environment helps researchers understand how individuals perceive and interpret the spaces they inhabit, revealing the complex interplay between the individual, community, and broader societal influences on their dwelling environment.

Following Rapoport's theory, this paper investigates the space of dwelling or home of the *hijras* at three different levels. The lower-level meaning conveys every day and instrumental meanings (Coolen & Ozaki 2004); it pertains

to the personal, subjective, and experiential aspects of how individuals perceive and use their immediate living spaces. This includes emotional responses, personal attachments, and day-to-day practices involving their spaces within their homes and neighborhoods. Thus, for the *hijras*, lower-level meanings uncover their everyday lived experiences as they form new families and identities. The middle-level meanings, according to the theory, convey identity, status, power, etc. (Coolen & Ozaki 2004). More precisely, they reflect the lived and shared understandings of a space within a community. This involves collective practices, norms, and the social roles that people enact in their homes and neighborhoods. This level, hence, helps identify the communal interactions and positions of the *hijras* within their locality.

The higher-level meanings relate to the abstract and deeper aspects, such as worldviews and philosophies (Coolen & Ozaki 2004). They pertain to overarching social structures and collective beliefs, including values, ideologies, and cultural symbols that influence perceptions of space. The *hijras* typically find homes by renting whatever is available to them in the face of exclusion; thus, decoding the physical shelter through spatial layout alone may rarely express the complex dynamics of their lifestyle. Therefore, it is crucial to uncover the symbolic meaning "*dera*" holds as their space of dwelling and home while they live in their unique realm under the label of *hijras*. This level helps us envision an altered notion of family formed among strangers living under the same roof. Overall, the study examines the meanings of spaces at different levels, uncovering the dynamics of the hijra lifestyle and upholding individuals' lived experiences as they navigate the everyday challenges of exclusion in the heart of the city.

## 4. RESEARCH DESIGN AND METHODOLOGY

The study is exploratory research intended to shed light on an unexplored area —the intersection of space and the *hijra* realm. Hence, it is a qualitative study relying on participants' narratives and our observational understanding. For this purpose, the study relies purely on findings that emerged from the field; hence, it is built on grounded theory- a research methodology that is grounded in data to produce new hypotheses or theory (Strauss, 1994; Glaser, 1967), which is useful to uncover social processes-social relationships, and behaviours of groups (Crooks, 2001).

Based on this, an inductive approach was used for data collection and analysis to investigate the experiences of *hijra* individuals around their dwellings and accordingly interpret their perceptions and the meanings of the spaces. The data collection, through multiple field visits from June 2023 to August 2024, involves participant observations, interviews, and focus group discussions. It also involved observing the interior and exterior of their housing conditions and spatial arrangements. Photographs of the interiors were taken with the verbal consent of the participants.

A total of six *deras* were visited from Dhaka city's North and South municipality, including four *deras* in Mirpur 12 (Duaripara, Alupotti, Jhutpotti), and Mirpur 10 (Muslim camp), and two others in Old Dhaka and Mugda (see Fig.1).

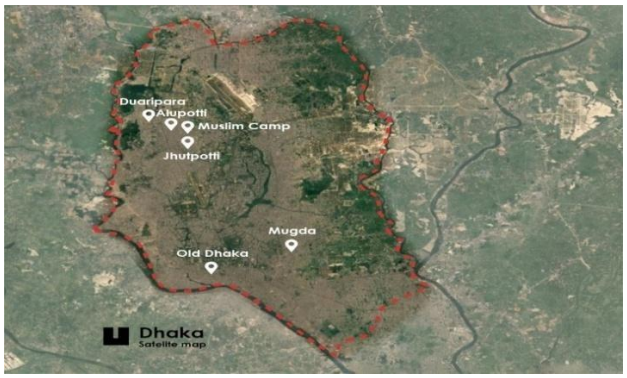



**Figure 1:** Map showing the location of the sites

Each *dera* consists of a *guruma* and their *chelas*, the number of whom varies per *dera* (see Table 1). The areas were selected based on a higher concentration of the *hijra* population and to have a broader range of perspectives.

The field-level data were collected from 23 hijra individuals using guiding questions that explored their daily activities, use of spaces, and individual experiences as *hijras* at home and beyond. Among these, 18 were one- to-one interviews, including four in-depth interviews with *gurumas* from Duaripara, Jhutpotti, Old Dhaka, and Mugda area. Additionally, 4 FGDs were conducted at Duaripara (4 members), the Muslim camp (4 members), Old Dhaka (5 members), and Mugda (5 members). Additionally, informal conversations were conducted with other *dera* members, as well as neighbors and social workers. Table 1 summarizes the number of participants per survey location.

**Table 1:** Participants' information as per locations

| Location | Members per *dera* (Nos) | Nos & role of Participants | Age (approx. range) |
|---|---|---|---|
| Alupotti | 5 | Two (2) *chelas* | One between 15 and 18 years |
| | | | One between 18 and early 20s |
| Jhutpotti | 20 | *Guruma* (1) | Late 40s |
| Duaripara | 30 | *Guruma* (1) | Early 40s |
| | | Three (3) *chelas* | Early to mid-30s |
| Muslim Camp | 6 | Four (4) *chelas* | Early to mid-30s |
| Mugda | 45 | *Guruma* (1) | Late 40s to early 50s |
| | | Four (4) *chelas* | Early to mid-30s |
| Old Dhaka | 30 | *Guruma* (1) | Late 40s to early 50s |
| | | Six (6) *chelas* | Early to mid-30s |

For this write-up, the findings are primarily based on the narratives of *hijra* individuals (anonymously) and are presented as direct quotes. The verbal responses were transcribed and translated from Bangla into English. Major themes and patterns were identified within the narratives following the framework of Rappoport using thematic analysis. The data were organized into subgroups based on inductive codes, including daily activities, estrangement, belonging, and others that emerged from the data.

The research is not only an attempt to shed light on an unexplored area, but it is also significant in terms of an academic co-production. It is an outcome of a collaborative project involving faculty (primary investigator and first author) and students from the Department of Architecture at the MIST. Data collection was primarily conducted by the students, followed by extensive discussions within the team and multiple validations with the community. The findings and discussions based on field-level observations are laid out in the following sections.

## 5. *DERA* AS AN EVERYDAY SPACE FOR *HIJRA* INDIVIDUALS: LOWER-LEVEL MEANINGS

The lower-level readings of dwelling reveal the role of home in the *hijras'* everyday life. The daily lives of *hijras* involve specific duties such as collecting money from local shops, begging, and seeking out houses with newborns or wedding ceremonies etc. Some also work with social workers as volunteers. After preparing themselves according to *hijra* attire and makeup, for example, *chelas* go out to their assigned areas of work in the morning. The nature of work and public presence is typically predetermined. For example, they never accept food during their work. It has been found that their *guruma* assigns everyday tasks. The *chelas* contribute most of their daily earnings to their *guru ma*, keeping only a small portion for themselves. In connection to the daily activities, a participant stated, *"The collection starts at 11 am. In 'Ulti Bhasha', this is called 'Challa Manga'. The collection time is from 11am to 5 pm. While collecting money, it is not allowed to eat from somewhere or take food from anyone. We go out in small groups in selected spots. After finishing collecting money, we come back to have lunch together in our guru ma's dera."*

Exceptions to this are the young ones who are still under training for *hijra* jobs and customs who stay at home and do household work. *"The young ones do not go out; it takes time to get used to the life around here; they do household chores like mopping, cleaning, and cooking. We don't send them outside to work until they are ready and willing to perform the hijra jobs",* says one *guru ma*. Joining the *deras*, young individuals aged between 11 and 20 years undergo training by their *guru mas* or seniors in *hijra* customs, dancing, singing, etc. The houses we visited had collections of musical instruments and music systems. Besides the young ones, *hijras* who earn through paid sex work have different routines as well as locations of work. Sometimes, some *deras* provide such services, like the one in Old Dhaka, and maintain restrictions on sharing information.

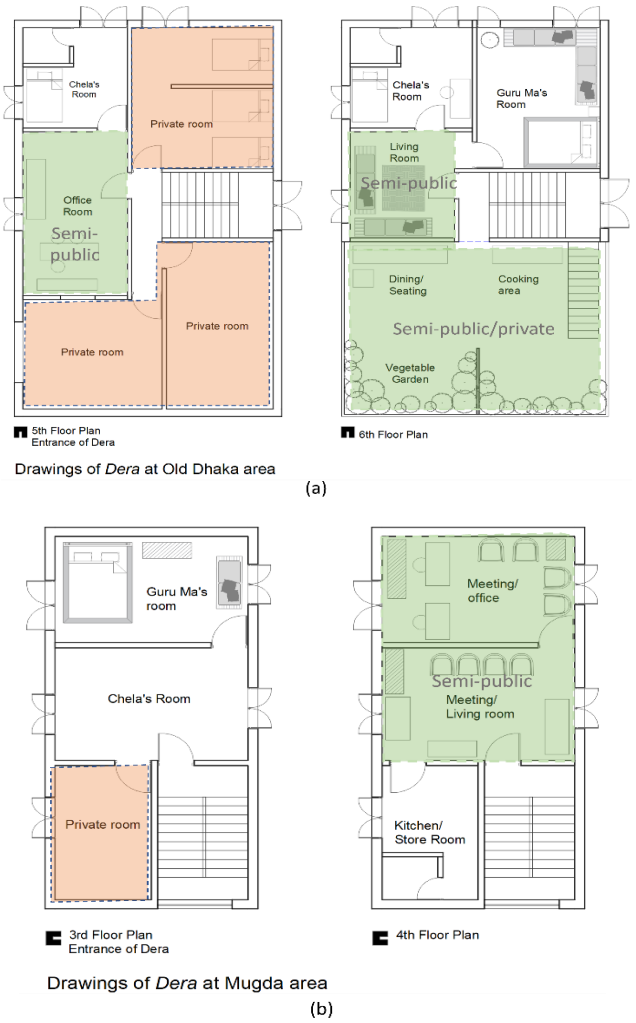



**Figure 2:** Schematic representation of the *deras* of Old Dhaka (a) and Mugda (b) demarcating the private and semi-public zones.

Such everydayness is reflected in their spatial dynamics. In the slum areas of Mirpur, houses are usually arranged as single rooms, which are often shared by several individuals, typically ranging from 5 to 10. During our visits, we observed one bed in each room and essential items stored in small wardrobes or cabinets. In more stable and *semi-pucca* settlements, like Duaripara, space is utilized more efficiently with shared kitchens and toilet services among neighbors. The young members were seen cooking in the alleys during the day, while most elders were away for work. In the afternoon, we found that most of the members were available for discussions.

In Old Dhaka and Mugda, the *deras* are situated in multistorey (4-5 storeys) buildings where the *hijras* live on rent, occupying two to three floors. Some *chelas* live in separate houses as they cannot accommodate all; however, these *deras* serve as their focal point. It has been found that they tend to appropriate the upper stories, having access to the rooftop where they frequently hold meetings and cultural performances. The overall spatial arrangements, illustrated through schematic plans in Figure 2, reflect a division of semi-public (meeting rooms, living rooms) and private (bedrooms). All kinds of social meetings and gatherings take place in the semi-public zone. Members of these *deras* are affiliated with various social works and different exhibits, including certificates, mementos (Fig. 3), etc, are displayed in the semi-public rooms. In both of the cases, the semi-public zone extends into the semi/open spaces (mainly the roof, also the terrace in the case of Old Dhaka), serving as the semi-private zone for all the socio- cultural trainings of the *dera members* to take place. Such spaces are also the locus of the *dera* members to interact and celebrate their *hijraness* and togetherness.

The spatial manipulation of the physical settings is tailored to serve the needs of the *hijra* lifestyle and hierarchy. The boundary between semi-public and semi-private is blurred as this area is used for socialization with both insiders and outsiders. No distinct dining area could be found, which usually acts as the semi-private zone for a typical urban home. The *chelas* usually dine in their living units on the floor or in the gathering areas. Sometimes they also dine with their *guru ma* in her room. Some rooms in the dwelling units were entirely private, inaccessible to visitors. It mainly exists in *deras* that provide sex work services. The houses seemed to remain introverted overall, with most of the windows sealed from the inside. Such layouts deviate from the usual sequence from a formal living room (semi-public) to the dining area (semi-private) and then to the bedrooms (private), as well as the gender binary norm that often assigns the semi-public space as the male and the private space as the female domain. This way, the *hijra* home diverges from the spatial norms of traditional South Asian homes (Podder & Shahidullah, 2024).

Additionally, the visuals of the interior were found to be different from a typical home in the city. No matter how shabby the exterior was, in most cases reflecting poverty, the interiors were commonly found to be quite colorful with green, orange, and red walls (Fig. 3). Colorful photographs, paintings, and decorative plaques were all over the walls, particularly in the semi-public spaces where they can showcase their vibrant lifestyle. Remaining colorful and vibrant inside the home, they create personal spaces that help them thrive despite external challenges. In addition to the photos and paintings in the common rooms, items such as a fish aquarium, plants, and photo frames were found in their *dera*, including the ones in Mirpur. Most of the houses also contained Arabic calligraphy and pictures of the Kaaba Sharif. Among all the rooms, the *guru mas'* rooms were found to be more attractive due to luxurious furniture, which reveals the internal hierarchy as well. Such territorial behaviors that involve placing objects with special significance or specific aesthetic qualities are commonly known as *personalization* (Becker, 1977; cited in Despres, 1991). Through personalization, the residents of *deras* nurture a sense of belonging and cultivate a sense of ownership while showcasing a brighter side of their lives altogether.



**Figure 3:** Photographs of the interiors of *Deras* showing vibrant semi-public and private (bedrooms) spaces.

Throughout the process of personalization, the home becomes a repository for memories of the lived experiences (Jackline, 2025; Malett, 2004), hence, spaces. However, the *deras* exhibited more of a collection of memories of their past and original families. Items such as framed photos of some of their parents and wall hangings with written "blessings of parents" in Bangla not only reflect spaces of *dera* as an act of personalization but also manifest their everyday cherishing of memories of their past. Their memoirs reflect emotional dilemmas: they assimilate with a new family while reminiscing about their original one. As one *hijra* participant said, *"Most of the nights I think of my parents and siblings".* Although the majority of them do not look back and reconcile with their original families, they reflect on their past to find comfort in feeling part of a *real* family while navigating their current lives as *hijras*.

Besides living the duality of past and present selves, the everyday life of the *hijras* is also marked by dual identities (Podder & Shahidullah, 2024). In the outside world, they

must carry their *hijra* identity by embodying the acts of *hijraness*. They have learned to utilize their differences to create unease and manipulate others to give them money. *"There are people in the city living luxurious lives, not worrying about money. But we have to work on the streets and yet earn very little. We have to interact with people, sometimes deceive them, what options do we have anyway?"*, one participant indicated their frustration and lack of scope to enter decent job markets, reflecting their self-awareness of the nature of their work. Sometimes, they adopt the appearances of performers; at other times, they instill fear or act as *mastaans* to extort money from local shops. However, during our visit to the *deras* for the study, the *hijras* were hospitable and friendly; they even offered us snacks. At home, these *hijras* can be themselves and are not required to adopt any tertiary identity to express themselves.

This way, beneath a disguise of duality, the *deras* become an everyday space for *self-expression*. It is the domain where *Hijras* can express their gender identity. They can embrace whichever traits from the gender spectrum they identify themselves with. Often, by singing and dancing together at home, they observe their shared sense of identity. The vibrant and colorful homes are an expression of their resilient *self* that they tend to celebrate. The *dera* is thus a place to celebrate their femininity that made them pariahs in the first place.

For these pariahs, the *deras* this way become an 'everyday space of refuge' from the humiliation and alienation of the outside world (Despres, 1991). *"Once, I was coming back from a marriage ceremony, and I was alone on the road. While I was walking down a road, some guys were calling me names. They were on a truck together. Suddenly, I felt something on my head. They threw stones at me, and my head got cut. I fell and became unconscious. That was a very humiliating night for me. We are always humiliated by people,"* said one study participant, describing the everyday hassle they have to face when they are out. According to a younger one, *"I do not like to go out, 'normal' people like you keep staring at me".* Within the *dera*, the cohort becomes emotional support toward each other: *"We understand each other",* as stated by a respondent. Hence, *dera* provides a (safe) haven for *hijra* individuals against the eyes of the outside world.

As a whole, examining the everyday lives of *hijras* through their dwelling spaces reflects their resilience and determination to continue living by embracing their *dera* as a personal space. *Dera* offers them shelter from external hostility and allows them to celebrate their identity. The everyday spatiality of the *deras* as homes reveals a distinct realm that differs from traditional norms. It also reflects the emotional dilemmas that *hijra* individuals endure in their adoption of *hijraness* while safeguarding their own aspirations. Their everyday lives and spaces are thus a blend of communal and individual efforts, as each strives to balance personal needs with the collective well-being of the group.

## 6. *DERA* AS A SPACE OF HUMANIZATION: MID-LEVEL MEANINGS

The mid-level meanings enable an understanding of identity, status, and power of a community through the reading of their dwelling space in relation to the surroundings and society. Considering home as a vital interface between society and individuals (Saunders & Williams, 1988), this section therefore explores the communal position of the *hijra* individuals within their neighborhood setting. This primarily includes discussion regarding the nature of their interactions with neighbors, where the spaces of *deras* serve as the 'locale'- a spatial and social unit of interaction through which basic forms of social relations are produced (Saunders & Williams, 1988; Giddens, 1984).

As discussed earlier, to society's eyes, *hijras* are unwanted company; people find them either fearful, hostile, or annoying. As a result, they share multiple levels of marginalization (social, economic, political, etc.) within mainstream society. Hence, their collective position in society is clearly at the very bottom. Legally, they don't have ownership of any lands or houses, nor can they claim inheritance, as families don't own them. They have no other choice but to live in rented houses. "*There are numerous deras in Bangladesh; everyone lives in rented dwellings*", according to one study participant.

However, based on their positionality and relationship with the mainstream population, securing a decent living in the city is quite a predicament. In this sense, getting access to housing can be said to be more of a social struggle than a legal or economic one. Because landlords refuse to sell or rent houses or properties to the *hijras*, even if they can afford it. Apart from that, there is resistance from neighbors as well. As per one *guru ma* from our study, *"No one really wants to rent us a home in apartments. Who doesn't want a life of convenience? Does anyone want to live on the streets? But not everybody wants to rent to us or share space with us. Especially in apartment flats".* She highlighted the complexities of getting access to any neighborhoods: *"Many fear that we will create a hassle about the rent, or will create chaos in the house. Sometimes, the landlord fears that we won't be able to mix with his other tenants or will make them uncomfortable. Other renters say they will leave if we move in."* As a result, with restricted rental opportunities, they end up living in hardship and poor conditions, mostly located within the urban fringes and slum areas.

Among the six *deras* in which the study was conducted, the *deras* in Old Dhaka and Mugda were in *pucca* (multistorey) buildings and good condition. However, the other *deras* contained *semi-pucca* and *kacha* makeshift settlements, mostly with substandard living spaces prone to overcrowding, poor ventilation, and frequent waterlogging incidents. From the outside, the environment looked unhygienic, unclean, and dark. One of the participants who was a visitor at the time of our visit to Duaripara, refused to take us to her original *dera*, saying, *"Where we live now is very unclean and in a slum. I guess you will feel uncomfortable there",* ashamed.

While they don't have control over which neighborhood they get access to, the interiority displays their urge to live

a decent, colorful life, as described in the earlier section. Groups that have comparatively better income tend to live in better conditions, such as in *semi-pucca* or *pucca* houses, which is also, of course, after getting access to that very neighborhood. In this connection, the *guru ma* from Duaripara emphasized their relationship with the neighbors in availing the current living conditions in *semi-pucca* house: *"Previously in this locality, people looked at us very differently. Most of us had to live in 'tong' (makeshift) houses inside the slum. Now, look at this house. Although we can afford to rent better than this house, we are now living in a better environment".*

Hence, the relationship between the *hijra* community and the local population is a critical aspect in deciding their position and living standards within the locality. It has been observed that with time, the *hijra* community can get along well with their neighbors. It is particularly evident in low-income neighborhoods, where poverty is a shared struggle. As our observation suggests, in the old Dhaka area, neighborly interactions are generally weak. The community is in a mixed-income area where families prefer not to interact with them. Neighbors, mostly from middle-income families, tend to avoid them. Whereas, in the Mugda area, interactions are significantly better. Neighbors know and show respect to the *hijra* community. Whenever the *hijras* receive aid from NGOs or other organizations, they share it with those around them. They even join local festivals and events, strengthening their bond with neighbors.

Similarly, in Duaripara, Mirpur, the *hijra* community has good relationships with their neighbors, who are mostly from lower-income groups. They help and know each other well. However, the relationship does not build in days but rather over years. According to the *guru ma* from Duaripara, the *hijras* constantly have to prove themselves to their neighbors: *"We have to assure them a lot that we are good people".* She further described the development of their relationship with time: *"When we first came here, little kids would run behind us saying 'hijra, hijra,' as if we were some sort of creatures in a zoo. Over 20 years, our relationship with the local people has developed. They even send us meat during Qurbani Eid festivals. They do it out of respect or fear, I don't know. But I like to assume that they love and respect us as neighbors.* " Her statements reveal that they have been living in the area for a couple of decades and like to believe they have a strong bond with their neighbors, despite their resistance at first.

Thus, in an urban slum, the *hijras* need to gain respect to be able to 'belong' and ensure survival (Hamzić 2019*).* To achieve this, the *hijra* community engages in income-generating activities strategically, taking care not to disrupt their relationships with neighbors. They choose spots for their money collection that are close enough for ease of work yet far enough to avoid interfering with their neighbors' lives. Not all members of the community engage in sex work at their *dera,* as they strive to maintain peaceful coexistence with those living around them. This coexistence, therefore, involves careful negotiations on their part. Through positive interactions, the *hijras* and their neighbors humanize each other and see beyond hostility and alienation.

During our visit to the *deras* in Mirpur, a positive relationship between the *hijras* and their neighbors could be observed. In Duaripara, we found dolls on the beds belonging to a neighboring child whom they babysat. Additionally, a teenage boy served us snacks, and upon noticing our confusion, the guru ma explained that he was a neighbor from the mainstream community. We also saw a *moulavi* teaching the Quran to a couple of local children in one of their rooms in the *dera* of Jhutpotti. These experiences highlight the prevalence of a decent neighborly relationship between the *hijras* and the mainstream residents in the neighborhood.

Besides, it has been observed that the *hijras* have to constantly negotiate community protection from the police (Hamzić, 2019) and against any threats of eviction and other forms of violence within the neighborhood. They also maintain liaisons with local political leaders, particularly the *gurus,* which ensures their stability within the locality to a great extent. The *gurus* with such connections hold greater power among their cohorts, and the *deras* in this process become a crucial site of negotiation, offering an economic and social model of co- existence that is united and strong enough to earn the *hijras* some substantial bargaining power (Hamzić, 2019). This way, *dera* becomes a space for negotiation of power and the spatial manifest of their existence.

Overall, the middle-level meanings suggest that *hijras* struggle to access adequate housing and encounter challenges when trying to enter neighborhoods due to residents' lack of acceptance. In slum settlements, they lead a marginal life shared with other marginal communities, where the *hijras* constantly have to negotiate social (co)existence through daily interactions with their surroundings. Throughout this process, *dera* becomes both a space of cultivating social relations and a demarcation of the *hijras'* existence on the ground. *Dera* provides the setting where mainstream society, unlike their typical encounters with hijras on the streets performing *hijraness,* interacts with them as neighbors and ultimately connects with them on a 'human' level. To ensure stability and security, the *hijras* have to maintain liaisons and negotiate with powerful institutions. Consequently, through the process of regular interaction with the surroundings, the *deras* becomes a space that fosters a sense of broader acceptance, contributing to a recognition of their identity as humans. This way, at the interface of home and neighborhood, a process of humanization begins.

## 7. *DERA* AS A SPACE OF DEFIANCE AND DUALITY: HIGHER-LEVEL MEANINGS

The higher-level meanings explore *dera* as a "home" to *hijras'* unique family in comparison to the conventional notion of family, as well as a space associated with the unique realm of *hijras*. Our imagination of home refers to the dwelling space of a family consisting of members connected by bloodline. For the *hijras,* such a conceptualization of 'family' naturally does not comply. Yet, a *dera* represents a home for the *hijras*, where they dwell in groups with a certain sense of belonging and

hierarchy, forming a family-like unit within each *dera*. Hence, to understand *dera* as a space of home, it is crucial to understand the formation of such families.

The notion of family for the *hijras* is the unit consisting of a *guru ma* and her *chelas.* The cohorts for each *dera* are formed in varied yet similar ways. As per our findings, many members of the community were cast out by their families after coming to know about their gender identities. Also, failing to manage a safe space inside their original families (Sharma, 2014), a majority of others left on their own. In this connection, a participant said, "*My parents used to torture me. Getting beaten by my parents was a regular thing for me. They used to beat me until my nose bled. I couldn't finish my studies and came here as soon as I got the chance".* Thus, a hostile attitude from their own families forces them to leave and join the *hijra* community.

Also, *w*hen a child with gender-atypical features is born, members of the *hijra* community approach them. *"My guru took me from my family, who were very poor, and brought me to Dhaka",* says another participant. Sometimes, after realizing their differences from their surroundings, they leave their family on their own and look for people with similarities. *"I came here very long ago when I was merely a teenager. My anomalies were not physical, but when puberty hit, I knew I was different from others. Then I left my family",* said one participant, uttering the pain of the feeling of *otherness*. Her story mirrors the experiences of many others in the community, who leave their birth families to find belongingness and security in the *deras.*

It is also commonly observed that persons with gender atypical features or opposite gender traits find a connection with the *hijra* community in terms of such 'belongingness.' As a participant stated in this regard, *"When I lived with my family, I used to spend so much time with the hijra community at various places such as Hatirjheel. I didn't stay at home most of the time". "Even when I was not a part of the community, I used to attend them. That's how I got merged with the community",* says another. This connection often surpasses the relation with the original family, primarily due to the humiliation they face from outside the family. In each case, the shared struggle of *otherness* ties the third gender people together beyond blood relations. *"I was loved by my parents. Right after they both died, my siblings started to make me leave my home. I also left my school. I found the community through someone from my school. She took me to celebrate 'Jalsha', where I saw people like me. After that, my guru ma took me in",* described one participant, emphasizing her connection to the community since long before she was even a part of it.

Moreover, the *hijra* community acts as a shelter for such uprooted and homeless persons. *"People like us, when they leave their family, they search for known people",* says one *guru ma,* depicting their empathy and stating their role toward each other based on the shared struggle. "*Some leave their home and contact us; we take them in. If we see anyone on the streets alone, we take them in",* she adds. *"They are like us; we all have similar stories".* It appears that they instantly identify with each other for being on the same gender spectrum, which is at odds with the 'normal' and share a similar experience of familial or social rejection.

Hence, the journeys from their original homes to the *deras,* although individual anecdotes, are alike in their state of abandonment and estrangement. These experiences often begin with a feeling of *otherness,* stemming from the inability to fit into what is considered 'normal'. The cohorts work as a 'found family' for each member, who gradually accepts them as their own and gets used to the unique way of living. Thus, the formation of these groups constituting the unit of the *deras* is significant and crucial to understanding the dynamics of *hijra* families. Podder & Shahidullah (2023) define this family as a 'fictive family'. The '*dera*' is, therefore, a home that shelters fictive families consisting of strangers who connect through both rejection from society due to otherness and a sense of belonging among the *hijras* by *sameness*.

In these fictive relationships. *Guru ma* embraces the role of a mother who takes the other members (*chelas*) as underlings under her protection. She provides not only protection and guidance but also emotional care and mentorship. The relationship between *guru ma* and her *chelas* is also one of control. The *guru ma* dictates the types of jobs and the share of income and works as the head of the household overall. In this connection, Podder & Shahidullah (2023) have shown that, besides belongingness, such an act of control also enables the fictive family to sustain itself. The *chelas*, on the other hand, consider each other sisters. *"We are sisters",* one of the participants emphasized while describing their relationships among the cohort. This shows the community's re-interpretation of familial terms within their social context. And, this way, through everyday interactions and mutual understandings over shared struggles, they form a sense of family with each other.

Yet, the homeliness of a *dera* is rather gradually acquired through hardship and struggle (Hamzić, 2019). The journey of establishing a place among a new cohort and developing a sense of ownership through cultivating belongingness is not an easy, straightforward road. The words of one of our participants in this connection seem quite significant: "*Here, people come from different families. Nor can everyone accept all these wholeheartedly. Some want this, others want that. Even siblings fight, and we are ten children from ten different mothers; we ought to have our differences"*. Pointing to the interviewees, she added, *"You are five different people from five mothers; don't you have your differences? No matter how close you are, can you move freely in your friend's house? You must feel hesitation. We were no different"*. Her statements illustrate the challenges of adapting to a new life, highlighting feelings of insecurity and vulnerability in an unfamiliar place among unknown people.

In addition, adverse experiences within the *deras,* primarily during earlier days, make *dera* not always an ideal space. A participant commented about her early days

in *dera* in this regard: *"They beat me a lot, I suffered many tortures".* Such experiences are quite common for most individuals, as our study suggests. Yet, they consider these incidents to be a part of regular family dynamics: *"They loved me like their child, punished me like their child. Don't your parents punish you? Do you leave your home because of that?"* says one participant. Her statement reveals the family hierarchy, where *guru mas* or other senior individuals (holding power in their groups, such as parents or elder siblings) can control and punish the underlings. The junior members, on the other hand, seek emotional support through a sisterhood among individuals at the same level, and, through all the good and the bad, they build a sense of family among their cohort. *"All of us are the same here, we don't judge each other",* stated a participant; while another reassured the bond of their cohort as a family: *"I want to live together with my family, which is this people,"*- through this statement, an utterance of acceptance of the community as their own, of their cohort as their family, and their *dera* as their 'home' can be imagined.

At the same time, *dera* is also the manifestation of their loss of a prescriptive form of family and home (Hamzić, 2019). It is evident in their yearning for a regular family and a regular home: "*Even if I want a family and a good home, it will never be possible, so I have accepted my fate the way it is".* Another participant added, "*Who doesn't want to live in their own place? All want a beautiful home, but I have accepted my fate".* Their statements reveal their desire for a home of their own. It also indicates that these individuals have learned to surrender to their reality. However, dwelling on the idea of one's own family is inscribed in their everyday life. *"I was once with my parents and siblings"*- during the interviews, a feeling of loss and estrangement was evident in their address of adoption of the *hijra* life.

In addition, *dera* also serves a crucial role beyond mere dwelling—it is the space where the process of becoming a *hijra* begins. Upon joining a *dera*, new members undergo training in hijra customs and traditions, as well as livelihood techniques, before they begin performing *hijra pesha.* In addition to being a home, this *dera* serves as a school where many vital skills are learned (Hamzić, 2019), ultimately helping individuals become part of the *hijra* community. Therefore, *dera* not only offers a place of dwelling but can also be understood as a space where third gender persons transform into *hijras.* Moreover, quite frequently, there are events of *jalshas* (dancing and singing performances) held in the *deras*, such as on the roofs of the *deras* at Old Dhaka and Mugda area. Therefore, in some cases, *dera* becomes the locus of their jobs, for performers (and also for sex workers) in particular. This way, the meaning of *dera* resonates more with the *hijra* identity than that of a simple dwelling space. *Dera*, as a space, becomes a 'symbol' of *hijraness* beyond its utility as a home.

Based on this particular incident, on the other hand, *dera* symbolizes fear and mystery from an outsider's perspective. Even persons of the third gender hold adverse ideas about *deras* before joining the community, which is evident in one of the study participants' statements: *"Being a hijra, I also feared them (the hijra community) at first. When I came to the dera, it was terrifying. But then I got used to it. Naturally, other people fear us."* While *dera* serves as a *haven* for the *hijras*, it carries a sense of discomfort to the outside world. People tend to identify *dera* as an unsafe space because of the perceived image of the *hijras* as *other* beings and *unfamiliar* creatures, and also the prevalent negative stereotypes. Thus, *dera*, as a discursive space, creates a fear of the unknown in our imagination.

Reading the meanings of *dera* at this level reveals a space that defies norms and reflects juxtaposition between the *hijra* realm and mainstream world, where dwells a duality of loss and belonging, past and present, and the loss of a dignified place in society with the creation of a new collective identity.

## 8. *DERA* AS A SOCIO-SPATIAL SYMBOL OF THE *HIJRA* REALM: DISCUSSION

Studying the *dera* through three levels of meanings uncovers the unseen spaces and unheard voices. The lower-level meanings reveal *dera* as a 'joyful centre' (Hamzić, 2019), characterized by its vibrant and flamboyant everyday spaces, beneath which the *hijras* seek refuge from the hostile world. Their everyday space reflects their acceptance of the new reality while negotiating with personal trauma and the predicaments of embracing the *hijra* life. Furthermore, the semi-fixed features (Coolen & Ozaki 2004; Rapoport, 1981) in some of their dwelling spaces, such as heavy or decorative furniture, vibrant interiors, etc., clearly demonstrate their desire to establish a place in society by showcasing their worth through wealth. This discussion, overall, enables insight into the unnoticed realm of *hijra* individuals and humanizes them before the eyes of the readers. It also reveals an altered notion of dwelling that counters the typical spatial norms and accommodates the *hijra* lifestyle, containing distinct (daily) activities. Such a notion of dwelling enables us to imagine a home beyond its conventional spatial setting within Dhaka and can add to the dialogues of home beyond a space (Mallett, 2004).

On the other hand, the middle-level meanings depict their communal interaction and position with the localities. It is understood that securing a house is more dictated by external forces than one's abilities. They require continuous negotiation on their part to access any neighborhood and ensure stability by carefully maintaining their relationships with the neighbors. Thus, there exists a constant negotiation of power and social contact between the *dera* and the neighborhoods, through which the *hijras* reinforce their presence and make their existence visible. Through a neighborhood-level interaction, *hijras* gain greater acceptance among mainstream communities. With better social position acquired through political and social liaisons, they can avail better living conditions. However, as the findings suggest, *hijras* may appropriate a place among the lower-end population, but even with power and economic position, they are rarely recognized among the higher-end society. In connection to this, the study believes

that a place-based inquiry into the *hijra* community's marginality can reveal a broader spectrum of (intersected) spheres that shape their positionality (e.g., class, gender, politics, etc.), and can be significant for future exploration in the conversations of enhancing social acceptance towards *hijras*.

Finally, at the higher level, *dera* is found to represent a space of "home" that defies the definition of family and disrupts the norms based on the gender binary. It is a space that is rather symbolic of the *hijra* identity. According to Hamzić (2019), *dera* functions as a 'post-home' that provides refuge from an unfavorable natal home and serves as a setting for the creation of a collective identity of 'thereness.' Podder & Shahidullah (2024) define these spaces as counter-homes that challenge the institutionalized notion of abnormality. In addition to these statements, the study finds *dera* to be a heterotopic space, a space that embraces the *otherness*.

A heterotopic home, according to Foucault's (1967) concept of heterotopia, can be imagined as a spatial context that juxtaposes or disrupts the ordinary, creating an 'other place' that exists outside the norms of everyday life, potentially representing alternatives to dominant social and cultural norms (Foucault & Miskowiec, 1984). Heterotopias are real places that act as "counter-sites," symbolizing, opposing, and transforming traditional sites, standing in contrast to utopias (Jadhav, n.d.). *Dera*, in relation to this, shelters the individuals rejected by society on the grounds of non-typical gender identity while defying the norm of a traditional home. It operates through 'fictivity' (Podder & Shahidullah, 2023) while adopting familial roles and hierarchy. *Dera* is a space that embraces everyday duality; beneath the colorful display of *hijraness*, individuals constantly negotiate their trauma and sense of identity, perform sisterhood while yearning for a regular family. For newcomers, *dera* serves as a space of 'liminality'; an ambiguous phase where the liminal personae are neither here nor there (Turner, 1969; cited in Wels et al., 2011). It offers both the negative and positive aspects of loss and belonging, as well as a space of ultimate transformation into a *hijra*. The meaning of *dera*, thus, surpasses the very idea of settlement, enabling inhabitants to experience home more as a journey than a destination (Hamzić, 2019). Through an image of fear, *dera* additionally becomes a spatial manifestation of *otherness*—the unique, mysterious, yet vibrant world of the *hijras*.

In addition, joining a *dera* does not guarantee overcoming the ill-treatment of *hijras* by the world, as it may offer limited protection while imposing its own hierarchies (Hamzić, 2019). On one hand, *dera* as a symbol of the *hijra* realm provides purpose to its members and attaches identities. On the other hand, it exploits their labor and compels them to adopt certain lifestyles and traits. While people recognized as a third gender are ostracized from their families, individuals with the label of *hijras* are not welcome in mainstream society either. Nonetheless, the community provides them with food and shelter, as well as purpose and identity. In connection to this, a participant's quote is significant: *"I don't want to go back to the mainstream as people don't value us"*. Hence, *hijraness and dera* provide them a certain level of dignity by making them 'visible' to the world.

*Hijraness, in this regard,* is found to be a journey of transformation of culture and identity. It is a collective identity through which the *hijras* appropriate their rights and place within the city. The realm of *hijra*, thus, can be understood as the 'infrapolitics of the powerless' (Scott, 1990) and 'tactics' (De Certeau, 1984) of the pariah to reclaim their space within the state and protect their communal self. In this process, *dera*, as both a symbolic and spatial hijra entity that transcends its physicality, becomes a powerful manifestation of the hijra existence as a locus for their daily negotiations with the personal self and society. In the face of societal marginalization, the *dera* stands as a testament to the *hijra* community's resilience. It embodies their collectiveness, offering a space where cultural practices are preserved and members find acceptance and purpose.

## 9. CONCLUSIONS

The paper, as a whole, attempted to delve into the lives of *hijra* individuals and uncover everyday narratives about how dera is shaped as a home. Toward this end, it analyzed what meanings the realm of *dera* holds at three levels- in terms of everyday space, a home, social position, and a symbolic space. Throughout the study, the personal and emotional experiences of *hijra* individuals have been explored. The findings presented in this paper offer a more humanized perspective on *hijras*, who face challenges at every level as they strive to establish their place in society as a minority. Uncovering the relationship between their *hijra* lifestyles and marginal living spaces in the city, the study advocates for their right to the city.

From within the field of the built environment, it invites dialogues around the inclusion of the largely neglected *hijra* population into the discourse of spatial justice. Special emphasis needs to be given to them within the broader category of the marginalized and destitute population within national housing policies (i.e., Ashrayan). However, despite the government. initiatives, the *hijras* are unable to come out of their ill fate mainly due to resistance from society on the ground. In connection to this, the study has shown that social acceptance of *hijra* individuals can be fostered through regular, human-level interactions, facilitating an understanding of *hijra*s as humans. Based on this idea, more humanized portrayals through television and media could be significant. It is essential to give special consideration to the inclusion of *hijra* individuals in schools, as fostering humanization begins in childhood. To support this, quotas could be established for *hijra* students in public schools and colleges. Additionally, incentives could be offered for mainstream students, along with organized programs that promote interaction among all students through cultural events and other activities. Inclusion is a complex process; however, it needs to start somewhere. The study embeds that "*hijra"* as an identity is a social construct rather than a natural fact, and thus believes that mass perceptions can be shifted to more "humane" terms.

**ACKNOWLEDGMENTS**

The authors would like to thank MIST for providing the necessary facilities and technical support required to successfully conduct the experimental investigations of this study.

**DATA AVAILABILITY STATEMENT**

Datasets generated during the current study are available from the corresponding author upon reasonable request.

**FUNDING DECLARATION**

This research was self-funded.

**ETHICS APPROVAL**

This study is an engineering experimental investigation. The MIJST Research Ethics Committee has confirmed that formal ethical approval was not required.

**ETHICS, CONSENT TO PARTICIPATE, AND CONSENT TO PUBLISH**

Not applicable.

**COMPETING INTERESTS**

The authors declare that they have no competing interests.

**AUTHOR CONTRIBUTIONS**

Author 1: S. Sameen - Research design, data analysis, and conceptual framework development.

Author 2: A. R. Hossain - Data collection and transcriptions.

Author 3: F. Jerin - Data collection and transcriptions.

Author 4: S. Shreya - Data collection and transcriptions.

Author 5: S. A. Anjum - Data collection and transcriptions.

Author 6: A. Mumtarin - Data collection and transcriptions.

Author 7: T. Tabassum - Data collection and transcriptions.

**ARTIFICIAL INTELLIGENCE ASSISTANCE STATEMENT**

Portions of this manuscript were assisted by an artificial intelligence language model (ChatGPT, Grammarly). The tool was used solely for language editing, text refinement, and clarity improvement. All content, data interpretation, analysis, conclusions, and final decisions were generated, verified, and approved by the authors. The authors take full responsibility for the accuracy and integrity of the manuscript.

**CONFLICT OF INTEREST DECLARATION**

The authors declare that they have no conflicts of interest.

**REFERENCES**

Alamgir, A., Brown, S., Gray, E., & Kelly, P. (2025). Exploring resistance, resilience, and refusal amongst Khawaja Sara and Hijra Communities in postcolonial Pakistan. *LGBTQ+ Family: An Interdisciplinary Journal, 21*(2), 116–130

Aziz, A & Azhar, S. (2019). Social exclusion and official recognition for Hijra in Bangladesh. *Journal of Research on Women and Gender*, 9(1), 3-19.

Barrett, M. and McIntosh, M. (1982). *The Anti-social Family*, Verso.

Becker, F. D. (1977). *Housing messages* Dowden, Hutchinson & Ross.

Boccagni, P., & Duyvendak, J. W. (2020). Making home. In J. R. Bowen, N. Dodier, J. W. Duyvendak, & A. Hardon (Eds) Practical Enquiry Critical Concepts for Social Science (pp. 205–218). Routledge eBooks. https://doi.org/10.4324/9781003034124-17

Bowlby, S., Gregory, S., & McKie, L. (1997). "Doing home": Patriarchy, caring, and space, *Women's Studies International Forum*, 20(3), 343–350.

Butler, J. (1990). *Gender Trouble: Feminism and the Subversion of Identity*, Routledge.

Butler, J. (1993). *Bodies of Matter: On the Discursive Limits of "Sex"*, Routledge.

Coolen, HCCH., & Ozaki, R. (2004). Culture, lifestyle, and the meaning of a dwelling. In J. D. Hulchanski, R. A. Murdie, & P. Campsie (Eds.), Adequate & affordable housing for all. Research, policy and practice; ISA International Housing Conference (pp. 1-15). CUCS Press.

Copeman, J. (2012). The Mimetic Guru: Tracing the Real in Sikh-Dera Sacha Sauda Relations, In J. Copeman & A. Ikegame (Eds.). *The Guru in South Asia*. Routledge.

Crooks DL. (2001). The importance of symbolic interaction in grounded theory research on women's health. *Health Care Women International.* 22(1-2):11-27. https://doi.org/10.1080/073993301300003054.

De Certeau, M. (1984). The Practice of Everyday life. Univ of California Press.

Del Castillo, N., Corpuz-Mendoza, A., (2010). The Meaning of the Meaning of Houses: An Interdisciplinary Study. On the Edge. Proceedings of the 44th Annual Conference of the Architectural Science Association. Unitec Institute of Technology.

Després, C. (1991). The Meaning of Home: Literature Review and Directions for Future Research and Theoretical Development. *Journal of Architectural and Planning Research*, *8*(2), 96–115. http://www.jstor.org/stable/43029026

Encyclopedia MDPI. (2021). Deras in Northern India. Retrieved from https://encyclopedia.pub/entry/32101

Finzel, A. (2021). A Space for Everybody? Conceptualisations of the Hijras in Indian English as a Showcase for Gendered Space in Indian Society. In M. Sadeghpour and F. Sharifian (Eds.), *Cultural Linguistics and World Englishes. Cultural Linguistics* (pp 193-216). Springer. https://doi.org/10.1007/978-981-15-4696-9_10

Foucault, M., & Miskowiec, J. (1986). Of other spaces. *Diacritics*, 16(1), 22. https://doi.org/10.2307/464648

Gaten, M. (1983). A Critique of the Sex/gender Distribution, In J. Allen, & P. Patton, (Eds.), Beyond Marxism? Interventions After Marx, (pp 142-161), Intervention Publishers.

Giddens, A. (1984), *The Constitution of Society: Outline of*

*the Theory of Structuration*, Polity Press.

Ghosh, B. (2018). A Diachronic Perspective of *Hijra* Identity in India, In S. Patra & S. Roy (Eds.). *Sociology of Motherhood and Beyond—Roots and Rejuvenation* (pp 107-110), Levant Books.

Glaser, B. G & Strauss, A.L. (1967). *The discovery of grounded theory: Strategies for qualitative research*, Aldine Transaction.

Grosz, E. (1994). *Volatile Bodies: Toward a Corporeal Feminism*, Allen and Unwin.

Hall, K. (1996). Lexical Subversion in the Hijra Community, in N. Warner (Eds.), Gender and Belief Systems: Proceedings of the Third Berkeley Women and Language Conference. Berkeley Women and Language Conference. Berkeley Women and Language Group (pp. 279-292).

Hamzić, V. (2019). The Dera Paradigm: Homecoming of the Gendered Other. *EthnoScripts*, 21(1).

Hinchy, J. (2019). The long history of criminalising Hijras. Himal Southasian. https://www.himalmag.com/.

Hossain, A. (2021). *Beyond emasculation: Pleasure and power in the making of Hijra in Bangladesh*, Cambridge University Press.

Hossain, M. S. (2010). Enforced ab/normalcy: the sex worker *hijras* and the (re)appropriation of s/he identity. In M. H. Ditmore, A. Levy, & A. Willman (Eds.), *Sex Work Matters: Exploring Money, Power, and Intimacy in the Sex Industry* (pp 117-139). Zed Books

Islam, A. (2016). *Right to education of the third gender of Bangladesh: An overview*. *Journal of Humanities and Social Science*, 21(9), 29-34.

Jackline, A. (2025). The concept of home: Cultural perspectives and personal reflections, 7(3), 63-67.

Jadhav, S. (n.d.). Michel Foucault's Theory of Heterotopia. *Re-thinking The Future*, https://www.re-thinkingthefuture.com/architecturalCommunity/a8932-michel-foucaults-theory-of-heterotopia/ Accessed 5 March. 2025.

Jami, H. & Kamal, A. (2017). Myths about *Hijras* (Male-to-Female Transgender of *Hijra* Community)? Role of Gender and Commonly Held Belief about Them, *Foundation University Journal of Psychology*, 1(4), 63-76.

Khan, S. I., Hussain, M. I., Parveen, S., Bhuiyan, M. I., Gourab, G., Sarker, G. F., Arafat, S. M. & J. Sikder. (2009). Living on the extreme margin: Social exclusion of the transgender population (Hijra) in Bangladesh, *Journal of Health, Population and Nutrition* 27 (4), 441-451.

Kellett, P & Moore, J. (2003). Routes to home: homelessness and home-making in contrasting societies, *Habitat International*, 27(1), 123-141, https://doi.org/10.1016/S0197-3975(02)00039-5

Märtsin, M. (2023). Homemaking away from home: A semiotic cultural psychology perspective. *Frontiers in Psychology*, *14*, 1215654. https://doi.org/10.3389/fpsyg.2023.1215654

Mallett, S. (2004). Understanding Home: A Critical Review of the Literature. *The Sociological Review*, *52*(1), 62–89. https://doi.org/10.1111/j.1467-954x.2004.00442.x

Massey, D. (1994). *Space, place, and gender*. University of Minnesota Press.

McNabb, C. (2018). *Nonbinary Gender Identities: History, Culture, Resources*. Rowman & Littlefield Publishers.

Of Other Spaces (1967), Heterotopias. (n.d.). *Michel Foucault, Info.* https://foucault.info/documents/heterotopia/foucault.heteroTopia.en/. Accessed 5 March. 2025.

Ozaki, R. (2005). House design as a representation of values and lifestyles: The meaning of use of domestic space, In G. R. Mira, D. L. Uzzell, E. Real & J. Romey (Eds.). *Housing Space and Quality of Life* (pp 97-111), Routledge.

Podder, A. K., & Shahidullah, F. B. (2023). Fictive home: the politics of urban homemaking of *Hijras* in Khulna, Bangladesh. *FARU Journal*, 10(2), 92–100. https://doi.org/10.4038/faruj.v10i2.254

Podder, A. K., & Shahidullah, F. B. (2024). Counter Home: Unravelling the Socio-Spatial Dynamics of Hijra Dwellings of Khulna, Bangladesh. *eTropic Electronic Journal of Studies in the Tropics*, 23(2), 235–269. https://doi.org/10.25120/etropic.23.2.2024.4060

Rapoport, A. (1969). *House form and culture*. Prentice-Hall.

Rapoport, A. (1981). Identity and environment: A cross-cultural perspective, In J.S. Duncan (Ed.), Housing and Identity: Cross-cultural perspectives, Croom Helm (pp 6-35).

Rapoport, A. (1988). Levels of meaning in the built environment. In F. Poyatos (Eds.), Cross-cultural perspectives in nonverbal communication, (pp 317-336), C.J. Hogrefe.

Roy, J. (2015). The "Dancing Queens": Negotiating Hijra Pehchān from India's Streets onto the Global Stage, *Ethnomusicology Review*, 20.

Saunders, P. and Williams, P. (1988). The Constitution of the Home: Towards a Research Agenda, *Housing Studies*, 3(2), 81–93.

Scott, J. C. (1990). *Domination and the arts of resistance: Hidden Transcripts*. Yale University Press.

Sharma, D. C. (2014). Changing landscape for sexual minorities in India. *The Lancet*, 383(9936), 2199- 2200.

Shawkat, S. S. (2016). Construction of Hijra Identity. [Bachelor's Theses, BRAC University]. BRAC University Institutional Repository. http://hdl.handle.net/10361/7804

Shroff, S. (2020). Operationalizing the "New" Pakistani Trans Gender Citizen. In A. Roy (Eds). *Gender, Sexuality, Decolonization: South Asia in the World Perspective* (pp 260-282), Taylor & Francis.

Shuvo, S. H. (2018) Life of Hijra in Bangladesh: Challenges to accept in mainstream, *International Journal of Natural and Social Sciences* 5(3), 60-67.

Singh, H., & Kumar, P. (2020). Hijra : an understanding. *Journal of Psychosocial Research*, 15(1), 77–87.

Singh, P. (2010). *Life and Work of Guru Arjan: History, Memory, and Biography in the Sikh Tradition*. Oxford

University Press.

Snigdha, R. K. (2021). Beyond Binaries: An Ethnographic Study of Hijra in Dhaka, Bangladesh. [Doctoral Dissertation, BRAC University, Auckland University of Technology]. AUT Research Repository. https://hdl.handle.net/10292/14422

Somerville, P. (1992). Homelessness and the Meaning of Home: Rooflessness and Rootlessness? *International Journal of Urban and Regional Research*, 16(4), 529–539.

Strauss, A., & Corbin, J. (1994). Grounded theory methodology: An overview. In N. K. Denzin & Y. S. Lincoln (Eds.), *Handbook of qualitative research* (pp. 273–285). Sage Publications, Inc.

Subramanian, P. (2022). Clapping Along or Clapping Back: Of the Discourse of Hijra Community's Resilient Happiness in Y-Film's Hum Hain Development Happy. *Society and Culture in South Asia* , 9(1), 81–103. https://doi.org/10.1177/23938617221076181

Turner, V. (1995). *The ritual process: Structure and Anti-Structure*. Transaction Publishers.

UNDP. (2010). *Hijras/Transgender Women in India: HIV, Human Rights and Social Exclusion*. United Nations Programme (UNDP). Retrieved from https://www.undp.org/india/publications/hijras/transgender-india-hiv-human-rights-and-social-exclusion.

Vanita, R. (2002). *Dosti* and *Tamanna*: Male-Male Love, Difference, and Normativity in Hindi Cinema, in D. Mines & S. Lamb (Eds.), *Everyday Life in South Asia* (pp 146-58). Indiana UP.

Vinay, V. (2022). The (Colonial) History of Sexuality: The Colonial Categorization of Sexuality in Colonized India. *MUNDI*, *2*(1).

Walker, L. (2002). Home Making: An Architectural Perspective. *Journal of Women in Culture and Society*, 27(3), 823-835. https://doi.org/10.1086/337927

Wardhaugh, J. (1999). The Unaccommodated Woman: home, homelessness and identity. *The Sociological Review*, 47(1), 91–109. https://doi.org/10.1111/1467-954x.00164

Wels, H., van der Waal, K., Spiegel, A., & Kamsteeg, F. (2011). Victor Turner and liminality: An introduction. *Anthropology Southern Africa*, 34(1–2), 1–4. https://doi.org/10.1080/23323256.2011.11500002

Young, M., (1990), A Tropology of the Dobu Mission, *Canberra Anthropology*, 3: 86–104.

MIJST
*MIST International Journal of Science and Technology*

# A Neural Network Based Software Defect Prediction Approach Using SMOTE and Noise Filtering-CLNI

**Ahmmed Bin Ashfaque[1], Abdus Sattar[2], Hosney Jahan[*3], M. Akhtaruzzaman[4], and Fernaz Narin Nur[5]**

[1]Department of CSE, Bangladesh Army University of Science and Technology, Fultola Khulna-9204, Bangladesh
[2]Department of Computer Science and Engineering, Military Institute of Science and Technology, Dhaka, Bangladesh
[3]Department of Computer Science and Engineering, East West University, Dhaka-1212, Bangladesh
[4]Department of Computer Science and Engineering, Daffodil International University, Savar, Dhake-1216, Bangladesh
[5]Quantum Robotics and Automation Research Group (QRARG), Mirpur, Dhaka-1216, Bangladesh

***Corresponding Email:** *hosney.jahan@ewubd.edu*

**ARTICLE INFO**

**Article History:**

*Received: 19th May 2025*
*Revised: 29th September 2025*
*Accepted: 13th October 2025*
*Published: 30th December 2025*

**Keywords**:

*Software Defect Prediction*
*SMOTE*
*CLNI*
*Dense Neural Network*
*Data Balancing*
*Feature Selection*

**ABSTRACT**

Software defects can cause significant loss and system failures in software development life cycle. Software Defect Prediction (SDP) is a vital step for ensuring the quality of software. Till now, a number of machine learning models have been proposed to predict potential defects and make the software more reliable. However, SDP models suffer from the problem of imbalanced dataset, resulting in poor prediction accuracy. To mitigate this, issue several data balancing techniques, i.e., over sampling, under sampling etc. have been proposed to balance the dataset. In some cases, the data balancing methods may further introduce noisy and mislabeled samples in the dataset. To deal with these issues, in this paper, we propose a neural network based approach that combines the oversampling technique Synthetic Minority Oversampling Technique (SMOTE) with the noise filtering technique Class Level Noise Identification (CLNI). Here, we applied three different CLNI methods which are Edited Nearest Neighbor (ENN), Repeated ENN (RENN) and All-KNN. Our aim is to make the dataset clean, balanced and efficient by combining SMOTE with CLNI. In addition, we applied a number of feature selection methods to identify the most important features, further contributing towards achieving better prediction accuracy. To evaluate the effectiveness of the proposed model, we conduct experiments on several benchmark datasets (MC1, PC1, PC2, PC3 and PC4) obtained from NASA MDP and (ML, LC and JDT) AEEEM repository. The experimental results have been evaluated and compared in terms of accuracy, precision, recall and AUC-ROC curve. The experimental results demonstrated that our proposed approach has achieved up to 98% accuracy and outperformed state-of-the-art approaches.

This work is licensed under a *Creative Commons Attribution-Non-commercial 4.0 International License.*

## 1. INTRODUCTION

In the domain of software engineering, the identification and classification of software defects is a critical activity during the testing phase of software development. With the increasing complexity of software systems and growing demands for higher reliability, it is necessary to ensure the quality of the software. In the modern era, where numerous software systems compete in terms of functionality and performance, predicting software defects has become a challenging task. Figure 1 and Figure 2 demonstrate the example of defective and non-defective code in the software.

The primary objective of predicting software defects is to reduce the effort of software testing through proper guideline. Proper software testing enables many software organizations to predict defects in a way that saves time, stays within budget, improves software quality, and facilitates better resource planning to meet project timelines (*Akintola et al., 2018*).

```
public static int defectiveSum(int[] arr) {
    int sum = 0;
    for (int num : arr) {
        sum = num;
        // Incorrectly overwrites the sum instead of accumulating
    }
    return sum;
}
```

**Figure 1**: Defective code example

```
public static int cleanSum(int[] arr) {
    int sum = 0;
    for (int num : arr) {
        sum += num;
        // Accumulate the sum correctly
    }
    return sum;
}
```

**Figure 2**: Non-defective code example

Till now a number of machine learning approaches have been applied in software defect prediction. However, the performance of these methods are often hindered by imbalanced datasets. Class imbalance is the major problem related to software defect dataset, where the unequal distribution between the number of defective instances (i.e. the minority class) is significantly smaller than the non-defective instances (i.e. the majority class) (*Feng et al., 2021*). This imbalance limits the classifiers ability to classify the minority class, often leading to misclassification error.

To address this problem, various data balancing techniques are available, i.e., oversampling, undersampling etc. Among them, SMOTE (*khleel et al., 2024*) and Random oversampling (*Khleel et al., 2024*) has been widely adopted to balance datasets by generating synthetic samples for the minority class. However, SMOTE has a notable drawback - it can introduce noise by generating synthetic instances from or near mislabeled or noisy data points (*Alkhawaldeh et al., 2023*), result in over-fit prediction model (*Rathore et al., 2024*). Because, SMOTE lacks a mechanism to distinguish between clean and noisy samples, it may inadvertently amplify existing errors in the data.

To mitigate these drawbacks, in this paper, we propose a neural network based approach that combines the oversampling technique SMOTE with the noise removing technique CLNI. Here, we applied three noise filtering techniques which are Edited Nearest Neighbor (ENN), Repeated ENN (RENN) and All-KNN (*Gupta et al., 2023*). These techniques act as a preprocessing step, enhancing data quality and improving the performance of classifiers. Our aim is to reduce the misclassification rate and overfitting problem by Integrating SMOTE with CLNI. In addition to this, we further applied a number of feature selection methods to achieve more accurate prediction. The feature selection methods used in our research are Correlation Coefficient, Mutual Information, Variance Threshold and Chi-Square. The objective of this research is to develop accurate software defect prediction model by addressing the challenges of class imbalance, data noise and irrelevant features through an integrated approach.

This research paper is divided into sections as follows: Literature review is presented in Section II. Methodology is illustrated in Section III. Result analysis is presented in Section IV. Conclusions are drawn in section V.

## 2. LITERATURE REVIEW

In this section, we review previous research on Software Defect Prediction (SDP), highlighting significant contributions in the areas of handling class imbalance, feature selection techniques and neural network approaches for early defect prediction in the Software Development Cycle (SDLC).

Software defect datasets are challenging to use due to their imbalanced class distributions. (*Ali et al., 2024*) used the SMOTE preprocessing approach with NASA MDP datasets (CM1, JM1, PC1, PC4, MC2, PC3, and MW1). Using the voting ensemble approach combined with machine learning algorithms such as RF, SVM, NB, and ANN to improve prediction performance. Their method achieved a training accuracy of 87.2% and a testing accuracy of 86.87%. SMOTE may introduce unnecessary noise. To overcome with this problem, (*Vuttipittayamongkol et al., 2022*) proposed neighborhood-based undersampling algorithm. This algorithm reduced the majority class and balance the ratio between majority and minority class. Experimental results observed on NASA datasets, having an AUC of 95.9% and an accuracy of 96.9% with 95% confidence level. Undersampling technique may possess loss of important data.

A real-time deep ladder network proposed to tackle the problem of SMOTE and undersampling by (*J. et al., 2023*). This method integrated with migration learning, a deep belief network combined with transfer component analysis superior that others.

Software defect datasets consist of large number of metrics such as line of code (LOC), complexity measures, cyclomatic complexity and so on. Many of them are irrelevant in software defect prediction. To reduce model's overfitting, (*Cetiner et al., 2020*) applied Principal Component Analysis (PCA) as a feature reduction technique, while comparing ten machine learning algorithms. They used Decision Tree, Naïve Bayes, K-nearest neighbor, Support vector machine, random forest, extra tress, adaboost, gradient boosting, bagging and multi-layer perceptron. The evaluation performance showed that Random forest achieved higher accuracy on PC1 dataset.

A five-stage framework for software defect prediction using NASA datasets proposed by (*Ali et al., 2024*). They combined genetic algorithm-based feature selection with heterogeneous classifiers (Random Forest, SVM and Naïve Bayes). Their iterative optimization process, utilizing an ensemble voting technique, achieved a maximum classification accuracy of 95.1%, while reducing execution time by over 50%.

Enhanced exploratory whale optimizer-based feature selection method along with random forest ensemble learning proposed (*Mafarja et al., 2023*) to software defect prediction while Siamese Dense Neural Network (SDNN) introduced by (*Zhao et al., 2018*), which combines similarity feature learning and distance metric learning using a contrast loss function with cosine proximity. Their experimental results demonstrated that SDNN outperforms traditional methods, particularly in scenarios with limited data and imbalanced class distributions.

The literature study highlights several challenges in software defect prediction, including noise introduction during resampling methods like SMOTE, the complexity of feature selection, and the high computational costs associated with

ensemble models and deep learning methods. The purpose of the research is to improve accuracy and efficiency in software defect prediction, addressing the limitations identified in previous studies.

## 3. METHODOLOGY

This research presents a software defect prediction approach that combines SMOTE and CLNI for data balancing, feature selection for selecting important features, and a Dense Neural Network for classification. Figure 3 depicts an overview of the approach consisting four phases: 1) Dataset collection, 2) Data preprocessing, 3) Feature selection, and 4) Prediction.

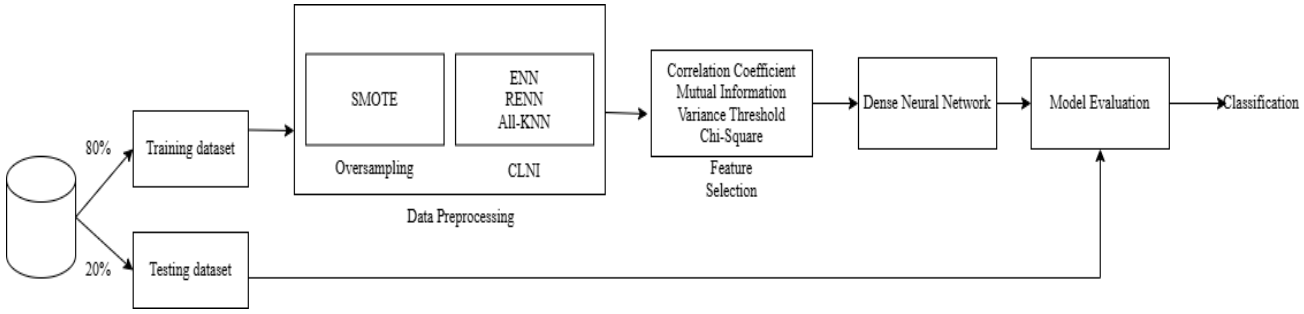



**Figure 3**: Overview of the Software Defect Prediction Model

### 3.1 Dataset Collection

To measure the effectiveness of our proposed approach, we considered a number of well-known and widely used datasets from NASA MDP (Metrics Data Program) repository and AEEEM dataset repository. They contain various software metrics which were organized and collected from various projects and widely used in software defect prediction related tasks. We selected MC1, PC1, PC2, PC3 and PC4 datasets from NASA MDP and JDT, ML and LC from AEEEM repository for our approach. Each of them consists of multiple attributes like Halstead metrics, code complexity metrics and many others. Table 1 and Table 2 describe the details of the NASA MDP and AEEEM dataset respectively.

**Table 1**
NASA MDP Dataset

| Dataset | Attributes | Modules | Defective | Non-defective |
|---|---|---|---|---|
| MC1 | 39 | 9466 | 68 | 9398 |
| PC1 | 40 | 1107 | 76 | 1031 |
| PC2 | 40 | 1563 | 160 | 1403 |
| PC3 | 40 | 1270 | 176 | 1094 |
| PC4 | 36 | 1694 | 458 | 1236 |

**Table 2**
AEEEM Dataset

| Project | Number of files | Percentage of Buggy Files | Number of metrics |
|---|---|---|---|
| LC | 399 | 9.26 | 71 |
| ML | 1862 | 13.16 | 71 |
| JDT | 997 | 20.66 | 71 |

### 3.2 Data Preprocessing

To preprocess the defect datasets, we applied two methods: data balancing with SMOTE and noise removing with CLNI. Though there are many noise filtering methods, but in our research we used only three of them. The details of these methods are discussed in the following subsections.

#### 3.2.1 Dataset Balancing with SMOTE

SMOTE creates new minority class by linear interpolation between existing samples and their neighbors (Elreedy et al., 2019). For each minority samples $X_0$, one of its K nearest neighbors X is chosen at random, and a synthetic dataset is created as follows:

**Algorithm: *SyntheticSampleGen(X_minority, N, k)***

***Input**: Minority class samples $x_minority$, number of synthetic samples N, number of nearest neighbors k*

***Output**: Augmented dataset with synthetic samples*

*Repeat N times:*
*Select a random sample $x_0$ from $x_minority$*
*Find its k nearest neighbors in $x_minority$*
*Choose one neighbor x at random*
*Generate a random value w between 0 and 1*
*Create a new sample z between $x_0$ and x using*

$$z = x_0 + w \times (x - x_0)$$

*Add z to the set of synthetic samples*
*Return $x_minority \cup \{z_1, z_2, \ldots . z_n\}$ as the augmented dataset*

#### 3.2.2 Noise Removal using CLNI

CLNI is a method to reduce the noise generated from the oversampling technique SMOTE. Many types of CLNI methods are available, among them, we performed ENN, RENN and All-KNN in our research.

**Edited Nearest Neighbors:** Edited Nearest Neighbors is an enhanced version of k-nearest Neighbors to eliminate noisy and mislabeled instances from the dataset.

**Algorithm *ENN (D, k)***

***Input**: Dataset D, number of neighbors k*

*For each instance x in D:*
*Find k nearest neighbors of x*
*Determine majority class among neighbors*
*If class(x) ≠ majority class:*
*Remove x from D*
*Return cleaned dataset D*

**Repeated ENN:** RENN removes noisy instances that differ from their neighbors. It repeats the process until no more instances are removed in an iteration.

**Algorithm: *RENN (D, k)***

***Input**: Dataset D, number of neighbors k*

*Repeat:*
*Initialize change_flag = False*
*For each instance x in D:*
*Find k nearest neighbors of x*
*Determine majority class among neighbors*
*If class(x) ≠ majority class:*
*Remove x from D*
*Set change_flag = True*
*Until change_flag is False*
*Return cleaned dataset D*

**All-KNN:** All-KNN reduces the borderline and mislabeled instances, in noisy or mislabeled datasets.

**Algorithm: *AllKNN (D, k_max)***

***Input**: Dataset D, maximum neighbors k_max*

*For k from 1 to k_max:*
*For each instance x in D:*
*Find k nearest neighbors of x*
*Determine majority class*
*If class(x) ≠ majority class:*
*Mark x for removal*
*Remove all marked instances*
*Return cleaned dataset D*

### 3.3 Feature Selection

To reduce the dimension of data to reduce the memory wastage, this paper applied Correlation Coefficient, Mutual Information, Variance Threshold and Chi-Square feature selection methods. The most significant features identified are included:

- LOC_BLANK,
- PERCENT_COMMENTS,
- LOC_COMMENTS,
- LOC_CODE_AND_COMMENT,
- NUMBER_OF_LINES,
- CALL_PAIRS,
- NUM_UNIQUE_OPERANDS,
- NUM_UNIQUE_OPERATORS,
- HALSTEAD_CONTENT,
- LOC_TOTAL,
- DECISION_DENSITY, and
- LOC_EXECUTABLE

#### 3.3.1 Correlation Coefficient

Correlation coefficient is a statistical technique used to measure and evaluate the strength and direction of the linear relationship between two variables (*Schober et al., 2018*). It is commonly quantified using metrics like Pearson's correlation coefficient for continuous data. Mathematically, it can be written as (Venkatesh et al., 2019),

$$\rho(x, y) = \frac{\sum_i (x_i - \bar{x})(y_i - \bar{y})}{\sqrt{\sum_i (x_i - \bar{x})^2 \, (y_i - \bar{y})^2}} \qquad (1)$$

The correlation coefficient ranges from -1 to 1, where values close to 1 indicate a strong positive relationship, values near -1 represent a strong negative relationship and values close to 0 suggest no linear relationship.

#### 3.3.2 Mutual Information

Mutual information is the measurement of how two variables mutually correlated with each other (*Venkatesh et al., 2019*). Mathematically,

$$\mathrm{I(m, n)} = \sum_{b \in B} \sum_{a \in A} p(m, n) \log \left( \frac{p(m, n)}{p(m) p(n)} \right) \qquad (2)$$

Where, $p(m, n)$ is the joint probability distribution of m and n, and $p(m)\ and\ p(n)$ are the marginal probability distribution of m and n.

#### 3.3.3 Variance Threshold

Variance Threshold is a simple and commonly used feature selection technique that removes low variance features from a dataset. The assumption behind this method is that features with very little variance across the samples are unlikely to contain useful information for distinguishing between classes or predicting the target variable. By specifying a threshold, features with variance below this threshold are eliminated (*McHugh et al., 2008*).

#### 3.3.4 Chi-Square

Chi-Square (*McHugh et al., 2008*) is a statistical test used to measure the association between categorical variables. Mathematically, it can be written as,

$$\chi^2 = \sum \frac{(\text{Observed} - \text{Expected})^2}{\text{Expected}} \quad (3)$$

It calculates the discrepancy between the observed and expected outcome for each category of data.

### 3.4 Prediction Model

In this stage, this paper used Dense Neural Network to train the dataset and classify them into Defective and Non-defective. We Applied grid search to identify the best parameters for our Dense Neural Network. The list of parameters used in our work is shown in Table 3.

**Table 3**
Parameter List for Dense Neural Network

| Parameters | Value |
|---|---|
| Neurons | 64 |
| Dropout_rate | 0.3 |
| Batch_size | 32 |
| Epoch | 30 |
| Optimizer | adam |

## 4. Result analysis

This section shows the performance of software defect prediction using Dense Neural Network in brief manner. This experiment was conducted on an 8GB RAM PC on Google Colaboratory using Python Programming Language. Experimental dataset was collected and processed for neural network analysis.

### 4.1 Evaluation Metrics

In order to evaluate the performance of our proposed approach, we used a number of evaluation metrics, i.e., accuracy, precision, recall and ROC-AUC. ROC-AUC plots the True Positive Rate or Recall against the False Positive Rate (FPR). AUC indicates the model's performance to distinguish between the classes.

### 4.2 Classification Result

For the classification purpose, we have used five datasets named MC1, PC1, PC2, PC3 and PC4 from NASA MDP and three datasets named LC, JDT and ML from AEEEM dataset repository. Performance evaluation metrics for both of them are shown from Table 4 to Table 7. Table 4 and Table 5 presents a comparative analysis of different CLNI techniques, ENN, RENN and All-KNN evaluated with feature selection and without feature selection respectively across three performance metrics: Accuracy, precision and Recall for MC1, PC1, PC2, PC3 and PC4 dataset.

**Table 4**
Performance comparison between different CLNI methods using NASA MDP dataset without feature selection

| | Accuracy | | | Precision | | | Recall | | |
|---|---|---|---|---|---|---|---|---|---|
| | **ENN** | **RENN** | **All-KNN** | **ENN** | **RENN** | **All-KNN** | **ENN** | **RENN** | **All-KNN** |
| **MC1** | 0.94 | 0.94 | 0.93 | 0.94 | 0.93 | 0.93 | 0.94 | 0.93 | 0.92 |
| **PC1** | 0.90 | 0.90 | 0.91 | 0.90 | 0.92 | 0.92 | 0.90 | 0.92 | 0.91 |
| **PC2** | 0.93 | 0.92 | 0.91 | 0.91 | 0.92 | 0.93 | 0.91 | 0.94 | 0.92 |
| **PC3** | 0.83 | 0.84 | 0.83 | 0.85 | 0.83 | 0.82 | 0.83 | 0.83 | 0.84 |
| **PC4** | 0.89 | 0.90 | 0.90 | 0.89 | 0.90 | 0.90 | 0.90 | 0.90 | 0.90 |

**Table 5**
Performance comparison between different CLNI methods using NASA MDP dataset with feature selection

| | Accuracy | | | Precision | | | Recall | | |
|---|---|---|---|---|---|---|---|---|---|
| | **ENN** | **RENN** | **All-KNN** | **ENN** | **RENN** | **All-KNN** | **ENN** | **RENN** | **All-KNN** |
| **MC1** | 0.98 | 0.99 | 0.98 | 0.98 | 0.98 | 0.98 | 0.98 | 0.99 | 0.98 |
| **PC1** | 0.95 | 0.95 | 0.96 | 0.94 | 0.95 | 0.96 | 0.95 | 0.95 | 0.97 |
| **PC2** | 0.98 | 0.98 | 0.97 | 0.97 | 0.97 | 0.97 | 0.98 | 0.98 | 0.98 |
| **PC3** | 0.87 | 0.87 | 0.88 | 0.87 | 0.86 | 0.88 | 0.87 | 0.87 | 0.88 |
| **PC4** | 0.93 | 0.93 | 0.95 | 0.93 | 0.93 | 0.95 | 0.95 | 0.94 | 0.95 |

Across all five datasets, RENN consistently achieves either the highest or comparable performance in all three metrics, accuracy, precision, and recall that indicating its effectiveness as an efficient noise-handling technique. All-KNN also performs competitively, surpassing RENN in datasets like PC1 and PC4, particularly in precision and accuracy. In contrast, ENN, generally ranks slightly below RENN and All-KNN across most datasets, especially in datasets like PC3, where its Precision drops. Overall, RENN appears to be the most balanced and reliable technique across diverse datasets, while All KNN shows strengths in select cases, and ENN maintains moderate but consistent performance. Dataset specific variation, especially in PC3,

highlights the importance of utilizing the noise identification method to dataset characteristics.

Table 6 and Table 7 presents a comparative analysis of different CLNI techniques, ENN, RENN and All-KNN evaluated with feature selection and without feature selection respectively across three performance metrics: accuracy, precision and recall for ML, JDT and LC dataset. By analyzing the performance of all datasets, it is observed that PC3 dataset underperforms due to is limited number of, highlighting the importance of having a sufficient amount of training data.

**Table 6**
Performance comparison between different CLNI methods using AEEEM dataset without feature selection

| | Accuracy | | | Precision | | | Recall | | |
|---|---|---|---|---|---|---|---|---|---|
| | **ENN** | **RENN** | **All-KNN** | **ENN** | **RENN** | **All-KNN** | **ENN** | **RENN** | **All-KNN** |
| **LC** | 0.93 | 0.90 | 0.90 | 0.89 | 0.91 | 0.91 | 0.90 | 0.89 | 0.90 |
| **ML** | 0.90 | 0.90 | 0.89 | 0.90 | 0.89 | 0.88 | 0.90 | 0.87 | 0.88 |
| **JDT** | 0.89 | 0.90 | 0.88 | 0.90 | 0.88 | 0.88 | 0.93 | 0.88 | 0.88 |

**Table 7**
Performance comparison between different CLNI methods using AEEEM dataset with feature selection

| | Accuracy | | | Precision | | | Recall | | |
|---|---|---|---|---|---|---|---|---|---|
| | **ENN** | **RENN** | **All-KNN** | **ENN** | **RENN** | **All-KNN** | **ENN** | **RENN** | **All-KNN** |
| **LC** | 0.98 | 0.95 | 0.94 | 0.98 | 0.95 | 0.94 | 0.97 | 0.94 | 0.95 |
| **ML** | 0.92 | 0.93 | 0.90 | 0.92 | 0.92 | 0.90 | 0.92 | 0.90 | 0.90 |
| **JDT** | 0.91 | 0.94 | 0.90 | 0.91 | 0.95 | 0.90 | 0.90 | 0.92 | 0.90 |

Among the evaluated CLNI techniques, ENN consistently demonstrates balanced and high performing results. This trend is observed across all datasets. It maintains a strong performance in terms of accuracy, precision, and recall. ENN proves to be the most efficient. RENN performs competitively, particularly excelling in precision, but shows slight tradeoffs in accuracy and recall. All-KNN, while perform yielding acceptable results, generally underperforms relative to ENN and RENN, indicating less efficient in handling noisy data. On the other hand, the LC dataset shows higher conflict and superior results across all methods, suggesting it is less affected by noise, whereas JDT and ML appear more sensitive to the choice of noise-filtering techniques.

Figure 4 and Figure 5 represents the comparative bar chart representation of the performance of various CLNI techniques on the dataset.

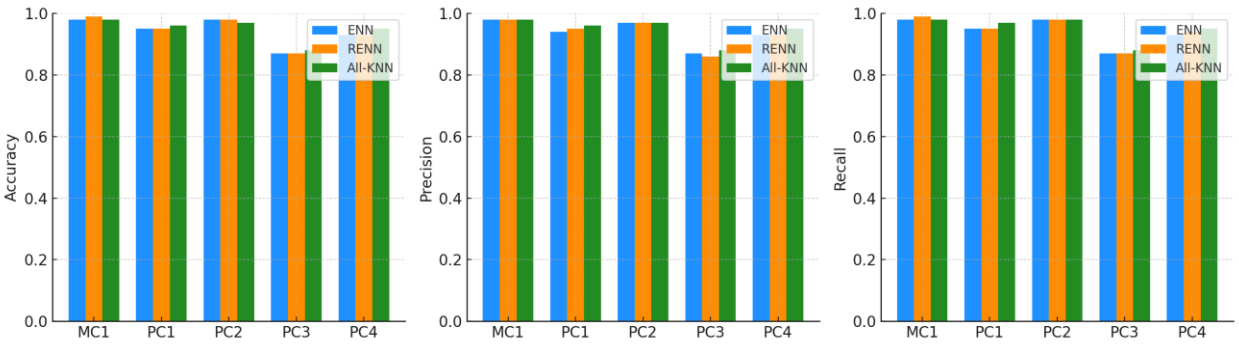



**Figure 4**: bar graph representation of the performance of the CLNI techniques for NASA MDP dataset

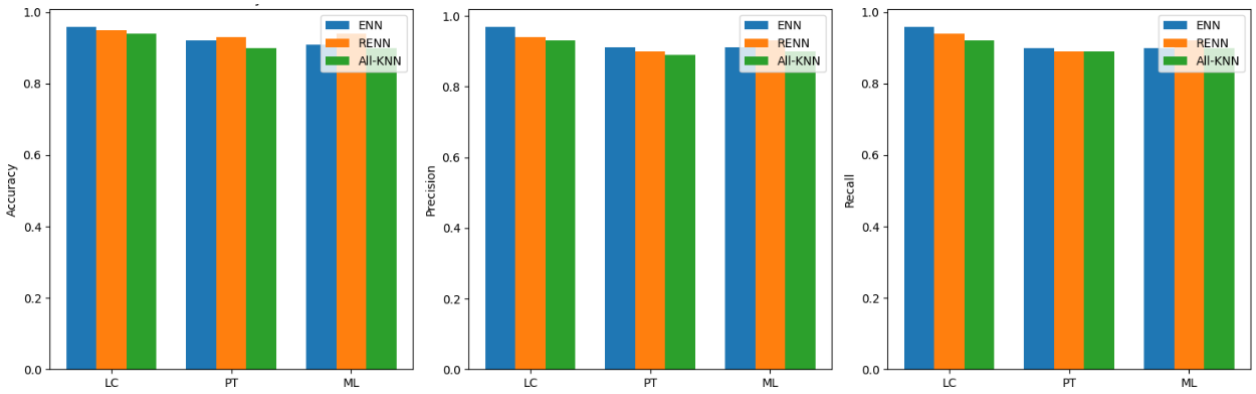



**Figure 5**: bar graph representation of the performance of the CLNI techniques for AEEEM dataset

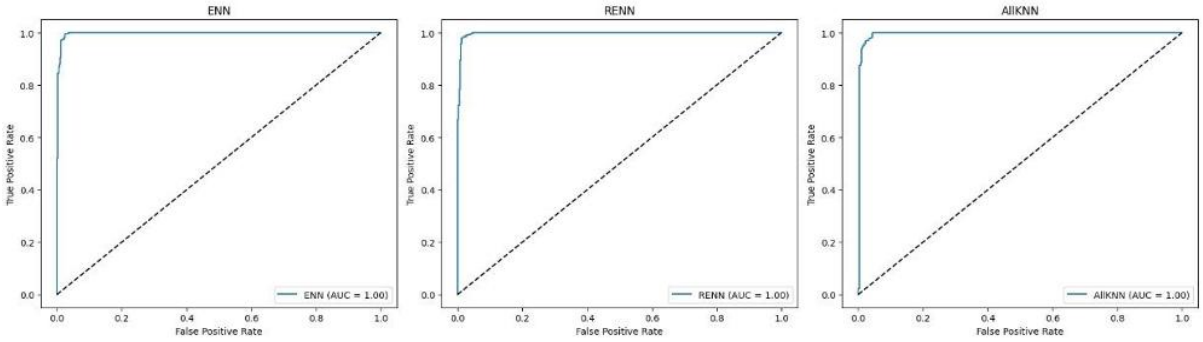



**Figure 6**: ROC-AUC curve for MC1 dataset

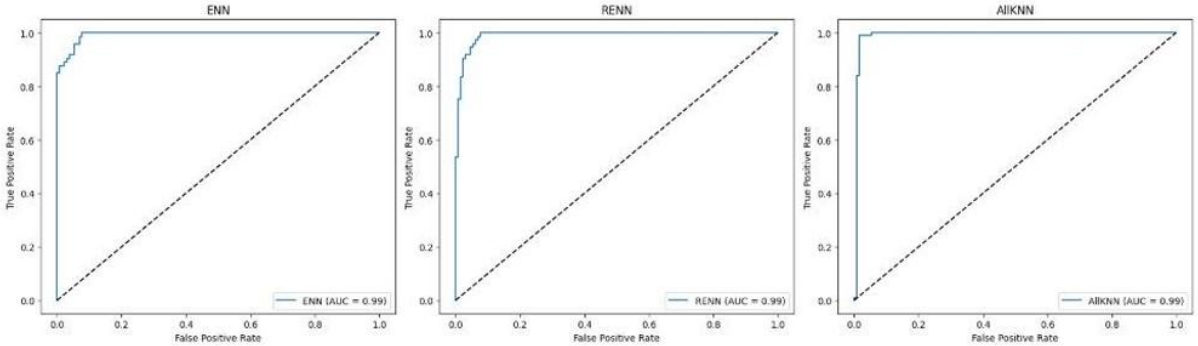



**Figure 7:** ROC-AUC curve for PC1 dataset

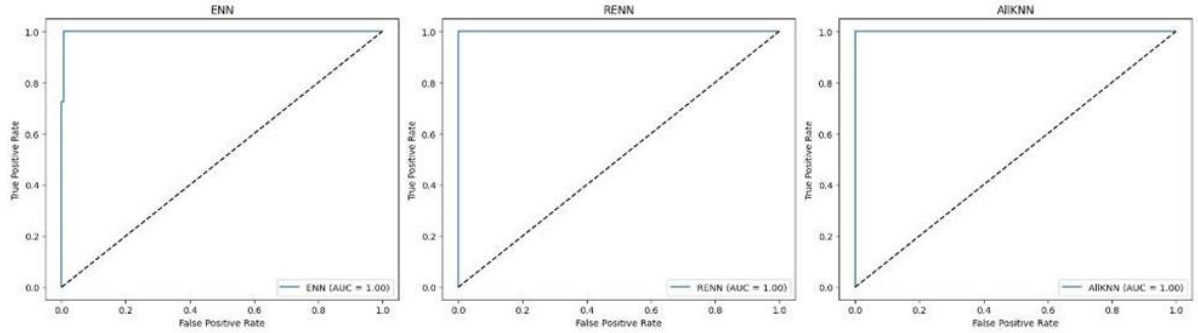



**Figure 8**: ROC-AUC curve for PC2 dataset

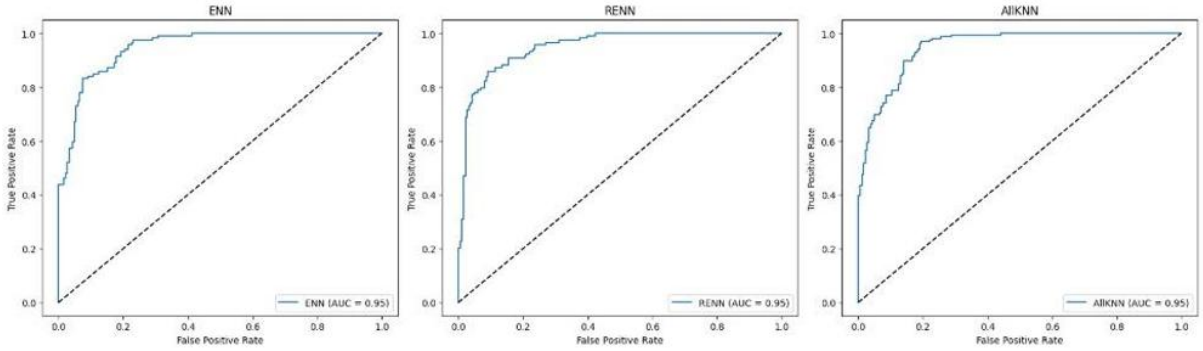



**Figure 9**: ROC-AUC curve for PC3 dataset

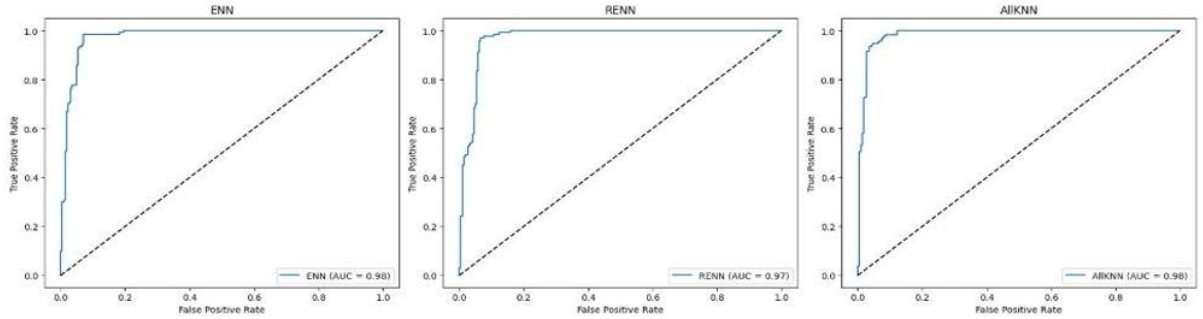



**Figure 10**: ROC-AUC curve for PC4 dataset

We further analyzed our results in terms of ROC-AUC curve. Figure 6 to Figure 10, all three methods, ENN, RENN, and All-KNN - show excellent performance on all datasets. For MC1 and PC2, the models reach a perfect score (AUC = 1.00), meaning they correctly separate the two classes every time, with no mistakes. The curves stay very close to the top-left corner, showing high accuracy with almost no false alarms. On the PC1 dataset, all methods score slightly below perfect (AUC = 0.99), still showing great results. ENN and RENN have smooth curves with very few errors, while All-KNN rises quickly, showing it catches most of the correct cases early. For PC3, the AUC drops to (0.95) for all three. This is still strong, but not as perfect as the others. It means the models are good but make a few more mistakes. All methods perform about the same here. The PC4 dataset has slightly lower scores: ENN (0.98), RENN (0.97), and All-KNN (0.96). ENN performs the best, while All-KNN is a bit lower, because it removes too much data when cleaning. In summary, all methods work very well, especially on MC1 and PC2. ENN is slightly more consistent across all datasets, making it a reliable choice.

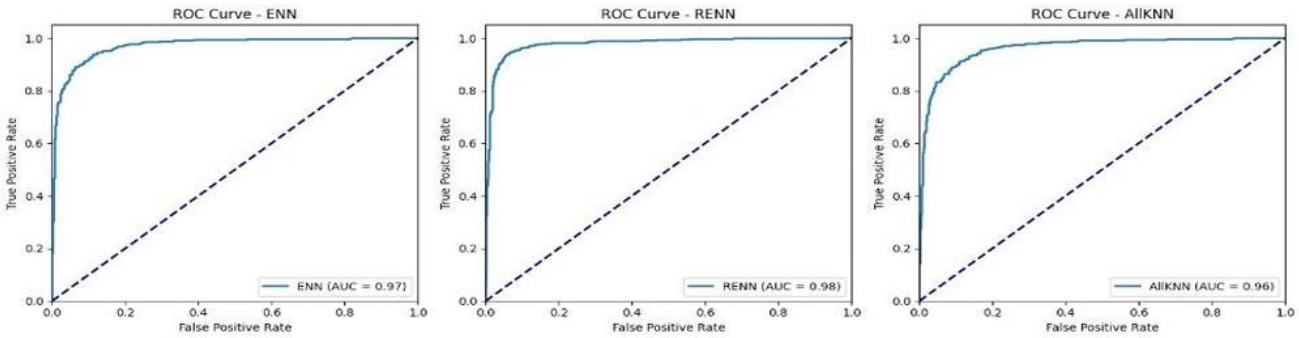



**Figure 11**: ROC-AUC curve for ML dataset

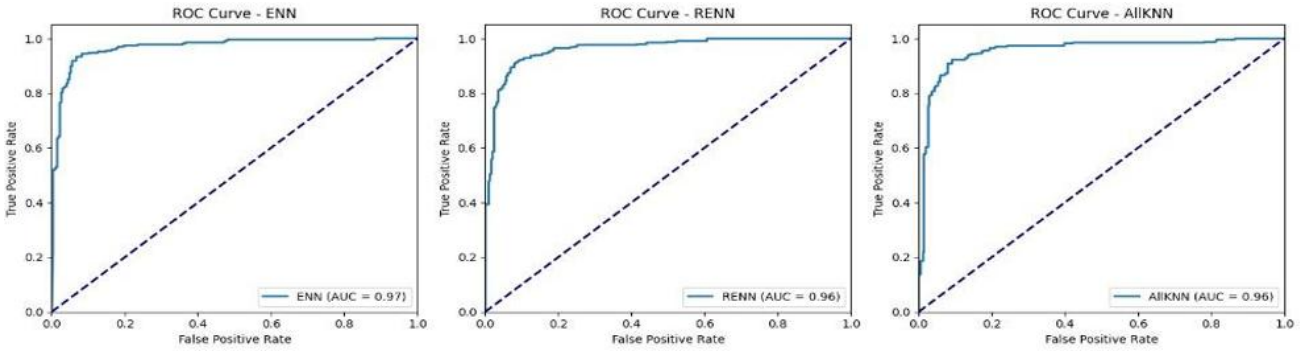



**Figure 12**: ROC-AUC curve for JDT dataset

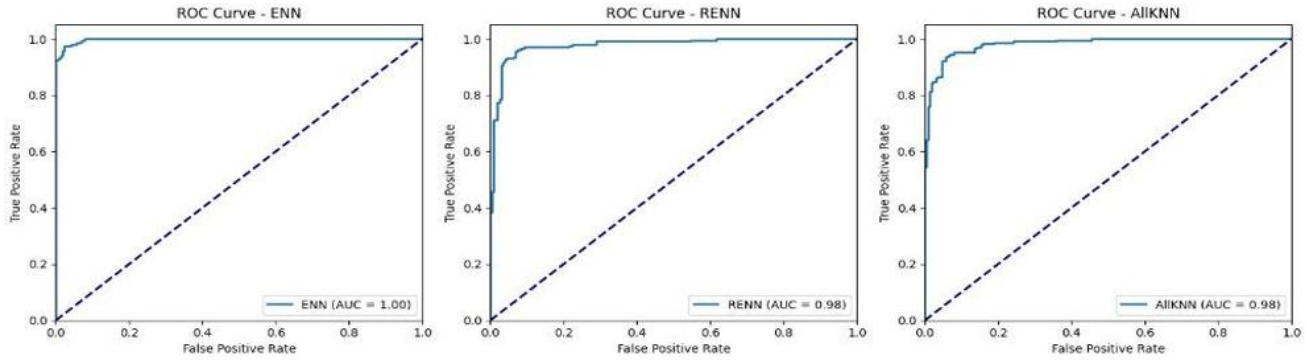



**Figure 13**: ROC-AUC curve for LC dataset

By analyzing the ROC-AUC curve for ML, JDT and LC dataset, it is observed that ENN consistently demonstrates a slight edge in performance, particularly on the LC and JDT datasets. On the LC dataset, ENN stands out with a perfect AUC of (1.00), clearly outperforming both RENN and All-KNN, which still achieve excellent scores of (0.98). In contrast, the ML dataset sees RENN take the lead with an AUC of (0.98), narrowly outperforming ENN (0.97) and All-KNN (0.96). For the JDT dataset, ENN once again leads at (0.97), while RENN and All-KNN both follow closely at (0.96). Through the performance gaps across methods are relatively small, ENN shows more consistent top-tier results across datasets.

### 4.3 Comparison with existing works

Table 8 presents a comparative analysis of various classification techniques applied to multiple datasets, focusing on the impact of balancing techniques, CLNI methods, and feature selection strategies. The results indicate that these preprocessing strategies contribute significantly in improving classification accuracy across different datasets.

**Table 8**
Comparison of Different Techniques on Various Datasets

| Ref | Balancing technique | CLNI technique | Dataset | Repository | Feature Selection Technique | Model | Result (Accuracy) |
|---|---|---|---|---|---|---|---|
| **Ali et al. (2024)** | - | - | CM1 | NASA MDP | - | Voting Ensemble | 86.87% |
| | | | JM1 | | | | 79.12% |
| | | | MC2 | | | | 68.42% |
| | | | MW1 | | | | 99.33% |
| | | | PC1 | | | | 82.16% |
| | | | PC3 | | | | 87.17% |
| **Proposed work** | SMOTE | ENN | MC1 | NASA MDP | Correlation Mutual Information Variance Threshold Chi-Square | Dense Neural Network | 99.02% |
| | | All-KNN | PC1 | | | | 97.42% |
| | | All-KNN | PC2 | | | | 99.63% |
| | | ENN | PC3 | | | | 88.58% |
| | | RENN | PC4 | | | | 95.34% |
| | | ENN | ML | AEEEM | | | 91.42% |
| | | All-KNN | JDT | | | | 94.53% |
| | | All-KNN | LC | | | | 95.43% |

## 9. CONCLUSIONS

Software defect prediction focuses on identifying faulty modules at the early stages of the software development life cycle. Developing an efficient and effective defect prediction model is crucial for reducing maintenance costs and improving software quality. In this research, we proposed a software defect prediction approach that integrates SMOTE with CLNI to achieve a more balanced dataset and improved prediction accuracy. The datasets are collected from NASA MDP and AEEEM. The model was evaluated using eight datasets with relevant features to assess its effectiveness. The results demonstrate that the proposed classification model yields promising performance compared to traditional approaches. However, when applied to different datasets, it is observed that the PC3 dataset underperforms due to its limited number of samples, highlighting the importance of having a sufficient amount of training data. Relying on a predefined feature selection method may limit the model's adaptability across diverse datasets. In future work, we aim to overcome this limitation by exploring uniform and adaptive feature selection strategies and evaluating the approach on a broader range of datasets.

## ACKNOWLEDGMENTS

The authors express their heartfelt gratitude to Bangladesh Army University of Science and Technology, Bangladesh; Military Institute of Science and Technology, Bangladesh; East West University, Bangladesh; Daffodil International University, Bangladesh, and Quantum Robotics and Automation Research Group (QRARG), Bangladesh.

## DATA AVAILABILITY STATEMENT

Datasets generated during the current study are available from the corresponding author upon reasonable request.

## FUNDING DECLARATION

This research was self-funded.

## ETHICS APPROVAL

This study is an engineering experimental investigation. The MIJST Research Ethics Committee has confirmed that formal ethical approval was not required.

## ETHICS, CONSENT TO PARTICIPATE, AND CONSENT TO PUBLISH

Not applicable.

## COMPETING INTERESTS

The authors declare that they have no competing interests.

## AUTHOR CONTRIBUTIONS

Author 1: Ahmmed Bin Ashfaque- Writing: Original draft, Review and editing, Formal analysis, Software, Validation, Visualization, Supervision

Author 2: Abdus Sattar2- Writing: Original draft, Review and editing, Formal analysis, Software, Validation, Visualization, Supervision

Author 3: Hosney Jahan- Writing: Original draft, Review and editing, Formal analysis, Software, Validation, Visualization, Supervision

Author 4: M. Akhtaruzzaman- Writing: Original draft, Review and editing, Formal analysis, Software, Validation, Visualization, Supervision

Author 5: Fernaz Narin Nur- Writing: Original draft, Review and editing, Formal analysis, Software, Validation, Visualization, Supervision

## ARTIFICIAL INTELLIGENCE ASSISTANCE STATEMENT

Portions of this manuscript were assisted by an artificial intelligence language model (ChatGPT, OpenAI). The tool was used solely for language editing, text refinement, and clarity improvement. All content, data interpretation, analysis, conclusions, and final decisions were generated, verified, and approved by the authors. The authors take full responsibility for the accuracy and integrity of the manuscript.

## CONFLICT OF INTEREST DECLARATION

The authors declare that they have no conflicts of interest.

## REFERENCES

Akintola, A. G., Balogun, A. O., Lafenwa-Balogun, F., & Mojeed, H. A. (2018). Comparative analysis of selected heterogeneous classifiers for software defects prediction using filter-based feature selection methods. *FUOYE Journal of Engineering and Technology*, *3*, 134–137.

Ali, M., Mazhar, T., Al-Rasheed, A., Shahzad, T., Yazeed Yasin Ghadi, & Muhammad Amir Khan. (2024). Enhancing software defect prediction: A framework with improved feature selection and ensemble machine learning. *PeerJ Computer Science*, *10*, e1860–e1860. https://doi.org/10.7717/peerj-cs.1860

Ali, M., Mazhar, T., Arif, Y., Shaha Al-Otaibi, Yazeed Yasin Ghadi, Shahzad, T., Muhammad Amir Khan, & Habib Hamam. (2024). Software defect prediction using an intelligent ensemble-based model. *IEEE Access*, 1–1. https://doi.org/10.1109/access.2024.3358201

Alkhawaldeh, I. M., Albalkhi, I., & Naswhan, A. J. (2023). Challenges and limitations of synthetic minority oversampling techniques in machine learning. *World Journal of Methodology*, *13*(5), 373–378. https://doi.org/10.5662/wjm.v13.i5.373

Cetiner, M., & Sahingoz, O. K. (2020, July 1). A comparative analysis for machine learning based software defect prediction systems. *IEEE Xplore*. https://doi.org/10.1109/ICCCNT49239.2020.9225352

Elreedy, D., & Atiya, A. F. (2019). A comprehensive analysis of synthetic minority oversampling technique (SMOTE) for handling class imbalance. Information Sciences, 505, 32–64.

Feng, S., Keung, J., Yu, X., Xiao, Y., Bennin, K. E., Kabir, M. A., & Zhang, M. (2021). COSTE: Complexity-based oversampling technique to alleviate the class imbalance problem in software defect prediction.

*Information and Software Technology, 129*, 106432. https://doi.org/10.1016/j.infsof.2020.106432

Gupta, M., Rajnish, K., & Bhattacharjee, V. (2023). Software fault prediction with imbalanced datasets using SMOTE-Tomek sampling technique and genetic algorithm models. *Multimedia Tools and Applications*. https://doi.org/10.1007/s11042-023-16788-7

J, A. A., & Judith, J. E. (2023). Enhanced deep learning approach for software defect forecasting. 1–7. https://doi.org/10.1109/aicera/icis59538.2023.10419998

Khleel, N. A. A., & Nehéz, K. (2024). Software defect prediction using a bidirectional LSTM network combined with oversampling techniques. *Cluster Computing*, *27*(3), 3615–3638. https://doi.org/10.1007/s10586-023-04955-9

Mafarja, M., Thaher, T., Al-Betar, M. A., Too, J., Awadallah, M. A., Abu Doush, I., & Turabieh, H. (2023). Classification framework for faulty-software using enhanced exploratory whale optimizer-based feature selection scheme and random forest ensemble learning. *Applied Intelligence*. Advance online publication. https://doi.org/10.1007/s10489-022-04427-x

McHugh, M. L. (2008). The Chi-square test: An introduction. *Biochemia Medica*, *18*(2), 112–118. https://www.researchgate.net/publication/5856449_The_Chi-square_test_an_introduction

Rathore, S. S., Chouhan, S. S., Jain, D. K., & Vachhani, A. G. (2022). Generative oversampling methods for handling imbalanced data in software fault prediction. *IEEE Transactions on Reliability, 71*(2), 747–762. https://doi.org/10.1109/TR.2022.3158949

Schober, P., Boer, C., & Schwarte, L. A. (2018). Correlation coefficients: Appropriate use and interpretation. *Anesthesia & Analgesia, 126*(5), 1763–1768. https://doi.org/10.1213/ANE.0000000000002864

Venkatesh, B., & Anuradha, J. (2019). A review of feature selection and its methods. *Cybernetics and Information Technologies, 19*(1), 3–26. https://doi.org/10.2478/cait-2019-0001

Vuttipittayamongkol, P., & Elyan, E. (2020). Neighbourhood-based undersampling approach for handling imbalanced and overlapped data. *Information Sciences, 509*, 47–70. https://doi.org/10.1016/j.ins.2019.08.062

Zhao, L., Shang, Z., Zhao, L., Qin, A., & Tang, Y. Y. (2018). Siamese dense neural network for software defect prediction with small data. *IEEE Access, 7*, 7663–7677. https://doi.org/10.1109/access.2018.2889061

## CALL FOR PAPERS

**MIJST invites to submit Unpublished, Original, and Innovative research works from any branch of Engineering, applied sciences, and related areas.**

**Submitted manuscripts will undergo a double-blind peer-review process. For submission of Manuscript template and authors' instructions, please visit journal website at: https://mijst.mist.ac.bd/mijst/index.php/mijst/**

**MIJST offers a faster peer-review process. There will be no charges for Registration, Online submission, Publication of manuscripts, and access to the published articles.**

## ABOUT MIJST

**MIST International Journal of Science and Technology (MIJST), published biannually (June and December), is a peer-reviewed open-access journal of the Military Institute of Science and Technology (MIST). This journal is a continuation of the 'MIST Journal of Science and Technology', published by MIST, under ISSN 1999-2009 from 2009 to 2011, ISSN 2224-2007 from 2012 to 2019, & E-ISSN 2707-7365 since 2020.**

**MIJST publishes original research findings as regular papers, review papers (by invitation). The Journal provides a platform for Engineers, Researchers, Academicians, and Practitioners who are highly motivated in contributing to the Engineering, Science, and Technology and Applied Sciences disciplines. MIJST welcomes contributions that address solutions to the specific challenges of the developing world.**

**The Journal is now indexed in the "DOI Crossref", "ISSN Portal", "BaglaJOL", "Creative Common", "Microsoft Academic Search", "Publons", "Semantic Scholar", "ScienceGate", "Scilit", "EuroPub", "Structurae" and "Open Journal System" databases and is accessible through the Google Scholar. The journal is also planned to be registered under the Asian Citation Indexing, Directory of Open Access Journals (DOAJ), SCOPUS, and Emerging Source Citation Indexing (ESCI) in course of time. The Journal aims to be one of the leading journals of the Country and the Region for its contributions in the advancement of Science and Technology. Unpublished innovative world-class research papers under the following subject areas are invited. Contributions from other areas of Engineering and Applied Sciences are also welcome.**

## SUBJECT AREAS:

- **AEROSPACE AND AVIONICS ENGINEERING**
- **APPLIED PHYSICS & SCIENCE**
- **ARCHITECTURE**
- **BIOMEDICAL ENGINEERING**
- **CHEMISTRY**
- **CIVIL ENGINEERING**
- **COMPUTER SCIENCE AND ENGINEERING**
- **ELECTRICAL, ELECTRONIC AND COMMUNICATION ENGINEERING**
- **ENVIRONMENTAL, WATER RESOURCES, AND COASTAL ENGINEERING**
- **INDUSTRIAL AND PRODUCTION ENGINEERING**
- **MATERIALS SCIENCE & ENGINEERING**
- **MECHANICAL ENGINEERING**
- **NAVAL ARCHITECTURE AND MARINE ENGINEERING**
- **NUCLEAR SCIENCE & ENGINEERING**
- **PETROLEUM AND MINING ENGINEERING**



***E-ISSN: 2707-7365***



***Journal URL***

**Publisher:** *R&D Wing, MIST, Dhaka, Bangladesh*
**Contact:** *R&D Wing, MIST, Mirpur Cantonment, Dhaka-1216, Bangladesh*
**Tel:** *88 02 8034194; +88 01733543389 FAX: 88 02 9011311*
**Email:** *mijst@mist.ac.bd; info@mist.ac.bd*